Max-Planck-Institut für Festkörperforschung

Stuttgart - Grenoble

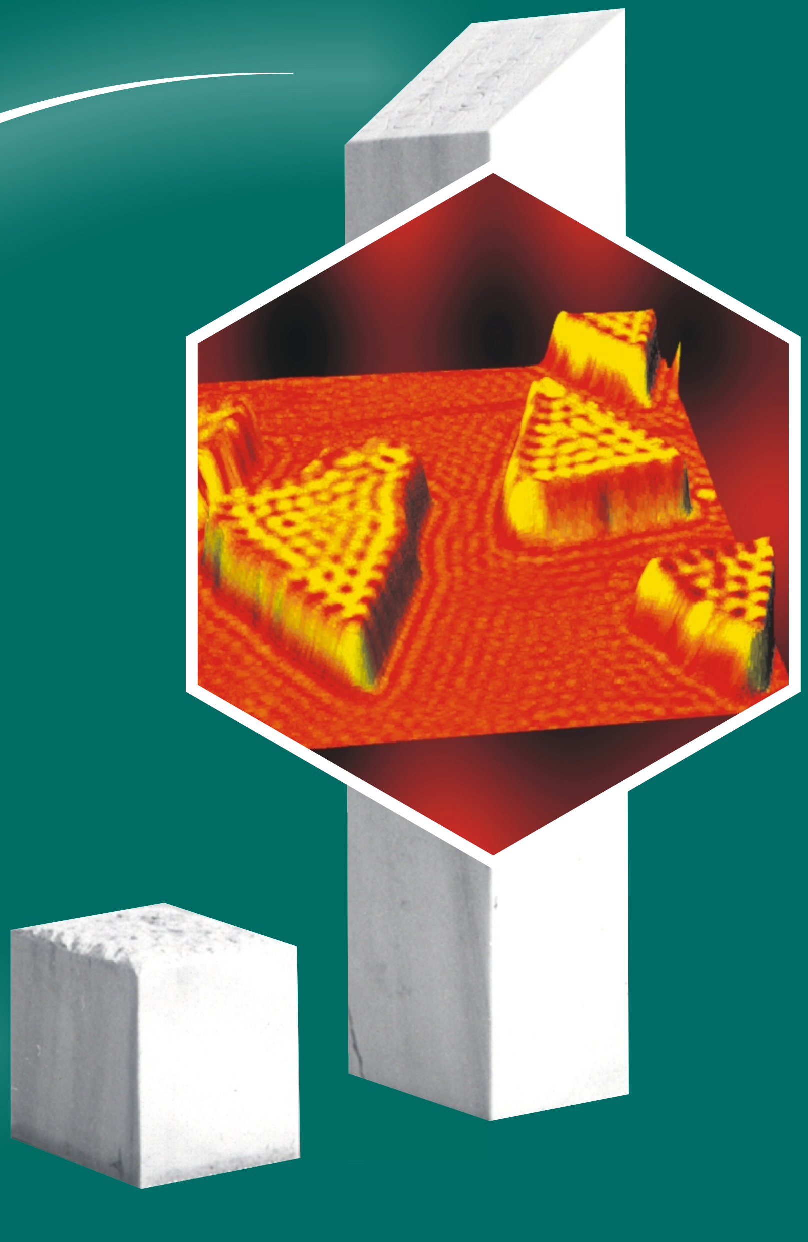

2003

MAX-PLANCK-INSTITUT FÜR FESTKÖRPERFORSCHUNG

STUTTGART — GRENOBLE

WISSENSCHAFTLICHER TÄTIGKEITSBERICHT

1. JANUAR 2003 – 31. DEZEMBER 2003

Stuttgart: Max-Planck-Institut für Festkörperforschung
Heisenbergstraße 1, D–70569 Stuttgart
Postfach: 80 06 65, D–70506 Stuttgart
Telefon: (0711) 6 89 – 0
Telefax: (0711) 6 89 – 10 10

Grenoble: C.N.R.S. – Max-Planck-Institut für Festkörperforschung
Avenue des Martyrs, B.P. 166
F-38042 Grenoble – Cedex 9 / France
Telefon: 33 / 476 85 56 00
Telefax: 33 / 476 85 56 10

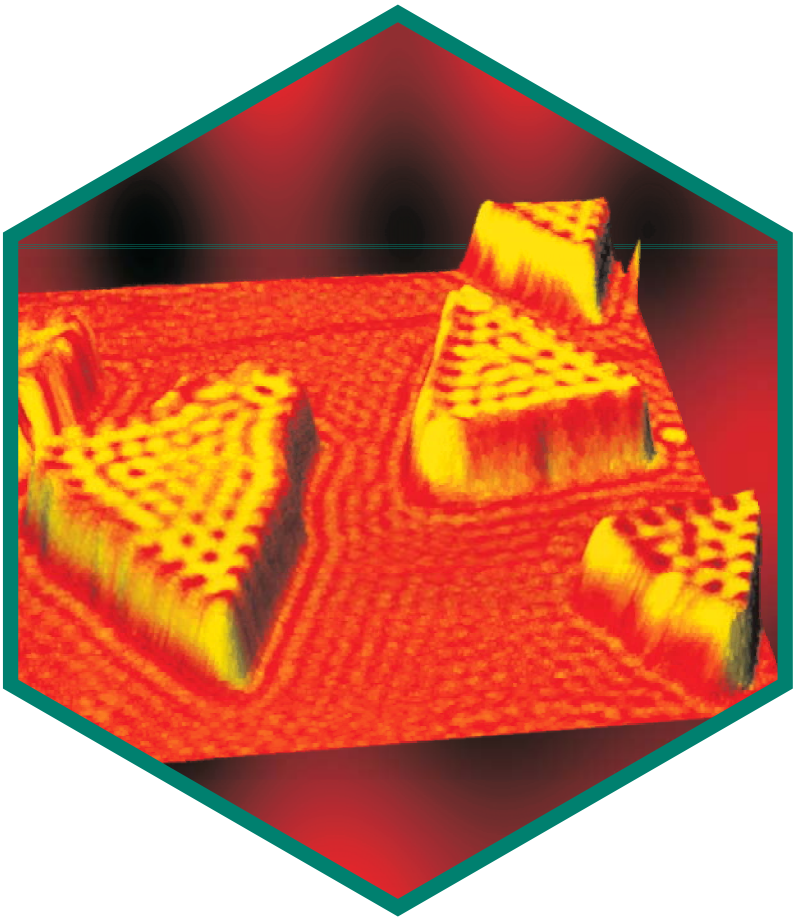

ABOUT THE HEXAGON ON THE TITLE PAGE

Spin-polarized electron gas at the surface of ferromagnetic Cobalt nanoislands grown on single crystal Cu(111). Here the data are shown in a 3D representation of the topography with the *dI/dV* (∼ local density of states) superimposed as a color-coding. The image size is 40 nm × 40 nm and the Co islands are 4 Å high. The observed modulation in the local density of states is recorded with a scanning tunneling microscope at cryogenic temperatures and is due to quantum interference of surface-state electrons scattering off the boundaries of the Co islands. *Ab initio* calculations reveal that the electronic state is spin-polarized of *sp*-majority character and thus plays an important role in understanding the magnetic properties of the Co nanostructures.

L. Diekhöner, M.A. Schneider, P. Wahl, and K. Kern;
A.N. Baranov, V.S. Stepanyuk, and P. Bruno (MPI-Halle)

[Physical Review Letters **90**, 236801 (2003); AIP Conference Proceedings **696**, 53 (2003)]

Dieser Bericht will ihnen einen Einblick in die wissenschaftlichen Arbeiten des Instituts im Jahre 2003 vermitteln. Er kann natürlich nicht vollständig sein. Die Ergebnisse der zahlreichen wissenschaftlichen Aktivitäten lassen sich inhaltlich nicht auf wenige Seiten reduzieren. Der erste Teil soll ihnen einen Eindruck von den wissenschaftlichen Arbeiten der Abteilungen und Servicegruppen geben. Der zweite Teil enthält die vollständige Veröffentlichungsliste sowie weitere nützliche Informationen über das Institut.
Wir möchten sie auch auf die Web-Seiten des Instituts hinweisen (www.fkf.mpg.de).

Am 27. Januar 2003 ist unser emeritierter Kollege Professor Dr. Ludwig Genzel kurz vor Vollendung seines 81. Lebensjahres verstorben. Er war einer der Gründungsdirektoren und hat das wissenschaftliche Profil des Instituts von Beginn an entscheidend mitgestaltet. Wir werden ihm ein ehrendes Andenken bewahren.

Wir danken allen Mitarbeiterinnen und Mitarbeitern für ihren Einsatz, ihre Leistungen und die sehr gute Arbeit.

Stuttgart – Grenoble DAS KOLLEGIUM

Mai 2004

Contents

SELECTED RESEARCH REPORTS

Reactions, syntheses and new structures

Physics and chemistry in low dimensions

Superconductivity and strongly correlated systems

Magnetic properties

Transport and dynamics

Spectroscopic methods

Chemistry

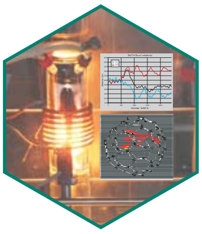

JANSEN’s department puts its main emphasis on basic research in the field of preparative solid state chemistry with the goal of developing modern materials. Classes of materials currently under investigation include oxides and nitrides of metals and non-metals as well as fullerenes, e.g., new binary and ternary oxides synthesized under high oxygen pressure, ionic conductors, structural oxide-ceramics and pigments, amorphous inorganic nitridic covalent networks, or endohedral fullerenes and fullerides. Besides employing traditional solid state synthesis methods, a large number of alternative techniques is used, e.g., the sol-gel-process, synthesis under high pressure, via an rf-furnace, at low temperatures in liquid ammonia, by electrochemical methods, or by low-temperature atomic beam deposition. Optimizing the syntheses of these materials is only a first, though crucial step, however. In addition, their chemical and physical properties, in particular optical, electrical and magnetic behavior, are analyzed both at high and low temperatures, with particular emphasis on X-ray diffraction and spectroscopic methods. This provides the basis for placing the results in the proper context regarding structure-property-relationships and modern concepts of bond-theory. A long-term goal of the department is to increase the predictability of solid state chemistry, i.e., to predict the existence of not-yet-synthesized compounds, calculate their properties, and finally provide prescriptions for their synthesis. This work involves both theoretical and synthetic aspects. On the theoretical side, structure candidates are determined using global optimization techniques, while on the preparative side kinetically controlled types of reactions that allow low-temperature synthesis of (possibly metastable) compounds are being developed. [11,74,86]

⬡ When simultaneously evaporating graphite and a metal in a rf-furnace, endohedral fullerenes can be synthesized in relatively high yields. Individual representatives like Ba@C_{74} are isolated by high performance liquid chromatograpy and subsequently characterized spectroscopically. The structures and the dynamic behavior of these fullerenes are investigated by using the Car-Parrinello molecular dynamics method.

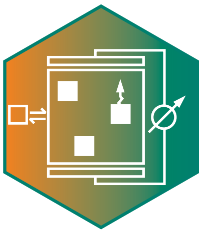

MAIER’s department is concerned with physical chemistry of the solid state, more specifically with chemical thermodynamics and transport properties. Of particular interest are ion conductors (such as proton, metal ion and oxygen ion conductors) and mixed conductors (especially perovskites). A major theme is the understanding of mass and charge transport, chemical reactivities and catalytic activities in relation to defect chemistry. Besides the clarification of local properties in terms of elementary mechanism, also their superposition to the overall system property is investigated (inhomogeneous systems, especially multiphase systems and functional ceramics). In this context interfaces and nanosystems are in the focus of interest. The research ranges from atomistic considerations and phenomenological modeling to electrochemical and thermochemical experiments. Since electrochemical investigation immediately affects the coupling of chemical and electrical phenomena, the research is directed towards both basic solid state problems as well as for the technology of energy and information conversion (fuel cells, Li-batteries, chemical sensors). [89,91,93]

⬡ Ionic and electronic charge carriers (point defects) are the relevant particles as far as chemical kinetics and mass transport is concerned. They are establishing the interaction with the neighboring phases and act on electrical and chemical driving forces.

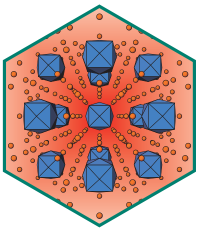

Simon's department emphasizes the investigation of metal-rich compounds (main group metals, *d* and *f* metals). The purpose of the work is on one side the development of concepts of structure and bonding (e.g., systematization of condensed cluster concept) and on the other side the search for new materials (e.g., metal-rich compounds, transition metal clusters, reduced rare earth halides, hydride, carbide, boride, boride carbide, aluminide and silicide halides of the rare earth metals, alkali and alkaline earth metal suboxides and subnitrides), phase relationships and relations between structure, chemical bonding and properties. Electron microscopy is used to characterize microcrystalline phases up to full structure refinement as well as analysis of real structure. Superconductivity is of special interest following a chemical view of the phenomenon in terms of a tendency towards pairwise localization of conduction electrons. Other fields of interest are structures of molecular crystals (in situ grown crystals of gases and liquids). Experimental techniques like diffractometry with X-rays and neutrons, XPS, UPS, HRTEM and measurements of magnetic susceptibility as well as electrical transport properties are used. [14,16,95]

⬡ $Ba_{14}CaN_6Na_{14}$ – Picodispersed salt in a metal.

Physics

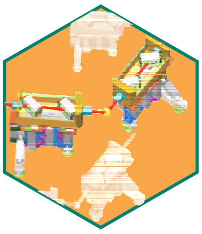

Keimer's department studies the structure and dynamics of highly correlated electronic materials by spectroscopic and scattering techniques. Topics of particular current interest include the interplay between charge, orbital and spin degrees of freedom in transition metal oxides and the mechanism of high-temperature superconductivity. Experimental techniques being used include elastic and inelastic neutron scattering, normal and anomalous X-ray scattering, Raman scattering off and in resonance as well as in high magnetic fields, spectral ellipsometry (including synchrotron radiation as a source), and optical and X-ray measurements under high pressure and high magnetic fields. Experiments at external neutron sources are carried out on a regular basis, and a spectrometer at the new research reactor FRM-II in Munich has recently been completed. The latter instrument uses a novel combination of triple axis and neutron spin echo techniques to optimize the energy resolution and allow the determination of lifetimes of magnetic and lattice vibrational excitations throughout the Brillouin zone. The group operates a high magnetic field facility for X-ray scattering at the National Synchrotron Light Source (NSLS) at Brookhaven National Lab (USA). At the NSLS and at the ANKA synchrotron in Karlsruhe, the group also operates Fourier ellipsometers for the far infrared spectral range. Close collaborations also exist with the crystal growth service group at the MPI-FKF where large, high-quality single crystals of oxide compounds are prepared with state-of-the-art optical furnaces, as well as with the high pressure and technology service groups. [62,67,83]

⬡ Central part of the novel triple axis spectrometer being built by Keimer's group at the research reactor FRM-II in Munich. Two pairs of resonant spin echo coils designed to achieve extremely high energy resolution are shown in both incident and scattered beams.

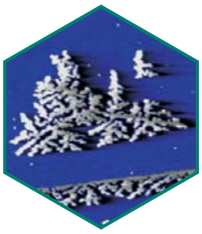

Research efforts in KERN's department are centered on nanometer-scale science and technology, primarily focusing on solid state phenomena that are determined by small dimensions and interfaces. Materials with controlled size, shape and dimension ranging from clusters of a few atoms to nanostructures with several hundred or thousand atoms, to ultrathin films with nanometer thickness are studied.

A central scientific goal is the detailed understanding of interactions and processes on the atomic and molecular scale. Novel methods for the characterization and control of processes on the atomic scale as well as tools to manipulate and assemble nanoobjects are developed. Of particular interest are: fundamentals of epitaxial growth and self-organization phenomena, atomic scale fabrication and characterization of metal, semiconductor and molecular nanostructures, quantum electronic transport in nanostructures, atomic scale electron spectroscopy and optics on the nanometer-scale. As surface phenomena play a key role in the understanding of nanosystems, the structure, dynamics and reactivity of surfaces in contact with gaseous or liquid phases are also in the focus of interest. [31,43,98]

⬡ The scanning tunneling microscope image in the logo of the Abteilung Kern shows a silver dendrite grown at 130 K on a platinum (111) surface.

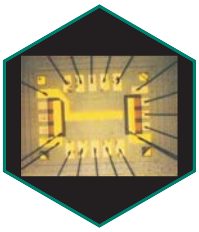

Electronic properties of heterostructures, quantum wells, superlattices, and carbon nanotubes, in particular the influence of quantum phenomena on the transport and optical response are the main topics in the VON KLITZING's department. Optical and transport measurements in magnetic fields up to B = 20 Tesla and temperatures down to 20 mK and scanning probe techniques are used to characterize the systems. The quantum Hall effect is studied by analyzing time-resolved transport, edge channels, the behavior of composite fermions and the response on microwave radiation. Electron-phonon interactions in low-dimensional systems and the phonon transmission through interfaces are investigated with ballistic phonon-techniques. Time-resolved photoconductivity, luminescence, and Raman measurements in magnetic fields are methods of characterizing the low-dimensional electronic systems. A strong current interest is the preparation of nanostructures either by selforganized growth or by synthetic routes. Coupled two- and zero-dimensional electronic systems are produced by highly specialized molecular-beam epitaxy growth and by electron-beam lithography. Phenomena like electron drag, Kondo resonance, single electron transistor and the interaction between electron and nuclear spins are investigated. The experiments are supported within the group by theoretical investigations of the transport and dynamic response of these low-dimensional electronic systems. [37,40,101]

⬡ Demanding technologies are needed for the preparation of devices used in quantum transport experiments. The figure shows a typical example where the combination of interrupted epitaxial growth, special etching processes, focused ion beam writing, contact diffusion, and gate evaporation leads to two electron layers with a distance of only 10 nm and separate contacts.

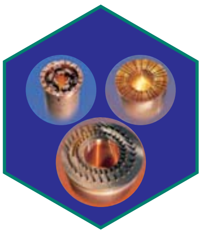

The Grenoble HML-Außenstelle of the Institute operates jointly with the French Centre National de la Recherche Scientifique (C.N.R.S.) the Grenoble High Magnetic Field Laboratory. During the first couple of years, there were two separate laboratories, the French and the German part, respectively; these have then been put together into one single laboratory on the basis of a contract for collaboration; Frenchmen and Germans working together, with one director and one single technical and scientific policy. This contract of collaboration between the C.N.R.S. and the MPG will end in 2004. The aim of the laboratory is to provide high magnetic fields with a wide range of scientific instrumentation (temperatures 30 mK to 1000 K, pressures up to 24 GPa, voltages nV to 50 kV, currents pA to several kA, etc.) allowing many interesting investigations. In the years 1990/1991, most of the technical installations were renewed and the dc-power supply was extended from 10 MW to 25 MW. We now have one of the world's most modern power and cooling installation for the generation of high magnetic fields in operation with a 20 MW resistive magnet producing a world record field in the 30 Tesla range in a bore of 5 cm. In addition, the MPG and the C.N.R.S. decided to finance a new hybrid system for fields in the 40 Tesla range, which will go into operation in 2004. All these magnets guarantee the leading role of the Grenoble HML also in the years to come. In accordance with its mission, the in-house research at the HML shows a considerable diversification into several fields in condensed matter physics, where the use of high magnetic fields is interesting or necessary, such as the study of metals, semiconductors, 2D electronic systems, magnetooptics, high-field NMR and ESR, polymers and all sorts of soft matter and even some biological systems. [28,29]

⬡ Stress and Cooling Optimized Tubular Solenoids and Bitter Coil. High-power magnets to produce stationary magnetic fields of more than 30 T with 20 MW.

Theory

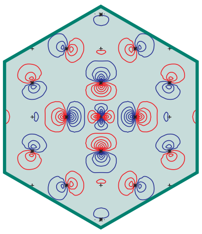

Condensed matter consists of atoms bound in a state where the quantum-mechanical kinetic energy of the electrons and the Coulomb interactions between the nuclei and electrons are in balance. The electrons play the key role in determining not only the cohesive, but also the electrical, magnetic, and optical properties of matter. The ANDERSEN department tries to improve the understanding of such properties by performing electronic-structure calculations and by developing methods. This involves: performing density-functional calculations for materials of current interest, improving the Muffin-Tin Orbital (MTO) method, deriving system-specific model Hamiltonians, and solving these. In 2003 we have, for example, performed density-functional calculations for molecular magnets and ferric wheels in order to understand magnetic anisotropy and exchange couplings. We have studied the bonding in a new cluster compound synthesized in Jansen's department and we have used NMTO Wannier-like functions together with dynamical mean-field theory (DMFT) to study Mott transitions and orbital order in the $3\,d^1$ perovskites, which have previously been investigated in Keimer's and Metzner's departments. Finally, the interplay between electron-phonon and Coulomb interactions in strongly correlated materials such as fullerides and cuprates has been studied using exact diagonalization and DMFT. [56,70,77]

⬡ Wannier-like orbital for the conduction band of the high-temperature superconductor $HgBa_2CuO_4$, plotted in the CuO_2 plane. This orbital has Cu $d_{x^2-y^2}$ symmetry and extends over several neighboring oxygen (*) and copper (+) sites. It was computed with NMTO method, using the local density approximation.

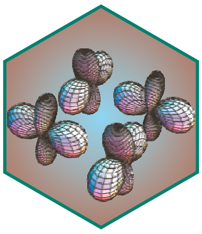

Electronic properties of solids are analyzed and computed in METZNER's department with a main emphasis on systems where electronic correlations play a crucial role, such as cuprates, manganites and other transition metal oxides. Besides symmetry-breaking phase transitions leading to magnetism, orbital and charge order, or superconductivity, correlations can also cause electron localization and many other striking many-body effects not described by the generally very successful independent electron approximation. Our present research focuses in particular on high-temperature superconductors with their complex interplay of magnetic, superconducting and charge correlations, and also on manganites and vanadates, whose electronic properties are determined by the interplay of orbital, spin and charge degrees of freedom. Another topic is the influence of lattice degrees of freedom on electronic properties, via Jahn-Teller distortion and electron-phonon interaction. Besides bulk properties of one-, two- and three-dimensional systems also problems with a mesoscopic length scale such as quantum dots and inhomogeneous quantum wires are studied. The correlation problem is attacked with various numerical and field-theoretical techniques: exact diagonalization, density matrix renormalization group (DMRG), dynamical mean-field theory (DMFT), functional renormalization group and (1/N)-expansion. Modern many-body methods are not only being applied, but also further developed within our group. [25,50,53]

⬡ Orbital order in a single layer of undoped $LaMnO_3$. The study of electronic properties of doped manganites, which show such remarkable phenomena like the colossal magnetoresistance, is an active research field because of the subtle interplay of charge, orbital, spin and lattice degrees of freedom.

Scientific Service Groups

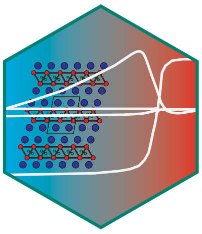

The Chemical Service Group (Kremer) develops techniques, provides experimental facilities and carries out measurements to support all experimental groups of the Institute with the characterization of the electrical transport and magnetic properties of new compounds and samples. This objective requires a great versatility of the employed experimental methods including the development and cultivation of experimental techniques to perform measurements on chemically highly sensitive and reactive small samples under inert protective conditions. Available are SQUID magnetometers, ac-susceptometers which allow measurements down to 0.3 K and magnetic fields up to 12 T, a self-developed contactless microwave transport method operating at 10 GHz, ac- and dc-electrical transport measurements in magnetic fields up to 12 T and temperatures down to 0.3 K. Materials currently under investigations are novel superconductors, unusual magnetoresistive materials, low-dimensional and frustrated magnetic systems and systems with unusual magnetic ground states. Typical examples of systems under investigation are the $RE_2C_2X_2$ (RE = Y, La; X = Cl, Br, I) superconductors, the 40 K superconductor MgB_2, spin-Peierls compounds, low-dimensional quantum chain systems, the magnetoresistive rare earth halide GdI_2. [80]

⬡ $Y_2C_2X_2$ – A halide superconductor. The white solid lines symbolize the electrical resistivity, the heat capacity and the magnetic susceptibility proving $Y_2C_2I_2$ to be a superconductor with a T_c of 10 K.

The Computer Service Group (Burkhardt) runs the Institute's central mail, print, software, backup and web servers, as well as the nine servers providing department specific services. All these servers use the Linux operating system. The server storage subsystems are designed redundantly using RAID technology and are backed up on a daily basis via the Tivoli Storage Manager (TSM) backup and archive service. Currently the total backup data volume is approaching 10 Tbyte.

The group supports about 800 PCs used as desktops and for data aquisition purposes. Out of these about two thirds run Windows and one third runs the Linux operating system. Every year about 100 PCs are replaced following a continuously updated hard- and software standard. As parallel high performance compute servers the Institute uses one IBM p655 with 32 POWER4 CPUs and one IBM SP with 84 CPUs. For applications less demanding in terms of memory and communication four Linux clusters with a total of 80 Intel Xeon (IBM xSeries 335) and 64 AMD Athlon CPUs (FSC hpcline) are a cost effective and rapidly growing computational resource.

The Institute's e-mail is handled by a central email server featuring improved virus and SPAM mail protection together with an encrypting web interface for the scientists abroad.

⬡ View inside the Tape library of the DV-FKF. Every night the data of 150 computers in the Institute is backed up. At the moment the total TSM backup and archive volume amounts to ten Terabytes.

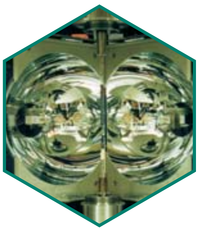

The Crystal Growth Service Group (Lin) applies, modifies and develops techniques, such as traveling solvent floating zone with infrared image furnace, Bridgman, top seeded solution growth, flux and Czochralski methods to grow single crystals from the melt or solution. A wide variety of crystals have been supplied to the physics and chemistry departments at the MPI-FKF and to outside collaborators. These range from isotopically pure semiconductors to fullerenes and transition metal oxides. Two floating zone furnaces are used predominantly to grow large single crystals of transition metal oxides for neutron and optical spectroscopy. Typical examples are superconducting oxides $Bi_2Sr_2Ca_{n-1}Cu_nO_{2+4n+\delta}$ (n = 1, 2, 3), $REBa_2Cu_3O_{7-\delta}$, $RE_{2-x}M_xCuO_4$, $SrFeO_3$ and cobaltite Na_xCoO_2. Gas phase methods are modified to grow crystals of II–VI and III–V compounds with defined isotopic components from low amounts of source materials. The grown crystals are also accurately characterized through the measurements of superconductivity, homogeneity, structure and chemical composition including cations and oxygen content, using SQUID, energy dispersive X-rays diffraction method, differential thermal and thermal gravimetry analysis, etc. The in situ observation using high-temperature optical microscopy reveals superconducting oxide melting/dissolution, nucleation and the change of phase under various growth conditions. [22]

⬡ A view of the inside chamber of the four ellipsoidal infrared image (TSFZ) furnace.

Research within the High Pressure Service Group (Syassen) is concerned with the effects of hydrostatic pressure on structural, lattice dynamical and electronic properties of crystalline solids and their high-pressure phases. The primary experimental methods are synchrotron X-ray diffraction and low-temperature optical spectroscopies. Materials currently under investigation are intermetallic compounds, semiconductors and their heterostructures, transition metal oxides, and low-dimensional solids. Pressure experiments in other research groups are supported through design of equipment and in scientific collaborations. [104,107]

⬡ Schematic view of a diamond window high-pressure cell.

The Central Information Service (Marx/Schier) for the institutes of the CPT division of the Max Planck Society, located at the Max Planck Institute for Solid State Research in Stuttgart, has access to many external commercial databases (especially from the host STN International, Fachinformationszentrum Karlsruhe). The information service offers searches for scientists at Max Planck Institutes, which cannot be done by themselves due to complexity or lack of access. Furthermore, the scientists are welcome to ask for help and support in all questions concerning scientific information. Today, databases are a major tool in processing the actual information flood in science. Bibliographic databases provide links to the original scientific literature. They are mostly online versions of printed abstract services like Chemical Abstracts or Physics Abstracts. Compound or material related searches are done in the files of the Chemical Abstracts Service, to which is no general access for Max Planck scientists until now. Beside these databases, covering general topics of science like chemistry and physics, there are many highly specialized databases on specific topics like computer science, material science, engineering, environmental sciences and many others. In addition various national and international patent files are available. Factual databases enable to search numerical data like chemical and physical properties of substances. The Science Citation Index provides the possibility to retrieve the citing papers of publications as well as total citation statistics of scientists, institutes or research disciplines for research evaluation. [117]

⬡ The archives of science are growing from the flood of information: one of the about 60 million substances in the compound file of the American Chemical Abstracts Service. Effective databases and search systems in conjunction with document delivery systems produce relief.

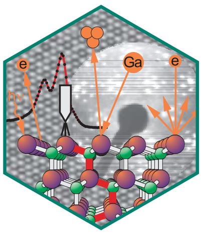

The Interface Analysis Service Group (Starke) investigates the atomic and electronic structure of solid-solid and gas-solid interfaces. Using electron spectroscopy techniques, quantitative low-energy electron diffraction, scanning probe microscopy and secondary ion mass spectrometry (SIMS), the atomic geometry and morphology as well as the chemical composition and bond coordination are determined for the sample surface and its immediate vicinity. Thin films and burried interfaces are accessible by sputtering techniques or sample cleavage methods. Experimental facilities available include a time-of-flight SIMS machine to quantify the chemical composition at the surface, within the film and at interfaces. Chemical and electronic properties are investigated in a multicomponent chamber containing high-resolution electron spectroscopy for chemical analysis. A scanning Auger microscope yields spectroscopic images with high lateral resolution. Sample morphology can be studied using an atomic force microscope and a white-light interferometer. The research activities of the group are directed towards growth and analysis of surfaces and ultrathin films of novel materials for semiconductor technology, e.g., wide bandgap semiconductors (SiC, GaN), metal silicides, as well as epitaxial metal films. Material growth, heterojunctions, metallization and ferromagnetic layers are investigated on an atomic level for a detailed understanding of the fundamental interactions involved in the growth process. In addition, molecular adsorbates are studied on these surfaces as model systems for a variety of applications. [46]

⬡ Chemical composition, electronic structure and atomic geometry are investigated for complex compound systems such as 4H-SiC (bottom). Scanning probe techniques provide real-space images (background), electron diffraction yields accurate geometry data (right), photoelectron spectra are analyzed for chemical information (left).

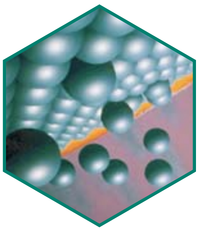

Main subject in the MBE Service Group (Dietsche/ Schmidt) is the preparation and characterization of III/V and group IV semiconductor heterostructures. We apply molecular beam epitaxy (MBE) for the material systems AlGaAs/GaAs, InGaAs and AlInGaP on GaAs substrate, and SiGe/Si on Si substrate. Our main interest is the preparation of low-dimensional nanostructures. Lateral confinement is achieved by island formation in epitaxial growth of strained heterostructures. We investigate an atomically defined in situ etching technique based on $AsBr_3$ within the MBE system. The group IV element MBE activities concentrate on the self-assembly of Ge/Si nanostructures and on devices such as inter- and intraband tunneling devices. Recently, a new subject is the formation of free-standing semiconductor nanotubes. The preparation is controlled by selective under-etching of strained epitaxial semiconductor bilayers. [33]

⬡ Atoms impinge, diffuse and nucleate on the surface of a heated crystalline substrate under ultrahigh vacuum conditions. This process is called molecular beam epitaxy.

The Optics and Spectroscopy Service Group (Kuhl) comprises the spectroscopy service lab and the ultrafast optics lab. The spectroscopy service lab provides experimental facilities for studying the optical properties of condensed matter by standard spectroscopic techniques. The laboratory is equipped with commercial grating and Fourier-spectrometers which allow absorption and reflection measurements over the total range from the ultraviolet to the far infrared. Data can be routinely taken at temperatures between 4 K and 300 K. Recently, the sample characterization techniques have been extended by standard Raman spectroscopy. The primary research subject of the ultrafast optics lab are time-resolved studies of ultrafast optical and electrical phenomena in solids. Several pico- and femtosecond laser systems including devices for the generation of sub-10 fs pulses as well as for the amplification of 150 fs pulses to 5 μJ at 200 kHz are available. Broad tunability of the photon energy is attainable by optical parametric amplifiers. Time-resolved photoluminescence, pump-probe experiments, degenerate four-wave-mixing and coherent Raman techniques are employed to investigate the coherent and incoherent relaxation dynamics of excitons, free carriers (electrons and holes) and phonons as well as carrier transport phenomena. Materials preferentially under investigation are III-V and II-VI semiconductors, in particular low-dimensional systems (quantum wells, quantum wires, and quantum dots). The variation of the relaxation processes and times as a function of the dimensionality of the carrier system are a central topic of the research.

Important current research projects are dealing with coherent light/matter coupling, control of light/matter interaction by nanostructuring, generation and dynamics of coherent phonons, generation and characterization of ultrashort optical, electrical and terahertz pulses. [109,112]

⬡ Optical parametric amplifier generating tunable femtosecond pulses for coherent semiconductor spectroscopy.

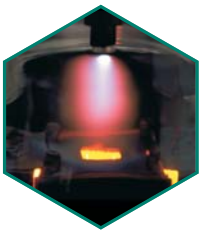

The Technology Service Group (Habermeier) offers service work in the fields of thin film preparation, microlithography and fabrication of contacts to semiconductors and ceramic materials. The experimental facilities include high vacuum evaporation and sputtering (dc, rf and reactive) techniques. Additionally, pulsed laser deposition systems are installed to prepare thin films with complex chemical composition such as high-temperature superconductors (HTS) and perovskites with colossal magnetoresistance (CMR). Dry etching techniques complement the spectrum of experimental techniques available. The research activities are closely related to the service tasks. Thin film deposition of doped Mott insulators such as HTS and CMR materials play a central role. The main focus of interest is the study of epitaxial strain in CMR and HTS thin films. Additionally, the preparation and investigation of magnetic and superconducting oxide superlattices (manganites, ruthenates and cuprates) and their mutual electronic interaction as well as the study of special oxide heterostructures are designed for polarized spin injection, exchange bias effects and magnetic flux-line pinning phenomena are of central interest. [65]

⬡ Pulsed laser deposition has become a widespread technique for the fabrication of epitaxial thin films of multicomponent materials like doped lanthanum manganites and superconducting materials.

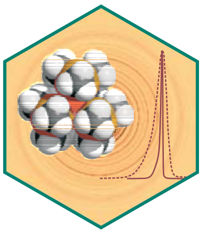

The X-ray Diffraction Service Group (Dinnebier) provides X-ray diffraction measurements of single crystals and powders in the laboratory at room and low temperature. Research within the X-ray diffraction service group is mainly concerned with the determination of crystal structures and microstructural properties (strain, domain size) of condensed matter from powder diffraction data. In addition, methodological development within this area is pursued. Special expertise in the field of solution and refinement of crystal structures from powder diffraction data can be provided. Scientific cooperation in the field of non-routine structure determination (phase transitions, disorder, anisotropic peak broadening, etc.) from powders is offered. This includes the performance of experiments at synchrotron and neutron sources at ambient and non-ambient conditions. Materials currently under investigation include organometallic precursors, binary and ternary oxides, ionic conductors, electronic and magnetic materials, and rotator phases. [18]

⬡ Quasispherical molecule of tetrakistrimethylstannylsilane with underlying two dimensional image plate powder diffraction pattern. The superimposed Bragg reflections demonstrate the difference in resolution between laboratory and synchrotron data.

Reactions, syntheses and new structures

The search for new compounds aiming at a better understanding of the solid state as well as unusual properties and new phenomena is an important aspect with long standing tradition in the research within the Institute. This search regularly pays off in surprising discoveries. Cs_2Pt clearly demonstrates the platinum atoms to be in a negative oxidation state: $(Cs^{2+})Pt^{2-}$. The extremely air and moisture sensitive compound crystallizes in the Ni_2In-type structure. The intercalation of Cu_3N with n-butyllithium to the nominal composition Li_xCu_3N turned into a surprising reaction. Cu^+ is partly substituted by Li^+ partly reduced to Cu^0 occupying the large cuboctahedra voids in the perovskite-type structure. The hydrogen insertion in LaI_2 changes the structure from tetragonal to hexagonal symmetry with a statistical intergrowth of MoS_2- and NbS_2-type structural fragments. The investigation of the crystal and molecular structure of alkali metal oxalates verifies for the first time a staggered oxalate anion in the solid state. Large single crystals of the quasi 1D chain spin system $NaCu_2O_2$ are grown by self flux technique. The nature of the magnetic interaction is predominantly antiferromagnetic.

Cs_2Pt, a platinide(-II) exhibiting complete charge separation

A. Karpov, J. Nuss, U. Wedig, G. Stollhoff, and M. Jansen

Several new compounds containing negatively charged gold anions have been synthesized in our group in recent years, where often similarities to the chemistry of the halogenides have been observed [Feldmann *et al.*, Angewandte Chemie **105**, 1107 (1993); Mudring *et al.*, Angewandte Chemie **112**, 3194 (2000)]. This behavior of gold has been attributed to the exceptional contraction of the 6*s* orbital due to relativistic effects, which, in addition, are responsible for gold having the highest electron affinity among all metals (2.31 eV).

A relativistic 6*s* contraction of comparable size has also been found in platinum. Furthermore, its electron affinity of 2.13 eV is higher than for any chalcogen atom that readily form negatively charged dianions. Nevertheless, no platinum anions had been known before. Recently, we have succeeded in synthesizing the first ionic compound containing platinum atoms in a negative oxidation state [Karpov *et al.*, Angewandte Chemie **115**, 4966 (2003)]. The synthesis has been performed by sealing cesium and platinum sponge in a tantalum ampoule, reacting at 700°C, leading to the growth of dark-red transparent hexagonal columns of Cs_2Pt. The compound is extremely air and moisture sensitive, but thermally stable up to $\approx 200°$C, where it decomposes to a not-yet identified phase containing less cesium.

Cs_2Pt crystallizes in the Ni_2In-type of structure. In this structure type, (Fig. 1), all positional parameters are fixed. Thus all structure-chemical properties of Cs_2Pt are fully determined by the values of the lattice constants, a $(=b)$ and c, or, equivalently, the volume and the c/a-ratio. Cs1 atoms are coordinated by six Pt and six Cs2 atoms at the same distance of 4.05 Å in the shape of a hexagonal prism (Fig. 1). Cs2 and Pt atoms are coordinated by three neighbors (Pt and Cs2 atoms, respectively) within the resulting hexagonal layers at a distance of 3.28 Å and six Cs1 atoms at a distance of 4.05 Å. Although the environments of Cs1 and Cs2 atoms differ significantly, they are energetically balanced with respect to their partial Madelung energies (MAPLE). We note, that the Ni_2In structure type is the end member of a sequence of polymorph modifications ($CaF_2 \rightarrow PbCl_2 \rightarrow Ni_2In$), observed for monochalcogenides under increased hydrostatic pressure. Thus, in accordance with the pressure-homologue rule, the Pt^{2-} ion might be considered as a higher homologue of the chalcogenide ions.

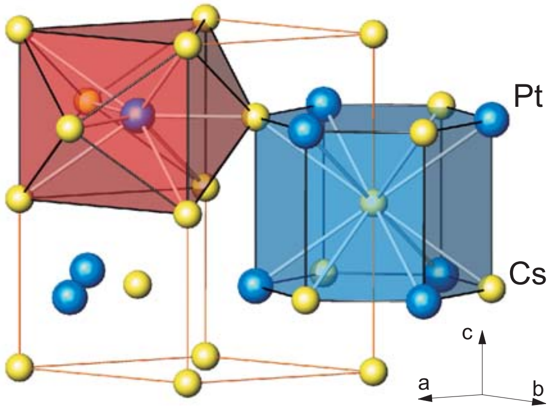

Figure 1: Perspective representation of the crystal structure of Cs_2Pt (red: $PtCs_9$-polyhedron, blue: $Cs_1Pt_6Cs2_6$-polyhedron, orange lines: unit cell edges).

Hence, we take the structure-chemical affiliation of Cs_2Pt to the family of alkali-metal monochalcogenides as a first indication of an ionic nature of this compound. However, the Ni_2In type is encountered both in (polar) intermetallic phases and in ionic crystals. Therefore, its adoption by Cs_2Pt is not sufficient proof for an ionic character of Cs_2Pt.

A strong hint that charge separation occurs are the red color and transparency of the crystals, which indicate the existence of a bandgap. This is confirmed by all theoretical calculations performed so far, irrespective of whether a density-functional (DFT) approach or the Hartree-Fock (HF) approximation has been used. The bandstructure (Fig. 2) shows bands with exclusively Pt 5*d* character. Their small splitting and dispersion indicate a basically closed *d* shell. The occupied Pt 6*s* bands lie either below (relativistic DFT) or above (non-relativistic DFT, HF) the 5*d* bands. Depending on the functional used (local or gradient corrected) and the basis set (linear muffin-tin orbital (LMTO) or Gaussian), the DFT values for the bandgap vary from 1.3 eV to 2.1 eV. In a non-relativistic calculation, the bandgap shrinks by nearly a factor of two, but the bandgap remains open nevertheless.

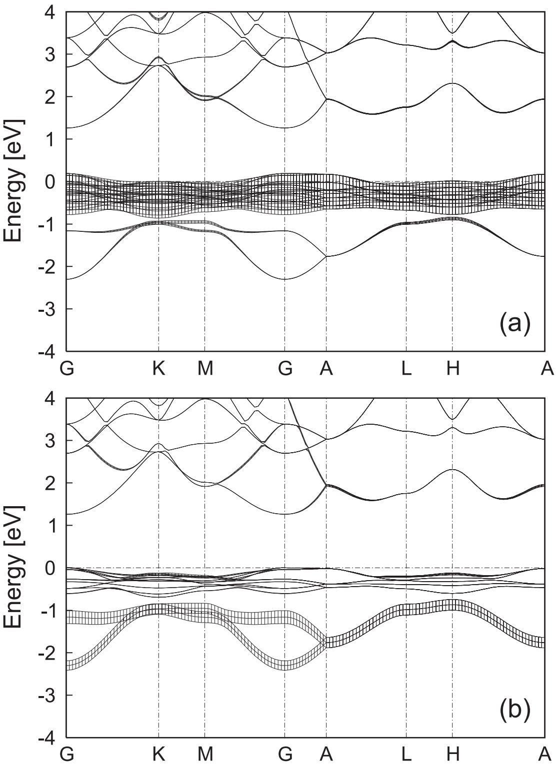

Figure 2: TB-LMTO-ASA bandstructure of Cs_2Pt. The widths of the bands exhibit the contributions of different atom orbitals: (a) Pt 5*d*, (b) Pt 6*s*.

While being important, the relativistic 6*s* contraction in platinum atoms is apparently not the only reason for the stability of the ionic Cs_2Pt compound. The domains of the electron localization function (ELF) shown in Fig. 3 exhibit the strong polarization both of the Pt^{2-} ions and the Cs^+ shells, in particular within the hexagonal Cs_2-Pt layers.

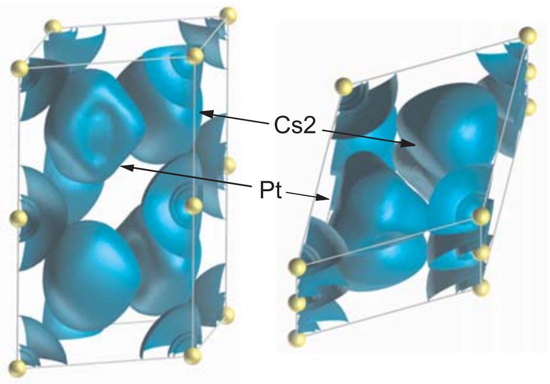

Figure 3: Domains of the electron localization function (ELF = 0.35) in Cs_2Pt.

A detailed charge analysis with the help of the Local Ansatz (LA) shows that the Pt 6*s* orbital (HF, LA: 1.97; LDA: 1.92) as well as the Pt 5*d* orbitals (HF: 9.97; LA: 9.92; LDA: 9.85) are indeed fully occupied. The Cs 6*s* and 6*p* orbitals are empty except for tails of the Pt orbitals. The small non-zero occupancy of the Pt 6*p* orbitals (HF: 0.32; LA: 0.36; LDA: 0.54) is due to a small hybridization with the 5*s*, 5*p*-core orbitals of the cesium atoms in the Cs2-Pt planes. the charge transfer mostly originates from these core states, plus a small contribution from the Pt 5*d*- and 6*s* orbitals. The lack of charge in the Cs2 cores amounts to 0.22 (HF) and 0.32 (LDA) respectively.

In order to further investigate the bonding in Cs_2Pt, CCSD(T) calculations with extended basis sets were performed for a hypothetical Cs_2Pt molecule. Freezing the 5*s*/5*p* semicore shell results in no bonding at all. The effects of various levels of approximation on the Cs–Pt bond length in the molecule are summarized in Fig. 4: the most significant effects on the bond length are observed when adding polarization functions and including semi-core valence correlation terms at the cesium atom. Besides relativistic effects, static and dynamic polarization of the Cs core appears to be likewise important for the bonding in Cs_2Pt. In a non-relativistic treatment, the bond length is larger by 0.14 Å. As in the case of the bond length, relativistic and electron correlation effects both contribute to a similar degree to the charge separation and strengthen the ionic character of Cs_2Pt.

Compared to the CCSD(T) results, the bond lengths calculated within the Hartree-Fock approximation are too large, while the LDA values are too small. The best agreement can be achieved using a gradient corrected functional (B-LYP). Analogous trends can be observed when comparing the calculated interatomic distances in the crystal with the corresponding experimental values. Note that since the relative deviations for the Cs1–Pt bond are smaller than for the Cs2–Pt bond within the hexagonal layers, the optimized *c* cell parameter is, just for geometrical reasons, too small, no matter whether HF or any DFT method is used. The LA correlation calculations lead to only small corrections of the HF results. This is due to the basis set restrictions in the solid state calculations in comparison to the molecular correlation treatment.

Thus, the results of our investigations on Cs_2Pt yield a consistent picture: both the structural-chemical relation to the alkali-metal monochalcogenides, the bandgap in the visible region of the electromagnetic spectrum as well as the charge analysis suggest an ionic arrangement consisting of Cs^+ and Pt^{2-} ions. Based on these results, Cs_2Pt joins CsAu and other aurides in providing experimental evidence for the relativistic stabilization of the $6s^2$ state.

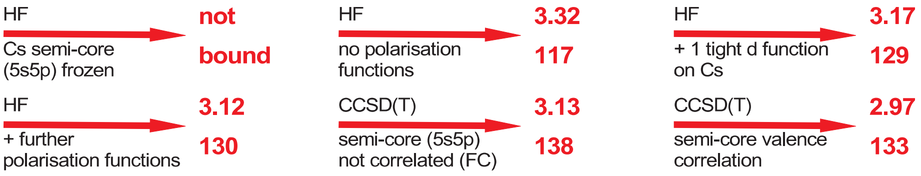

Figure 4: Cs-Pt bond length [Å] and bond angle [°] of the Cs_2Pt molecule.

Lithium copper exchange in Li-intercalated Cu_3N – with a remark on Cu_4N

F. Gulo, J. Köhler, A. Simon, and R.K. Kremer

Cu_3N crystallizes in the (*anti*-)ReO_3-type structure, an open cubic framework of Cu_6N octahedra sharing their apex atoms according to $Cu_{6/2}N$. It has been demonstrated that the large cuboctahedral void in the structure can be filled by Pd to yield (*anti*-) perovskite-type $PdCu_3N$ ($A^{XII}B^{VI}X^{II}$, see Fig. 5) corresponding to a cubic close packed (fcc) metal atom sublattice with part of the octahedral voids filled by N atoms. A recent report on superconductivity of $MgNi_3C$ initiated our interest in non-oxidic perovskites. Here we report on the successful chemical intercalation of Cu_3N with lithium, which however, turned into a surprising reaction.

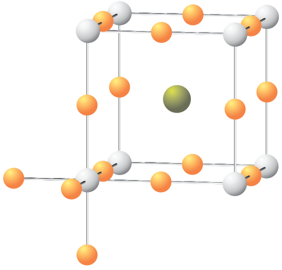

Figure 5: Projection of the structure of a perovskite/anti-perovskite ABX_3. Grey bullets correspond to B, orange to X and green to A atoms. For Cu_3N the A-site is empty, for Cu_4N or $PdCu_3N$ fully occupied and for Li_xCu_3N partially occupied by Cu.

Treatise of freshly prepared dark green Cu_3N with n-butyllithium at 60°C leads to black powder samples with the nominal composition Li_xCu_3N. The value x depends on the amount of Li offered, and according to chemical analyses we obtained Li_xCu_3N with $0 \leq x \leq 1.0$. Short reaction times of less than one day yield products, which obviously exhibit a gradient of the Li content within single grains as indicated by slightly diffuse X-ray diffraction (XRD) patterns. Prolonged reaction times of three days result in products contaminated by elemental Cu. Selected XRD patterns of the intercalation products Li_xCu_3N for $x = 0, 0.42$ and 0.85 are shown in Fig. 6. The basic pattern of the perovskite Cu_3N is maintained, and only a slight line broadening with increasing scattering angle is observed for intermediate Li contents which might be due to the above mentioned grain heterogeneity and/or a lowering of cubic symmetry. The broadening is, however, small enough that all patterns can be indexed in a primitive cubic lattice with cell parameters increasing from $a = 3.812(1)$ Å for $x = 0$ to $a = 3.833(1)$ Å for $x = 1.0$. The increase of the unit cell volume for Li_xCu_3N is somewhat unusual if compared with other intercalated systems of ReO_3 type host lattices, e.g., $Li_{0.35}ReO_3$. However, the obvious decrease in intensity for all reflections based on a primitive lattice – h, k, l with mixed even and odd indices – with increasing Li content in the series Li_xCu_3N comes as a surprise (Fig. 6) as the contribution of the Li atoms to the scattering intensity is approximately two orders of magnitude smaller than that of the sum of all other atoms. Only an occupation of the centers of the cuboctahedral voids (A-sites) in the Cu_3N framework by Cu atoms can account for the observed intensity changes. Obviously, the intercalation of Cu_3N by Li is accompanied by a substitution of Cu^+ by Li^+. This assumption is confirmed by crystal structure refinements in $Pm\bar{3}m$ on the basis of the X-ray powder diffraction data which show that the intercalation/reaction products can be described as $Li(2)_{x-y}Cu(2)_y[Li(1)_yCu(1)_{3-y}N]$ where x corresponds to the amount of intercalated Li determined by chemical analyses and y to the amount of Cu being replaced by Li determined by structure refinement, respectively. The exchange reaction at relatively low temperatures is understood in terms of the well-known high mobility of Cu^+ as a monovalent d^{10} ion in many other systems.

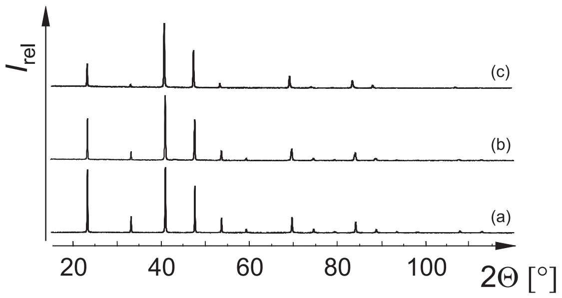

Figure 6: Powder X-ray diffraction patterns ($CuK\alpha_1$) for (a) Cu_3N, (b) $Li_{0.42}Cu_3N$ and (c) $Li_{0.85}Cu_3N$.

The coordinations of the atoms in Li_xCu_3N are those in the perovskite structure ABX_3. The N atoms occupy the octahedral B-sites coordinated by Cu(1) and Li(1) atoms, comparable to Cu_3N. Li(1) and Cu(1) atoms occupy the X-site and are linearly coordinated by two N atoms at distances ranging from 1.91 Å to 1.92 Å, which are only slightly shorter than the Li–N distances in Li_3N (Li–N = 1.94 Å). The Cu(2) atom occupies the A-site, i.e., it is cuboctahedrally coordinated by 12 nearest Cu(1) neighbors at distances around 2.7 Å, which are longer than in fcc Cu metal, 2.55 Å, but similar to the Pd–Cu distances, 2.73 Å, in $PdCu_3N$. X-ray powder diffraction data do not allow to locate the Li(2) atoms within the cuboctahedral cavities, but according to size Li(2) should not lie in the center.

Of particular interest is the chemical bonding in $Li(2)_{x-y}Cu(2)_y[Li(1)_yCu(1)_{3-y}N]$. Measurements of the magnetic susceptibility are not yet conclusive. However, based on bond distances and electronegativities of the elements the assignment of the oxidation states -3 for N, and $+1$ for both Li and Cu(1) appears reasonable. Electroneutrality then demands that Cu(2) is Cu^0. Based on the large electronegativity difference of Cu and Li, Cu^+ is reduced to Cu^0 which instead of separating as metallic copper is captured in the optimally sized voids of the Cu_3N-type framework. The same oxidation states with Pd^0 should hold for $PdCu_3N$. This description of bonding sheds light on the remarkable reaction of Mn_3N which is isostructural to Cu_3N with metals at higher temperatures leading to MMn_3N (M = Ga, Ag, Cu ...). A similar (*anti*-) perovskite, $Cu_4N = Cu[Cu_3N]$, is even formed in the thermally labile Cu/N system as a thin film by plasma deposition. In a conventional view such a film consists of fcc copper with part of the octahedral voids filled by N atoms. However, the distinctly different bonding of the two types of Cu atoms – only one of them being coordinated to the anions – rather relates Cu_4N to the remarkable suboxides of alkali metals or subnitrides of alkaline earth metals which are composites of ionic and purely metallic substructures, e.g., in $3\,Cs_7O = Cs_{10}[Cs_{11}O_3]$ or in $Na[Ba_3N]$.

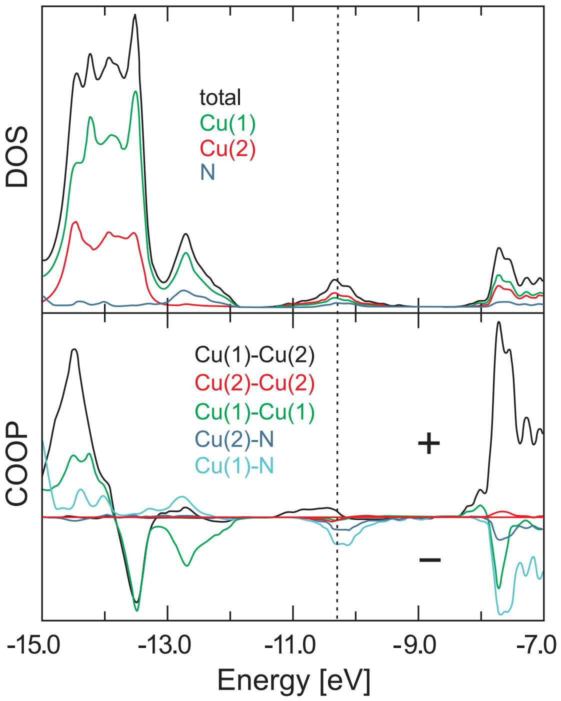

Figure 7: Density of states (DOS) and crystal orbital overlap population (COOP) for Cu_4N (Fermi level indicated by dotted line). In the COOP curves $+$ corresponds to bonding and $-$ to antibonding interactions.

For a more detailed analysis of the chemical bonding in Li_xCu_3N phases, particularly with respect to the charge distribution between Cu(1) and Cu(2) one can learn from bandstructure calculations on Cu_4N. According to calculations using the Wien code Cu_4N is a metal and Cu(1) and Cu(2) both contribute to the relatively low density of states (DOS) at the Fermi level. Extended Hückel calculations yield quite identical results and are therefore used as basis of further analysis of the chemical bonding, see Fig. 7. The Mulliken population analysis for Cu_4N results in 10.77 e$^-$ for Cu(1), 11.07 e$^-$ for Cu(2) and 5.83 e$^-$ for N. As a comparison, for Cu_3N one obtains 10.73 e$^-$ for Cu(1) and 5.81 e$^-$ for N. Hence the oxidation state +1 can be assigned to Cu(1) in Cu_4N as in Cu_3N and the former has to be described as $Cu^0[Cu_3^{1+}N^{3-}]$ with an 'extra' electron localized on Cu(2) as a first approximation. However, crystal orbital overlap population curves show as expected significant overlap between Cu(1) and Cu(2) and Cu(1) and Cu(1) states, whereas due to the large distance of 3.81 Å the overlap between Cu(2) and Cu(2) states is negligibly small, see Fig. 7. At the Fermi level the Cu(1)–Cu(2) bonding interactions are clearly dominating. A similar bonding situation for the Cu–N framework can be expected for the Li_xCu_3N phases.

The structural change of lanthanum diiodide upon hydrogenation

M. Ryazanov, A. Simon, and Hj. Mattausch

Layered metallic diiodides of rare earth elements are of considerable interest. GdI_2 was found to be a giant magnetoresistive material at room temperature, and the results of bandstructure calculations for LaI_2 indicated that it might be modified to be a superconductor.

LaI_2 crystallizes with the tetragonal Ti_2Cu structure. Square planar nets of La atoms are sandwiched by nets of I atoms. Each La atom is surrounded by a cube of I atoms slightly compressed along the *c*-axis. Bandstructure calculations revealed strong nesting characteristics at the Fermi surface of LaI_2. However, no superconductivity or charge-density wave instability was found and their absence was attributed to insufficient electron-phonon interaction. A more detailed study of electronic structure showed the presence of Van Hove singularities 0.1 and 0.5 eV below the Fermi level. Moving the Fermi level closer to the saddle points via hole doping of LaI_2 could result in superconductivity. However, previous attempts to substitute La by Ba, as well as to localize part of the conduction electrons via hydrogen insertion into the structure failed in producing superconductivity.

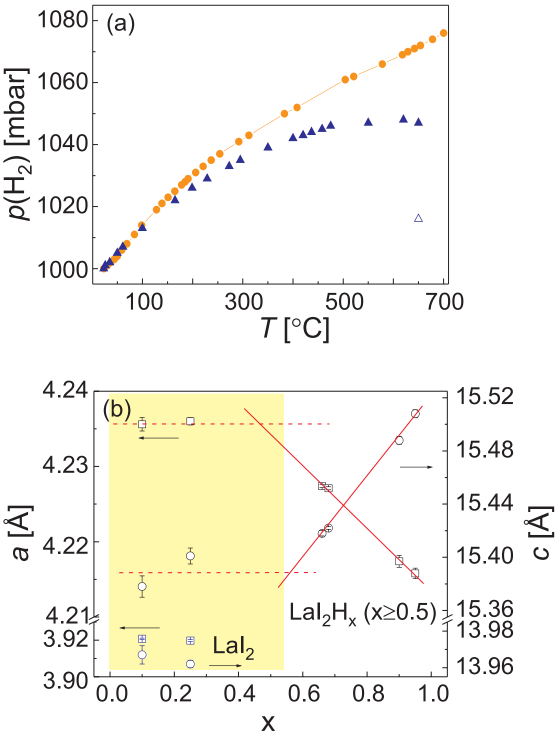

Figure 8: (a) Temperature dependence of the hydrogen pressure in a system with (filled triangles) and without (filled circles) LaI_2 at a heating rate of 5°C/min. Point (open triangle) indicates the pressure drop after keeping the sample at 650°C for 5 hours. (b) Lattice parameters of LaI_2H_x as a function of H content. The miscibility gap between LaI_2 and LaI_2H_x is painted out.

Figure 8 shows the temperature dependence of H-pressure with and without LaI_2 sample. The deviation in pressure above 150°C indicates the beginning of hydrogen absorption, which is complete after prolonged heating at 650°C and changes the color of the metallic dark purple LaI_2 into light gray. The composition of the final product LaI_2H_x, estimated from the difference of H pressure after cooling was $x = 0.97$ in good agreement with an analytically determined composition, $x = 0.95(3)$. The formulation as LaI_2H is justified.

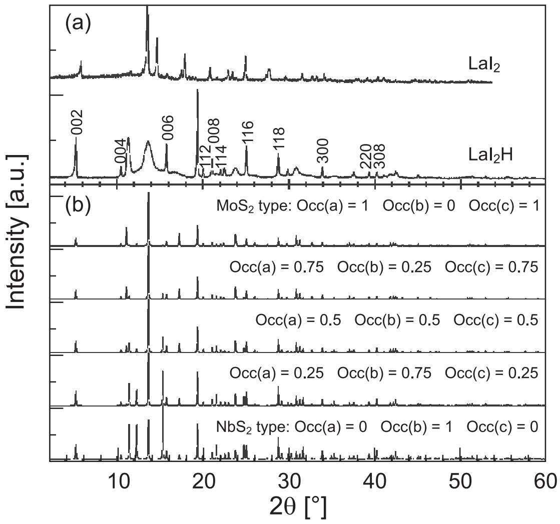

Figure 9: (a) X-ray diffraction patterns of LaI_2 and LaI_2H. The hexagonally indexed reflections in the pattern of LaI_2H are marked (strongest reflection: 110). (b) Calculated diffraction patterns for LaI_2H based on 2H–MoS_2 and 2H–NbS_2 structure types (Fig.10), as well as those simulated with a disorder in the metal atom position by varying the site occupation factors (Occ) of the metal atoms. (The letters a,b, and c denote the atomic position in terms of close-packed stacking notation.)

The X-ray diffraction (XRD) pattern of LaI_2H differs considerably from that of the diiodide as shown in Fig. 9(a). It exhibits essentially two sets of diffraction peaks. Based on the sharp peaks indexed as 00l and hhl the structure of LaI_2H is hexagonal, $P6_3/mmc$ with $a = 4.2158(7)$ Å and $c = 15.508(3)$ Å. The other set of broad peaks refers to reflections hkl with $h - k = 3n \pm 1$ for the same unit cell. The XRD patterns clearly indicate the change of symmetry from tetragonal to hexagonal upon hydrogenation of LaI_2. A more definite description of the structure of LaI_2H is hampered by the disorder expressed in the diffuse peaks. However, to a first approximation the structure is related to that of 2H–MoS_2 and 2H–NbS_2 (Fig. 10) as shown by the comparison with diffraction patterns of the latter two types in Fig. 9(b). Assuming a disorder in the metal atom positions alone as indicated in Fig. 9(b) does not model the characteristic features of the LaI_2H diagram. In particular, the broadness of peaks near $2\Theta = 14°$ and 17° can only be accounted for by the simultaneous presence of multilayer stacking sequences (2 to 5 layers) and the construction of an envelope to the resulting multipeak structure. The pattern refinement by involving stacking faults into the structure revealed a statistical intergrowth of 70% MoS_2- and 30% NbS_2-type structural fragments for the sample prepared at 650°C whereas samples prepared at 730 to 800°C are composed of 10% MoS_2- and 90% NbS_2-type stacking.

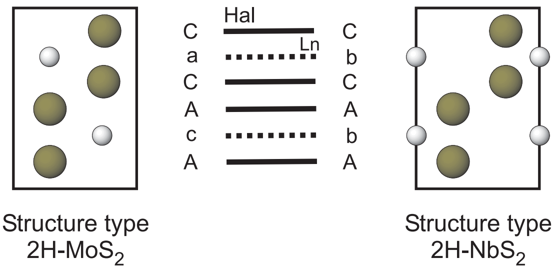

Figure 10: Stacking variants of the 2H–MoS_2 and 2H–NbS_2 structure types used for the simulation of the heavy-atom arrangement in LaI_2H projected along [100].

The change of the layer symmetry from tetragonal to hexagonal upon hydrogenation can be rationalized in terms of very efficient 2-electron/4-center bonding of the H atom, which lies in the plane of three surrounding La atoms. The structural change is the reason for the miscibility gap between LaI_2 and $LaI_2H_{0.5}$ (Fig. 8(b)) which exists in contrast to e.g., GdI_2/GdI_2H_x.

Crystal and molecular structures of alkali oxalates – first proof of a staggered oxalate anion in the solid state

R.E. Dinnebier, S. Vensky, and M. Jansen

Alkali oxalates play an important role in nature and chemistry. The sodium and potassium salts of oxalic acid are found in many plants (clover, sorrel, salicornia, spinach, rhubarb, bamboo shoots, cacao, roots, and tree barks). Oxalates find some technical and medical applications such as stain removal in photography, metal coatings for stainless steel, nickel, chromium, titanium and their alloys, cleaning and bleaching of natural fibers, textile dyeing, anticoagulants in medical tests, and dental seals. Furthermore potassium and sodium oxalate complexes are able to pass the gastric mucous membrane and therefore they are the main components of kidney stones.

Nevertheless, the long-standing efforts aimed at understanding the characteristic structural features of the oxalate anion using conventional concepts of chemical bonding still remain without a closure. In the first place, the C–C bond lengths of oxalates anions (1.567(2) Å) are about 0.04 Å too large for two sp^2 hybridized C atoms (1.515 Å). This well-established experimental fact is indicative for a bond order of one or even less.

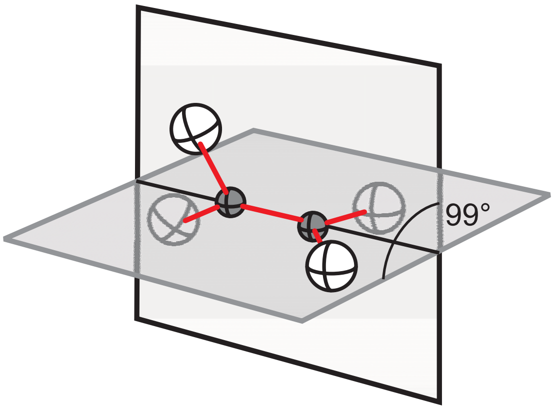

Figure 11: Sketch of the oxalate anion as found in $Cs_2C_2O_4$.

Thus, one would expect a staggered conformation (point symmetry D_{2d}) of the oxalate anions to be preferred (Fig. 11). This view is strongly supported by quantum mechanical calculations. However, experimentally the opposite is found: only few exceptions from planarity (D_{2h}) have been reported so far. If crystal structures with R-values $>$14% are disregarded, only $NaHC_2O_4{\cdot}H_2O$ (twist angle of 13°), KHC_2O_4 (13°), $(NH_4)_2C_2O_4{\cdot}H_2O$ (27°), $(NH_4)_2C_2O_4{\cdot}H_2O_2$ (28°), and $BaC_2O_4{\cdot}0.5H_2O$ (30°) remain to be considered. Evidently, in each of these instances the oxalate is involved in significant bonding interactions, i.e., H bonds. This raises the question, whether the strong prevalence of the planar configuration is related to intermolecular interactions rather than to the intramolecular electron density distribution. In order to empirically clarify this issue, we have undertaken a systematic structural investigation of ionic oxalates that exhibit the lowest possible covalent bonding to the cations, i.e., the anhydrous oxalates of potassium, rubidium and cesium.

Due to the hygroscopic nature of the oxalates, only few instances of successful single crystal syntheses of solvent-free oxalates in sufficient size and quality for single crystal analysis have been reported so far: by diffusion ($Ag_2C_2O_4$), slow evaporation from an aqueous solution ($Li_2C_2O_4$, $Na_2C_2O_4$, $K_2Be(C_2O_4)_2$) or hydrothermal crystallization (SrC_2O_4).

Therefore we performed high-resolution X-ray powder diffraction experiments on beamline X3B1 of the Brookhaven National Synchrotron Light Source in transmission geometry to determine the crystal structures of $K_2C_2O_4$ (I), α-$Rb_2C_2O_4$ (II-α), β-$Rb_2C_2O_4$ (II-β), and $Cs_2C_2O_4$ (III) at ambient conditions. In order

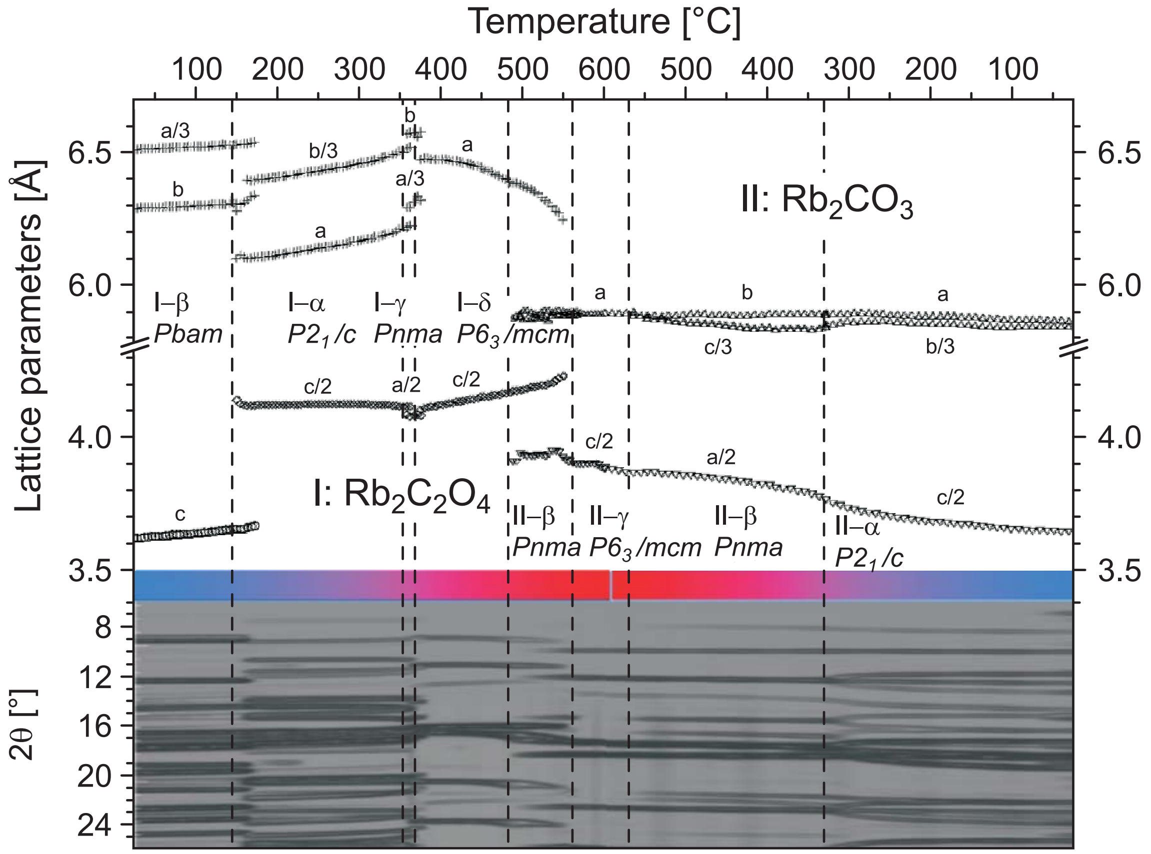

Figure 12: Dependence of lattice parameters on temperature for $Rb_2C_2O_4$ and its decomposition product Rb_2CO_3 during heating up to 600°C (4h) and consecutive cooling down to room temperature (2h) as derived from fast angle dispersive X-ray powder diffraction with an image plate detector (bottom).

to understand order-disorder phenomena and decomposition at elevated temperature, powder samples of $M_2C_2O_4$ ($M = K, Rb, Cs$) were investigated during heating up to 600°C and consecutive cooling down to room temperature using *fast* angle dispersive X-ray powder diffraction with an image plate detector (beamline X7B, NSLS). By this a variety of new crystal structures of high-temperature phases could be identified and solved. As an example $Rb_2C_2O_4$ (Fig. 12) is given showing four phases of $Rb_2C_2O_4$ and three phases of the decomposition product Rb_2CO_3 (most of which were previously unknown). The crystal structures of the alkali metal oxolates were solved using a global optimization method in direct space followed by consecutive Rietveld refinements using either restraints or rigid body notation.

Freshly prepared anhydrous rubidium oxalate consists of a mixture of two phases with the α-phase (II-α) as the predominating phase. Heating the α-phase above room temperature or storing at room temperature for some time leads to a complete transition into β-rubidium oxalate (II-β). Interestingly, a back-transformation from the β- to the α-phase sometimes occurs upon heating, followed by two additional phase transitions at higher leading temperatures to more or less disordered phases (Fig. 12).

The crystal structures of (I) and (II-β) are isotypic. They can be viewed as distorted AlB_2-type layer structures (3% distortion from hexagonal metric). The center of gravity of the oxalate anion is in the origin of a hexagonal unit cell and two alkali cations are located close to $\frac{1}{3}\,\frac{2}{3}\,\frac{1}{2}$ and $\frac{2}{3}\,\frac{1}{3}\,\frac{1}{2}$ (Fig. 13), thus forming alternating layers of oxalate anions and alkali cations. The planar oxalate anions are located on a mirror plane, forming infinite parallel chains along *c*-direction with the length of the *c*-axis as spacer. Each oxygen atom of the oxalate anions is coordinated to four alkali cations. Pairs of potassium cations (distance 3.502(1) Å; rubidium cations 3.643(1) Å) which are interconnected by parallel (C–C bond) oxalates in a zig-zag manner, form infinite parallel double chains along *c*-axis.

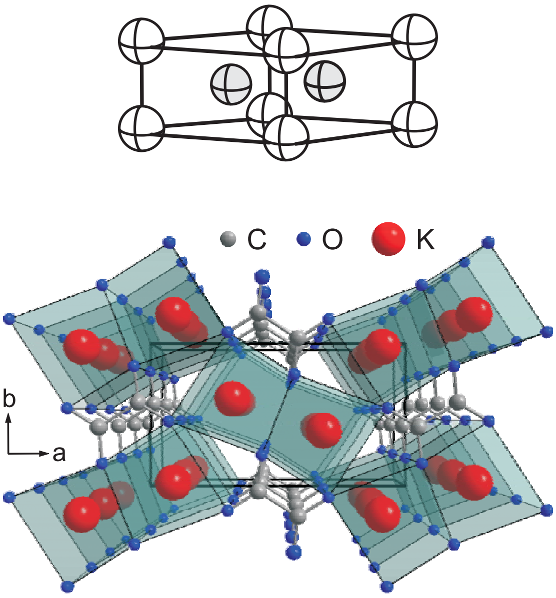

Figure 13: Packing (bottom) and packing scheme (top) of $K_2C_2O_4$ respectively β-$Rb_2C_2O_4$ at ambient conditions.

In *a*-direction, the double chains are alternately inclined by approximately ± 20° against the *a*-axis, leading to a herringbone arrangement (Fig. 13). Each alkali cation is surrounded by eight oxygen atoms in form of a distorted cube. Two cubes form a pair via a common face, and these pairs are stacked to infinite chains along *c*-axis via common faces. Therefore, each cube shares three faces with neighboring cubes. Four of the side edges of a double cube are shared with four neighboring double cubes. Each oxalate chain is connected to four double chains of alkali cations and vice versa.

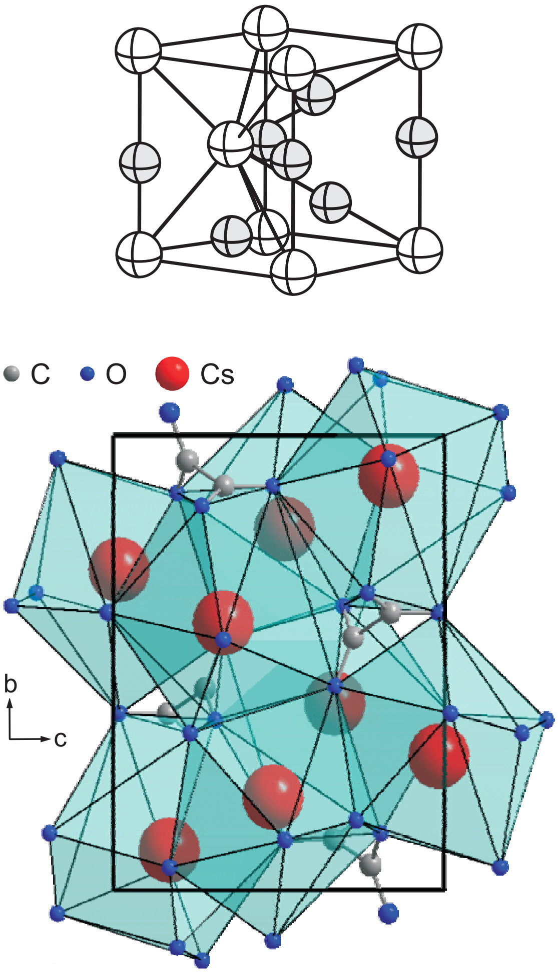

Figure 14: Packing (bottom) and packing scheme (top) of $Cs_2C_2O_4$ respectively α-$Rb_2C_2O_4$ at ambient conditions.

In contrast to the crystal structures of (I) and (II-β), the isotypic crystal structures of (II-α) and (III) are not layer but framework structures (Fig. 14). Each of the two crystallographically different alkali cations is surrounded by a different number of oxygen atoms forming irregular polyhedra. The alkali atoms Cs(1) and Rb(1), respectively, are coordinated to nine oxygen atoms (distances 3.069(9) Å to 3.557(9) Å for cesium; 2.888(6) Å to 3.386(5) Å for rubidium) which belong to six different oxalate anions in form of a distorted tetragonal antiprism capped at one of its trigonal planes. Consequently, two of the oxalate anions are side-on coordinated to the alkali cation, while one is end-on coordinated. Each alkali cation Cs(1)/Rb(1) is surrounded by eight alkali cations (six Cs(2)/Rb(2) and two Cs(1)/Rb(1)) in the second neighbor shell. Two alkali cations are located on top of the tetragonal planes, while each of the remaining six atoms is located on top of a trigonal face. The trigonal faces, built by the two side-on coordinated oxalate anions, are not capped. The alkali cations Cs(2)/Rb(2) are coordinated to ten oxygen atoms (distances 3.015(8) Å to 3.737(9) Å for cesium; 2.816(7) Å to 3.580(7) Å for rubidium) belonging to only five different oxalate anions in form of an irregular polyhedron. This can best be described as a distorted trigonal prism with twisted roof and two additional oxygen atoms capping each of the tetragonal side faces of the prism.

The roof is twisted by approximately 45°. Two end-on coordinated oxalate anions form the tetragonal base plane of the prism. Two oxygen atoms of two different oxalate anions form the roof. One of these oxalates is coordinated with only one oxygen atom therefore having the shortest alkali oxygen distance of 3.015(8) Å for cesium, and 2.816(7) Å for rubidium, respectively, while the other anion is coordinated with three oxygen atoms building one of the two caps. The other cap is formed by a side-on coordinated oxalate anion. Each alkali cation Cs(2)/Rb(2) is surrounded by eight alkali cations (six Cs(1)/Rb(1) and two Cs(2)/Rb(2)) in the second neighbor shell. The position of the centers of gravity of the oxalate anions form a *hcp*-type structure (maximum deviation of 3% and 0.8° from hexagonal metric respectively) with the (idealized) positions of the oxalate anions at $\frac{2}{3}\,\frac{1}{3}\,\frac{1}{4}$ and the alkali cations at 0 0 0, $\frac{1}{3}\,\frac{2}{3}\,\frac{1}{4}$. This is the type of packing found in Ni_2In ($P\frac{6_3}{m}mc$) (Fig. 14).

The oxalate anion itself is twisted by 99(1)° for (III) (94(3)° for (II-α)) (Fig. 11). This can be attributed to packing effects in the cesium (rubidium) compound. The influence of hydrogen bonding as found for other, slightly twisted oxalates can be excluded. The lengthening of the C–C bond of the oxalate anion (> 1.54 pm) is consistent for all oxalates and can be explained by molecular orbital theory.

The crystallographic relationship between these two different crystal structures (*Pbam* and $P2_1/c$) can be understood from the following group-subgroup relationship: $Pbam \rightarrow Pbam$ (doubled *c*-axis, which is not observed) $\rightarrow P2_1/c$. Figures 13 and 14 show the relations of the packing of the two different crystal structures. It is clearly visible that (apart from an internal twist within the oxalate anion) displacive movements of both the alkali cations and the center of gravity locations of the oxalate anions occur. No major rearrangements within the crystal structures are necessary.

It may be speculated that the driving force for the structural phase transition between (II-β) and (II-α) is related to the increased polarizability and/or size of the rubidium cation

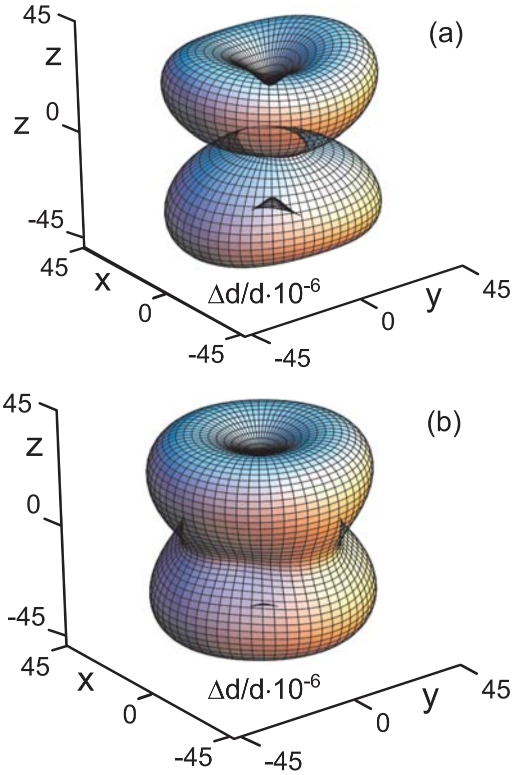

Figure 15: 3-dimensional semi-transparent representation of the microstrain distribution of (a) $K_2C_2O_4$, and (b) β-$Rb_2C_2O_4$ at ambient conditions. The *x*-axis is horizontal, *z*-axis vertical and the *y*-axis points out of the paper. The scale is in $\Delta d/d{\cdot}10^{-6}$ strain.

compared to the potassium cation. An unfavorable cation to anion size ratio for a given packing creates stress in certain directions in a crystal structure. This is directly related, via the elastic constants, to the anisotropic microstrain (Fig. 15).

The latter can be derived from high-resolution powder diffraction data. Three-dimensional anisotropic strain distributions of (I) and (II-β) on an equal scale immediately reveal an increase in strain within the layers of alkali respectively oxalate layers with an increase in the size of the cation. In both cases, the strain perpendicular to the layers is relatively low, leaving the packing in the perpendicular direction essentially unchanged. It should be noted that for cesium oxalate, no significant anisotropy of the microstrain was found.

The neutral, solvent-free alkali oxalates clearly show a strong dependence of the coordination numbers on the size of the alkali cations, starting with four (tetrahedron, lithium), six (octahedron, sodium), eight (cubic, potassium and β-rubidium) to nine respectively ten (cesium and α-rubidium).

The structures of the water containing alkali oxalates are completely different from their corresponding anhydrous compounds. As a result, it has become obvious that the conformation of the oxalate anion, when acting as a weak interacting ligand, is mainly determined by packing effects: bonded to non-polarizing cations K^+, Rb^+, and Cs^+, the planar as well as the much rarer staggered conformations have been observed.

Flux-growth and characterization of $NaCu_2O_2$ single crystals

A. Maljuk, A.B. Kulakov, M. Sofin, L. Capogna, J. Strempfer, R.K. Kremer, C.T. Lin, M. Jansen, and B. Keimer

Low-dimensional spin systems are expected to show a rich phase diagram and novel magnetic properties originating from quantum fluctuations. An interesting example is provided by quasi 1D chains of spin ($s = 1/2$) Cu^{+2} ions with competing nearest and next-nearest interactions. From this point the $NaCu_2O_2$ compound should have very interesting magnetic properties. $NaCu_2O_2$ (NCO) was synthesized for the first time over 10 years ago by partial melting of the Cu_2O and Na_2O_2 mixture. The very fine NCO single crystalline grains were mechanically extracted from the inhomogeneous product of reaction [Tams *et al.*, Journal of Alloys and Compounds **189**, 241 (1992)]. Till now no attempts have been made to grow single crystals of $NaCu_2O_2$ compound, probably due to experimental difficulties when dealing with high-reactivity compounds sensitive to moisture and (sometimes) oxygen, showing high volatility of the respective alkaline component and reactivity to all container materials at high temperatures. Here we report the first successful growth of NCO single crystals by the self-flux technique.

DTA-TG analysis was carried out using a NETZSCH STA-449C system. Small amounts of NCO substances were heated in an Ar/O_2 gas flow with the oxygen content of 10^{-3}, 0.2, 5 and 50% respectively. A high-temperature optical microscope (HTOM) ‘Olympus’ MS-11 equipped with an optical heating system (MS-E1S, ‘ULVAC-RICO’, Japan) was employed to visualize the melting point of the samples at different oxygen pressures. A compositional analysis of materials was carried out by single crystal and powder X-ray diffraction (XRD) technique, and inductively coupled plasma atomic emission spectroscopy (ICP-AES) method. The magnetization of a single crystal of $NaCu_2O_2$ was measured as a function of temperature in a superconducting quantum interference device magnetometer ('Quantum Design', model MPMS 7.0).

Our DTA-TG experiments demonstrated that the $NaCu_2O_2$ phase is stable only at an oxygen content of 10^{-3}% and less. HTOM, DTA-TG and direct melting experiments show that the $NaCu_2O_2$ compound melts incongruently at $(905 \pm 5)°C$ and has the eutectic with NaCuO phase at $(843 \pm 5)°C$ in argon atmosphere (5 N). Based on these data large-size and plate-like single crystals of NCO were grown by the self-flux method in an argon flow (5 N). The initial composition was a mixture of Na_2O (97%) and CuO (99.9%) with a 1:5 weight ratio. A total load of 50–60 g, weighed and mixed in a box filled with argon, was put in a Pt crucible covered with a tight Pt lid and heated to 940°C. The soak time was 1–2 h, the crystallization range 940–870°C and the cooling rate 1.5–2.0°C/h. The residual flux was decanted at 860–870°C. The weight loss due to the Na_2O evaporation was about 0.6 wt.% per hour at 1000°C. Thus, the growth time did not exceed 2 days. The best crystals were obtained when 1 wt.% of Na_2O was added to the initial charge in order to compensate the evaporation effect of Na_2O. Figure 16 shows typical plate-like NCO crystals with dimensions of $7 \times 3 \times 0.1\,mm^3$.

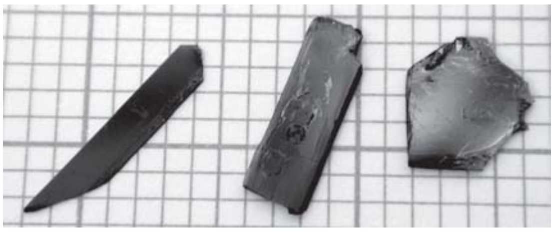

Figure 16: As-grown NCO single crystals, the small grid division is 1 mm.

All crystals are black with a metallic luster and have the (*a*,*b*) habit. ICP-AES analysis shows that all grown crystals have the correct stoichiometry Na:Cu = 1:2, and no Pt was detected. It should be mentioned that among all crucible materials (Pt, Pt/Au, Au, Ag, YSZ, Al_2O_3) only pure platinum crucibles were stable against the melt corrosion in argon flow.

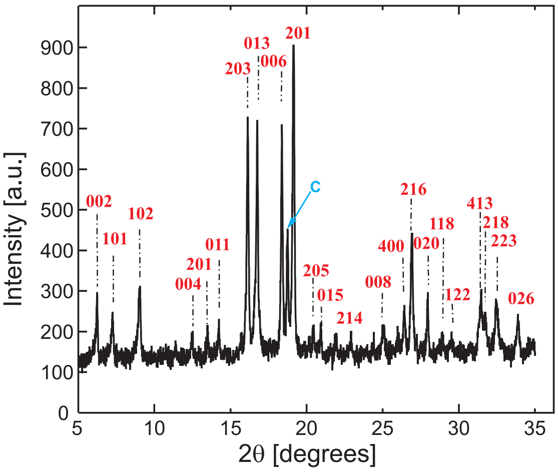

Figure 17: Powder XRD pattern of the as-grown NCO crystal. All peaks corresponded to the pure $NaCu_2O_2$ phase (MoK_α-radiation).

Figure 17 shows the powder XRD pattern of the as-grown NCO crystal. All reflections can be indexed in the orthorhombic space group *Pnma*. No traces of impurity phases were found in the sample. The spurious peak (marked as C) between the (006) and (201) Bragg-reflections arises from the experimental setup (i.e., from the collimator). The lattice parameters derived from the powder XRD data are: $a = 6.2087(1)$ Å, $b = 2.9343(1)$ Å and $c = 13.0648(3)$ Å. The X-ray rocking curve measured on a single crystal of NCO is given in Fig. 18. The profile of the (800) Bragg-reflection has a FWHM of 0.03 degree at room temperature, indicating the excellent crystal quality of the sample.

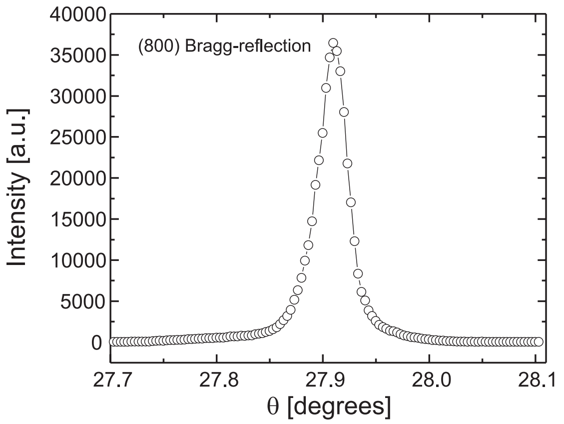

Figure 18: X-ray rocking curve of $NaCu_2O_2$ crystal, (800)-Bragg-reflection, (MoK_α-radiation).

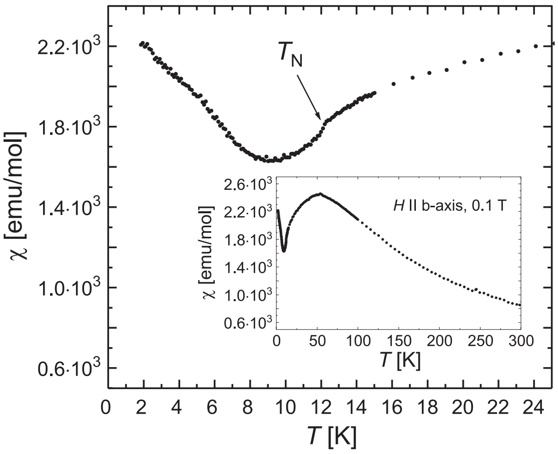

Figure 19: Magnetic susceptibility as a function of temperature for the $NaCu_2O_2$ single crystal.

The zero field cooled susceptibility shows a magnetic transition to a Néel ordered state at $T_N = 12.25$ K (Fig. 19). The high-temperature susceptibility ($150\,K < T < 300\,K$) follows a Curie-Weiss law (inset of Fig. 19) with a negative Curie temperature $\vartheta = -21.73$ K, indicating that the nature of the magnetic interactions is predominantly antiferromagnetic. The effective magnetic moment μ_{eff}, calculated per 1 mol of $NaCu_2O_2$ is $1.8\,\mu_B$. It corresponds to one unpaired electron per mol of $NaCu_2O_2$ (theoretical value $1.73\,\mu_B$). The calculated value, $\mu_{eff} = 1.8\,\mu_B$, correlates well with the assumption of the mixed valence state of copper atoms in the structure: half of copper atoms are in the valence state Cu^{+1} ($s = 0$) and the other half is in the valence state Cu^{+2} ($s = 1/2$). The neutron diffraction experiments have been performed on powder samples to solve the magnetic structure, and it has been found that the frustration leads to an incommensurability of the spin arrangement. Preliminary resistivity measurements (4-points technique) show an insulating behavior for the NCO single crystals.

Physics and chemistry in low dimensions

A central research theme at our Institute is the controlled growth and the subsequent experimental and theoretical investigation of the physical properties of low-dimensional and nanometer-sized structures. The wide spectrum ranges from semiconductor quantum wells and dots, over surface structures and electronic states, to clusters and carbon nanotubes. The presented highlights involve universal scaling of conductance in one-dimensional Luttinger liquids with impurities, testing models for quantum corrections to the ballistic electronic transport and polaronic interaction in two-dimensional electron gases, dispersion of surface electronic states and image states as deduced from STM resolved energy dependent interference patterns, growth of novel unstrained GasAs/AlGaAs quantum dots via hierarchical self assembly, Kondo-effect in electrostatically coupled quantum dots, narrow bandgap semiconductors made from nanotube peapods, thermal stability of C_{60} alkali metal compound clusters, and the controlled growth of cubic iron silicide islands and monolayers on Si(111) substrates.

Transport in Luttinger liquids with impurities

S. Andergassen, T. Enss, W. Metzner, and U. Schollwöck;
V. Meden and K. Schönhammer (Universität Göttingen)

In one-dimensional metals electrons can move freely only in one direction, while they are confined in the two transverse directions. Transverse confinement can be realized naturally in special molecules and solids with a strongly anisotropic structure, or artificially by a suitably chosen gate potential in a semiconductor heterostructure. Another possibility is to let atoms form chains on surfaces. The interaction between electrons in one-dimensional metals leads to *Luttinger liquid* behavior with various unusual properties not present in conventional (Fermi liquid) metals. In particular, the low-energy behavior of Luttinger liquids is dramatically affected by impurities. Already the presence of a single static impurity affects transport properties drastically. Carbon nanotubes enable experimentalists nowadays to analyze the effect of one or a few imperfections in an otherwise perfectly clean one-dimensional metallic system. As a consequence of the electron-electron repulsion the backscattering amplitude generated by the impurity grows at low energy scales, such that the impurity acts as an increasingly high barrier. This behavior can be traced back to the power-law singularity of the $2k_F$ density response function in a Luttinger liquid. On the other hand, a weak hopping amplitude bridging the ends of two semi-infinite chains scales to zero at low energies. It was hence argued that at low-energy scales physical observables always behave as if the impurity would split the one-dimensional system in two pieces with open boundary conditions at the end points, even if the (bare) impurity potential is relatively weak (Kane and Fisher 1992). As a consequence universal scaling behavior is expected in the low-energy limit, with exponents depending only on bulk parameters of the system, not on the impurity properties, except in special situations such as resonant double barriers.

In the last few years *functional renormalization group* (RG) methods have been developed by various groups, including ours, as a new computational tool in the theory of interacting Fermi systems. These methods are particularly powerful in low dimensions. The low-energy behavior usually described by an effective field theory can be computed ab initio for a concrete microscopic model, by solving a differential flow equation with the energy scale as the flow parameter. Thereby also the non-universal behavior at intermediate energy scales is obtained. We have applied such a functional RG scheme to one-dimensional fermionic lattice models with short-range interactions and various types of impurities. The flow equations are non-perturbative in the impurity strength while perturbative in the electron-electron interaction. We keep the full functional form of the renormalized impurity potential, instead of replacing it approximately by the scattering amplitudes at the Fermi level. This is particularly useful for transport through double barriers at resonant energy levels. Our functional RG results are checked against exact density-matrix renormalization group (DMRG) data for systems with up to 1000 sites. The functional flow equations can be solved with high accuracy for systems as large as 10^6 sites. The expected universality characterized by power-laws and universal scaling functions has been confirmed by the functional RG, but it turned out that very large systems (more than 10^4 sites) are required to reach the universal regime for moderate impurity and interaction parameters. We have computed spectral properties of single particle excitations, the density profile, and recently also transport properties for various prototype models, which we focus on in the following. Due to the flexibility of the functional RG we are able to treat several distinct impurity potentials such as local site impurities, hopping impurities (weak links) and also double barriers.

In Fig. 20 we show results for the conductance of an interacting chain with a single weak link [Meden *et al.*, Europhysics Letters **64**, 769 (2003)]. The chain is coupled smoothly to non-interacting leads. The different data points corresponding to varying impurity strengths and different lengths N_W of the interacting chain collapse on a single curve, if plotted as a function of the scaling variable $\mathrm{x} = (N_W/N_0)^{1-\mathrm{K}}$, where the parameter K depends only on bulk properties of the system and N_0 is a reference length scale depending also on the impurity strength. The scaling curve itself depends only on the bulk parameter K, in agreement with a field-theoretical analysis of the asymptotic behavior of the system.

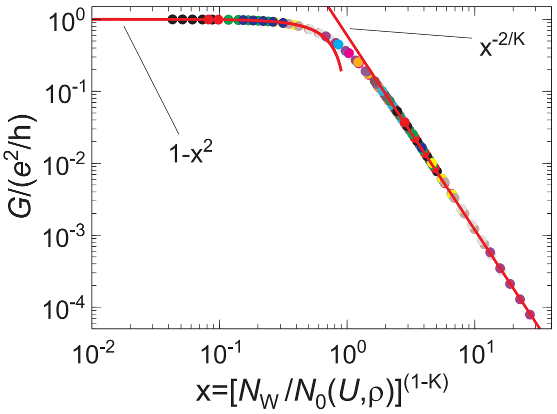

Figure 20: Scaling plot of the conductance between the ends of long chains containing interacting fermions, for different impurities and system sizes; the interacting chain is coupled smoothly to non-interacting leads; all points lie perfectly on a single scaling function which depends only on bulk parameters of the system, not on the impurity strength.

The functional RG also captures complex crossover phenomena at intermediate scales, such as in the temperature dependence of the conductance through a resonant double barrier. In Fig. 21 we show results for various symmetric double barriers of different size, that is with a varying number of sites between the two barriers. In all cases one reaches the unitarity limit $G \to 1$ (in units of e^2/h) in the zero-temperature limit, as expected for resonant scattering in a Luttinger liquid, but for spatially well-separated double barriers one obtains non-monotonous behavior with different power-laws at different

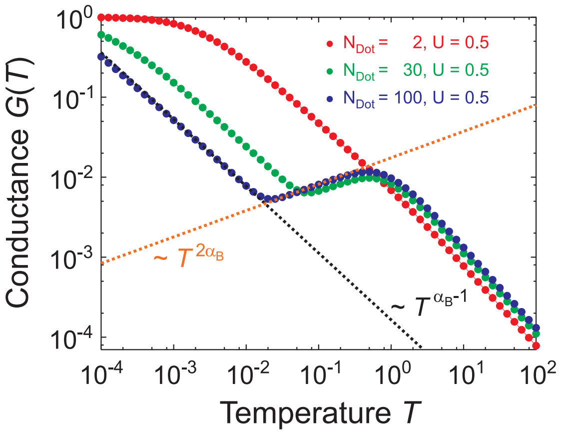

Figure 21: Conductance through a resonant double barrier as a function of temperature; for spatially well separated double barriers one obtains non-monotonous behavior with different power-laws at different scales: at intermediate temperatures the two barriers act as independent resistors in series, such that the generic power-law suppression of the conductance is observed, while at very low temperature resonant tunneling leads to an increase of the conductance until the unitarity limit is reached.

scales. At intermediate temperatures the two barriers act as independent resistors in series, such that the generic power-law suppression of the conductance through barriers is observed, while at lower temperature resonant scattering leads to an increase of the conductance towards unity.

Our functional RG method can also deal with other geometries and boundary conditions besides strictly one-dimensional systems with open ends or coupled to leads. In particular, persistent currents in a ring threaded by a magnetic flux can also be computed by the same method.

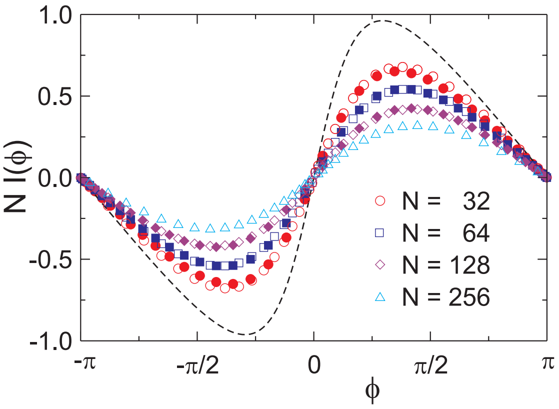

Figure 22: Persistent current in a ring with N-sites and a single impurity as a function of the magnetic flux threading the ring; results from the functional RG (open symbols) agree almost perfectly with exact DMRG results (filled symbols); the persistent current in the absence of interactions is shown as dashed line.

In Fig. 22 we show results for the persistent current in interacting rings with a single impurity as a function of the magnetic flux [Meden *et al.*, Physical Review B **67**, 035106 (2003)]. The functional RG results agree almost perfectly with exact numerical results from a density matrix renormalization group (DMRG) calculation. Interaction effects suppress the persistent current, and the suppression becomes stronger for larger systems.

Corrections to conductivity due to electron-electron interaction in 2DEG: ballistic case

V. Renard and J.-C. Portal (Grenoble High Magnetic Field Laboratory);
E.B. Olshanetsky and Z.D. Kvon (Institute of Semiconductor Physics, Novosibirsk, Russia);
N.J. Woods, J. Zhang, and J.J. Harris (University College, London)

Since the first observation of an apparent metallic state in two-dimensional electron systems (2DEG) [Kravchenko *et al.*, Physical Review B **50**, 8039 (1994)] the interest in the quantum corrections to conductivity has been renewed. In these systems the conductivity increases when the temperature decreases: a metallic behavior. Quantum corrections could explain this apparent violation of the scaling theory of localization: there can be no extended states in two dimensions for non-interacting particles.

Soon after the observation of this behavior, electron-electron interactions were suggested as a possible origin (because the phenomenon was observed in systems with large r_s ratio between Coulomb and Fermi energy).

Unfortunately, until recently [Gold *et al.*, Physical Review B **33**, 1076 (1986)] all the theories of the conductivity in 2DEG taking into account interactions were valid in the diffusive regime for which $T\tau/\hbar \ll 1$ and direct comparison with experiments (lead in the ballistic regime $T\tau/\hbar \gg 1$) was impossible.

The purpose of our work when we started to study a 2DEG formed at a Si/SiGe heterojunction was to test recent theories [Zala *et al.*, Physical Review B **64**, 214204 (2001); Gornyi *et al.*, Physical Review Letters **90**, 076801 (2003)] also valid for the intermediate and ballistic regime ($T\tau/\hbar \geq 1$). They take into account interaction and predict a possible metallic temperature dependence of the conductivity in zero field [Zala *et al.*, Physical Review B **64**, 214204 (2001)] and a negative parabolic magnetoresistance when magnetic field is applied [Gornyi *et al.*, Physical Review Letters **90**, 076801 (2003)].

In our sample $k_B T\tau/\hbar = 0.89 \cdot T$ (i.e., intermediate and ballistic regime for our range of temperatures). As can be seen from Fig. 23 theories [Zala *et al.*, Physical Review B **64**, 214204 (2001); Gornyi *et al.*, Physical Review Letters **90**, 076801 (2003)] qualitatively describe correctly the measurement that we have made in our sample. Unfortunately, the quantitative description is less clear.

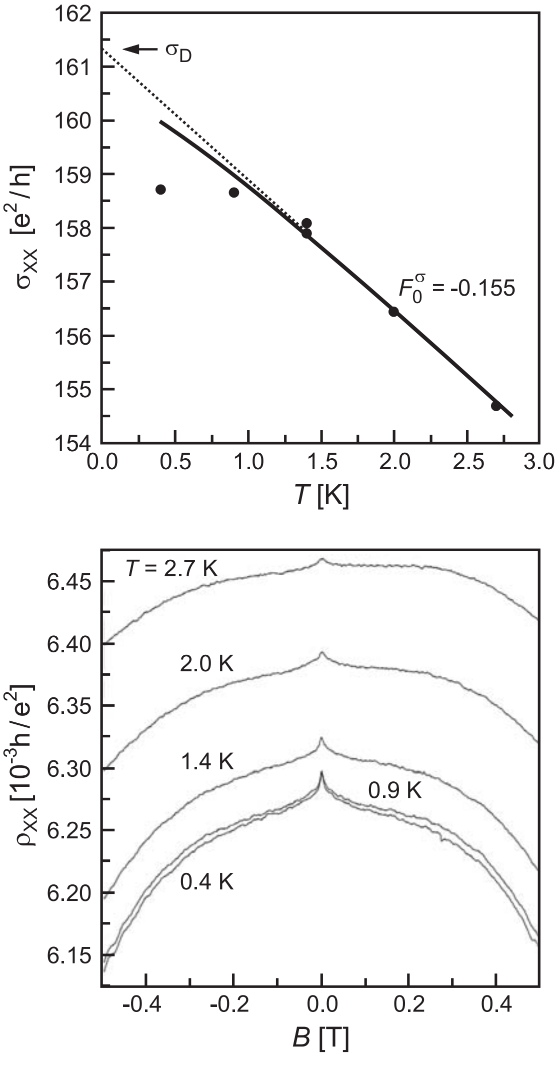

Figure 23: Zero-field temperature dependence of the conductivity of our sample and low-field magnetoresistance at different temperatures.

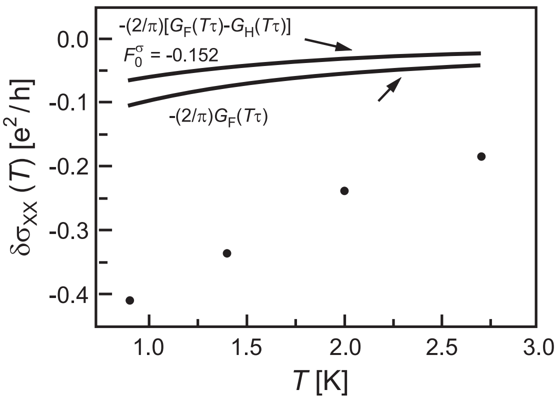

Figure 24: Correction to the conductivity obtained experimentally (dots) from the slope of ρ versus B^2 dependence and theoretical fit (black lines).

From the zero-field measurements we obtain a large value of the interaction parameter $F_0^\sigma = -0.152$ as compared to values obtained in systems with similar r_s. Moreover, it appeared impossible to fit our results for the correction to conductivity (obtained from the experimental slope of ρ versus B^2 data) to the prediction of Gornyi *et al.* [Physical Review Letters **90**, 076801 (2003)]. Figure 24 shows this theoretical predictions plotted for $F_0^\sigma = -0.152$; contribution from the singlet (G_F) only and the sum of the triplet and the singlet channels are represented ($G_F + G_H$).

We attribute this mismatch between our measurements and the theoretical predictions to the fact that none of these theories integrate both long- and short-range disorder. We believe that these two types of disorder are present in our sample and that a theory taking both of them into account would explain our results.

Polaronic interaction in a quasi two-dimensional electron gas

C. Faugeras and G. Martinez (Grenoble High Magnetic Field Laboratory);
K.J. Friedland, R. Hey, and A. Riedel (Paul Drude Institut, Berlin);
Yu. Bychkov (L.D. Landau Institut for Theoretical Physics, Moscow, Russia)

In polar semiconductors, the longitudinal optical vibration of the lattice, the LO phonon, develops a macroscopic electric field that couples to itinerant electrons through the Fröhlich interaction. The most spectacular manifestation of this interaction is the resonant magneto-polaron coupling, i.e., an anticrossing behavior between the $|n = 0 + 1\,\mathrm{LO\ phonon}>$ and the $|n = 1>$ states, n being the Landau level (LL) index, when the cyclotron frequency $\omega_c = eB/m^*$ is tuned to the LO phonon frequency ω_{LO} (B is the magnetic field and m^* the electron effective mass). However, recent studies [Poulter *et al.*, Physical Review Letters **86**, 336 (2001)] indicate that this effect is not so trivial and, in fact, was never clearly observed in a two-dimensional electron gas (2DEG).

We have performed cyclotron resonance experiments on a series of high mobility ($> 10^6\ \frac{\mathrm{cm}^2}{\mathrm{Vs}}$) and high density (ranging from $5.8 \cdot 10^{11}\ \mathrm{cm}^{-2}$ to $12 \cdot 10^{11}\ \mathrm{cm}^{-2}$) GaAs single quantum wells (QW). These QW are sandwiched between two-short period superlattices δ-doped with silicon donors. In order to avoid the *reststrahlen* band of GaAs, the epilayers were lifted-off from their original GaAs substrate and bonded onto a silicon substrate which is transparent in the infrared range of energy. Far infrared transmission measurements were performed at 1.8 K in the tilted Faraday configuration described in the previous report.

In this configuration, we observe a pronounced anticrossing behavior involving the cyclotron resonance (CR) mode and a mode with an energy lying below the measured LO phonon energy. As one can see in Fig. 25, the anticrossing energy strongly depends on the tilt angle, but the pinning energy of the CR absorption remains the same for a given sample.

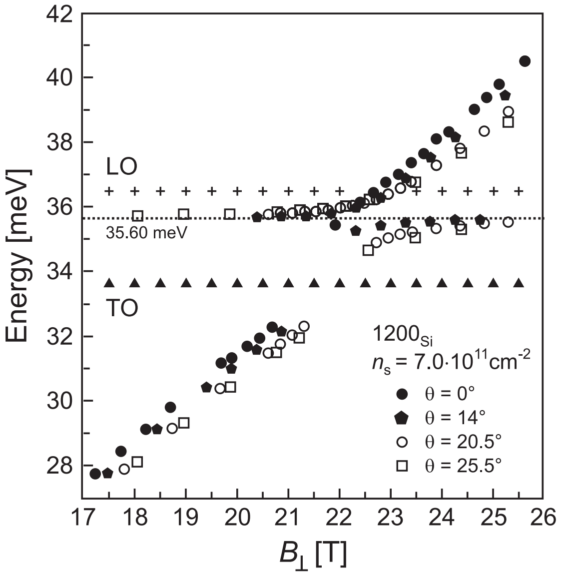

Figure 25: Position of the maxima of absorption as a function of the perpendicular component of the magnetic field for sample 1200.

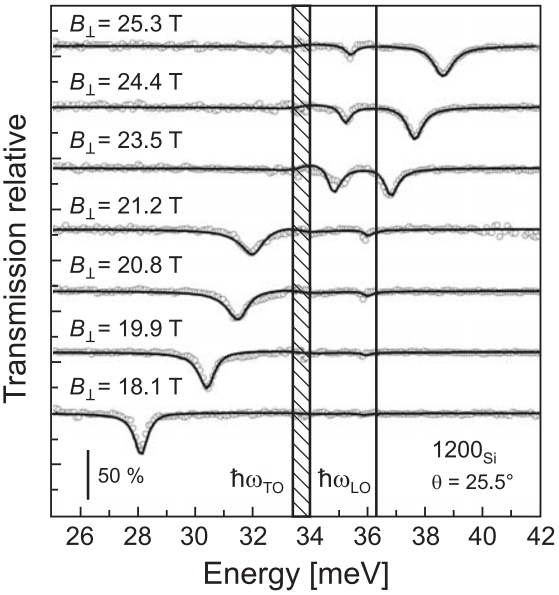

Figure 26: Fit of the relative transmission curves for sample 1200 at $\theta = 25.5°$. Open circles are experimental points, and continuous lines are the corresponding calculated relative transmission spectra. The hatched region corresponds to that of $\hbar\omega_{TO}$.

We have calculated the dielectric response of these systems using the formalism described in the previous section to reproduce the observed spectra. As can be seen in Fig. 26, this model reproduces well the observed behavior, that is the anticrossing behavior with a mode the energy of which lies in the *reststrahlen* band of GaAs. This model contains all the physics necessary to explain the observed anticrossing and to identify the second mode involved.

The second mode results from the coupling of the inter-electric-subband to the LO phonon mode that develops in a doped QW [Pinczuk *et al.*, Solid State Communications **36**, 43, (1980)]. This hybrid mode and the cyclotron resonance mode are coupled by symmetry and not by any specific electron-phonon interaction.

This hybrid mode and the pure LO phonon mode cannot exist together and, since the model used reproduces qualitatively all the observed singularities, we argue that this suggests that the concept of Fröhlich polaron mass may have no effective application in a real material.

Quantum coherence of surface- and image-state electrons

L. Diekhöner, P. Wahl, M.A. Schneider, and K. Kern;
A.N. Baranov, V.S. Stepanyuk, and P. Bruno (MPI für Mikrostrukturphysik, Halle)

Electronic states at the surface of solid materials have received substantial attention due to their reduced dimensionality and their relevance for many applications such as chemical reactions and fundamental properties like electron screening and dynamics. In nanostructures these states are confined further calling for a characterization on an atomic scale to investigate their properties. Scanning Tunneling Microscopy (STM) allows to study the electronic structure on a local (atomic) scale since the local density of states (LDOS) is proportional to the differential tunneling conductivity dI/dV which can be measured using a lock-in technique. At surfaces and nanostructures with quasi-free two-dimensional electronic states the electron density is modulated due to scattering and interference at step edges and defects. The standing wave patterns thus formed can be used to extract fundamental properties of the surface electrons.

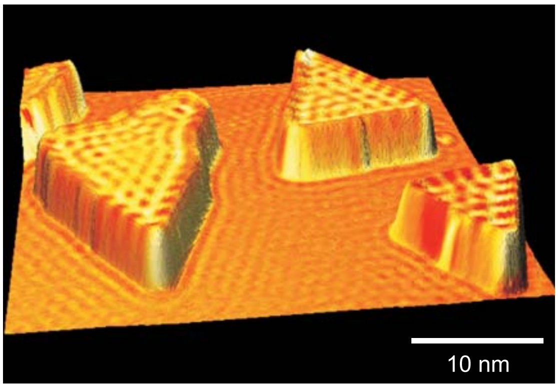

Figure 27: Representation in 3D of the topography of 2 ML high Co islands on Cu(111), where the dI/dV signal (LDOS) has been superimposed as a color-scale. $V = 0.5$ V, $I = 1.8$ nA.

Figure 27 shows a typical STM image of a Cobalt island on Cu(111), a model system to study the intrinsic coupling between electronic and magnetic properties in magnetic multilayer systems. It shows the well-known compact islands of triangular shape and bilayer height. The topography is shown in a 3D representation where the color coding is given by the simultaneously obtained dI/dV signal. On the Cu(111) surface we observe the well-known standing electron wave patterns in the LDOS. We also observe a similar pattern of Friedel oscillations on the Co islands, characteristic for a free-electron-like surface state. Although the STM normally is not sensitive to the k-space, the periodicity of the modulation is a direct measure of the wavelength and thereby the wavevector ($k_{\|}$) of the electronic state. As the bias was varied we observed a continuous variation of the wavelength of the interference pattern, i.e., a dispersion of the electronic state.

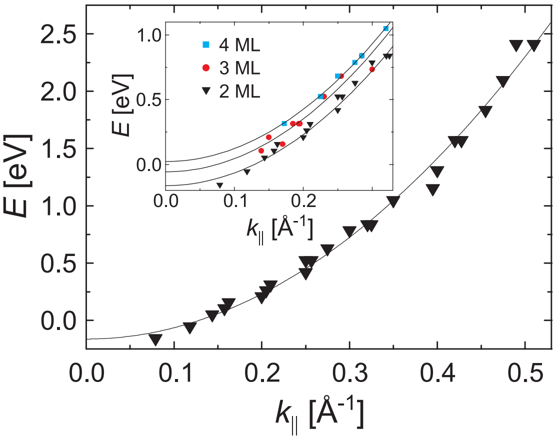

Figure 28: Dispersion relation of the electronic state determined from standing electron waves on Co islands. The inset shows the coverage dependence of the dispersion. The solid lines represent parabolic fits.

The $E(k_{\|})$ dispersion is presented in Fig. 28. The data are well-fitted by a parabolic dispersion relation $E(k_{\|}) = E_0 + \hbar^2 k_{\|}^2 / 2\,m^*$, described by an onset just below the Fermi level at $E_0 = -0.16$ eV and an effective mass $m^* = 0.38\,m_e$, where m_e is the free electron mass. All energies are relative to E_F. On higher coverage islands the standing electron waves were also observed. For 3 and 4 ML we find a parabolic dispersion with an unchanged effective mass and a small shift of the onset to higher energies with increasing coverage such that the state becomes completely unoccupied at 4 ML (inset of Fig. 28). Varying the thickness of the islands thus allows us to control the population of the state.

A.N. Baranov, V.S. Stepanyuk and P. Bruno performed *ab initio* calculations of the electronic states for 2, 3 and 4 ML of Co on Cu(111). The calculations are based on the local spin density approximation of density functional theory and the Korringa-Kohn-Rostoker Green's function method for low-dimensional systems. It was shown that the observed electronic state giving rise to standing electron waves on the Co islands is a spin-polarized state of *sp*-majority character.

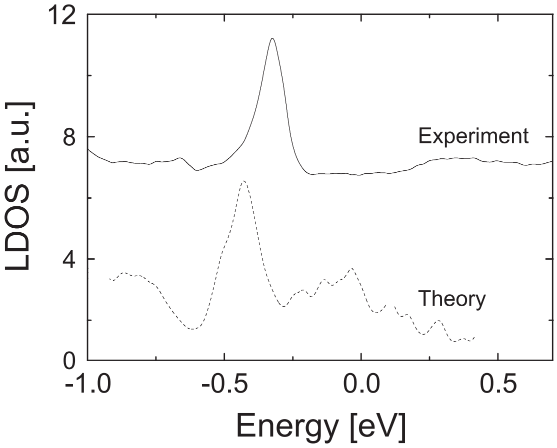

Figure 29: The upper graph (solid line) shows an STS spectrum on a 2 ML high Co nanoislands. The lower graph shows the calculated LDOS 2.1 Å above a 2 ML Co film on Cu(111). ($E_F = 0$ eV).

The calculations showed that the *sp*-majority electrons have a parabolic dispersion relation in good agreement with the experiment. Furthermore, the scanning tunneling spectroscopy (STS) studies of Co islands on Cu(111) showed the presence of an energetically localized state below E_F inducing a very intense and sharp peak in the LDOS at –0.31 eV (Fig. 29). The calculations of the LDOS above Co on Cu(111) (Fig. 29) and the charge density distribution showed that this feature originates from a $d_{3z^2-r^2}$-minority state. Due to the spin-polarized nature of this state and the very strong intensity, we believe that it may be of use in future tunneling magnetoresistance devices.

So far the quantum interference pattern in the LDOS maps has only been measured for surface-state electrons. We have recently shown that this also is possible for image-state electrons. At metal surfaces image-potential states form a Rydberg series of unoccupied states. They are confined along the surface normal by the classical image potential on the vacuum side and the bandstructure of the crystal on the other side. Energy, dispersion and lifetimes of these states have been intensively investigated mostly by two-photon photo emission (2PPE).

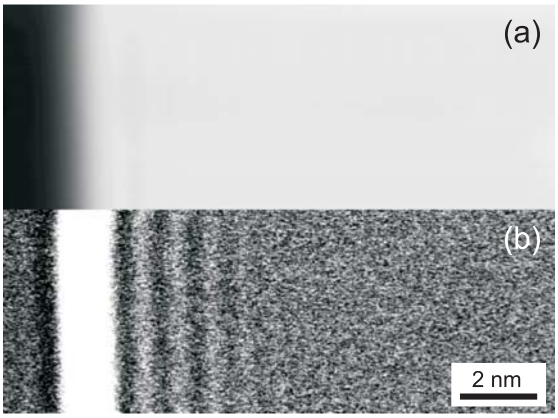

Figure 30: (a) STM topography of an artificially created step on Cu(100) taken at 5.2 V bias voltage. (b) dI/dV-map of the same place. The image-state electrons reflected at the step edge create a density modulation which appears as a standing wave pattern in the dI/dV-map.

We have studied the image states on Cu(100) by STM and STS at low temperatures. The far extension into the vacuum and the high LDOS of the image states at the surface makes them accessible to the STM. They appear at rather high bias voltages (4–8 V) due to a Stark shift induced by the electric field between STM tip and surface. Like the surface-state electrons discussed above, the image-state electrons behave as a two-dimensional electron gas in the surface plane, why electrons injected into these states on Cu(100) show a quantum interference pattern in the LDOS (Fig. 30(b)).

We determined the energies of the series of states as well as the dispersion relation and the momentum resolved lifetime of the n = 1 state. The decay of the modulation amplitude with distance from the step is correlated with the phase coherence length and thereby the lifetime. The standing wave pattern decays with increasing distance from the step edge due to geometric factors and to a loss of coherence.

We find a parabolic dispersion with an effective mass of 0.9 m_e, and lifetimes in excellent agreement with 2PPE data (Fig. 31). This shows that the motion of the electrons parallel to the surface is not noticeably affected by the field of the STM tip. The group of Th. Fauster (Erlangen) determined by 2PPE a dependence of the lifetimes of electrons in image states on their direction of motion on vicinal Cu surfaces. In a collaboration we used the local characterization of scattering processes at step edges to explain these observations as being due to an asymmetric backscattering probability at step edges.

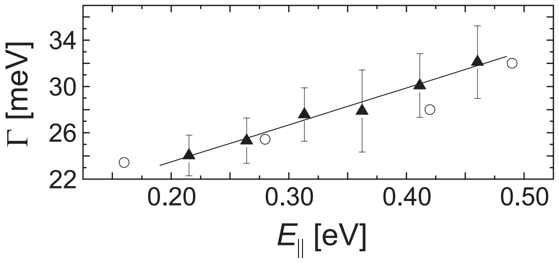

Figure 31: Phase coherence lengths of the interference pattern at a step edge converted into linewidths $\Gamma(E)$. Solid symbols are the data taken by STM, the solid line is a linear fit to them; open symbols represent linewidths determined by 2PPE measurements from Berthold *et al.* [Physical Review Letters **88**, 056805 (2002)].

Due to the local character of the measurement the STM can therefore be used to study the dynamical behavior of image-potential-state electrons confined laterally to nanostructures and to characterize the scattering properties of surface defects and adsorbates.

Novel unstrained GaAs/AlGaAs quantum dots grown by hierarchical self-assembly

A. Rastelli, R. Songmuang, C. Manzano, G. Costantini, K. Kern, and O.G. Schmidt;
S. Stufler and A. Zrenner (Universität Paderborn);
A. Schliwa and D. Bimberg (Technische Universität Berlin)

Semiconductor quantum dots (QDs), often referred to as ‘artificial atoms’, are nanocrystals in which the motion of carriers is confined in all directions. QDs are attracting much interest because they can be used to fabricate novel optoelectronic devices taking advantage of their δ-function-like density of states. Among other applications, QDs have been proposed as building blocks of future quantum computers. Most of the studies on the coherent properties of QDs and manipulation of QD states by means of light have been carried out on two semiconductor systems in which defect-free QDs are obtained by self-assembly during epitaxial growth:

(i) In(Ga)As/GaAs: due to the lattice mismatch, three-dimensional (3D) In(Ga)As islands spontaneously form on top of a thin wetting layer (Stranski-Krastanow growth mode); QDs are obtained by GaAs overgrowth of the islands.

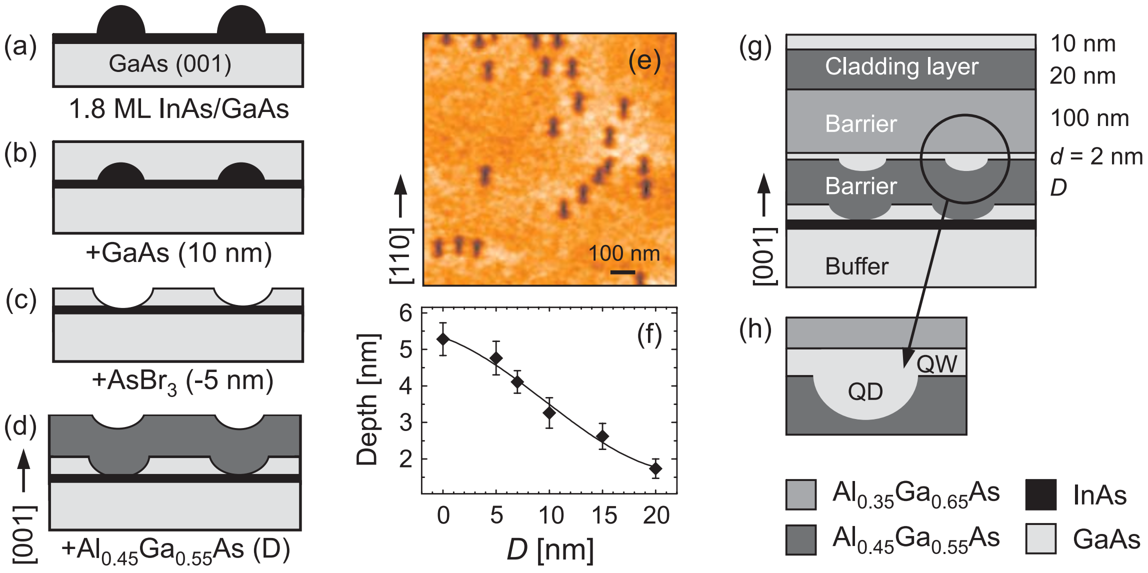

Figure 32: (a)–(d) Illustration of the self-assembly steps needed to produce an AlGaAs surface with nanoholes. (e) AFM image of GaAs nanoholes overgrown with $D = 10$ nm of $Al_{0.45}Ga_{0.55}As$. (f) Average depth of nanoholes as a function of D. Error bars represent standard deviations. (g) Sketch of the full heterostructure containing inverted GaAs quantum dots (QDs) below a quantum well (QW), as shown in (h).

(ii) GaAs/AlGaAs: shallow QDs naturally occur at thickness fluctuations of thin GaAs/AlGaAs quantum wells (QWs). The former method leads to strained QDs with large confinement energy E_c, but significant intermixing usually occurs during the fabrication process, rendering the QD morphology and composition poorly known. In the latter approach intermixing is reduced and transition energies can be tuned in the optimal spectral range of sensitive Si-photodetectors, but the morphology of the fluctuations is not controllable and E_c is small.

By using a solid-source molecular beam epitaxy (MBE) system equipped with an $AsBr_3$ etching unit, we have combined the advantages of the above approaches, obtaining 3D GaAs/AlGaAs QDs via multistep (*hierarchical*) self-assembly.

The novel structure is illustrated in Fig. 32. We first grow *self-assembled* InAs islands on GaAs(001) at low rate and relatively high substrate temperature $T_s = 500°C$ (a). The InAs islands are overgrown with 10 nm of GaAs (b) and then etched for nominal 5 nm by $AsBr_3$ gas. Strain-enhanced etching results in the preferential removal of the buried InAs islands and in the *spontaneous* formation of nanoholes at their place (c) [Songmuang *et al.*, Applied Physics Letters **82**, 2892 (2003)]. Subsequently, we deposit a layer of $Al_{0.45}Ga_{0.55}As$ with thickness D on the GaAs surface with nanoholes. Because of the low surface diffusivity of Al at T_s, GaAs nanoholes are *transferred* to the AlGaAs surface (d). Figure 32(e) shows an atomic force microscopy (AFM) image of GaAs nanoholes overgrown with 10 nm of AlGaAs. By performing a statistical analysis on the hole morphology as a function of D, we find that the average hole depth (Fig. 32(f)) decreases as the AlGaAs overgrowth proceeds. Moreover, holes shrink along the $[1\bar{1}0]$ direction (not shown) and become elongated. This indicates that holes tend to fill up mainly because of material diffusing along the $[1\bar{1}0]$ direction, where surface diffusivity of Al and Ga are maximum.

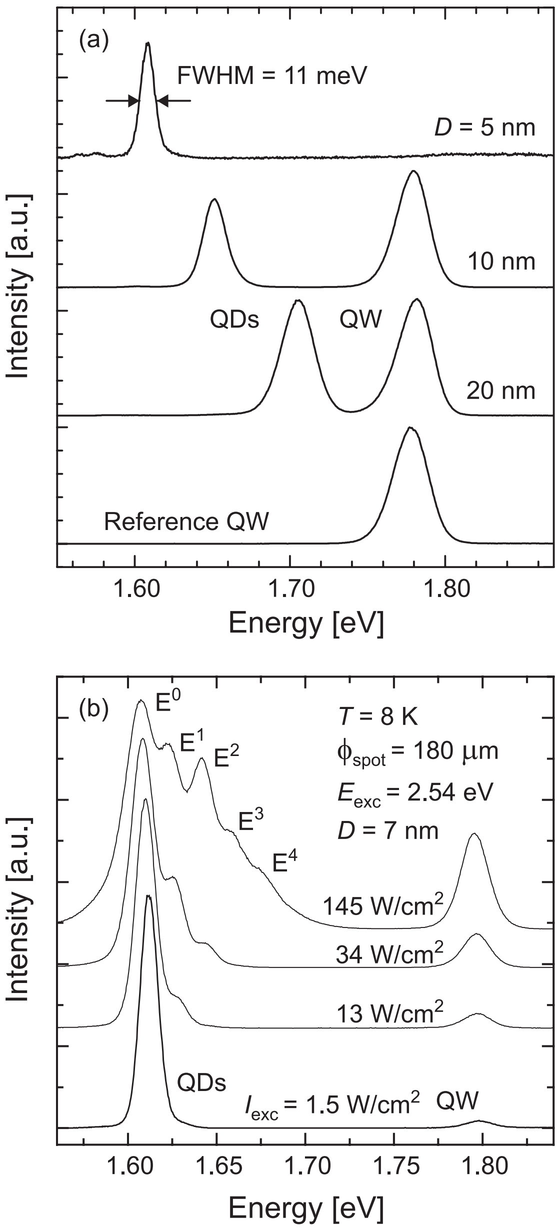

Figure 33: (a) Low excitation intensity photoluminescence spectra ($I_{\mathrm{exc}} = 1.5\,\mathrm{Wcm}^{-2}$) of samples with different AlGaAs barrier thickness D (Fig. 32). (b) PL spectra for a sample with $D = 7$ nm. With increasing I_{exc}, well-defined excited states E^1, E^2, E^3, E^4 appear while the peak E^0 slightly red-shifts. Measurement temperature T, laser spot diameter ϕ_{spot} and excitation energy E_{exc} are indicated.

In order to produce GaAs QDs, the AlGaAs holes need to be filled with GaAs. This is done by overgrowing the holes with 2 nm of GaAs at T_s and by annealing the sample for 2 minutes at T_s. This results in the *spontaneous* recovery of an atomically flat surface. A 100 nm thick $Al_{0.35}Ga_{0.65}As$ barrier, a 20 nm thick $Al_{0.45}Ga_{0.55}As$ cladding layer and a 10 nm thick GaAs cap complete the structure (Fig. 32(g)). With this layer choice, we obtain 'inverted' GaAs/AlGaAs QDs below a thin QW (Fig. 32(h)). Because of the negligible intermixing, QD size and shape are fully determined by the size and shape of the holes on the $Al_{0.45}Ga_{0.55}As$ surface. Therefore, a simple way to tune the QD size is to vary D (Fig. 32(f)).

The optical properties of the structure shown in Fig. 32(g) were studied by standard photoluminescence (PL) spectroscopy, as a function of D. Figure 33(a) shows a series of low excitation intensity ($I_{\mathrm{exc}} = 1.5\,\mathrm{Wcm}^{-2}$) spectra collected at 8 K. The bottom spectrum corresponds to a reference 2 nm thick $Al_{0.45}Ga_{0.55}As/GaAs/Al_{0.35}Ga_{0.65}As$ QW without QDs. The peak at energy $E_{\mathrm{QW}} = 1.777$ eV is due to the bound-exciton recombination in the asymmetric QW. The broad emission is mainly due to the roughness of the inverted $Al_{0.45}Ga_{0.55}As/GaAs$ interface.

When nanoholes are present on the $Al_{0.45}Ga_{0.55}As$ surface prior to GaAs overgrowth, a second peak appears at an energy E^0. We assign this peak to carriers confined in the QDs. With increasing D, E^0 shows a pronounced blue shift as expected because of a reduction of the average hole depth. Remarkably, the sample with $D = 5$ nm displays an ultranarrow QD emission line with full width at half maximum (FWHM) of 11 meV. We achieved even FWHM = 8.9 meV by tuning other growth parameters. In addition, large confinement energies of $E_c = E_{\mathrm{QW}} - E^0 \approx 200$ meV or more can be obtained with this method.

A distinctive feature to be expected for QDs is a state filling effect and the appearance of excited states as I_{exc} is increased. This is what we observe in Fig. 33(b) for a sample with $D = 7$ nm. At least 4 well-defined excited states in the energy range from E^0 to E_{QW} are visible and even more appear at higher I_{exc} (not shown). A similar behavior is observed for other samples with very weak inhomogeneous broadening, such as that with $D = 5$ nm.

A subtle effect noticeable in Fig. 33(b) with increasing I_{exc} is a monotonic red shift of the E^0 peak. The total shift measured by varying I_{exc} from 1.58 to 145 W cm^{-2} is 3.7 meV. In order to understand this behavior and to gather further insight in the optical properties of our QDs, we performed single-QD PL and PL excitation (PLE) spectroscopy measurements (Fig. 34(a)) on a sample containing QDs with very low surface density ($0.5\,\mu\text{m}^{-2}$). The spectra show extremely narrow lines, with widths limited by the measurement resolution (about 200 μeV), witnessing the high quality of the structure. At low excitation (spectrum PL1 in Fig. 34(a)) the single line is due to ground-state excitons (X) confined in the QD. At higher I_{exc} (spectra PL2 and PL3 in Fig. 34(a)), peaks appear at the low-energy side of X. We identify a biexcitonic line (XX) separated by 3.0 meV from the X line and probable multiexcitonic lines. In spectrum PL3 such lines become more intense than the X line and are responsible for the red-shift of the E^0 peak in Fig. 33(b). Spectra PL2 and PL3 show features also on the high-energy side of X. At very high I_{exc} (spectrum PL3) many lines evolve and merge into broad peaks similar to those observed in Fig. 33(b), most probably because a large number of carriers populates the investigated QD and its surroundings. For this reason we focus our attention on the few peaks appearing at moderate excitation power (spectrum PL2). Some of them (e.g., those labeled with A and B) can be attributed to recombination of excited-state excitons. This is confirmed by the PLE spectrum shown in Fig. 34(a) obtained by scanning the excitation energy E_{exc} and detecting the light emission at the X energy. Similar spectra were obtained for several other QDs in the same sample confirming the good ensemble homogeneity.

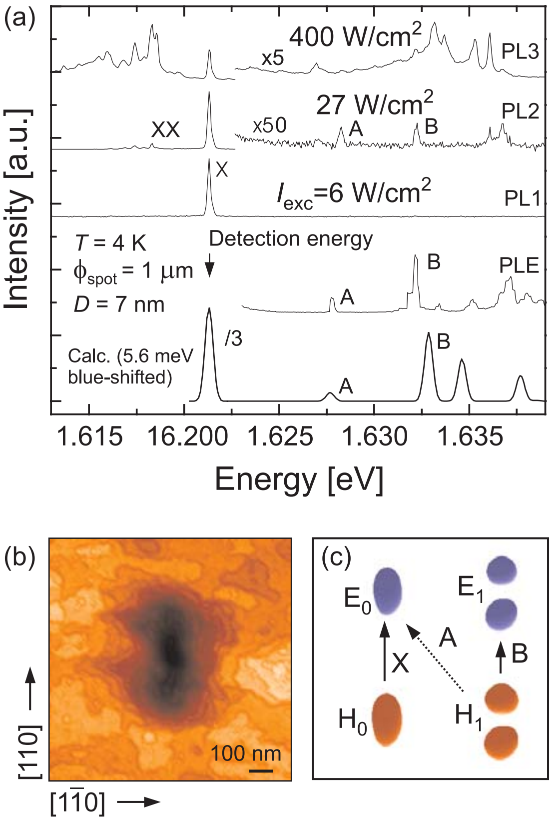

Figure 34: (a) PL ($E_{\text{exc}} = 1.96$ eV) and PLE spectra of a single QD for different I_{exc}. Ground-state excitonic (X), biexcitonic (XX) and excited state excitonic transitions (e.g., A and B) are visible. The bottom graph is the calculated excitonic absorption spectrum for a QD with geometry given by the STM topograph shown in (b). (c) 3D representations of ground and first excited-state wavefunctions for electrons (E) and holes (H) in the QD, giving rise to the transitions X, A and B.

Thanks to the negligible intermixing and absence of strain, we can calculate the optical properties of our QDs by taking as input nominal layer compositions and measured QD geometry. To exclude influences of the surface oxide, we determined the hole morphology at high-resolution by ultrahigh vacuum scanning tunneling microscopy (STM). Figure 34(b) shows an STM topograph (taken at constant current) of a typical nanohole after overgrowth with $D = 7$ nm of $Al_{0.45}Ga_{0.55}As$. With the hole geometry given by STM and a QW thickness of 2 nm (Fig. 32(h)), we calculate the excitonic absorption spectrum of such a GaAs QD by using 8-band $k{\cdot}p$ theory. The calculated spectrum, shown in Fig. 34(a), is blue-shifted by 5.6 meV so that the energy of the ground state transition matches the measured one. We have no access to the exact geometry of the QD measured by PL, but the shift is well within the FWHM (12 meV) of the inhomogeneously broadened E^0 peak for this sample. We see that the position of the peaks A and B is well reproduced by the calculation. In a single particle picture, with electron and hole levels labeled $\mathrm{E_j}$ and $\mathrm{H_j}$, respectively, these two absorption lines originate from the $\mathrm{H_1-E_0}$ and $\mathrm{H_1-E_1}$ transitions, as depicted in Fig. 34(c). Since the overlap integral of wavefunctions with different index j is small (see representation of the envelope wavefunctions in Fig. 34(c)) the calculated A peak is less intense than the B peak. This result is in good agreement with the experimental PLE spectrum shown in Fig. 34(a).

To our knowledge, this is the first direct comparison of a calculated absorption spectrum with no adjustable structural parameters to measured single-QD PL and PLE spectra. In fact, in Stranski-Krastanow grown QDs assumptions are necessary on shape and compositions.

Two electrostatically coupled quantum dot systems as a new realization of the Anderson impurity model

D. Quirion, U. Wilhelm, J. Schmid, J. Weis, and K. von Klitzing

In the last decade, quantum dots weakly coupled to leads – denoted in the following as quantum dot systems – have been the subject of many studies in electrical transport. Due to the electron-electron interaction on the quantum dot site, Coulomb blockade and single-electron charging effects are observed. Due to their in situ tunability – for instance, the electron number on the quantum dot and tunnel coupling to the leads – quantum dot systems are considered as model systems which mimic also basic properties of single atoms or molecules between leads. In the more recent years, it has been experimentally demonstrated, that such systems show under certain conditions Kondo physics as it was already predicted in 1988 by mapping the Anderson impurity model [Anderson, Physical Review **124**, 41 (1961)] on a single quantum dot system (see review by Kouwenhoven and Glazman [Physics World, 33, January 2001]). The presence of a spin-degeneracy on the quantum dot site induces at low temperature correlated electron tunneling between the quantum dot and the leads, forming overall a spin-singlet state. A highly conductive channel of transport is opened between the leads via the quantum dot, which even reaches the conductance $2e^2/h$ in the case of symmetric tunnel couplings to the leads – the value also found for a spin-degenerate one-dimensional channel. Increasing the temperature breaks the correlations, the Kondo effect is destroyed, and the Coulomb blockade effect is recovered.

The Anderson impurity model describes a spin-degenerate energy level at an impurity or quantum dot site which is coupled via tunneling to a Fermi sea containing electrons of both spin orientations. In other words, it describes two separate electron subsystems labelled by a two-valued index which is usually identified with the spin quantum number (Fig. 35(a)). The two spin electron systems interact only on the impurity site through Coulomb interaction which suppresses double occupancy of the impurity. As we proposed [Wilhelm *et al.*, Physica E **9**, 625 (2001)], one may interpret the ‘spin’ index of the Anderson impurity model differently which

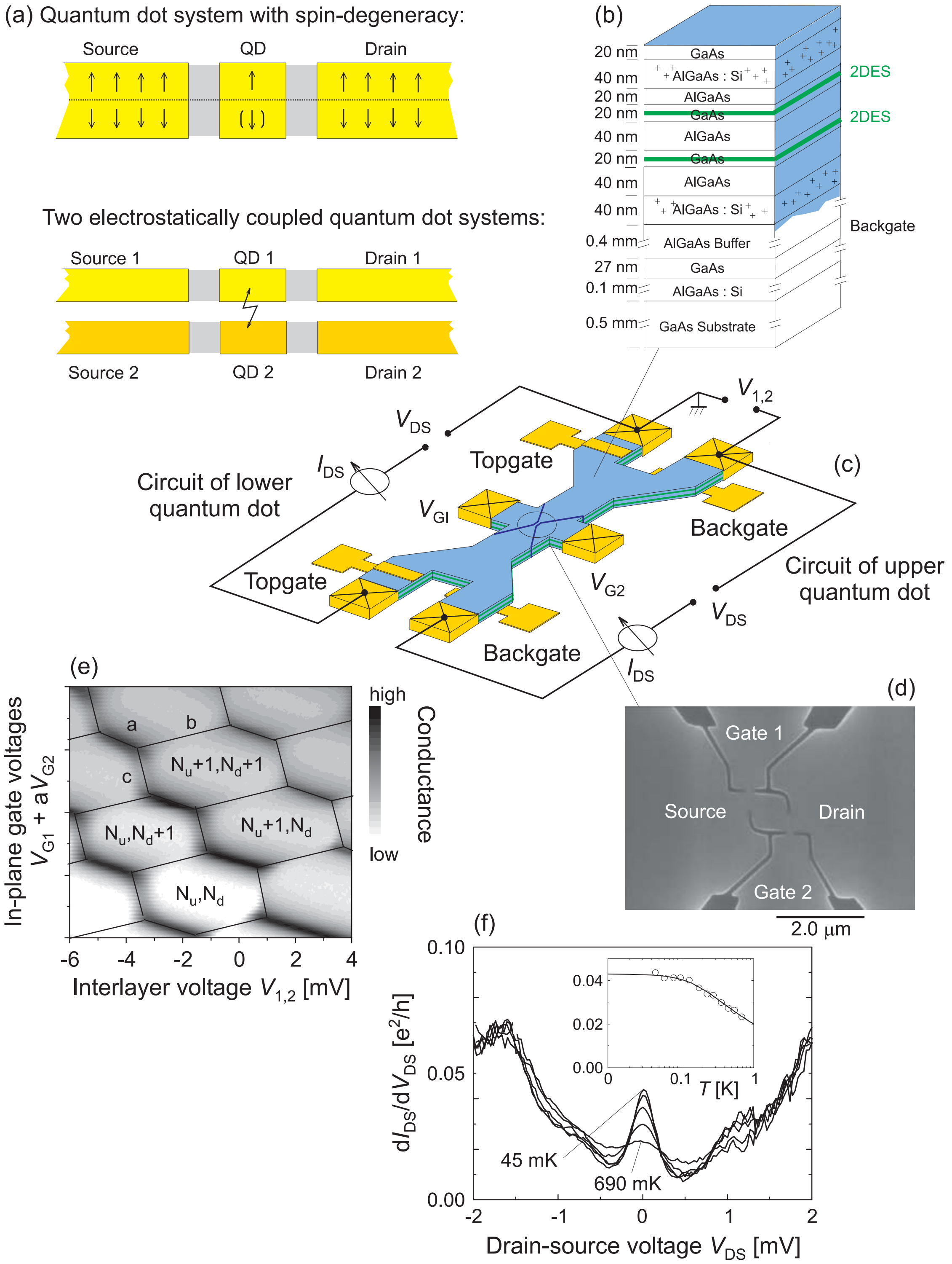

Figure 35: (a) Possible realizations of the Anderson impurity model: Single quantum dot system with spin-degeneracy or two electrostatically coupled quantum dot systems without spin-degeneracy. (b) GaAs/AlGaAs heterostructure used for the sample. (c) Sketch of the experimental setup. (d) Scanning electron microscope image of the etched heterostructure surface. (e) Conductance through upper quantum dot as a function of the in-plane gate voltages V_{G1} and V_{G2}, and the interlayer voltage $V_{1,2}$. (f) Differential conductance dI_{DS}/dV_{DS} versus drain-source voltage V_{DS} on a point on the line 'c' marked in (e) for different temperatures ($T = 45, 80, 180, 360, 690$ mK). Inset: temperature dependence of the peak height at $V_{DS} = 0$.

gives a new realization of the Anderson impurity model: the label marks two electrostatically coupled quantum dots with separate leads to each quantum dot (Fig. 35(a)). This mapping is valid if (1) an energetical degeneracy is present in occupying either the upper or the lower quantum dot, (2) the ground state of each quantum dot is not degenerated and excited states are energetically well separated. Our goal has been to verify this idea experimentally.

Base for the sample is a GaAs/$Al_xGa_{1-x}As$ heterostructure ($x = 0.33$), grown by Molecular Beam Epitaxy in the MBE group of the Institute. The heterostructure contains two quantum wells with a two-dimensional electron system (2DES) in each well, separated by an insulating 40 nm thick AlGaAs barrier. The full layer sequence is shown in Fig. 35(b). In a further step, the two quantum dot systems are defined on top of each other by reactive ion etching through the two quantum wells. A scanning electron microscope image of the etch pattern at the heterostructure surface is shown in Fig. 35(d). The two-dimensional electron system in each quantum well is divided by the etched grooves and the electrostatic depletion around them into the quantum dot region, the source and drain regions, and in addition into two regions usually denoted as in-plane gates. At low temperature, the electron systems confined in quantum dots have an extension of about 0.3 μm in diameter weakly coupled by respective tunnel barriers to the source and drain regions. The electron systems in the two quantum dots are strongly electrostatically interacting through the 40 nm thick AlGaAs layer which, however, prevents due to its thickness any tunnel current between both quantum dot systems. The quantum dot systems are separately contacted by alloying metal and by using top and back gates for locally depleting the upper or lower 2DES (Fig. 35(c)). The properties of the quantum dots are tuned by voltages applied to the two in-plane gates and the voltage $V_{1,2}$ applied between the 2DESs of the two quantum wells. All the measurements presented here were performed in a ^{3}He–^{4}He dilution refrigerator at base temperature $T = 45$ mK. To measure the differential conductance dI_{DS}/dV_{DS}, a lock-in modulation technique is used with an applied rms amplitude of 2.5 μV added to the dc drain-source voltage V_{DS}.

Figure 35(e) shows the conductance (differential conductance at $V_{DS} = 0$) in greyscale through the upper quantum dot as a function of a linear combination of the in-plane gate voltage V_{G1} and V_{G2}, and the interlayer voltage $V_{1,2}$.[*] Dark regions indicate high conductance, light regions low conductance. A honeycomb-like pattern is visible which is expected for two strongly electrostatically coupled single-electron transistors. Within each honeycomb cell, a certain configuration of the electron numbers of the two quantum dots is found, for instance (N_u, N_d). Crossing a borderline between two adjacent cells, at least in one quantum dot the number of electrons is changed by one. Along the borderlines labelled by ‘a’, single-electron tunneling occurs through the upper quantum dot due to the electrostatic degeneracy between the charge states characterized by a change only in the upper quantum dot, for instance from (N_u, N_d) to $(N_u + 1, N_d)$. Along the borderlines labelled by ‘b’, single-electron transport is possible through the lower quantum dot, while the upper quantum dot is in the Coulomb blockade regime. Along the lines labelled by ‘c’, finite conductance through the upper quantum dot is detected although this is not expected in the picture of single-electron tunneling. However, due to the electrostatic degeneracy, it is possible to have there a surplus electron *either* on the upper *or* lower quantum dot, i.e., for instance, the charge states $(N_u, N_d + 1)$ and $(N_u + 1, N_d)$ are energetically equivalent.

---

[*] In this parameter regime, the lower quantum dot was only connected by tunneling to one lead so that no conductance could be measured. However, this does not affect the conclusions presented in the following, but leaves signature at larger drain-source bias [Wilhelm *et al.*, Physica E **14**, 385 (2002)].

This allows for so-called ‘co-tunneling’ – an electron leaves one dot while another electron enters the other dot. This is the lowest order of correlated electron tunneling switching the charge state of both quantum dots at the same time by quantum mechanical correlation.

However, due to the analogy to the Anderson impurity model along the borderline ‘c’, we expect that it is not enough to treat correlated electron tunneling in perturbation theory: a Kondo-correlated state should form at low temperature leading to high conductance through both quantum dots at the same time. To prove this, the differential conductance is measured at points on the borderline ‘c’ as a function of drain-source voltage V_{DS}, and indeed – as shown in Fig. 35(f) – a peak is found at $V_{\mathrm{DS}} = 0$ which disappears in a logarithmic way with increasing temperature. A semi-empirical fit of the experimental data gives a Kondo temperature $T_{\mathrm{K}} = 850\,\mathrm{mK}$ and a zero-temperature conductance $G_0 = 0.043\,e^2/h$ (inset of Fig. 35(f)). We checked that Kondo resonances due to a spin-degeneracy in the single quantum dot do not occur in the neighboring honeycomb cells for this parameter range. Therefore, the behavior observed is induced by the charge degeneracy due to the electrostatic coupling between the two quantum dots. However, the measured Kondo temperature is surprisingly high. But an enhancement of the Kondo temperature is expected in the *combination* of a spin-degeneracy for each quantum dot and the electrostatic degeneracy between both quantum dots. In our experiment the spin-Kondo effect alone might not be visible in the neighboring honeycomb regions because our working temperature is too high and therefore these correlations are destroyed. To prove the hypothesis of an enhanced Kondo temperature, the spin-degree of freedom can be frozen out by applying a high magnetic field so that only the electrostatic degeneracy remains. Such experiments will be performed in the near future to clarify the unusual high Kondo temperature.

Transport properties of nanotube peapods

D. Obergfell, J.C. Meyer, and S. Roth;
Shihe Yang and Shangfeng Yang (The Hong Kong University of Science and Technology)

Novel one-dimensional systems based on carbon nanotubes can be created by filling single-walled carbon nanotubes (SWNTs) with various materials. A special case are ‘peapods’, where the nanotubes are filled with fullerenes. We have investigated the complex systems of *metallofullerene peapods*, where the fullerenes themselves are filled with metal atoms (these fullerenes are named *endohedral metallofullerenes*). The endohedral metallofullerenes arrange in a regular fashion and thereby form a linear array in the interior of the SWNTs. A schematic of such a metallofullerene peapod is sketched in Fig. 36(a). C_{82} fullerenes each encaging a single dysprosium atom have been inserted into SWNTs by heating both materials in vacuum at 500°C for 48 h. The metallofullerenes sublimate and are able to enter the single-walled nanotubes through their open ends or through defects at the side walls given that the diameters of the tubes are adequate. To verify the success of the filling procedure, transmission electron microscopy (TEM) was done on the Dy metallofullerene peapods (which are written as $(\mathrm{Dy@C_{82}})_n\mathrm{@SWNT}$ in a short way). The TEM image in Fig. 36(b) depicts three Dy metallofullerene peapods in which the SWNTs are completely filled with Dy metallofullerenes.

One can not recognize tubes at the lower left and the upper right part of Fig. 36(b) because these regions are covered with amorphous carbon or other residues of the production process.

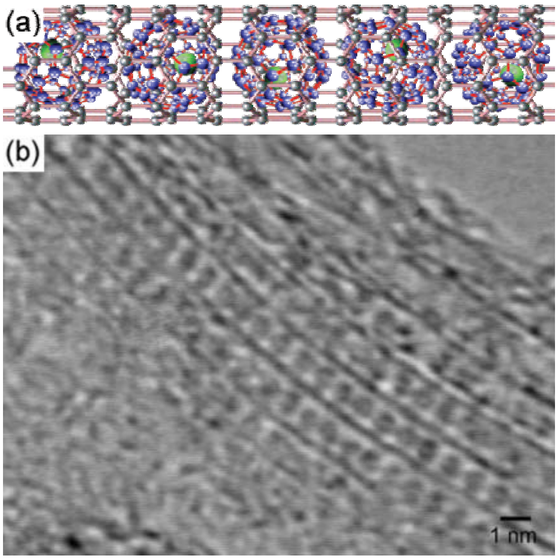

Figure 36: (a) Schematic of a metallofullerene peapod. A metallofullerene peapod consists of a single-walled carbon nanotube (SWNT) surrounding a linear array of fullerenes which each encage a single metal atom. Within this work $(Dy@C_{82})_n@SWNT$ material was used. (b) TEM image of at least three completely filled dysprosium metallofullerene peapods. However, one has to keep in mind, that TEM is a very local probe and that despite of this TEM micrograph not all SWNTs of the sample material have to be filled like the tubes depicted here.

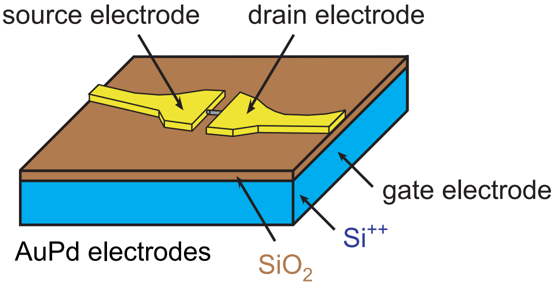

Figure 37: Schematic of a metallofullerene peapod in transistor configuration: metallofullerene peapods are adsorbed on a highly doped silicon chip with a 200 nm SiO_2 layer. Two AuPd electrodes are put on top of each peapod by electron beam lithography. One of the metal electrodes is used as source, the second as drain contact. The highly doped silicon substrate functions as back gate electrode.

The electrical properties of the dysprosium metallofullerene peapods were studied in field effect transistor (FET) configuration (Fig. 37) after successful synthesis of the $(Dy@C_{82})_n@SWNT$ samples. For this purpose, the $(Dy@C_{82})_n@SWNTs$ were deposited on highly doped silicon chips with 200 nm silicon oxide layers. Two AuPd electrodes were put on top of potentially single Dy metallofullerene peapods by electron beam lithography. The metal electrodes are used as source and drain contacts whereas the highly doped silicon substrate serves as back gate.

For each metallofullerene peapod the dependencies of the source drain current I_{sd} on the source drain voltage V_{sd} and on the gate voltage V_g were measured at 4.2 K. The data are displayed in Fig. 38. In general, the transport mechanism of a nanoscale structure in transistor configuration can be analyzed by measuring the transfer characteristics, i.e., the dependence of the channel current I_{sd} on the gate voltage V_g. If the source drain current does not depend on V_g, the structure behaves in a metallic way. If the system is semiconducting, the current I_{sd} can be strongly modulated by sweeping the gate voltage V_g. This is due to shifting the band structure with respect to the Fermi level of the system. For a p-type semiconductor the current I_{sd} is high for large negative values of the gate voltage whereas the channel current is suppressed for large positive values of V_g. A *n*-type semiconductor behaves in the opposite way.

Transfer characteristics have been measured for the Dy metallofullerene peapods, several $(Dy@C_{82})_n@SWNTs$ exhibited a special feature called *ambipolar behavior* (Fig. 38(b)), which is a high source drain current both for large negative and large positive gate voltages in combination with a regime of suppressed current for intermediate values of V_g. Consequently one is able to get access to both hole and electron conduction by sweeping the gate voltage, where the regime of suppressed current stands for the band gap of the system.

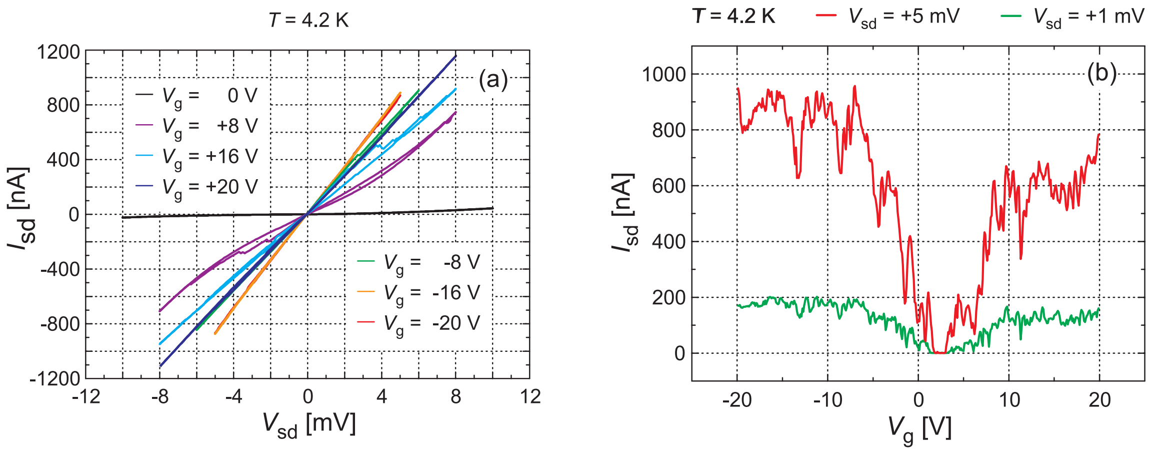

Figure 38: (a) Output characteristics $I_{sd}(V_{sd})$ of one of the investigated dysprosium metallofullerene peapods for different values of the gate voltage V_g at 4.2 K. The differential resistance for small values of V_{sd} is approximately 850 kΩ ($V_g = 0$). (b) Transfer characteristics $I_{sd}(V_g)$ of the same $(Dy@C_{82})_n$@SWNT at 4.2 K. The Dy metallofullerene peapod exhibits so-called *ambipolar transport behavior*, i.e., high conductance for large negative and positive gate voltages and suppressed conductance for an intermediate regime of V_g.

Lee *et al.* [Nature **415**, 1005 (2002)] have performed Scanning Tunneling Spectroscopy (STS) on a single $(Gd@C_{82})_n$@SWNT and found that the band gap is narrowed at the sites where the $(Gd@C_{82})$ metallofullerenes are located. Therefore it is likely to get ambipolar transport behavior in metallofullerene peapods [Shimada *et al.*, Applied Physics Letters **81**, 4067 (2002)]. The band gap narrowing caused by the insertion of metallofullerenes could be the reason for the ambipolar transport behavior of the dysprosium metallofullerene peapods investigated within this study.

Moreover a large gate coupling constant α can allow for being able to access both p- and n-conduction. The gate coupling factor α is defined by $\alpha = C_g/C_\Sigma$, where C_g is the capacity between the nanotube and the gate electrode and C_Σ the total capacity of the nanotube with respect to the source, drain and gate electrode. Knowing α, the band gap E_g of a semiconducting SWNT can be received according to $E_g = \alpha\, \Delta V_g\, e$, where ΔV_g is the width of the suppression region in the $I_{sd}(V_g)$ plot. Values for the gate coupling factor are usually extracted from the Coulomb blockade diamond diagram. Since the metallofullerene samples investigated did not exhibit Coulomb blockade oscillations at 4.2 K, and since α can vary from sample to sample despite of the same substrate/electrode material, the α value could not be determined here. There are publications on electrical transport in samples made from empty SWNTs, where the samples show ambipolar transport behavior and have large values for α ($\alpha \approx 0.2$) [Babić *et al.*, Nanotechnology **14**, 327 (2003)].

Another explanation for the ambipolar behavior might be that the samples investigated comprise ‘nearly metallic’ SWNTs with curvature-induced small band gaps [Kane *et al.*, Physical Review Letters **78**, 1932 (1997)]. Finally the contacts can have important influences as well [Heinze *et al.*, Physical Review Letters **89**, 106801 (2002)].

Future work will deal with the task to carry out transport measurements and TEM investigations on the very same nanotube peapod, in order to check whether the SWNTs investigated by electrical transport measurements are filled with fullerenes indeed. In addition this new technology will allow to figure out whether the channels of the nanotube field effect transistors are individual SWNTs or thin bundles.

‘Magic’ C_{60} – alkali metal compound clusters

A. Enders, N. Malinowski, D. Ievlev, W. Branz, and K. Kern

The study of free clusters of only a few atoms in size reveals important insight into the fascinating physics at the frontier between well-known bulk systems and purely atomistic phenomena. Numerous experiments show that physical and chemical properties of bulk materials significantly change if the sample size is decreased to clusters of only a few atoms. The reduced coordination in small clusters not only results in modified bond length and strength, electronic structure or magnetic properties with respect to bulk, even the crystallographic structure can be dependent on the cluster size and temperature.

The study of small clusters by means of time-of-flight mass spectrometry (TOF) allows to make conclusions about the cluster structure and the bonding forces forming it. Here, small clusters leaving the cluster source are accelerated by an electrical field pulse. From the measurement of the flight time of the clusters through the drift tube of the spectrometer their mass can be determined directly. This technique can conveniently be used to explore the thermal stability of the clusters, if a heating stage allowing for adjusting the cluster beam temperature is added directly after the cluster source. Heating promotes structural ordering of initially disordered clusters, and at the same time causes evaporation of atoms or molecules, reducing the cluster size. Clusters of particularly stable structure stronger resist this evaporation process and can be identified by a set of pronounced – commonly dubbed as *magic* – peaks in the mass spectrum. The set of magic peaks provides information about the cluster structure, but also tells about the chemical bonding between the building blocks forming the cluster.

The reflectron time-of-flight mass spectrometer (TOF) used for the experiments presented here allows high-resolution mass spectroscopy with a resolution of $m/\Delta m = 1.5{\cdot}10^4$ within the mass range up to $2{\cdot}10^7$ a.m.u.. The clusters are formed within a noble gas condensation cell and transported through the system to the detector by a jet of He atoms. A novel heating/cooling stage allowing to adjust the cluster temperature between 150 K and 1800 K is added to the setup directly after the cluster source, as shown in Fig. 39. Inside the stage the clusters thermalize with the He bath by collisions, thus assuming the desired temperature. The advantage of this combined design is that the clusters can be exposed to a well-defined temperature for a specific time period. On the other hand, losses in the spectra quality due to delayed fragmentation inside the drift tube of the TOF are suppressed.

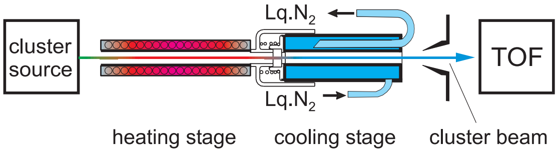

Figure 39: Experimental setup. After leaving the source and before analysis in the time-of-flight mass spectrometer (TOF) the clusters pass the heating stage, followed by the thermally decoupled cooling stage, for adjusting the temperature.

Thermal stability of small $(C_{60})_n$ clusters: Using the setup in Fig. 39 the thermal decay of small fullerene clusters was studied. The peak intensity of small $(C_{60})_n$ clusters in the mass spectra is recorded in the temperature range between 150 K and 500 K. The peak intensity of the C_{60} dimer, trimer and tetramer, normalized to the measured intensity at 150 K, is shown as a function of temperature in Fig. 40. The data show that the dimer, $(C_{60})_2$, starts to decay at 160 K and is completely vanished from the mass spectra at 210 K. At room temperature, also the $(C_{60})_3$, and at 400 K the $(C_{60})_4$ completely decay and disappear in the spectra. The low thermal stability is due to the weak bonds between the C_{60} molecules. In contrast to the strong covalent intramolecular bonds the intermolecular bonds are due to weak van-der-Waals interaction, which can easily be broken by thermal excitation. The observed decay behavior can be reproduced by canonic molecular-dynamic simulations assuming a Pacheco-Ramalho potential to describe the intermolecular interactions.

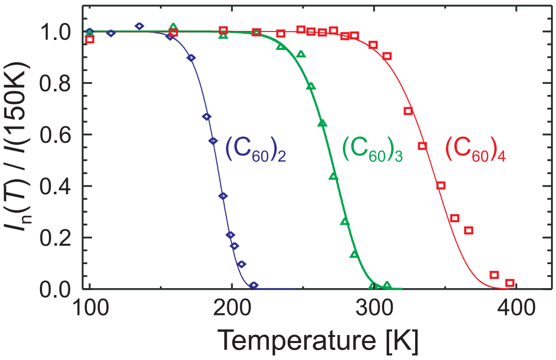

Figure 40: Thermal stability of small $(C_{60})_n$ clusters (n = 2–4). The clusters are heated in a He bath with a dwell time of 0.5 ms. The peak intensities from the mass spectra are normalized to the measured intensity at 150 K.

Thermal stability of mixed C_{60} – metal clusters: The thermal stability of C_{60} clusters can significantly be enhanced by adding alkali or alkaline-earth metal atoms, such as Potassium or Barium, to the cluster, thus forming C_{60}-metal compound clusters. Experimentally, this is achieved by simultaneous thermal evaporation of fullerenes and metal inside the condensation cell from two separate crucibles. The initially disordered clusters evaporate atoms and molecules during annealing in the heating stage, and only particularly stable configurations can be detected at elevated temperatures. A mass spectrum of $(C_{60})_nBa_m$ clusters which have been annealed to 1780 K is shown in Fig. 41(a). In this spectrum, groups of peaks of clusters with a fixed number of C_{60} molecules 'n', and a varying number of Ba atoms 'm', are visible. The most stable cluster configurations appear with strongest intensity and are labeled in the plot. It turns out that at 1780 K those clusters are magic which consist of n C_{60} molecules and $m = 2n - 1$ Ba atoms if $n \leq 4$, and 2n or more Ba atoms if $n > 4$. The experiment clearly shows that the thermal stability of small C_{60} clusters in combination with Ba is substantially enhanced, in comparison to pristine C_{60} van-der-Waals clusters.

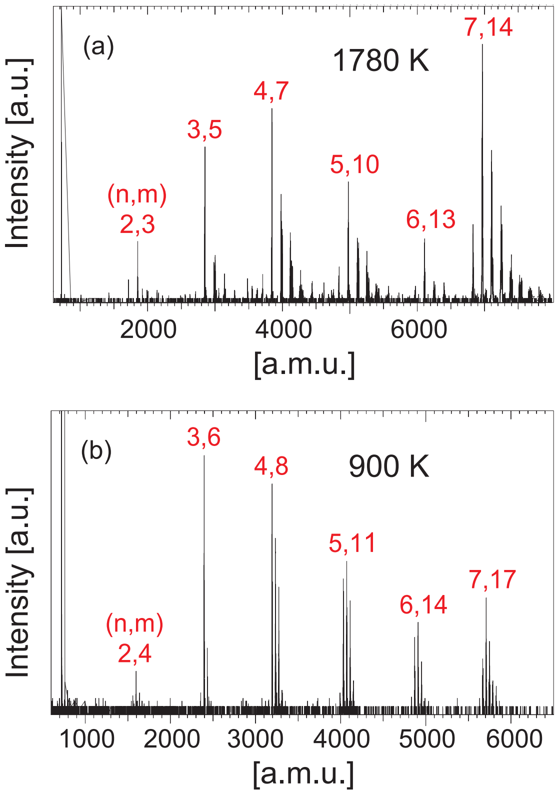

Figure 41: Mass spectra of (a) $(C_{60})_nBa_m$ clusters and (b) $(C_{60})_nK_m$ clusters, at elevated temperatures. The combinations (n,m) of the most stable clusters are indicated.

Increased stability of particular cluster configurations has been observed for several materials in the past and is usually ascribed to the formation of either closed geometrical or electronic shells. To determine which case applies for the $(C_{60})_nBa_m$ clusters, comparative experiments have been performed with Potassium. Since K has a similar ionic radius as Ba but half as much valence electrons, the results should help to discriminate between electronic and geometrical effects.

A mass spectrum of $(C_{60})_nK_m$ clusters taken at 900 K is shown in Fig. 41. Here, different magic numbers (n,m) as compared to the C_{60}-Ba clusters are observed. Most stable clusters are made of *n* C_{60} molecules and $m = 2n$

K atoms for $n \leq 4$ and 2n+1 or more K atoms for $n > 4$, respectively. The following conclusions can be drawn from the experiments: (i) The observed magic numbers for $(C_{60})_nBa_m$ and $(C_{60})_nK_m$ clusters at high temperatures are neither in agreement with geometrical nor with electronic shell filling. (ii) For a given number of C_{60} molecules in the cluster those with Ba are more stable than those with K. (iii) For a given number of C_{60} molecules the most stable configuration accommodates more atoms of K than of Ba.

From these results, a new model accounting for a balance between attractive and repulsive intermolecular interactions is developed, which is consistent with the observed magic cluster configurations. On one hand, it is well-known that the valence electrons of the alkali metal atoms are transferred into the lowest unoccupied t_{1u}-molecule orbital of the C_{60}, which can accommodate up to 6 electrons. Experiments show that K transfers one electron to the C_{60}, while Ba can transfer roughly 2 valence electrons, thus turning into a positively charged ion. The resulting ionic bond between the molecule and the metal atom is the reason for the enhanced thermal stability of the clusters. The more metal atoms add to the cluster and the more electrons are being transferred, the higher the thermal stability. This binding mechanism is opposed by the Coulomb repulsion between the positively charged metal ions, which is the stronger the more metal ions are in the cluster, or the larger their charge. The Coulomb repulsion tries to maximize the distance between the anions, which stretches – and therefore weakens – the ionic bonds. The competing mechanisms are illustrated in Fig. 42. The thermally most stable magic cluster configuration for C_{60} alkali metal compound clusters is therefore determined by the optimal balance between the two counteracting forces, where the ionic bonds are as strong as possible while the Coulomb repulsion is still sufficiently small.

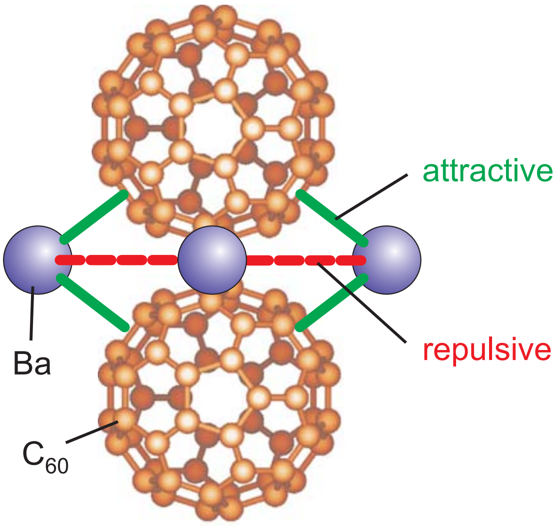

Figure 42: Force equilibrium in a $(C_{60})_2Ba_3$ cluster: attractive ionic bonding due to electron transfer from Ba to C_{60} (green) is opposed by Coulomb repulsion (red).

The experiments clearly show that the method of cluster heating has significant influence on the observed result. In this work the clusters have been thermalized with a He bath of given temperature by a sufficient amount of collisions, over a comparatively long time of the order of milliseconds. The obtained magic numbers are different from those observed previously [Martin *et al.*, The Journal of Chemical Physics **99**, 4210 (1993); Martin *et al.*, Physical Review Letters **72**, 3542 (1994)], where the clusters have been heated by short laser pulses. In such experiments, the energy is transferred to the cluster within nanoseconds by absorption of photons, thus causing ‘bell-like’ excitations. As a result, geometrical shell filling and electronic shell filling is found to govern the stability of $(C_{60})_nBa_m$ and $(C_{60})_nK_m$, respectively. As can be seen in Fig. 41, the clusters with closed shells are not visible here, meaning that they are less stable than the other configurations. It is therefore concluded that even though shell filling provides stability to the clusters, the strong destructive Coulomb repulsion due to the large amount of metal ions diminishes the ability to withstand longer annealing periods.

Atomic scale controlled growth of cubic iron silicide on Si(111): c(8×4) – reconstruction

U. Starke; M. Krause, F. Blobner, S. Müller, L. Hammer, and K. Heinz (Universität Erlangen)

The epitaxial deposition of iron silicide on semiconductor surfaces attracts growing interest due to a variety of potential technological applications such as the incorporation of non-volatile memories or optoelectronic transmitters into the Si technology, but also further miniaturization of Schottky devices. In particular, thin (less than 10 Å) iron silicide films can be crystallized on Si(111) in novel structures that differ from the bulk silicide phases. Yet, the homogeneous development of these films depends on the precise atomic scale control of surfaces and interfaces. The present paper elucidates the crucial role of this atomic scale tailoring for the development of new materials for the case of a well-ordered, 3 Å thick iron silicide film and presents the novel structure of this c(8×4) phase.

The silicide films were prepared in ultrahigh vacuum by deposition of Fe onto Si(111) and subsequent annealing to about 550°C. In the initial growth regime this leads to heterogeneous island nucleation as demonstrated by scanning tunneling microscopy (STM). At coverages as low as 0.05 monolayers (ML) three types of islands can be found, representing three-dimensional growth (Type A), triangular, single layer islands with disordered surfaces (Type B) and well-ordered iron silicide patches growing 1.5 Å below the original Si(111) surface level (Type C), respectively. Figure 43(a) shows this heterogeneous island nucleation after deposition of 0.2 ML Fe.

At higher coverages, however, the relative weight of the three island types changes as shown in Fig. 43(b)–(f). The flat B-type islands as well as three-dimensional growth (A-type) are suppressed while the flat silicide depressions (C-type) start to spread over the surface and eventually form a closed layer. While these silicide patches are still terminated by adatoms in (2×2) periodicity, empty state STM images reveal the presence of two types of adatom configurations characterized by brighter and darker protrusions. These adatoms form a well-ordered arrangement corresponding to a c(8×4) superstructure on the Si(111) substrate with three rotational domains on a typical length scale of 100 to 300 Å (Fig. 43(c)).

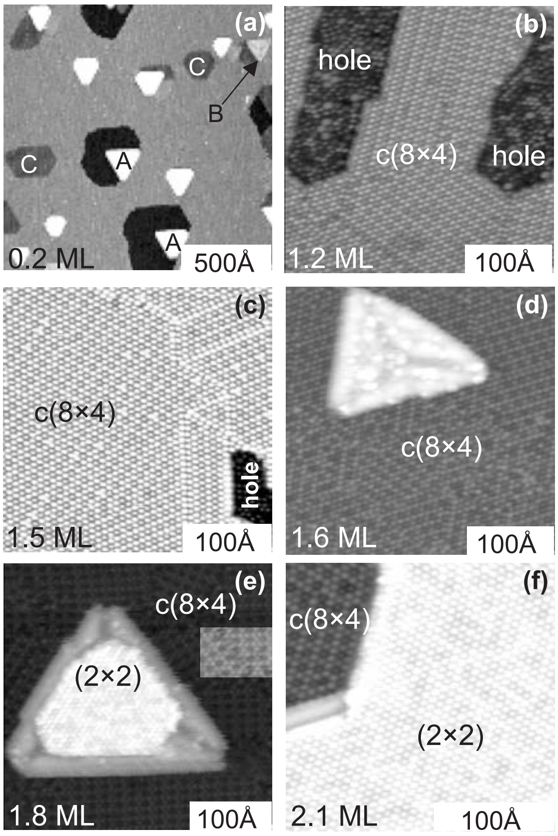

Figure 43: STM images of iron silicide films reacted from different initial Fe coverages ($U_{\text{tip}} = -0.9$ V to -1.9 V): (a) 0.2 ML with inhomogeneous island formation; (b) 1.2 ML with c(8×4) islands and disordered holes; (c) 1.5 ML with flat c(8×4) film; (d) 1.6 ML with B-type island on top of c(8×4) phase; (e) 1.8 ML with B-type island changing to A-type, inset: c(8×4) structure with amplified contrast; (f) 2.1 ML, (2×2) displacing c(8×4) areas.

Detailed inspection of the C-type islands in the initial heterogeneous growth regime also discloses this bias-dependent c(8×4) periodicity and corroborates the interpretation that it is indeed this island type that eventually covers the whole surface. Below 1.5 ML Fe coverage, the c(8×4) patches are interrupted by shallow holes (Fig. 43(b)) which eventually, at about 1.5 ML, disappear (Fig. 43(c)). At higher initial iron coverage, the c(8×4) patches are decorated by islands with disordered surfaces similar to B-type islands (Fig. 43(d)), until at 2 ML and above large (2×2) areas are formed corresponding to A-type islands (Fig. 43(e),(f)).

So, 1.5 ML initial iron coverage apparently is the critical value for a homogeneous c(8×4) layer which suggests, that this c(8×4) reconstructed film has a definite thickness. However, even at 1.5 ML Fe the silicide film is not completely flat on a large scale. In contrast, original terraces of the clean Si(111) surface, which were delimited by more or less straight step edges in a distance of 300–1000 nm, are split up into a two level percolation structure. The structures formed have characteristic lengths of the order of 100 nm, and their edges are strongly meandering (Fig. 44(a),(b)). The detailed inspection of an atomically resolved image of the boundary between two adjacent c(8×4) terraces of different height provides further insight into the atomic properties of the c(8×4) phase. The terrace boundaries often contain small (7×7)-Si(111) remnants as shown in Fig. 44(c). The difference between the two c(8×4) terrace heights is determined from STM image histograms (Fig. 44(d)) to be 3.1 Å. Similarly, we can measure the step height between the c(8×4) terraces and the (7×7) adatom level. Of course, that varies slightly with tunneling voltage, since electronic effects play a certain role. Nevertheless, the step heights retrieved are in the range of 1.2 Å to 1.7 Å between the lower c(8×4) patch and the (7×7) patch, and 1.4–1.9 Å between the (7×7) area and the next c(8×4) level.

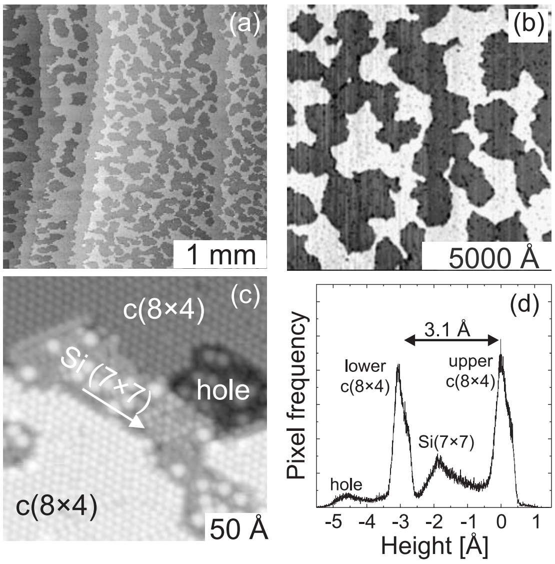

Figure 44: (a) STM image of a c(8×4) film on adjacent substrate terraces, (b) meandering iron silicide films with two different levels of c(8×4) reconstruction ($U_{\mathrm{tip}} = -1.9$ V). (c) Details of a step between upper and lower terrace. (d) Corresponding image histogram. ($U_{\mathrm{tip}} = 1.4$ V).

Thicker (still < 10 Å films in (2×2) periodicity (Fig. 43(f)) are known to possess $FeSi_2$ stoichiometry resulting from 50% iron depletion of FeSi in CsCl structure [Starke *et al.*, Journal of Applied Physics **91**, 6154 (2002)]. Transferring this model to the c(8×4) structure with its 1.5 ML iron would correspond to three Fe-Si layers of such structure. However, a comparison of the experimental step heights (Fig. 44(c),(d)) with detailed theoretical considerations (interface coordination, layer spacing, etc.) reveals that the reacted iron is distributed into only two Fe layers with an average of 25% Fe vacancies [Krause *et al.*, Physical Review B **68**, 125306 (2003)]. Thus, the ultrathin film deviates from the $FeSi_2$ stoichiometry. The silicide film is completed by 3 Si layers plus the (2×2) adatoms. Upper and lower terrace in the resulting model (without vacancies) are displayed as side view in Fig. 45(g) together with a (7×7)-Si(111) patch. A four-layer model as shown on the right side of Fig. 45(g) can be ruled out.

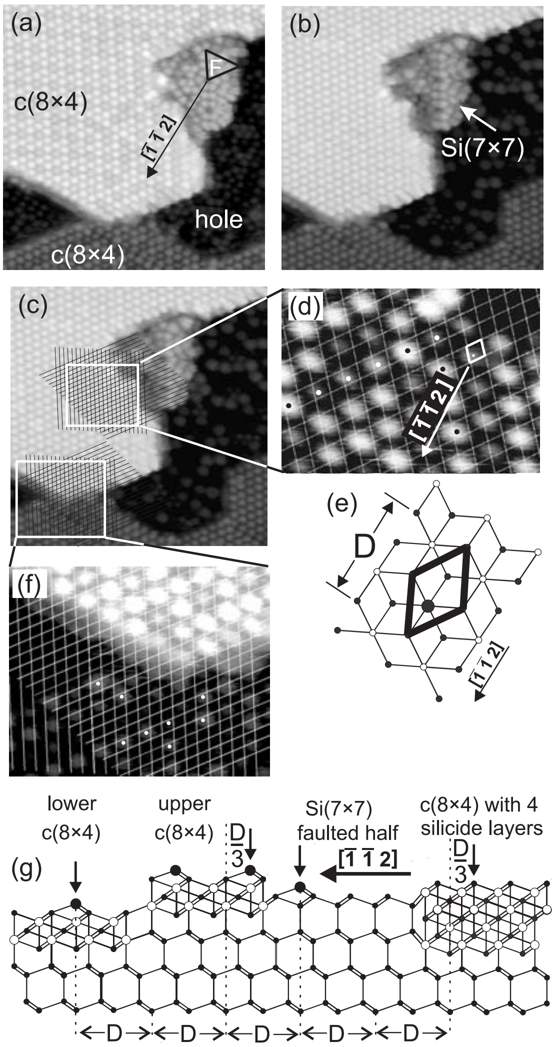

Figure 45: STM images of upper and lower c(8×4) levels with an area of residual (7×7) reconstruction [250 Å × 250 Å], (a) $U_{\mathrm{tip}} = -0.6$ V, (b) $U_{\mathrm{tip}} = +0.6$ V. (c),(d),(f) Overlayed grids depict the registry shift between adatoms in the (7×7) and the c(8×4) structures. (e) Top view of the 3 topmost silicide layers and a Si adatom. (g) Side view model in $\{\bar{1}10\}$ projection. Bonds within the plane are drawn as single lines, double lines indicate two bonds directed by 60° into and out-of-plane. Open spheres: Fe, dark spheres: Si.

On the course towards a complete structural model for the silicide film in addition to the layer arrangement we need to determine the local position of the (2×2) arranged adatoms. Also we have to find a suitable film structure (Fe vacancy distribution) giving rise to their different appearance in STM, which eventually leads to the development of the c(8×4) super-periodicity. From direct STM imaging of defects, i.e., where adatoms are locally missing, the adatoms appear to be positioned in three-fold coordinated hollow sites. However, since these holes are small, the influence of the tip shape might invalidate such an assignment. It would be preferable to have a direct proof for the threefold hollow site derived from the undisturbed c(8×4) structure. Additionally, one needs to discriminate between two alternatives. In threefold coordination, the adatoms could reside either above the Fe atoms of the first Fe layer or above the Si atoms in the second Si layer (so-called T4- or H3-sites). This information can be derived from a triangulation method using the Si(111)-(7×7) patches as reference. The adatoms of the (7×7) reconstruction are known to reside in T4 coordination and the lateral registry of the adatoms is well-defined by the underlying substrate. By identification of the faulted and unfaulted halves of the (7×7) unit cell from bias-dependent STM images (Fig. 45(a),(b)) we know the orientation of the substrate and in turn the lateral registry shift between different layers. By projecting a (1×1) grid on the adatom positions of the (7×7) area we find the adatoms of the upper c(8×4) terrace to be shifted by (–1/3,–1/3) in $[\bar{1}\bar{1}2]$ direction or a third of the unit cell diagonal D/3 as displayed in Fig. 45(c)–(e). From the side view model in the respective orientation, i.e., parallel to the $(\bar{1}10)$-plane as shown in Fig. 45(g) we can now determine the adatom position in the silicide. In the faulted half of the (7×7), the adatoms reside directly above the atoms of the lowest atomic plane displayed. The respective grid positions in the upper c(8×4) island correspond to the topmost Si layer of the silicide. Thus, the position of the adatoms (arrow) corresponds to a T4-site, which is also visualized in a top view (Fig. 45(e)). The same triangulation procedure can be done for the depressed c(8×4) regions (Fig. 45(f)). In that case the adatoms occupy the same positions as in the (7×7) band as displayed at the left edge of Fig. 45(g).

Since the adatoms reside above the Fe positions, it is tempting to assign the different appearance of adatoms within the c(8×4) unit cell to a mixture of true T4-sites and adatoms above Fe vacancies with correspondingly deviating heights and electronic structure. However the number of defects within the unit cell is higher than the number of corresponding adatoms. The primitive unit cell designated by the matrix $\binom{4\,2}{0\,4}$ contains 32 Fe positions in the whole film and correspondingly 8 vacancies, while it includes only one dark and three bright adatoms. Also, very different energetics are to be expected between the two arrangements raising questions for a respective driving force. For a further clarification the different adatom configurations were inspected by density functional theory (DFT) calculations. In these calculations Si adatoms in a (2×2) periodic arrangement were put on top of a Si-terminated surface of FeSi with CsCl-structure and fully relaxed. The most favorable adatom site found for a defect-free FeSi was the H3 hollow site being about 0.5 eV per (2×2) unit cell lower in energy than the T4-site right above the Fe atoms. Yet, the uncovered surface remains energetically preferred, irrespective of the choice of the chemical potential. However, this situation changes when Fe vacancies are introduced below the T4-site. This configuration is by about 1 eV lower in energy than the (very similar) normal H3-site – and preferable to an uncovered surface. Thus, by transferring the results (evaluated for a simple FeSi substrate) to the c(8×4) structure we have to assume that all of the adatoms reside above defect sites, which consumes about half of the vacancies available in the whole film. The other half, however, must then be responsible for the observed STM contrast of adatoms via indirect, lattice-mediated interactions. The problem now is to arrange the four remaining vacancies within the primitive unit cell of the c(8×4) structure. If they would all be in the upper Fe layer in between the already present (2×2) ordered defects below the adatoms, an extreme disproportion in their distribution would be required since all Fe-sites available are situated right in the middle of two neighboring adatoms. It is possibly more reasonable it is to place at least part of the defects also right at the interface. Unfortunately, the local configuration of a defect at the interface is hardly predictable. So, it is not clear whether the lower coordinated Si atoms remain stable at all. As a consequence, severe local restructuring may arise involving even substitution or place exchange of Fe and Si atoms. This, in combination with local lattice strain induced correspondingly, might lead to a complex reconstruction network at the interface. However, neither the structure nor the energetics of such an interface reconstruction can be sufficiently modelled at the present stage and further experimental as well as theoretical work is required for a detailed understanding.

Superconductivity and strongly correlated systems

The study of transition metal oxides and their physical and chemical properties is one of the central themes in this Institute. These oxides are characterized by strong electronic correlations and, therefore, require new theoretical concepts for their description, as is discussed in the report by Held *et al.* The most prominent examples among the transition metal oxides are the high-T_c superconductors and the non-superconducting manganites, titanates and vanadates, whose fascinating magnetic properties, like the colossal magnetoresistance in the manganites, are still poorly understood. The article by Horsch *et al.* deals with the complex magnetic behavior in YVO_3, while Andersen *et al.* investigate the influence of a structural $GdFeO_3$-type distortion on the electronic structure of several vanadates and titanates. Most reports in this section concentrate on various aspects of superconductivity like stripe order (Hinkov *et al.*) and ferromagnetic/superconducting bilayers (Soltan *et al.*). The article by Lemmens *et al.* is devoted to the recently discovered low-T_c superconductor $Na_xCoO_2 \cdot yH_2O$. Although the strong electronic correlations are central to the emergence of high-T_c superconductivity, little attention has so far been payed to the role of phonons in strongly correlated systems. This issue is treated in the article by Koch and Zeyher.

Electronic structure calculations with dynamical mean field theory – elementary cerium as an example

K. Held; A.K. McMahan (LLNL, University of California, Livermore);
R.T. Scalettar (University of California, Davis)

One of the most important challenges of theoretical solid state physics is the development of tools for the accurate calculation of material properties. In this respect, density functional theory within the local density approximation (LDA) turned out to be unexpectedly successful, and established itself as *the* method for realistic solid state calculations in the last century. This is surprising because LDA is a serious approximation to the Coulomb interaction between electrons

$$H_{\text{Coulomb}} = \sum_{i \neq j} \frac{e^2}{4\pi\varepsilon_0} \frac{1}{|\mathbf{r}_i - \mathbf{r}_j|}. \tag{1}$$

Here e denotes the electron charge, ε_0 the dielectric constant of vacuum, r_i and r_j the positions of the electrons i and j. Due to Eq. (1), the movement of every electron i is correlated with every other electron j. Within the LDA approximation, these correlations and also the quantum mechanical exchange is only treated rudimentarily. Basically, an electron at r_i sees a time-averaged density of the other electrons $\rho(r_i)$, with a corresponding *local* LDA potential $V_{\text{LDA}}(\rho(r_i))$.

The success of LDA shows, however, that this treatment is sufficient for many materials, both for calculating ground-state energies and bandstructures, implying that electronic correlations are rather weak in these materials. Yet, there are important classes of materials where LDA fails, such as transition metal oxides or heavy fermion systems. In these materials the valence orbitals are the 3*d* and 4*f* orbitals. Hence the distance $|\mathbf{r}_i - \mathbf{r}_j|$ is particularly small for two electrons on the same lattice site, and electronic correlations are particularly strong.

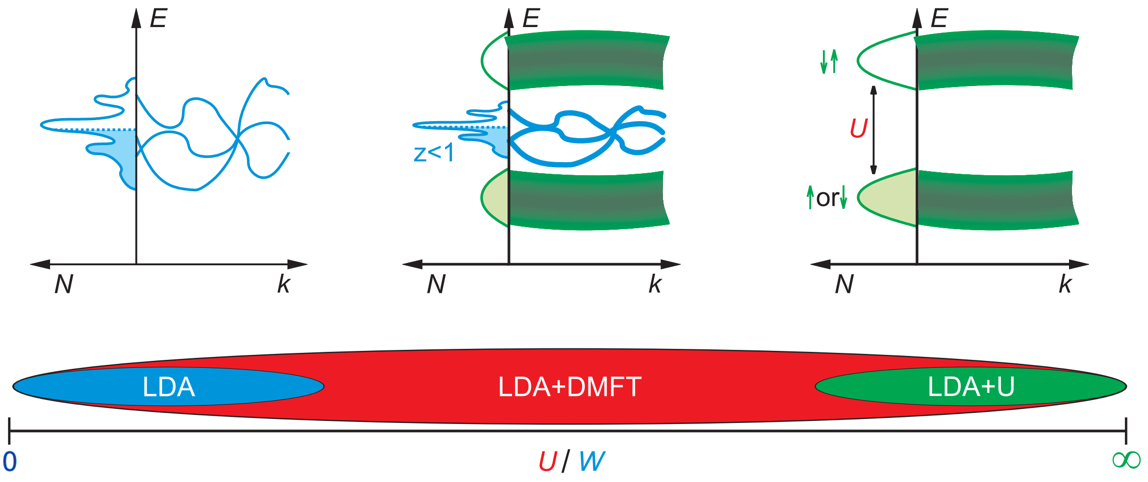

Figure 46:

Weakly correlated metal:
The on-site Coulomb interaction U is weak compared to the LDA bandwidth W; and LDA gives the correct answer, typically a (weakly correlated) metal for which we schematically draw a density of states N at energies E and the bandstructure (E versus wavevector k).

Strongly correlated metal:
In this intermediate regime, one has already Hubbard bands, like for $U/W \gg 1$ (right hand side), but at the same time a remainder of the weakly correlated LDA metal (left hand side), in form of a quasiparticle peak: the ($U = 0$) LDA bandstructure is reproduced, albeit with its width and weight reduced by a factor Z and life-time broadening effects.

Mott insulator:
If the Coulomb interaction U becomes large ($U \gg W$), the LDA band splits into two Hubbard bands, and we have a Mott insulator with only the lower band occupied (at integer fillings); such a splitting can be described by the so-called LDA+U method.

The entire parameter regime and physics is described by LDA+DMFT.

Many such transition metal oxides are Mott insulators, where, due to the on-(lattice-)site Coulomb repulsion U, the LDA bands are split into two sets of bands. Other transition metal oxides and heavy fermion systems are strongly correlated metals, with heavy quasiparticles at the Fermi energy, described by an effective mass or inverse weight $m/m_0 = 1/Z \gg 1$, see Fig. 46.

Dynamical mean-field theory (DMFT) is a modern, non-perturbative many-body technique, which describes such kind of correlation physics. It was first applied to model Hamiltonians – with big success. Hence, DMFT was recently merged with the conventional LDA approach for calculating materials with strong electronic correlations realistically. This LDA+DMFT method has proved to be a breakthrough for such calculations, which might not be astonishing as it is able to describe the full range of materials from weakly to strongly correlated metals to Mott insulators, see Fig. 46. For an introduction to LDA+DMFT see Held *et al.* [Psi-k Newsletter **56**, 65 (2003), psi-k.dl.ac.uk/newsletters/News_56/Highlight_56.pdf].

An example – Cerium undergoes a dramatic isostructural volume change ('collapse') of 15% under pressure which is widely believed to arise from changes in the degree of 4*f* electron correlations, as is reflected in both the Mott transition and the Kondo volume collapse models.

We reinvestigated this old problem, now being able to do realistic LDA+DMFT calculations without free parameters. We did calculations at different *fcc*-lattice volumes, taking into account 6*s*, 6*p*, 5*d*, and 4*f* linear muffin-tin orbitals and employing quantum Monte Carlo simulations to solve the DMFT equations.

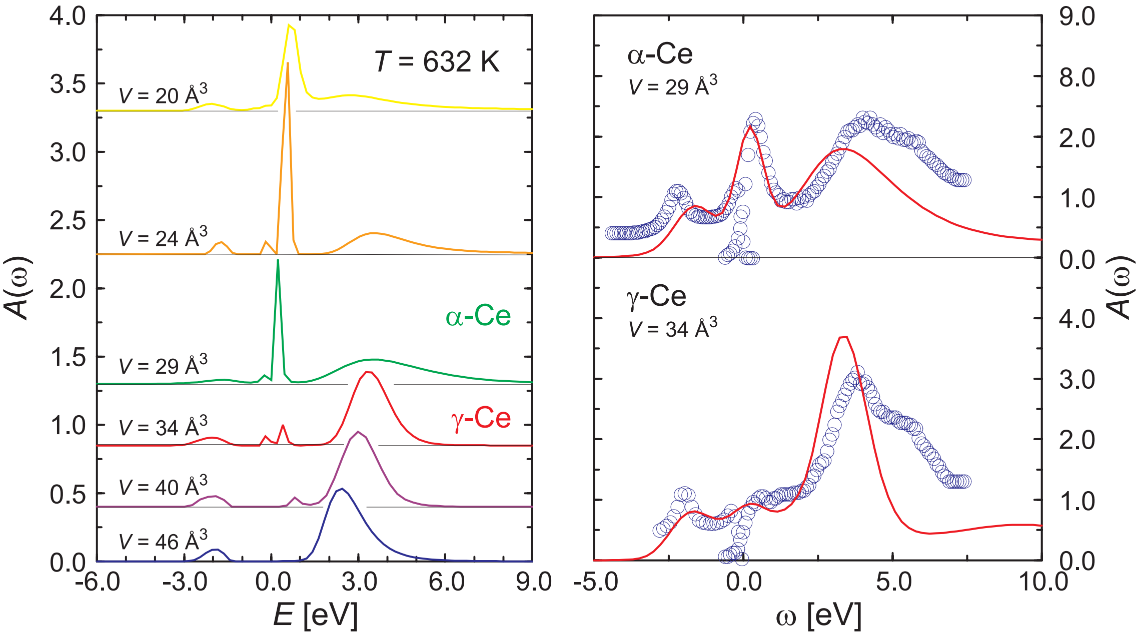

Figure 47: Left: 4*f* spectral function $A(\omega)$ at different volumes and $T = 632$ K ($\omega = 0$ corresponds to the chemical potential; curves are offset as indicated). Right: Total LDA+DMFT *spdf*-spectrum (solid line) in comparison with the combined photoemission and BIS spectrum.

The LDA+DMFT spectral evolution of the Ce 4*f* electrons is presented in Fig. 47 and shows upon increasing volume, i.e., upon increasing the LDA bandwidth, changes very similar as those discussed in Fig. 46. In particular, the weight of the central quasiparticle resonance is dramatically reduced when going from the experimentally α-volume ($V \approx 29$ Å^3) to the γ-volume ($V \approx 34$ Å^3). In the right part of Fig. 47, we show the total LDA+DMFT *spdf*-spectrum for α-Ce and γ-Ce (broadened with the experimental resolution 0.4 eV), which agrees very well, without adjustable parameters, with experiment.

Figure 48(a) shows our calculated LDA+DMFT energies as a function of atomic volume at three temperatures *relative* to the paramagnetic Hartree Fock (HF) energies E_{PMHF}, i.e., the energy contribution due to *electronic correlations*.

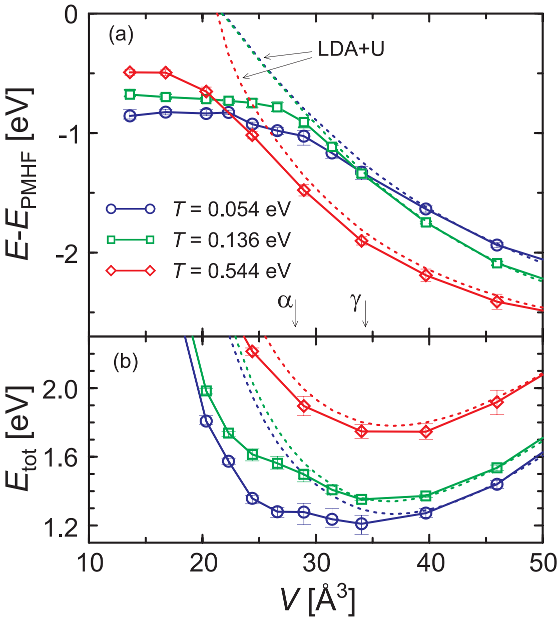

Figure 48: (a) Correlation energy $E - E_{\mathrm{PMHF}}$ as a function of atomic volume at three temperatures (LDA+DMFT: symbols; LDA+U: dotted lines); arrows: observed volume collapse from the α- to the γ-phase. (b) Total energy versus volume. The double well structure emerging with decreasing temperature gives rise to a first-order volume collapse.

We also present the polarized HF energies which resemble LDA+U calculations and, as one can see in Fig. 48(a), correctly reproduce E_{DMFT} at large volumes. With decreasing volume, however, the LDA+DMFT energies bend away from these LDA+U solutions; one can gain energy by the build-up of the quasiparticle peak (Fig. 47). Thus, at $T = 0.054\,\mathrm{eV} \approx 600\,\mathrm{K}$, a region of negative curvature in $E_{\mathrm{DMFT}} - E_{\mathrm{PMHF}}$ is evident within the experimentally observed two phase region (arrows). It is this negative curvature which gives rise to the very shallow minimum in the total energy (Fig. 48(b)) and, eventually, to a double well at low temperatures. Such a double well (actually, already a region of negative curvature is sufficient) signifies a first-order phase transition between the two minima, a volume collapse.

Outlook – The general aim is the further development and application of LDA+DMFT, in particular to transition metal oxides and to calculate further physical quantities like the optical and thermal conductivity, magnetic and orbital susceptibilities, and angular resolved spectra. As a more specific outlook, we would like to refer to a joint project of one of us with M. Feldbacher, A. Yamasaki, and O.K. Andersen to calculate, by LDA+DMFT, the metal-insulator transition in $\mathrm{LaMnO_3}$ observed under pressure by our colleagues from the High Pressure Group. The LDA part of this calculation has already been performed, reproducing the results of Pickett and Singh at zero pressure and showing a stark widening of the LDA bandstructure under pressure.

Dimerization versus orbital moment ordering in the Mott insulator $\mathrm{YVO_3}$

P. Horsch, G. Khaliullin, and A.M. Oleś

Many transition metal oxides are Mott-Hubbard insulators, in which local Coulomb interaction $\propto U$ suppresses charge fluctuations and leads to strongly correlated 3*d* electrons at transition metal ions. When degenerate *d* orbitals are partly filled, the *orbital degrees of freedom* have to be considered on equal footing with electron spins, and the magnetic properties of undoped compounds are described by spin-orbital superexchange (SE) models. Such SE interactions are strongly frustrated on a perovskite lattice, leading to enhanced quantum effects. In systems with e_g orbital degeneracy (manganites, cuprates) this frustration is usually removed by a structural transition that occurs well above the magnetic ordering temperature and lifts the orbital degeneracy via the cooperative Jahn-Teller (JT) effect.

A different situation arises when t_{2g} orbitals are partly filled like in titanium and vanadium oxides. As the JT coupling is much weaker, the intrinsic frustration between spin and orbital degrees of freedom may show up in this case.

In addition to SE, spin $\vec{S}_i$ and orbital $\vec{l}_i$ variables are coupled also via atomic spin-orbit interaction, $H_{\mathrm{so}} = \Lambda \sum_i (\vec{S}_i \cdot \vec{l}_i)$. The interplay between *intersite* SE and *on-site* H_{so} should lead to rich physics which has not been explored until now.

The magnetic properties of the cubic vanadate $\mathrm{YVO_3}$ show several puzzling features, among them a splitting of spin waves along the ferromagnetic (FM) direction within the *C*-AF phase indicating a dimerization in the magnetic sector [Ulrich *et al.*, Physical Review Letters **91**, 257202 (2003)]. Here *C*-AF denotes a magnetic structure with antiferromagnetic (AF) bonds in the *a*,*b*-plane and FM bonds along the cubic *c*-axis.

We show that such an exotic C-AF phase follows from the realistic spin-orbital model for vanadates that emphasizes the competition between SE bond physics and intraatomic spin-orbit coupling $\propto \Lambda$. We investigate the phase diagram of this model and show that *orbital moments* are induced in the C phase by finite Λ which, for large Λ, form a novel orbital moment (OM) phase [Horsch *et al.*, Physical Review Letters **91**, 257203 (2003)].

The superexchange in cubic vanadates originates from virtual charge excitations, $d_i^2 d_j^2 \rightarrow d_i^3 d_j^1$, by the hopping t which couples pairs of identical t_{2g} orbitals. When such processes are analyzed on individual bonds $\langle ij \rangle \parallel \gamma$ along each cubic axis $\gamma = a,b,c$, one finds the spin-orbital Hamiltonian with $S=1$ spins ($J = 4t^2/U$),

$$H = J \sum_{\gamma} \sum_{\langle ij \rangle \parallel \gamma} \left[\frac{1}{2} (\vec{S}_i \cdot \vec{S}_j + 1) \hat{J}_{ij}^{(\gamma)} + \hat{K}_{ij}^{(\gamma)} \right] + H_{so}. \quad (2)$$

In contrast to usual Heisenberg magnets the exchange integrals are not constants, but are operators reflecting the dependence of the interactions on the orbital state. The orbital operators $\hat{J}_{ij}^{(\gamma)}$ and $\hat{K}_{ij}^{(\gamma)}$ depend on pseudospin $\tau = 1/2$ operators $\vec{\tau}_i = \{\tau_i^x, \tau_i^y, \tau_i^z\}$, given by two orbital flavors that are active along a given direction γ. For instance, *yz* and *zx* orbitals are active along c-axis (because their hopping matrix element t is finite, while that for *xy* vanishes). We label these orbitals as a and b, as they lie in the planes orthogonal to these axes. The c (*xy*) orbitals are occupied ($n_{ic} = 1$), as suggested by the electronic structure and by the lattice distortions in YVO$_3$ and hence only the $\{a,b\}$ orbital degeneracy remains. The electron densities in a and b orbitals satisfy the local constraint $n_{ia} + n_{ib} = 1$. For illustration we give the exchange interaction $\hat{J}_{ij}^{(c)}$ for a bond along the c-direction:

$$\hat{J}_{ij}^{(c)} = (1 + 2R) \left(\vec{\tau}_i \cdot \vec{\tau}_j + \frac{1}{4} \right) - r \left(\vec{\tau}_i \otimes \vec{\tau}_j + \frac{1}{4} \right) - R, \quad (3)$$

where the operators $\vec{\tau}_i \cdot \vec{\tau}_j$ and $\vec{\tau}_i \otimes \vec{\tau}_j = \tau_i^x \tau_j^x - \tau_i^y \tau_j^y + \tau_i^z \tau_j^z$ describe the fluctuations of a and b orbitals. These pseudospin operators can be represented by Schwinger bosons which create (annihilate) electrons in a or b orbitals: $\tau_i^x = \frac{1}{2}(a_i^\dagger b_i + b_i^\dagger a_i)$, $\tau_i^y = \frac{1}{2} i (a_i^\dagger b_i - b_i^\dagger a_i)$, $\tau_i^z = \frac{1}{2}(n_{ia} - n_{ib})$. Hund's exchange $\eta = J_H/U$, which determines the multiplet structure of d^3 excited states, enters via the coefficients $R = \eta/(1-3\eta)$ and $r = \eta/(1+2\eta)$. Hence the orbital sector is described by a Heisenberg model as well, whose anisotropy is controlled by the Hund coupling. Combined with the spin operator in Eq. (2) this poses a rather subtle quantum mechanical problem, where the exchange interaction in front of $\vec{S}_i \cdot \vec{S}_j$, including its sign, is controlled by the orbital correlations and vice versa, the orbital interactions depend on the nature of the spin correlations.

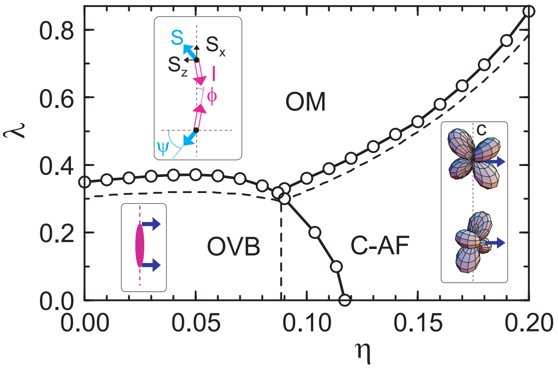

Figure 49: Phase diagram of the spin-orbital model in the (η, λ)-plane at $T = 0$, reflecting the competition between orbital valence bond (OVB), staggered orbitals (C-AF), and orbital moment ordering (OM), as obtained by exact diagonalization of a four-site embedded chain for $\phi = 11°$ (circles), and in mean-field approximation (dashed lines). Orbital moments in the OM phase (violet arrows) induce spin canting (blue arrows) with angle ψ. (Estimated parameters for YVO$_3$ are: $\eta \simeq 0.12$, $\lambda \sim 0.3$–0.4.)

Three different ground states are realized, depending on the strength of the Hund coupling η and the spin-orbit interaction $\lambda = \Lambda/J$ (Fig. 49). When both λ and η are small, orbital singlets form along the c-direction which couple spins pairwise ferromagnetically, while the coupling between such pairs is AF and weak. The orbital valence bond (OVB) state becomes unstable at larger Hund coupling η, which favors uniform

FM correlation along *c*. While orbitals fluctuate strongly in the OVB phase they reveal real orbital order in the *C*-AF phase. Spin orbit coupling H_{so} rotates spins into the *ab*-plane. The small tilt of VO_6 octahedra with angle ϕ induces weak orbital moments that lead to a small canting of spins out of this plane, and the out-of-plane component alternates along *c*. At large λ the system enters another phase where real orbital order is destroyed due to local orbital fluctuations introduced by H_{so}, and orbital moment order controls the magnetic structure. An example for the variation of correlation functions and spin components as function of λ is shown in Fig. 50 for the transition from the OVB into the orbital moment phase.

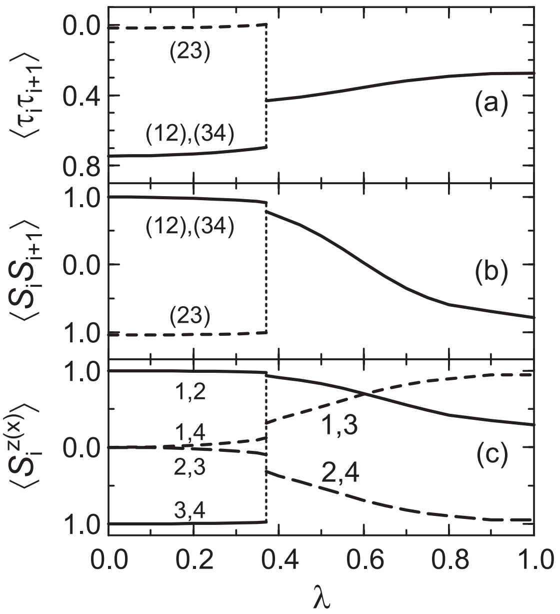

Figure 50: Pair correlations along *c*-axis: (a) orbital $\langle\vec{\tau}_{\mathrm{i}}\cdot\vec{\tau}_{\mathrm{i+1}}\rangle$, (b) spin $\langle\vec{S}_{\mathrm{i}}\cdot\vec{S}_{\mathrm{i+1}}\rangle$, and (c) spin components $\langle S^z_{\mathrm{i}}\rangle\perp c$ (full lines) and $\langle S^x_{\mathrm{i}}\rangle\,||\,c$ (dashed, long-dashed lines), as functions of λ for the OVB ($\lambda<\lambda_c\simeq 0.37$) and the OM ($\lambda>\lambda_c$) phase, found by the exact diagonalization at $\eta=0.07$. FM/AF bonds (ij) in the OVB phase are shown by solid/dashed lines in (a) and (b), while $\mathrm{i}=1,2,3,4$ labels a sequence of V atoms along *c*-direction.

Up to now, the sole experimental evidence for dimerization of the *C* phase is the splitting of FM spin waves in a recent neutron scattering study of Ulrich *et al.* [Physical Review Letters **91**, 257202 (2003)]. Importantly, no corresponding lattice dimerization was observed. This already suggests that this is a new phenomenon distinct from the usual Peierls distortion, i.e., controlled by the interplay of spin and orbital degrees of freedom.

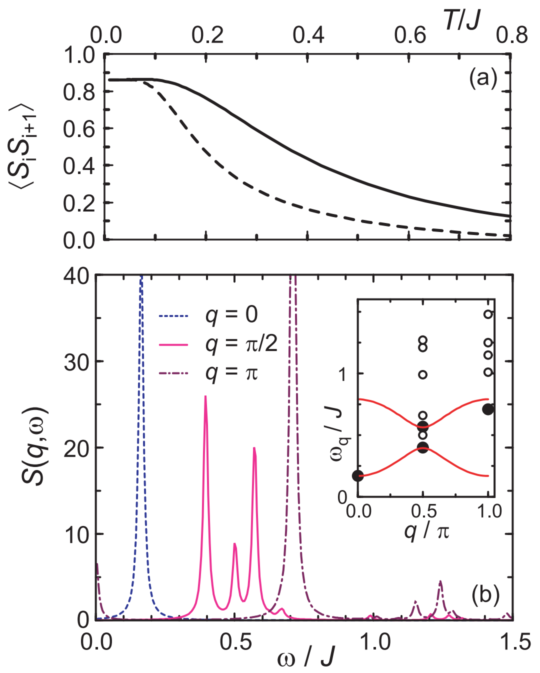

Figure 51: Dimerization in the *C*-AF phase at $T>0$: (a) spin-spin correlations $\langle\vec{S}_i\cdot\vec{S}_{\mathrm{i+1}}\rangle$ on strong and weak FM bonds (solid and dashed line); (b) spin response $S(\mathbf{q},\omega)$ in the dimerized *C*-AF phase for $\mathbf{q}=(0,0,\mathrm{q})$ with $q=0,\frac{\pi}{2},\pi$. Inset: filled (open) circles indicate strong (weak) features in $S(\mathbf{q},\omega)$; lines show the fitted spin-wave dispersion with a gap at $q=\pi/2$ resulting from orbital-Peierls dimerization ($\eta=0.12$, $\lambda=0.4$).

Figure 51(a) shows that the *C*-AF phase indeed dimerizes at finite temperature, yet not at $T=0$. This is due to an intrinsic instability towards alternating orbital singlets, reminiscent of the physics of the OVB phase. However, orbital dimerization can only take place when the ferromagnetic correlations along the chains are sufficiently weakened by thermal fluctuations. The spin correlations $\langle\vec{S}_{\mathrm{i}}\cdot\vec{S}_{\mathrm{i+1}}\rangle$ (Fig. 51(a)), found using exact diagonalization with open boundary conditions, alternate here between strong and weak FM bonds due to the orbital Peierls dimerization, $2\delta_\tau=|\langle\vec{\tau}_i\cdot\vec{\tau}_{i+1}\rangle-\langle\vec{\tau}_{\mathrm{i}}\cdot\vec{\tau}_{\mathrm{i-1}}\rangle|$, which has a distinct maximum at $T\approx 0.24\,\mathrm{J}$ for $\eta=0.12$.

To study the consequences for the spin excitations we have calculated the dynamical spin structure factor $S(\mathbf{q},\omega)$ (Fig. 51(b)). The results were obtained by exact diagonalization of a four-site cluster with periodic boundary conditions at $T=0$, assuming the same orbital Peierls dimerization $2\delta_\tau$ as found above for $T/J=0.25$. At $\mathbf{q}=(0,0,\frac{\pi}{2})$ we observe a splitting of the spin wave similar to experiment. The finite energy of the $\mathbf{q}=(0,0,0)$ mode results from the Λ-term and the mean-field coupling to neighbor chains. Additional features seen in $S(\mathbf{q},\omega)$, e.g., for $q=(0,0,\pi)$ at $\omega\approx 1.25\,J$, are attributed to the coupling to orbital excitations. The spin-wave energies can be fitted by a simple Heisenberg model with two FM coupling constants: $J_{c1}=-5.7$, $J_{c2}=-3.3$ meV, and a small anisotropy term, as shown in the inset (solid lines). Although these values are strongly reduced by spin-orbit coupling, they are still larger than those extracted from the spin waves in YVO$_3$: $J_{c1}^{\mathrm{exp}}=-4.2$ and $J_{c2}^{\mathrm{exp}}=-2.0$ meV at $T=85$ K. We attribute this overestimate of exchange interactions to quantum fluctuations involving the occupancy of *xy* orbitals (leading to $n_{\mathrm{ic}}<1$).

Summarizing, we have shown that the spin-orbit coupling Λ competes with Hund's exchange in the spin-orbital model for cubic vanadates. It leads to a new orbital moment ordered phase at large Λ and can explain qualitatively the spin canting and large reduction of magnetization in the *C* phase. We argue that the transition to the *C*-AF phase, which is observed in YVO$_3$ at $T_{\mathrm{N1}}\approx 77$ K, emerges from a competition of *quantum effects* due to orbital moment formation at $\Lambda>0$ and *thermal fluctuations*, which opens the way towards dimerized orbital and spin correlations triggered by superexchange.

How chemistry controls electron localization in 3d^1 perovskites

O.K. Andersen and J. Nuss; E. Pavarini (INFM Pavia and MPI-FKF);
S. Biermann and A. Georges (Ecole Polytechnique Palaiseau);
A. Poteryaev and A.I. Lichtenstein (NSRIM Nijmegen)

Transition metal perovskites have been studied for decades because of their unusual electronic and magnetic properties arising from narrow 3*d* bands and strong Coulomb correlations. The 3d^1 perovskites are particularly interesting since despite the lack of multiplet effects similar materials have very different electronic properties: strontium and calcium vanadate are correlated metals with mass-enhancements of respectively 2.7 and 3.6, while lanthanum and yttrium titanate are Mott insulators with gaps of respectively 0.2 and 1 eV.

Associated with the increasing electron localization along this series is a structural GdFeO$_3$-type distortion (Fig. 52 top): Whereas SrVO$_3$ is cubic, the corner-sharing BO$_3$ octahedra of the other perovskites are tilted and rotated in such a way that there are 4 equivalent octahedra per primitive cell. The reason often given for the progression of this distortion is that the size of the A cation relatively to that of the BO$_3$ octahedron shrinks along the series, i.e., that $r(\mathrm{Sr}^{2+})\sim r(\mathrm{La}^{3+})>r(\mathrm{Ca}^{2+})\sim r(\mathrm{Y}^{3+})$, while $r(\mathrm{V}^{5+})<r(\mathrm{Ti}^{3+})$. In addition, local density approximation (LDA) band structures (Fig. 52 bottom) point to the role of covalency between the cation *d* states (green) and the oxygen 2*p* states (blue): In cubic SrVO$_3$ each Sr ion has 12 nearest oxygens at the face centers. The 3*d* band of Ca lies lower, and thereby closer to the oxygen 2*p* band than the 4*d* band of Sr, and it is therefore conceivable that a GdFeO$_3$-type distortion, which pulls some of the oxygen neighbors closer to the A ion and thereby

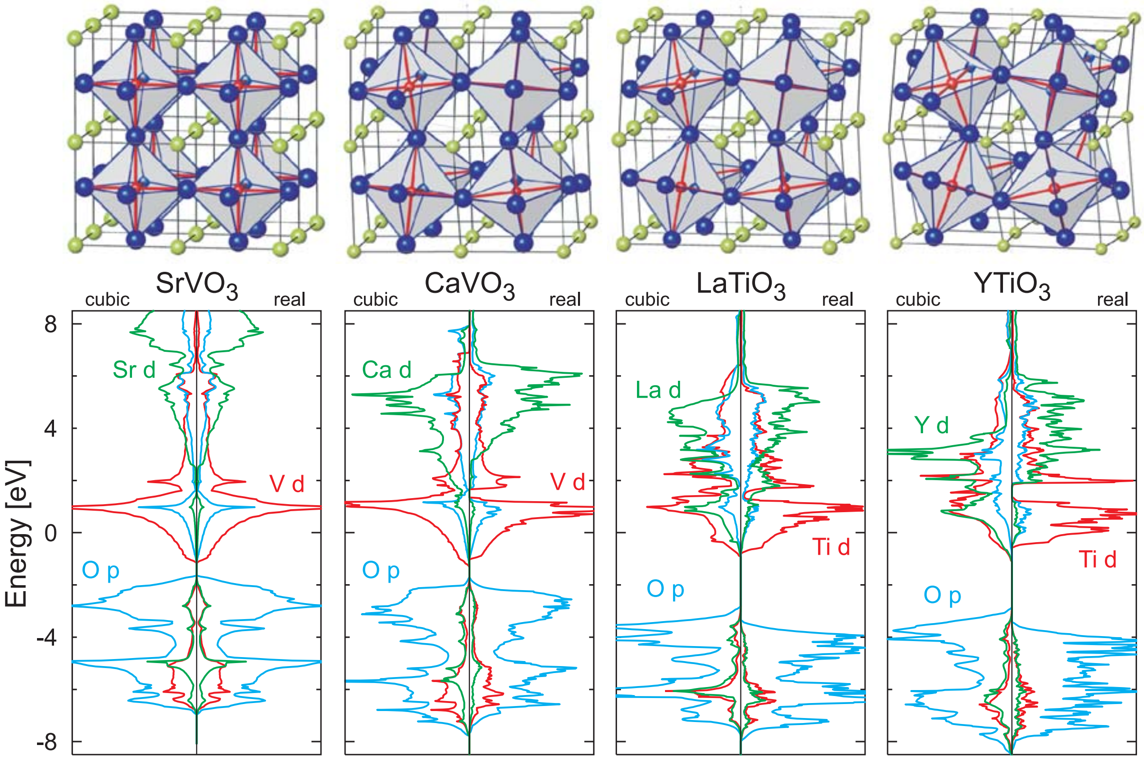

Figure 52: Top: Structures of the $3d^1$ perovskites, A(green) B(red) O_3(blue). In a global, cubic *xyz*-system directed approximately along the BO bonds, the orthorhombic translations are $a = (1,\text{-}1,0)\,(1+\alpha)$, $b = (1,1,0)\,(1+\beta)$, and $c = (0,0,2)\,(1+\gamma)$, with α, β, γ small. In the *Pbnm* symmetry, the *ab*-plane through A is a mirror $(z \leftrightarrow -z)$, and so is the *bc*-plane through B $(x \leftrightarrow y)$ when combined with the translation $(b-a)/2$. The $GdFeO_3$-type distortion tilts the corner-sharing octahedra around the *b*-axis (by 0, 9, 12, and 20°) and rotates them around the *c*-axis (by 0, 7, 9, and 13°) as we progress from cubic $SrVO_3$ via $CaVO_3$ and $LaTiO_3$ to $YTiO_3$. Bottom: LDA partial-wave-projected densities of states (DOS) calculated for the real structures (right-hand panels) and for hypothetical cubic structures with the same volume (left-hand panels). The blue, red, and green DOS are projected onto respectively all O *p*, all B *d*, and all A *d* partial waves. For the B *d* band, t_{2g} is below e_g whereas the opposite is true for the A *d* band in the cubic structure. The Fermi level is at zero energy.

increases the covalency with those, is energetically more favorable in $CaVO_3$ than in $SrVO_3$. The figure shows the associated increase of the Ca $4d-\text{O}\ 2p$ gap. Going now from the vanadates to the titanates, the A and B cations become first- rather than third-nearest neighbors in the periodic table, and the A *d* band therefore becomes nearly degenerate with the Ti 3*d* band, and more so for Y 4*d* than for La 5*d*. Here it is only the $GdFeO_3$ distortion which, through increase of the A $d-\text{O}\ 2p$ covalency, pushes the A *d* band above the Fermi level. This, as well as the concomitant lowering of the O 2*p* band, is seen in the figure.

The B 3*d* band is split by covalency with the 2*p* orbitals on the O_6 octahedron into three $pd\pi$-coupled, low-lying t_{2g} bands and two $pd\sigma$-coupled, higher-lying e_g bands. Simplest theories for the electronic properties of the d^1 perovskites are therefore based on a Hubbard model with 3 *degenerate*, $\frac{1}{6}$-filled t_{2g} bands per B ion. For such a model, the metal-insulator transition occurs when the ratio of the on-site Coulomb repulsion to the one-electron bandwidth exceeds a critical value $U_c\,/\,W \approx 2$. The progressive localization of the electron along the series is therefore ascribed to a progressive reduction of the t_{2g} bandwidth due to the increased bending of the $pd\pi$ hopping paths (BOB bonds) and, as may be seen from Fig. 52, also to the increased theft of oxygen character by A orbitals. This may not be the full explanation of the Mott transition, however, because if the orbital degeneracy can be reduced, U_c/W will be reduced because there are more hopping processes in many-particle than in single-particle theory. Now, reduction of the orbital degeneracy requires a t_{2g} *level-splitting*, Δ, merely of size ZW, the bandwidth associated with quasiparticle excitations. Close to the Mott transition, $Z \sim 1 - U_c/W$. Unlike in e_g-band perovskites such as the d^{3+x} manganites where large (10%) cooperative Jahn-Teller (JT) distortions of the octahedra indicate that the e_g degeneracy is reduced and the orbitals are spatially ordered, in the t_{2g}-band perovskites the octahedra are almost perfect. The t_{2g} orbitals have therefore often been assumed to be degenerate. If that is true, Khaliullin *et al.* predicted that quantum fluctuations will lead to an *orbital liquid* [Ulrich *et al.* in the Progress Report 2002, pp 47–51]. Moreover, an important experimental constraint on the nature of the orbital physics is the observation of an isotropic, small-gap spin-wave spectrum in both insulators. This is remarkable because $LaTiO_3$ is a 3-dimensional antiferromagnet with $T_N = 140\,K$, a small moment ($0.45\,\mu_B$), and a recently discovered small JT distortion (3% stretching along a), while $YTiO_3$ is a ferromagnet with a low Curie temperature ($T_C = 30\,K$), a good-sized moment ($0.8\,\mu_B$), and a JT distortion of different type (3% stretching along alternatively x and y).

We have calculated the electronic properties in the high-temperature ($T > T_{N,C}$) paramagnetic phases using a low-energy multiband Hubbard Hamiltonian,

$$H = H^{\mathrm{LDA}} + \frac{1}{2}\sum\nolimits'_{imm'\sigma\sigma'} U_{imm'}\,\hat{n}_{im\sigma}\,\hat{n}_{im'\sigma'} - \mathrm{d.c.}, \tag{4}$$

whose one-electron part is given by the local approximation to density-functional theory (LDA) and whose on-site (i) Coulomb interactions are included for a subspace of localized orbitals *(im)*. The LDA provides a parameter-free account of the materials dependence, i.e., the chemistry. Recently it has become possible to solve this Hamiltonian in the dynamical mean-field approximation (DMFT), as is described in the contribution by Held *et al.* (see pp 50). In previous LDA+DMFT implementations it was assumed that the on-site block of the single-particle Green function is diagonal in the space of the correlated orbitals which were taken as orthonormal LMTOs, approximated by truncated and renormalized partial waves. These approximations are good for cubic t_{2g} systems such as $SrVO_3$, but they deteriorate with the degree of distortion. We have therefore used localized *Wannier functions* and included the non-diagonal part of the on-site self-energy in the DMFT.

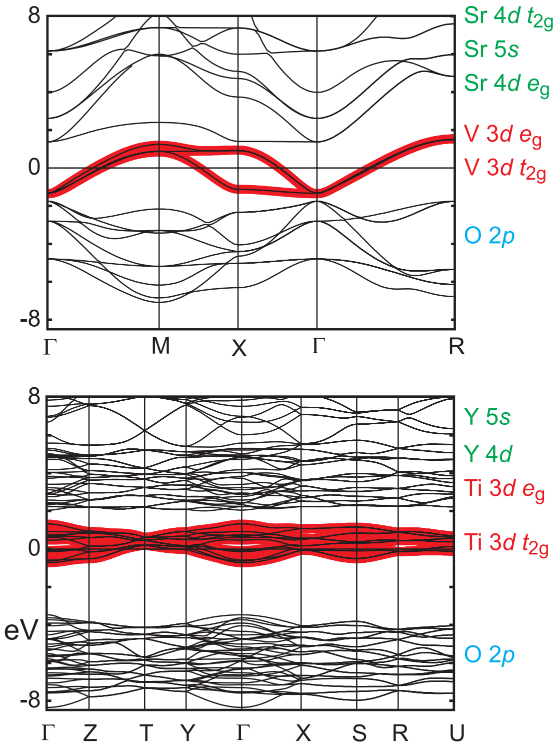

Figure 53: LDA energy bands of cubic $SrVO_3$ (top) and orthorhombic $YTiO_3$ (bottom). The t_{2g} bands obtained with the full (black) and downfolded (red) NMTO basis sets are identical.

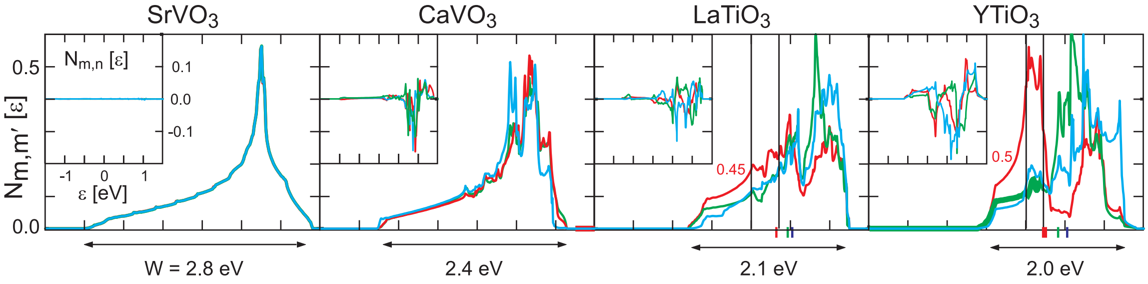

Figure 54: LDA on-site DOS matrix, $N_{mm'}(\varepsilon)$, in the representation of t_{2g} Wannier orbitals which diagonalizes the on-site term of H^{LDA}. The insets give the off-diagonal elements. In the vanadates, the eigenfunctions are *xy*, *yz*, and *zx*. In $SrVO_3$, these orbitals are degenerate, but in $CaVO_3$, the energy of the *xy* orbital (blue) is $\Delta = 0.08$ eV below that of the two other orbitals. In the titanates there are three singly-degenerate levels with the lowest (red) being 0.14 eV below the middle in $LaTiO_3$ and 0.20 eV in $YTiO_3$. The lowest-energy eigenfunctions are shown in Fig. 56.

For an isolated set of bands, a set of Wannier functions constitutes a *complete*, orthonormal set of orbitals with *one* orbital per band (Fig. 53). For the d^1 perovskites we take the correlated orbitals to be three localized B t_{2g} Wannier orbitals, and in H^{LDA} we neglect the degrees of freedom from all other bands. In order to be complete, such a Wannier orbital must have a tail with e.g., O *p* and A *d* characters. Our Wannier orbitals are symmetrically orthonormalized N^{th}-order muffin-tin orbitals (NMTOs), which have all partial waves other than B *xy*, *yz*, and *zx* downfolded. For the on-site Coulomb interactions we use the common assumption that, as in the isotropic case, they can be expressed in terms of two parameters, U and J. The former we take to be 5 eV for all four perovskites, and the latter has been calculated to be 0.68 eV for the vanadates and 0.64 eV for the titanates. The self-energy can now be obtained from the solution of an effective Anderson impurity model which involves only 3 correlated orbitals. All components of the self-energy matrix $\Sigma_{mm'}(\omega)$ between different Wannier functions on a given B-site are taken into account. From this 3×3 matrix, by use of the symmetry (Fig. 52), we construct a 12×12 block-diagonal self-energy matrix. This is then used together with $H^{\mathrm{LDA}}(\mathbf{k})$ to obtain the Green function at a given **k**-point. Fourier transformation over the entire Brillouin zone yields the local Green function associated with a primitive cell and its 3×3 on-site block is used in the DMFT self-consistency condition in the usual manner. The 3-orbital impurity problem is solved by a quantum Monte Carlo scheme which is accurate at high temperature.

Figure 54 displays the LDA on-site DOS matrix, $\mathrm{N}_{mm'}(\varepsilon)$, in that representation of the t_{2g} Wannier orbitals which diagonalizes the on-site term of H^{LDA}, i.e., the ligand and crystal-field term. The t_{2g} band of cubic $SrVO_3$ consists of three degenerate subbands, and since the *xy*,*yz*, and *zx* orbitals hardly interact, each subband is nearly 2-dimensional and gives rise to a nearly logarithmic DOS peak. Going to $CaVO_3$, the bandwidth is reduced from 2.8 to 2.4 eV for the reasons mentioned before, and the energy of the *xy* orbital (the center of gravity of $N_{\mathrm{xy,xy}}$) is lowered by 0.08 eV compared to that of the degenerate *xz* and *yz* orbitals. Going from the vanadates to the titanates, the increased misalignment and loss of oxygen character further reduce the bandwidths to 2.1 and 2.0 eV. Moreover, the *xy*, *yz*, and *zx* Wannier orbitals mix and the levels split with the middle (highest) being 0.14 (0.20) eV above the lowest in $LaTiO_3$, and 0.20 (0.33) eV in $YTiO_3$. Finally, there are strong off-diagonal elements of the DOS matrix even in the eigenrepresentation of $H^{\mathrm{LDA}}_{\mathrm{on}}$. In $YTiO_3$, the diagonal DOS element for the orbital with the lowest energy exhibits a pseudogap. Despite the strong increase of the level splittings, Δ, they remain an order of magnitude smaller than the t_{2g} bandwidths, and also smaller than the subband-widths.

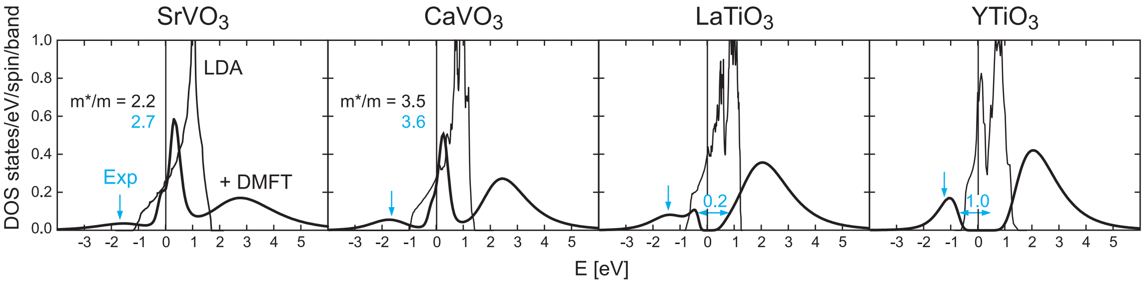

Figure 55: LDA DOS (thin) and LDA+DMFT spectral function calculated with $U=5\,\mathrm{eV}$ and $T=770\,\mathrm{K}$ (thick). Results from optical conductivity and photoemission measurements are indicated in blue.

As a consequence, the eigenfunction for the lowest level is occupied by merely 0.45 electron in $LaTiO_3$ and 0.50 in $YTiO_3$. Nevertheless, the splittings are large compared with the spin-orbit splitting (20 meV) and kT, and they are not caused by the JT distortions, as we have verified by turning them off in the calculations.

By performing LDA+DMFT calculations for several values of U between 3 and 6 eV, we found that the critical ratio $(U-2J)_c\,/\,W$ decreases from 2 to 1.4 when going along the series. This is consistent with an increasing Δ, and it indicates that the Mott transition is driven as much by the decrease of effective degeneracy (from 3 to almost 1) as by the reduction of bandwidth. As shown in Fig. 55, the main features of the experimental photoemission spectra for all four materials, as well as the correct values of the mass enhancements for the metals and the Mott-Hubbard gap for the insulators, are reproduced by taking U constant ≈ 5 eV. This is satisfying, because U is expected to be similar for vanadates and titanates. Despite very similar bandwidths for $LaTiO_3$ and $YTiO_3$, the gaps are very different, 0.2 and 1 eV. This is consistent with our findings that the t_{2g} level splittings are larger and $(U-2J)_c\,/\,W$ smaller in $YTiO_3$ than in $LaTiO_3$. Diagonalization of the matrix of occupation numbers reveals that for the titanates *one orbital per site is nearly full* and that this orbital is nearly identical with the one we obtained from the LDA as having the lowest energy. The Coulomb correlations increase its occupation from 0.45 to 0.88 in $LaTiO_3$ and from 0.50 to 0.96 in $YTiO_3$. This orbital polarization increases around the metal-insulator transition and becomes complete thereafter. In the vanadates, each orbital is approximately 1/3 occupied for all U in the range from 0 to 6 eV. The nearly complete orbital polarization in the titanates indicates that correlation effects in the paramagnetic Mott insulating state considerably decrease orbital fluctuations, and makes it unlikely that $YTiO_3$ is a realization of an orbital liquid. In $LaTiO_3$ some orbital fluctuations are still active, although quite weak. Whereas the localization is caused by Coulomb correlations, the chemistry (LDA) selects the orbital (Fig. 56). For illustration of the orbital order, we have placed this orbital on each of the 4 Ti-sites. Although $LaTiO_3$ and $YTiO_3$ have the same space group, their orbital orders look different. This difference reflects the extent to which the orbital has the *bc*-plane through Ti as a mirror, and is only quantitative. What causes this particular Ti t_{2g} orbital to have the lowest energy is *cation covalency* and crystal-field effects: the positive (blue) lobes have bonding $3z_{111}^2-1=(xy+xz+yz)/\sqrt{3}$ character on the *nearest* A cations and the negative (red) lobes have bonding xy character on the next-nearest A cations which continues in bonding $(x-y)/\sqrt{2}$ character on the oxygen closest to that cation. The former type of AB covalency dominates in $LaTiO_3$, while the latter type of ABO covalency dominates in $YTiO_3$, where the shortest YO bond is merely 10% longer than the TiO bond. The LDA pseudogaps as well as the level splittings are thus caused by the A d character not used to drive the $GdFeO_3$ distortion, but left behind in the Ti t_{2g} band (Fig. 52).

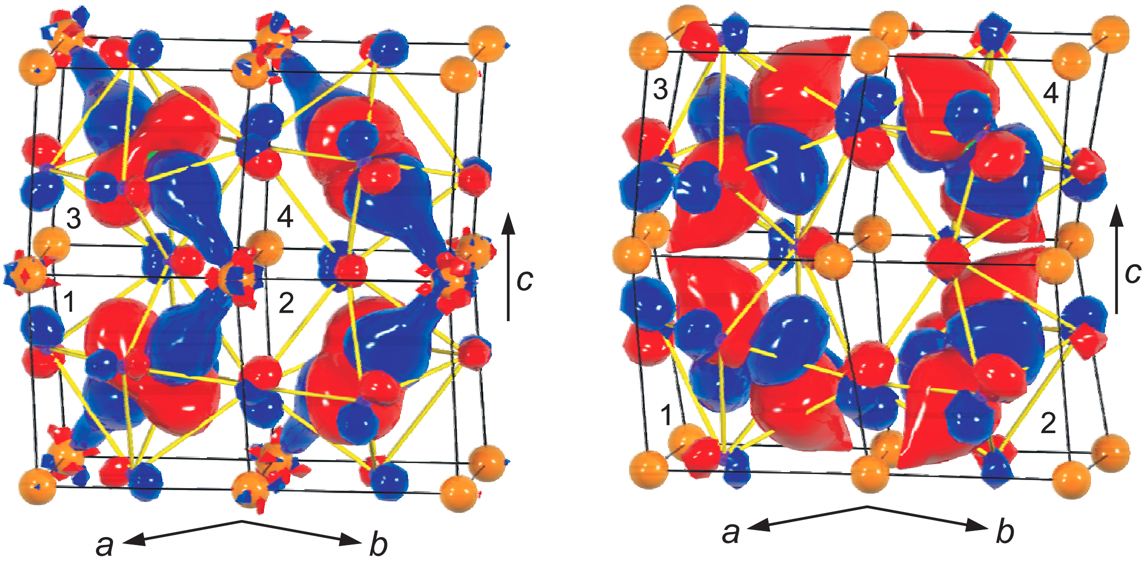

Figure 56: The almost fully occupied localized orbital in $LaTiO_3$ (left) and $YTiO_3$ (right), placed on each of the 4 Ti-sites to exhibit the orbital order. On site 1, this orbital is the linear combination $0.586|xy\rangle + 0.275|xz\rangle + 0.762|yz\rangle$ of the Ti t_{2g} Wannier functions in $LaTiO_3$ and $0.622|xy\rangle - 0.029|xz\rangle + 0.782|yz\rangle$ in $YTiO_3$. Blue and red indicate respectively positive and negative values. A relatively low numerical value of the contour has been used in order to bring out covalency effects.

The different JT distortions of the oxygen square in $LaTiO_3$ and $YTiO_3$ are a reaction to, rather than the cause of the difference in the orbital orders. The difference in the orbital orders is reflected in the hopping integrals between nearest neighbors: $t_x = t_y = 99\,(38)$ meV and $t_z = 105\,(48)$ meV for $LaTiO_3$ ($YTiO_3$). These hoppings are fairly isotropic and twice larger in $LaTiO_3$ than in $YTiO_3$. Moreover, the hoppings to the two excited orbitals are stronger in $YTiO_3$ than in $LaTiO_3$. All of this is consistent with $LaTiO_3$ being 3-dimensional anti- and $YTiO_3$ ferromagnetic at low temperature, and it warrants detailed future calculations of the spin-wave spectra.

We have thus seen that the B t_{2g} degeneracy *is lifted* at the classical level. This is not due to the small JT distortions via OB $pd\pi$-coupling, but to the $GdFeO_3$-type distortion. This distortion is driven by the increasing OA $pd\sigma$-covalency, and it primarily pulls 4 of the 12 oxygens neighboring a given A cation closer to it. Moreover, 2 to 4 of the 8 A cations neighboring a given transition metal ion (B) are pulled closer. The B t_{2g} orbitals couple to the OA distortion via oxygen (BOA $d p\pi$–$pd\sigma$), and they couple directly (AB $dd\sigma$) to the AB distortion.

In conclusion, we have extended the LDA+DMFT approach to the non-cubic case using ab initio downfolding in order to obtain a low-energy Wannier Hamiltonian. Applying this method to the Mott transition in $3d^1$ perovskites, we have explained the photoemission spectra and the values of the Mott gap without adjustable parameters, except a single value of U. The Mott transition is driven by correlation effects and $GdFeO_3$-type distortion through reduction, not only of bandwidth, but also of effective orbital degeneracy. Correlation effects and cation covalency suppress orbital fluctuations in the high-temperature paramagnetic insulating phase of $LaTiO_3$ and $YTiO_3$.

Anisotropic two-dimensional spin excitations in an untwinned high-temperature superconductor

V. Hinkov, D. Manske, A. Kulakov, C.T. Lin, and B. Keimer;
S. Pailhès, P. Bourges, and Y. Sidis (CEA Saclay, France)

The fundamental building block of the copper oxide superconductors is a Cu_4O_4 square plaquette. In most of these materials, the plaquettes are slightly distorted and form a rectangular lattice. An influential theory of high-temperature superconductivity predicts that this two-dimensional lattice is intrinsically unstable towards a 'striped' state with *one-dimensional* spin and charge order. Static stripe order has indeed been reported in specific layered copper oxides in which superconductivity is suppressed, but the theory also predicts phases in which robust superconductivity coexists microscopically with liquid-crystal-like stripe order. The liquid-crystal order parameter is expected to align itself preferentially along one of the axes of the rectangular lattice, generating a quasi-one-dimensional pattern in scattering experiments. Fluctuating stripes can be identified by virtue of their characteristic quasi-one-dimensional charge and spin excitations. Since charge excitations hybridize strongly with lattice vibrations, quasi-one-dimensional spin excitations are the most explicit fingerprints of the predicted stripe fluctuations.

Detecting such fluctuations requires an energy- and momentum-resolved probe that is sensitive to electronic magnetic moments. These requirements are uniquely met by inelastic neutron scattering, and incommensurate spin excitations observed in several families of layered copper oxides have indeed been interpreted as evidence for fluctuating stripes. However, all neutron scattering experiments thus far reported have been carried out on 'twinned' crystals with either equal or only slightly different proportions of micron-scale twin domains in which the rectangular Cu_4O_4 plaquettes are rotated by 90° with respect to one another. Since the scattering pattern from fully twinned crystals consists of equal contributions from both twin domains, even perfectly one-dimensional spin fluctuations generate a four-fold symmetric pattern, so that they cannot be discriminated from microscopically two-dimensional fluctuations. The results of prior neutron scattering experiments on partially detwinned, underdoped $YBa_2Cu_3O_{6+x}$ crystals with a domain population ratio of $\approx$ 2:1 have been interpreted as evidence of a one-dimensional character of the magnetic fluctuations [Mook *et al.*, Nature **404**, 729 (2000)]. However, as the signals from majority and minority domains were superimposed in these experiments, the full geometry of the incommensurate spin excitations could thus far not be determined.

Using neutron scattering from a large mosaic of very high quality, fully untwinned, nearly optimally doped $YBa_2Cu_3O_{6.85}$ crystals, we have resolved this issue definitively. Because of the slightly different lengths of the lattice parameters a and b in the CuO_2 planes, the (2,0,0) and (0,2,0) crystallographic Bragg reflections occur at different wavevector transfers $\boldsymbol{Q}$. Since neutron scattering is a bulk probe, scans through these reflections directly reveal the bulk population ratio of the two twin domains. Figure 57(a) shows that this ratio is about 20:1, that is, one order of magnitude larger than that of previous neutron scattering work on partially detwinned $YBa_2Cu_3O_{6+x}$ crystals. In contrast to prior work, the contribution of the minority domain is thus well below the experimental background level and does not add significant systematic uncertainties to the data analysis.

Figure 57(b) shows representative magnetic neutron scattering data from this crystal array. The overall features of the neutron cross section are in good agreement with prior work on twinned crystals. Due to antiferromagnetic correlations between spins in the CuO_2 plane, the

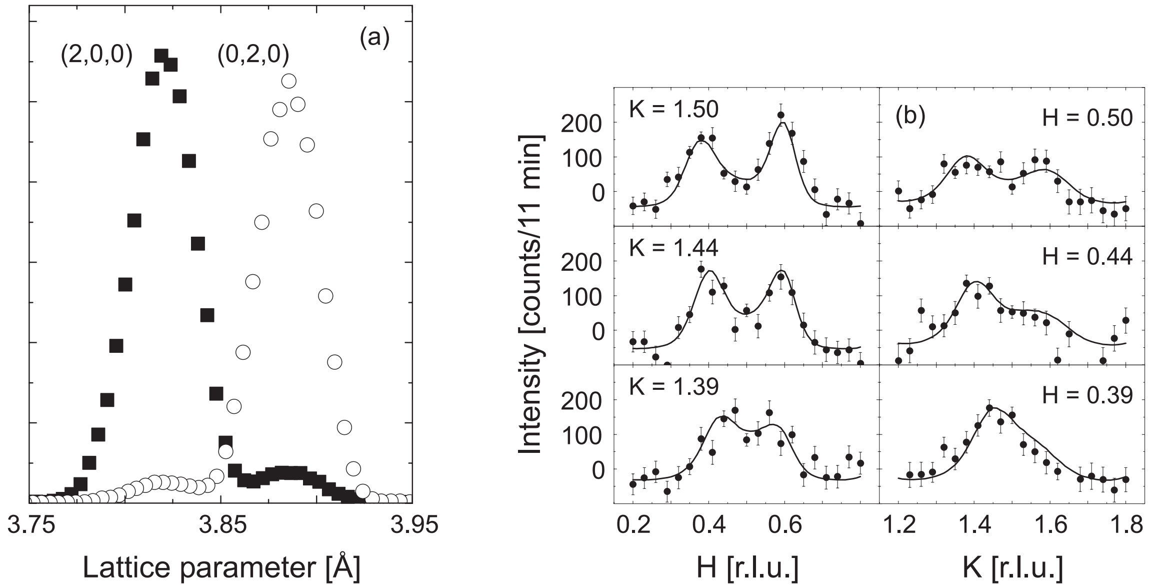

Figure 57: (a) Longitudinal elastic scans through the (2,0,0) and (0,2,0) crystallographic Bragg reflections of the multicrystal mosaic, demonstrating a twin domain population ratio of ≈ 20:1. (b) Constant-energy scans of the magnetic neutron scattering cross section at 35 meV along the in-plane axes a^* and b^* of the reciprocal lattice. The wavevector is quoted in reciprocal lattice units (r.l.u.).

spectral weight of low-energy spin excitations in $YBa_2Cu_3O_{6+x}$ is centered around the in-plane wavevector $\boldsymbol{Q}_{AF} = (0.5,1.5)$ (equivalent to (π,π) square lattice notation with unit lattice constant). In agreement with prior work on twinned $YBa_2Cu_3O_{6+x}$, the magnetic excitations are strongly enhanced below the superconducting transition temperature. The lowest-energy excitations are incommensurate (Fig. 57(b)). The incommensurate excitation branches disperse towards $\boldsymbol{Q}_{AF}$ with increasing excitation energy, and they merge at $\hbar\omega_0 = 41$ meV.

The new aspect of this work is the determination of the in-plane anisotropy of the spin excitations. Well-defined incommensurate peaks are observed in scans along both a^* and b^* (Fig. 57(b)). A full set of constant-energy scans reveals that the locus of maximum magnetic intensity forms a circle around $\boldsymbol{Q}_{AF}$. Together with a series of constant-energy scans at other excitation energies (not shown), this demonstrates the two-dimensional geometry of the spin excitations along the entire dispersion surface. These results are at variance with claims of a one-dimensional spin fluctuations geometry based on earlier neutron scattering work on partially detwinned samples. While the dispersion surface of the spin excitations is thus isotropic within the CuO_2 layers, both the amplitude and the width of the incommensurate peaks exhibit pronounced in-plane anisotropies. At $\hbar\omega = 35$ meV, for instance, the scans along a^* are more intense and about a factor of three sharper than those along b^* (Fig. 57(b)). We have carried out a comprehensive map of the neutron scattering cross section. In order to extract the magnetic spectral weight from the experimentally determined scattering profiles, we have numerically convoluted a model cross section with the instrumental resolution function. Figure 58(a) provides a full representation of the magnetic spectral weight resulting from this analysis.

We now discuss possible theoretical explanations for the anisotropic magnetic scattering pattern shown in Fig. 58(a). Theories based on a one-dimensional, static array of stripes cannot account for the two-dimensional scattering pattern. The map of the magnetic intensity does, however, bear some resemblance to the scattering pattern generated by a nematic liquid crystal close to a nematic-to-smectic critical point. In this scenario, the structural anisotropy between *a*- and *b*-axes may act as a weak aligning field for the nematic director. However, no predictions for the magnetic fluctuation spectrum of a liquid-crystalline stripe phase have thus far been reported.

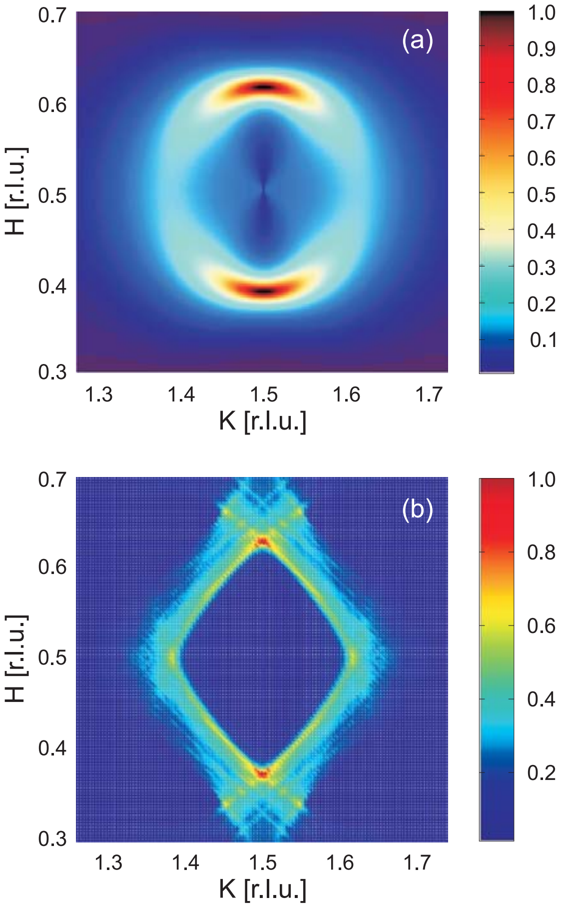

Figure 58: (a) Experimentally determined constant-energy cut of the magnetic spectral weight at 35 meV. (b) Result of an RPA-calculation of the same constant-energy cut.

We have therefore explored an alternative model according to which the sharp magnetic excitations are due to a magnon-like bound state in the superconducting energy gap. The magnetic spectrum consisting of this collective mode as well as particle-hole spin-flip excitations can be numerically computed in the random phase approximation (RPA). In the absence of experimental information about the in-plane anisotropy, prior calculations in this framework had only considered the influence of the CuO_2 layers, ignoring a possible influence of the *b*-axis oriented CuO chains. Based on the observed *c*-axis modulation of the intensity, we can rule out a direct contribution from the CuO chains to the observed magnetic signal. However, an indirect influence of the CuO chains on the spin dynamics in the layers cannot be excluded. The plane-derived Fermi surfaces are predicted to exhibit a $\approx 5\%$ in-plane anisotropy due to the hybridization between orbitals centered on chains and layers and the different in-plane Cu–O bond lengths along *a* and *b* [Andersen *et al.*, Journal of Physics and Chemistry of Solids **56**, 1573 (1995)]. A preliminary RPA model calculation taking this bandstructure anisotropy into account yields a qualitative description of the in-plane anisotropy of the magnetic dynamics. This is illustrated by a comparison of the calculated constant-energy cut of the magnetic spectral weight at 35 meV (Fig. 58(b)) with the experimentally determined magnetic spectrum at the same excitation energy. Especially, the enhancements along the (H,1.5) direction close to H = 0.4 and H = 0.6 are reproduced. This agreement demonstrates that the observed anisotropy in the spin dynamics can also be addressed within Fermi liquid theories without the necessity to invoke models based on fluctuating stripes.

Ferromagnetic/superconducting bilayer thin film structures: a model system for spin diffusion length estimation

S. Soltan, J. Albrecht, G. Cristiani, and H.-U. Habermeier

The proximity of materials with different functionalities and long-range order can give rise to novel phenomena that do not exist in the constituent materials. The class of perovskite-type transition metal oxides with the general formula ABO_3 are especially suitable for such investigations due to their rich variety of ordering phenomena ranging from piezoelectricity, ferroelectricity to ferromagnetism, antiferromagnetism, and superconductivity. Stimulated by the discovery of cuprate high-temperature superconductors, the technology to prepare single crystal type thin films of these multicomponent perovskites has been developed to a high standard. These technological achievements open the possibility to prepare heterostructures and superlattices composed of different ABO_3 oxides, in which the mutual interaction between layers can be studied and bear the possibility to develop new types of functional electronic devices.

Of special interest are heterostructures and superlattices with ferromagnetic (FM) and superconducting (SC) constituents whose antagonistic order parameters are thought to be mutually exclusive in homogeneous systems. However, a coexistence is possible in layered structures, such as the ferromagnetic superconductor $RuSr_2GdCu_2O_8$ or in artificially grown FM/SC superlattices where novel types of combined ground states are postulated.

In this contribution we describe transport and magnetic measurements of heterostructures that consists of superconducting $YBa_2Cu_3O_7$ (YBCO) and half-metallic $La_{2/3}Ca_{1/3}MnO_3$ (LCMO). Special emphasis is put on the role of self-injection of spin-polarized quasiparticles. The charge carriers in $La_{2/3}Ca_{1/3}MnO_3$ are nearly 100% spin-polarized. This allows one to study the self-injection of spin-polarized charge carriers into the YBCO layers and subsequently to estimate the spin diffusion length.

Epitaxial bilayers for different thickness of optimally doped YBCO and LCMO films are grown by pulsed laser deposition onto single crystalline $SrTiO_3$ substrates. The thickness of LCMO was kept at 50 nm while that of YBCO was varied from 10 to 100 nm. The X-ray diffraction patterns in Fig. 59 testify for the single-phase textured growth of the films and are indicative of a slight tensile strain of 0.4% for YBCO.

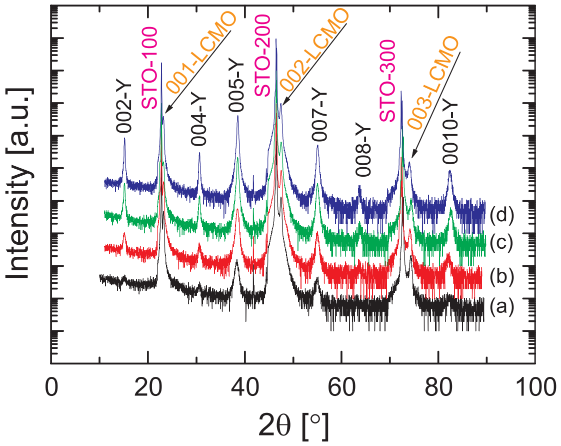

Figure 59: X-ray pattern for the bilayer structures with thickness of $t_{\mathrm{LCMO}} = 50$ nm and (a) $t_{\mathrm{YBCO}} = 20$ nm, (b) 30 nm, (c) 50 nm, and (d) 100 nm respectively. Only the (00l) peak is found, i.e., the both layers are grown textured on the STO (100) substrate.

Figure 60 shows the normalized magnetization (zero field cooling) versus temperature of a 50 nm LCMO/30 nm YBCO heterostructure. We observe the onset of FM ordering at $T_{\mathrm{Curie}} \cong 150$ K and a strong diamagnetic signal at $T_c = 75$ K at the SC transition.

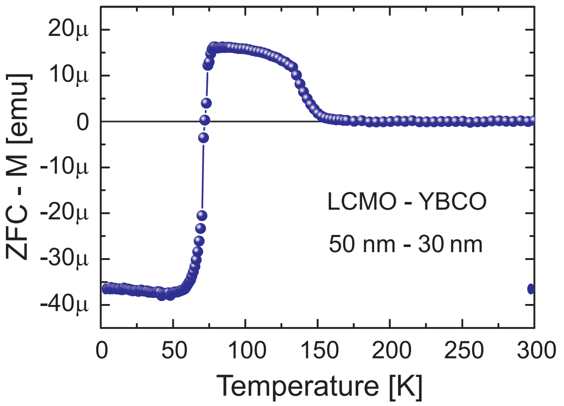

Figure 60: Temperature dependence of the magnetization (M) for a bilayer of $t_{\mathrm{LCMO}} = 50\,\mathrm{nm}$ and $t_{\mathrm{YBCO}} = 30\,\mathrm{nm}$ (zero field cooled, applied field 10 Oe).

Figure 61 displays the ratio of $T_c/T_{c-\mathrm{bulk}}$ for the heterostructures and for single layer YBCO films. It can be seen that the critical thickness of the YBCO layer, as determined from a steep drop in T_c, is about 30 nm in the heterostructures as compared to 10 nm in the pure films. We only note here that we obtained similar results for the critical current density j_c, which shows a substantial decrease for $t_{\mathrm{YBCO}} < 40\,\mathrm{nm}$ in the heterostructures. The general trend that T_c as well as T_{Curie} strongly depend on the relative thickness of the constituents has been confirmed in superlattices composed of $\mathrm{YBa_2Cu_3O_{7-x}/La_{2/3}Ca_{1/3}MnO_3}$ and $\mathrm{YBa_2Cu_3O_{7-x}/SrRuO_3}$.

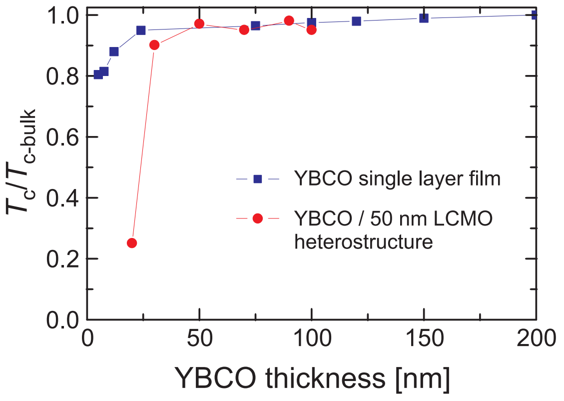

Figure 61: Thickness dependence of T_c for single layer YBCO films (squares) and LCMO/YBCO bilayers of different YBCO thickness (circles).

Besides technological materials related aspects such as incomplete oxygenation, interface roughness, or chemical reaction at the interfaces, several intrinsic mechanisms can account for the observed T_c reduction, such as the conventional proximity effect or a massive charge carrier transfer across the interface. However, based on a quantitative analysis we can rule out all of these scenarios. Charge redistribution close to the interface is a well-known phenomenon. Nevertheless, estimates based on the depletion layer model of semiconductor theory in conjunction with the Lindhard dielectric function for an anisotropic degenerate Fermi gas reveal that the depletion layer should involve only a few monolayers. Alternatively, we discuss a model that is based on the, controversy discussed, self-injection of quasiparticles from the ferromagnet into the superconductor where the large magnetic exchange energy in the LCMO layer is the driving force. In to the classical proximity effect, the injection of spin-polarized quasiparticles into the SC layer leads to a T_c reduction which can be described as:

$$\frac{\Delta(n_{\mathrm{qp}})}{\Delta(0)} \approx 1 - \frac{2n_{\mathrm{qp}}}{4N(0)\,\Delta(0)}$$

Here $\Delta(n_{\mathrm{qp}})$ is the perturbed SC gap in the presence of the density n_{qp}, of spin-polarized quasiparticles. $N(0)$ and $\Delta(0) \approx 20\,\mathrm{meV}$ in YBCO are the density of states and the unperturbed energy gap at $T = 0\,\mathrm{K}$, respectively. The self-injection occurs along the *c*-axis across the highly transparent interface and is governed by the large exchange splitting energy, $\Delta E_{\mathrm{ex}} \approx 3\,\mathrm{eV}$, of the LCMO layer. The temperature dependence of n_{qp} can be written in the simple form:

$$n_{\mathrm{qp}}(T) \approx 4N(0)\Delta(0)\sqrt{\frac{\pi}{2}\frac{\Delta(T)k_BT}{\Delta(0)^2}}\; e^{-\frac{\Delta(T)}{k_BT}}$$

In analogy to classical FM/SC structures, the spin diffusion length should be $\xi_{\mathrm{FM}} \approx (l_0 v_F \tau_s)^{1/2}$ where $l_0(T = 0\,\mathrm{K}) \approx 20\,\mathrm{nm}$ is the mean free path in YBCO and the spin relaxation time, τ_s, is given by:

$$\tau_s \approx 3.7\frac{\hbar k_B T_c}{\Delta E_{\mathrm{ex}}\Delta(T)}, \quad \text{with} \quad \Delta(T) \sim \Delta(0)\sqrt{1-\frac{T}{T_c}}$$

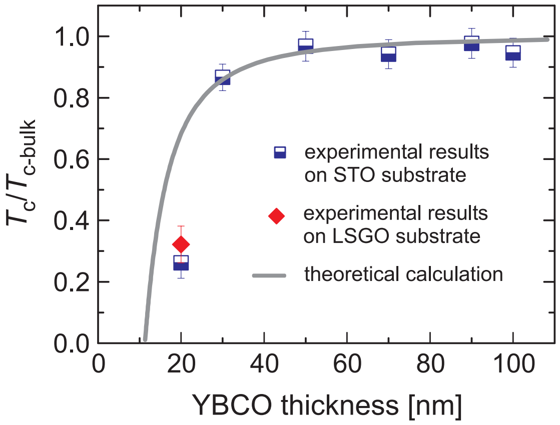

Figure 62: Ratio between the SC transition temperatures of bilayers with different YBCO thickness and the one in bulk YBCO (squares). The model (solid line) gives a good description of the experimental data.

Combining these equations we obtain a relation which contains the spin diffusion length and its temperature dependence. First of all, we have to estimate the critical spin density in the superconductor where T_c becomes severely suppressed. Here we assume that spins in high-temperature superconductors can be viewed as unitary scatterers, similarly like Zn or Ni impurities in YBCO which strongly reduce T_c for concentration of 2–10%. Accordingly, a critical spin density is achieved over a distance of $d_{\text{crit}} \approx 3\,\xi_{\text{FM}}$ within the YBCO layer. This enables us to model the experimental data where the only fitting parameter is the temperature-dependent quasiparticle density. As shown in Fig. 62 we obtain a good fit to the experimental data with $\xi_{\text{FM}} = d/3 = 10$ nm.

In conclusion, we have investigated experimentally the effects of the diffusion of spin-polarized quasiparticles in a bilayer structure of manganate and a cuprate. From X-ray analysis we have shown, that $YBa_2Cu_3O_{7-x}$ thin films can be grown epitaxially on thin epitaxial films of $La_{2/3}Ca_{1/3}MnO_3$. Transport and magnetization measurements confirm the coexistence of ferromagnetism and superconductivity at low temperature in these structures. We find that the transition temperature of the superconducting film drastically decreases for thinner $YBa_2Cu_3O_{7-x}$ films. Using a simple model we determined the spin diffusion length of the spin-polarized quasiparticles from $La_{2/3}Ca_{1/3}MnO_3$ into the superconductor $YBa_2Cu_3O_{7-x}$ to be in the range of $\xi_{\text{FM}} \approx 10$ nm.

Superconductivity and phase separation in $Na_xCoO_2{\cdot}yH_2O$ single crystals

P. Lemmens, N.N. Kovaleva, X.N. Zhang, D.P. Chen, C.T. Lin, and B. Keimer;
K.-Y. Choi (RWTH Aachen); F.C. Chou (CMSE, MIT, Cambridge)

The recent discovery of superconductivity (SC) in the layered cobalt oxohydrate $Na_xCoO_2{\cdot}yH_2O$ [Takada *et al.*, Nature **422**, 53 (2003)] has obtained considerable attention. Its transition temperature $T_c = 4.6$ K, is much lower than those of the layered copper oxides, but higher than that of Sr_2RuO_4, the only other known layered transition metal oxide which exhibits SC. Furthermore, it has been proposed that the SC state may be unconventional, possibly even with spin triplet pairing. This has brought renewed attention to the exceptional electronic and magnetic properties of the water-free, non-superconducting compound Na_xCoO_2 which is a metal with an anomalously enhanced thermoelectric power that may be relevant for cryoelectronic applications. Its magnetic properties strongly depend on Na content, for example, static antiferromagnetic order occurs only for Na-rich samples with $x > 0.75$. A low-spin state scenario with $S = 1/2$ for Co^{4+} and $S = 0$ for Co^{3+} is commonly assumed where the number of $s = 1/2$ Co moments is determined by the ratio of $Co^{4+}/Co^{3+} = 1 - x$. The most attractive property of the cobaltites is that superconductivity, long-range Néel ordering and other signatures of electronic correlations can be tuned by the Na content of the compound.

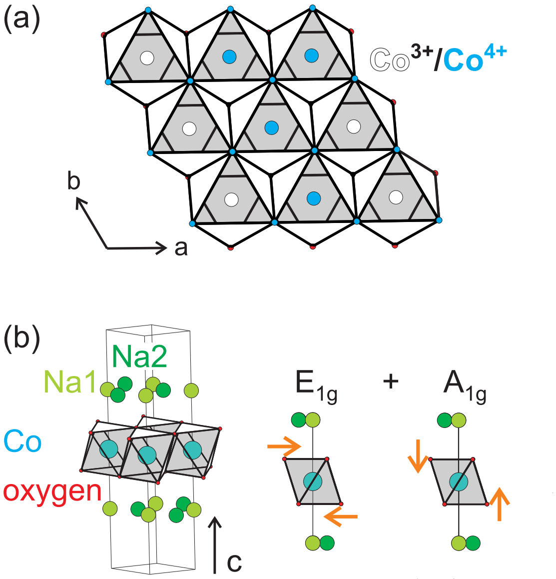

Figure 63: (a) View on the *ab*-plane of the hexagonal structure of Na_xCoO_2. (b) Sketch of the unit cell and Raman-active oxygen displacements of $Na_{0.7}CoO_2$ for in-plane light polarization. The eigenvectors of the oxygen displacements are sketched. In the unit cell the two Na-sites and the CoO_6 octahedra are denoted.

Figure 63(a) shows the *ab*-plane of the hexagonal structure of Na_xCoO_2 with a triangular lattice of Co ions and CoO_6 octahedra that constitute the CoO_2 layers. Shell model calculations reveal Raman-active oxygen displacements of in-plane E_{1g} and out-of-plane A_{1g} symmetry with frequencies of approximately 460 and 580 cm^{-1}. The inversion symmetry of the Co-sites inhibits their contribution to the Raman signal. The Raman-active phonons shown in Fig. 63(b) probe the most important aspects of this compound: the in-plane correlations and charge disproportionation on Co-sites as well as the out-of-plane correlations related to the coupling between the CoO_2 planes.

We performed Raman scattering experiments to investigate the possible relationship between electronic correlations and superconductivity and to clarify the role of hydration in $Na_xCoO_2 \cdot yH_2O$. The availability of high-quality single crystals from the Crystal Growth Service Group at MPI-FKF initiated several experimental and theoretical activities in our department, like muon spin rotation (μSR), neutron scattering, and infrared ellipsometry. Recent results for $Na_{0.83}CoO_2$ are summarized by Bayrakci *et al.* [Physical Review B **69**, 100410(R) (2004)]. More details on the preparation and characterization are given by Chen *et al.* [Physical Review B **69** (2004), in print].

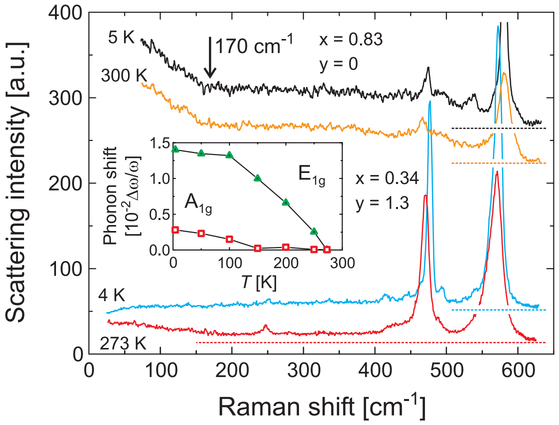

Figure 64: In-plane (xx) Raman spectra on single crystals with $x = 0.83$; $y = 0$ (top) and $x = 0.35$; $y = 1.3$ (bottom) as function of temperature. The inset shows the temperatures dependence of the phonon frequency for $Na_{0.35}CoO_2 \cdot 1.3\,D_2O$. Spectra have been given an offset for clarity as indicated by the dashed horizontal lines.

Raman scattering of $Na_xCoO_2 \cdot yH_2O$ is dominated by sharp modes due to phonon scattering and a continuum of scattering attributed to electronic Raman scattering. In Fig. 64 data are shown at two different temperatures for $Na_{0.83}CoO_2$ and $Na_{0.35}CoO_2 \cdot 1.3\,D_2O$. In this experiment incident and scattered light are both parallel to the CoO layers allowing modes of E_{1g} and A_{1g} symmetry. For $Na_{0.83}CoO_2$ we observe a sharp maximum at 580.7 cm^{-1} and a second mode with weaker intensity at 475 cm^{-1}. These maxima are attributed to the above discussed Raman-active oxygen displacements of the CoO_6 octahedra. There is no obvious change with temperatures of the excitation spectrum beside a maximum at 540 cm^{-1} probably related to an E_{2g} mode that increases in intensity at low temperatures.

Raman spectra of the SC, hydrated single crystal are shown in Fig. 64 (bottom). Compared to $Na_{0.83}CoO_2$ the higher energy out-of-plane mode is renormalized considerably leading to a shift from 580.7 to 572.5 cm^{-1}. This softening must be attributed to the reduced interplane coupling and near-doubling of the unit cell in the SC, hydrated phase. In contrast, the in-plane mode is not shifted appreciably as it mainly concerns bonds within the CoO_2 layers. The small hardening from 475 to 477 cm^{-1} may be understood as a moderate response to the decreasing thickness of the CoO_2 layers with hydration. Concerning the intensities of the phonon modes there is a large effect for the in-plane E_{1g} mode. In the non-SC sample this mode is strongly damped. The ratio of the two phonon intensities is determined to be 0.2 for the non-SC sample and 0.8 for the SC sample.

Systematic investigations of the phonon intensity as function of stoichiometry give evidence that the damping of the in-plane E_{1g} mode is intrinsic and related to disorder within the CoO_2 layers [Lemmens, *et al.*, Journal of Physics: Condensed Matter **16**, S857 (2004)]. It may be based on charge disproportionation of the mixed Co^{4+}/Co^{3+} ion sites or induced by the partially occupied Na-sites. Both mechanisms may even coexist. It is interesting to note that the ratio of phonon intensities does not change with temperature. This implies, that the related structural or electronic inhomogeneity in the CoO_2 layers is static.

In the following we will discuss the scattering continuum that extends from low energies with a kink at 170 cm^{-1} up to about 500 cm^{-1}. From the data shown in Fig. 64 and Fig. 65 on an enlarged scale it is evident that the continuum does not change its frequency dependence with composition. However, in contrast to the phonon intensity, its intensity is strongly reduced in the SC sample. There is further evidence for a pronounced temperature evolution for $T < T^* = 150$ K as shown in Fig. 65. Below this temperature the kink is no more observable in the SC sample and with decreasing temperature a depletion of spectral weight is observed.

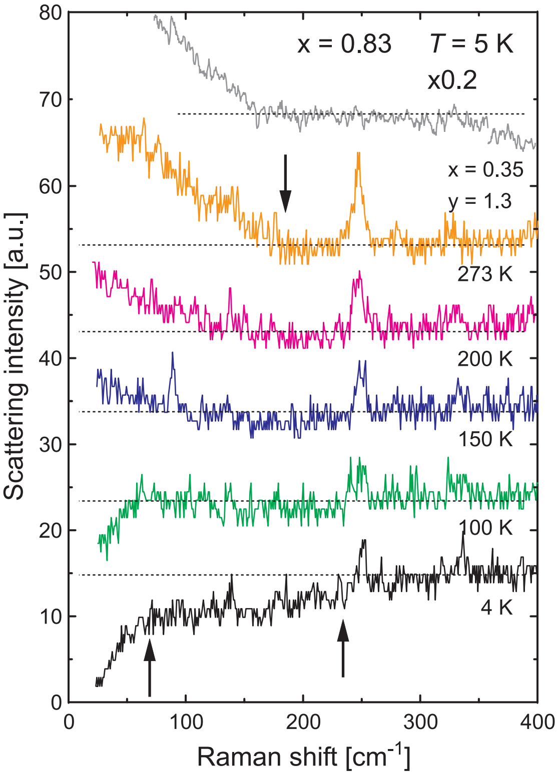

Figure 65: Low-energy Raman spectra on single crystals with $x = 0.35$; $y = 1.3$ and $x = 0.83$; $y = 0$ in (xx) light polarization. Curves are shifted for clarity and the dashed lines extrapolate the continuum for $250 \leq \Delta\omega \leq 400$ cm^{-1} to lower energies. The arrows mark characteristic energies of the continuum of scattering at 185 cm^{-1} at high temperatures and 70 and 230 cm^{-1} at low temperatures. A sharp excitation at about 250 cm^{-1} is attributed to an in-plane IR-active phonon mode.

The negligible temperature dependence of the continuum in the Na-rich, magnetically ordered $Na_{0.83}CoO_2$ ($T < T_N = 19.8$ K) excludes magnetic Raman scattering as its origin. In contrast, electronic excitations or electronic mass fluctuation should be considered. Electronic Raman scattering is visible in many correlated metals if fluctuations of the electronic mass, e.g., on anisotropic Fermi surface sheets are involved. A sufficient anisotropy of the Fermi surface exists due to the triangular structure of the Co-sites and their contribution to the electronic states at E_F. The frequency dependence of the observed continuum, however, is anomalous, as normal metals show a $1/\Delta\omega$-dependence. However, high-temperature superconductors (HTSC) show a very similar frequency-independent continuum that extends up to energies of 0.5 eV. The concept of a *marginal Fermi liquid* with a constant scattering rate describes this anomalous behavior. In the cobaltites the continuum extends to energies only up to $500\,\mathrm{cm}^{-1} \approx 60\,\mathrm{meV}$. This energy scale is smaller than in HTSC as in the present case also the electronic bandwidth and coupling constants are strongly reduced. The Néel temperatures of the two classes of materials differ by a factor of roughly 30. The large intensity of the Raman scattering continuum in $Na_{0.83}CoO_2$, that is a factor 6–10 larger than in SC samples, can be taken as one fingerprint of anomalous electronic correlations in the Na-rich, non-superconducting phase. There is probably a relationship between this large intensity, the anomalous Hall coefficient and the enhanced thermopower.

The reduction and spectral depletion observed in SC single crystals observed for $T < T^* = 150\,\mathrm{K}$ is interpreted as evidence for a suppression of low-energy fluctuations due to a gap formation. For a BCS-type superconductor a depression of low-energy excitations is expected at $T \ll T_c$ for Raman shifts $\Delta\omega < 2\,\Delta_{BCS} = 3.5 \cdot T_c \approx 11\,\mathrm{cm}^{-1}$, with $T_c = 4.6\,\mathrm{K}$. The much larger energy and temperature scales suggest that some other kind of ordering phenomenon (apart from SC) is at the origin of this gap feature. A likely candidate is a charge disproportionation onto distinct Co^{4+}/Co^{3+}-sites. Such a disproportionation, may it be of long or short-range order type, should suppress a part of the low-energy electronic fluctuations related to the Co t_{2g} states at the Fermi energy. Such an electronic phase separation is in accordance with the the importance of electronic correlations for the SC state in cobaltites. It has even been proposed that the SC phase should be embedded in a phase with coexisting charge and magnetic order [Tanaka *et al.*, Physical Review Letters **91**, 257006 (2003)]. Further experimental and theoretical investigation of these phenomena are clearly needed to enhance our understanding of this exciting class of materials.

Renormalization of the electron-phonon coupling in the one-band Hubbard model

E. Koch and R. Zeyher

The relevance of phonons for high-temperature superconductivity has been debated since the discovery of the high-T_c cuprates. Very early superconductivity-induced changes in the position and width of the phonons had been observed in $YBa_2Cu_3O_{7-\delta}$ by Raman scattering. These results could be quantitatively explained in terms of electron-phonon coupling constants calculated from first principles. Replacing Yttrium by other rare earth ions allowed to determine the frequency dependence of the induced self-energy which could very accurately be explained by theory and thus allowed a determination of the superconducting gap. The rather small magnitudes obtained for the electron-phonon coupling at the zone center as well as the absence of spectacular phonon renormalizations near T_c throughout the

Brillouin zone in neutron scattering suggested, however, that phonons play only a minor role in the microscopic mechanism for high-T_c superconductivity. More recently, interest in the electron-phonon coupling has been revived due to spectacular isotope effects, found not only in T_c, but also in the magnetic penetration depth and the frequency-dependent conductivity. Also strong renormalization effects of the electrons near the Fermi surface have been discovered in several cuprates. They have been attributed to phonons as well. Interest in the electron-phonon coupling was further fueled by quantum Monte Carlo simulations of the Hubbard-Holstein model, which suggest that the coupling shows pronounced forward scattering, and no substantial suppression at large U and small dopings. Although performed at quite high temperatures and for finite values of U, the findings are similar to those in the $1/N$ expansion of the *t*-*J*–model by Kulić *et al.* [Physical Review B **49**, 4395 (1994)].

The theoretical description of the electron-phonon coupling is, however, notoriously difficult. Quantum Monte Carlo, while in principle exact, is limited to fairly high temperatures (sign-problem) and small systems (computational effort). On the other hand, the $1/N$ expansion works at essentially zero temperature and in the bulk limit, but only applies to large U. To investigate the U dependence of the electron-phonon coupling we have used a different slave-boson method, based on the Kotliar-Ruckenstein formalism which works for low temperatures, large systems, and arbitrary values of U.

This linear response technique was originally developed by Koch [Physical Review B **64**, 165113 (2001)] for studying the charge response of the Hubbard model and could be adapted for the calculation of the static electron-phonon vertex $\Gamma(\mathbf{p},\mathbf{q})$, shown in Fig. 66. This vertex function acts as a momentum-dependent, multiplicative renormalization factor for the bare electron-phonon coupling. It is defined through the linear change in the one-particle Green's function $G(p)$ due to an external field V_{q}:

$$\frac{\delta G(p)}{\delta V_{\mathrm{q}}} = G(p)\,\Gamma(p,q)\,G(p+q).$$

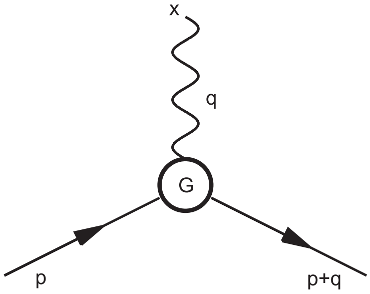

Figure 66: Electron-phonon vertex within linear response. The thick solid lines are the dressed propagators of the Hubbard model. The wavy line denotes the phonon – considered as a static external field.

In the following we consider dispersionless phonons, with local coupling to the electron density. Moreover, we focus on the static vertex, i.e., we consider only static fields $V_{\mathbf{q}}$.

Our results for the one-band Hubbard model with nearest (t) and next-nearest (t') neighbor hopping are displayed in Fig. 67. The plots show the static electron-phonon vertex for scattering for electrons on the Fermi surface. The effect of next-nearest neighbor hopping is illustrated by comparing calculations for $t' = 0$ and $t' = –0.35\,t$. We find that in both cases the on-site Coulomb interaction strongly reduces the electron-phonon coupling. This is not completely unexpected, as the charge response should be strongly suppressed by an on-site Coulomb interaction. Turning attention to the coupling as a function of momentum transfer $\mathbf{q}$ we find that $\Gamma(\mathbf{q})$ shows a broad peak around $\mathbf{q} = 0$. We do, however, *not* find a particularly pronounced forward scattering, as would have been expected from the results of the $1/N$ expansion for the *t*-*J*–model.

In fact, the electron-phonon vertex is often strongest close to $\mathbf{q} = (\pi,0)$. This difference between the two approaches is due to the different choice of the renormalization factors in the

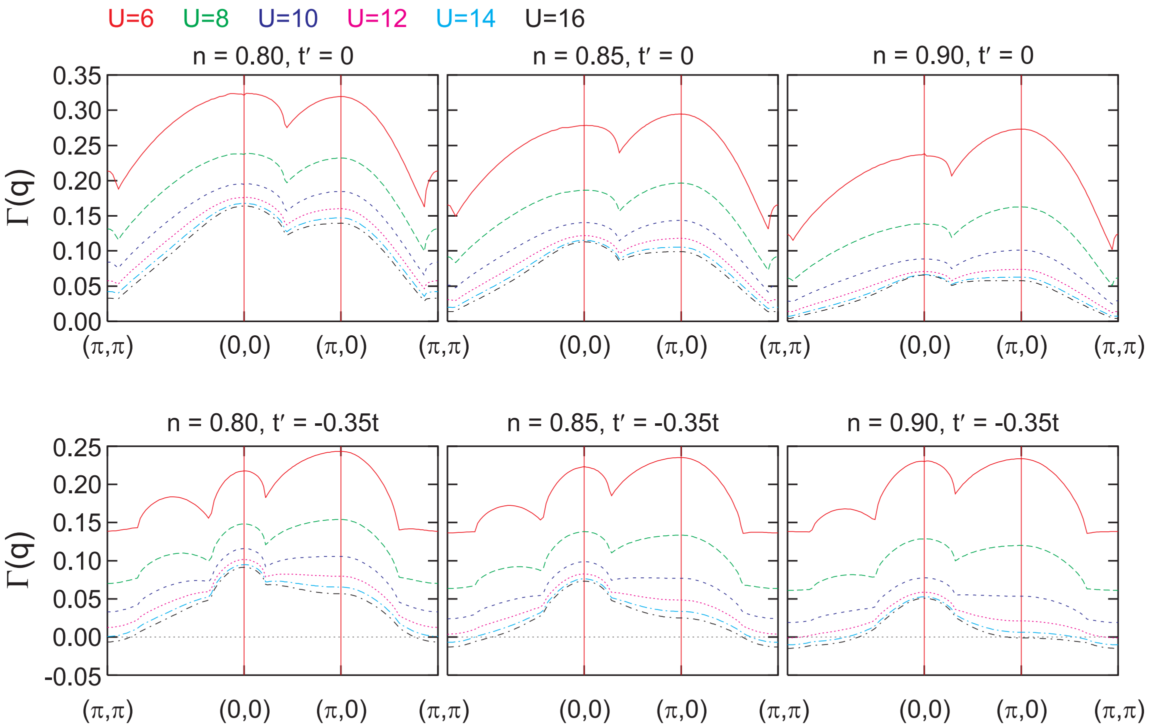

Figure 67: Electron-phonon vertex $\Gamma(\mathbf{q})$ for scattering electrons on the Fermi surface. Calculations are for the Hubbard model on a 1000×1000 lattice with $t'=0$ (top) and $t'=-0.35\,t$ (bottom) at an inverse temperature $\beta=500/t$. Fillings and Hubbard U are indicated in the plots. We find that in all cases the vertex function is strongly reduced with increasing U. For large U the changes become small and eventually $\lim_{U\to\infty}\Gamma(\mathbf{q})=0$ is reached.

saddle-point equations. The $1/N$ expansion relies on the smallness of $1/\delta N$, i.e., it breaks down at small dopings δ. This can be seen from the fact that in leading order the charge-charge correlation function remains finite for $\delta\to0$, though the exact correlation function vanishes in this limit. The Kotliar-Ruckenstein method, on the other hand, reproduces this limit correctly in leading order, which makes it plausible that in this case the charge vertex is smaller than in the 1/N expansion, especially at smaller dopings. Which of the two methods is more reliable, in particular near optimal doping, is, however, not entirely clear and can probably only be definitely judged by comparison with exact numerical methods.

To assess the importance of the electron-phonon coupling for superconductivity we calculate the renormalization factor

$$\Lambda_\alpha=\frac{\int_{FS}\frac{dp}{|\mathbf{v_p}|}\int_{FS}\frac{dp'}{|\mathbf{v_{p'}}|}g_\alpha(\mathbf{p})\Gamma(\mathbf{p},\mathbf{p}'-\mathbf{p})g_\alpha(\mathbf{p}')}{z^2\int_{FS}\frac{dp}{|\mathbf{v_p}|}\int_{FS}\frac{dp'}{|\mathbf{v_{p'}}|}g_\alpha^2(\mathbf{p})} \qquad (5)$$

for the pairing channels $g_s(\mathbf{p})=1$, $g_{s^*}(\mathbf{p})=\cos(p_x)+\cos(p_y)$, $g_{p_x}(\mathbf{p})=\sin(p_x)$, $g_{d_{x^2-y^2}}(\mathbf{p})=\cos(p_x)-\cos(p_y)$, and $g_{d_{xy}}(\mathbf{p})=\sin(p_x)\sin(p_y)$. Λ_α is equal to the ratio $\lambda_\alpha/\lambda_\alpha^{(0)}$, where λ_α and $\lambda_\alpha^{(0)}$ denote the dimensionless electron-phonon coupling constants in the interacting and non-interacting cases, respectively. To gauge the importance of forward scattering we also calculate the renormalization factor for transport,

$$\Lambda_{tr}=\frac{\int_{FS}\frac{dp}{|\mathbf{v_p}|}\int_{FS}\frac{dp'}{|\mathbf{v_{p'}}|}\Gamma(\mathbf{p},\mathbf{p}'-\mathbf{p})\,|\mathbf{v}(\mathbf{p})-\mathbf{v}(\mathbf{p}')|^2}{2z^2\int_{FS}\frac{dp}{|\mathbf{v_p}|}\int_{FS}\frac{dp'}{|\mathbf{v_{p'}}|}|\mathbf{v}(\mathbf{p})|^2}\,. \qquad (6)$$

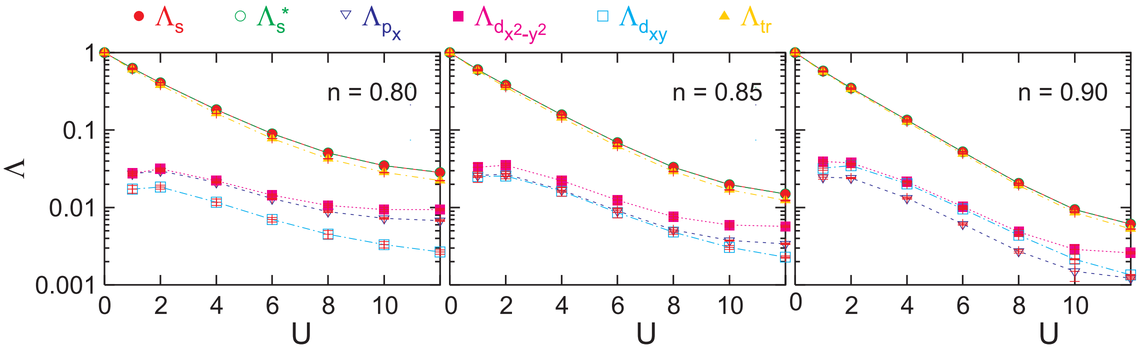

Figure 68: Renormalization constants Λ_α for different pairing channels and Λ_{tr} relevant for transport for the Hubbard model with $t' = 0$. Calculations were performed for lattices of increasing size at decreasing temperatures, performing the **p** integrals over the whole Brillouin zone and weighting with minus the derivative of the Fermi-Dirac distribution $-f'(\varepsilon_p) = \beta f(\varepsilon_p)(1 - f(\varepsilon_p))$, which becomes a delta function for $T = 0$. Convergence of the $T \to 0$ extrapolation has been checked by comparing Λ_s and Λ_{s^*}, which are equal only for $T = 0$. Error bars for the extrapolation are plotted, but are usually smaller than the size of the plotting symbols.

The results are shown in Fig. 68. We find that for $U \lesssim 10$ the *s*-wave couplings decrease almost exponentially with U and then start to saturate at these very low values. For the special case of the Hubbard model with nearest neighbor hopping only ($t' = 0$) we have $\Lambda_s^* = \Lambda_s$, since g_{s^*} is constant on the Fermi surface. Moreover $\Lambda_{tr} \approx \Lambda_s$, reflecting that there is no pronounced forward scattering; only for larger U does Λ_{tr} become somewhat smaller than Λ_s. But by then both coupling constants are already very small. The higher pairing channels are even weaker, starting from zero at $U = 0$, going through a maximum around $U = 2$ only to decay almost exponentially. We can thus conclude that within Kotliar-Ruckenstein slave-boson theory and restricting the system to be paramagnetic the contribution of Holstein phonons to superconductivity is very small [Koch *et al.*, cond-mat/0401089 (2004)].

Magnetic properties

Magnetism in solids is a typical quantum phenomenon and of high technological importance. Although magnetism is very well described by Heisenberg-type models, the conditions for magnetism to arise and the type of magnetic ordering are, in general, quite difficult to predict. This is demonstrated in the article by Hönnerscheid *et al.*, where co-crystallisates of chroniumarene complexes and C_{60} molecules are shown to be paramagnetic, although the constituents are diamagnetic. Other complicated molecular crystals (single-molecule magnets) are studied in the article by Kortus and Pederson. It seems that the presence of a transition metal in this and the previous example are responsible for the magnetic behavior. More familiar are the $S = 1/2$ quantum chain systems presented by Ahrens *et al.*, since spin chains of this type are being investigated both experimentally and theoretically for several years. The article by Lebon *et al.* deals with the magnetic and charge order in $SrFeO_3$, a transition metal oxide whose electronic structure is similar to that of $LaMnO_3$. Since the latter is known for its colossal magnetoresistance upon doping, the study of $SrFeO_3$ could provide some insight into the physics of the manganites, in particular their magnetoresistive behavior.

Phase transitions, dimerization and spins in bis-arene chromium C_{60} fullerides

A. Hönnerscheid, R. Dinnebier, and L. van Wüllen;
J. Rahmer and M. Mehring (Universität Stuttgart); M. Jansen

Fullerene containing compounds are fascinating materials exhibiting interesting properties including superconductivity and ferromagnetism. The origin of this wealth of properties is the strong electron acceptor character of fullerenes, and the narrow triply degenerate t_{1u} band that favors strong electron phonon coupling and electron-electron correlations. Chemically, an outstanding feature is the ability of C_{60} to aggregate via the formation of covalent bonds.

One new class of fullerides are those consisting of co-crystallisates of chromium arene complexes and C_{60} molecules. We have investigated two examples, $Cr(C_7H_8)_2C_{60}$ ($= CrTol_2C_{60}$) [Hönnerscheid *et al.*, Journal of Chemical Physics **115**, 7161 (2002)] and $Cr(C_9H_{12})_2C_{60}$ ($= CrMes_2C_{60}$), which have been synthesized in toluene as microcrystalline powders from the neutral species C_{60} and $Cr(C_7H_8)_2$ and $Cr(C_9H_{12})_2$, respectively. Surprisingly, we observe a large charge transfer of about one electron from the supposedly very stable chromium complexes to C_{60}, resulting in ionic compounds that contain two complex ions, C_{60}^- and $CrTol_2^+/CrMes_2^+$, respectively. In order to study this unexpected behavior, we have performed SQUID, ^{13}C-MAS NMR, ESR and DTA measurements for both compounds confirming the presence of unpaired electrons. In addition, both solids are found to exhibit significant effects in their magnetic behaviors at a temperature of about 250 K and 170 K, respectively, in the former case indicating a first-order and in the latter case a (probably) higher-order phase transition.

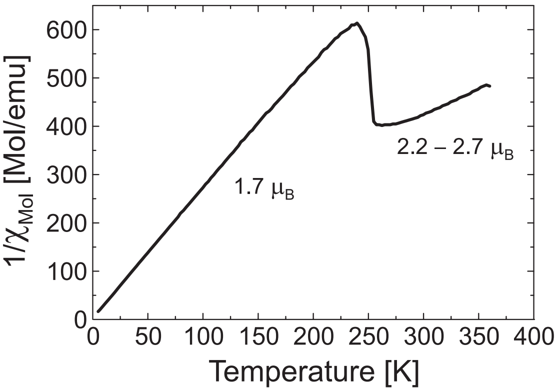

Figure 69: Inverse molar susceptibility of $CrTol_2C_{60}$ versus temperature ($B = 5\,T$). Magnetic moments are calculated from the slope using the 'spin-only' approximation.

In spite of the constituting components C_{60} and $Cr(C_7H_8)_2$ being diamagnetic, the product phase $CrTol_2C_{60}$ is clearly paramagnetic (Fig. 69). The $1/\chi$ versus T graph shows a change in magnetic behavior at 250 ± 5 K. For the low-temperature regime a magnetic moment of $1.72 \pm 0.01\,\mu_B$ per formula unit results which would correspond to one unpaired electron when applying the 'spin-only' formula. Similarly, the magnetic moment of $2.5 \pm 0.2\,\mu_B$ in the high-temperature phase would be consistent with the assumption of two independent paramagnetic centers, both carrying a spin $S = 1/2$, one localized at C_{60} and the other on the chromium complex. Below the phase transition only the paramagnetic center on the chromium complex remains, while the spin on the C_{60} anions disappears, which can be explained by dimer formation.

This is supported by the analysis of the temperature-dependent ^{13}C-MAS NMR spectrum. The dominating signal at 185 ppm is assigned to the fullerene carbon nuclei, where the small linewidth combined with the absence of spinning sidebands reflects the rapid rotation of the C_{60} cage. The paramagnetic downfield shift of ≈ 40 ppm relative to pristine C_{60} suggests a negatively charged C_{60}. With decreasing temperature, the most important observations are a gradual broadening of the C_{60} signal and the appearance of a new resonance at 145 ppm in the temperature range of 250–254 K at the expense of the 185 ppm signal. This is most likely due to the presence of either uncharged C_{60} species or $(C_{60})_2^{2-}$ di-anions, in accordance with published data on the dimer formation in alkali metal (A) fullerides AC_{60}.

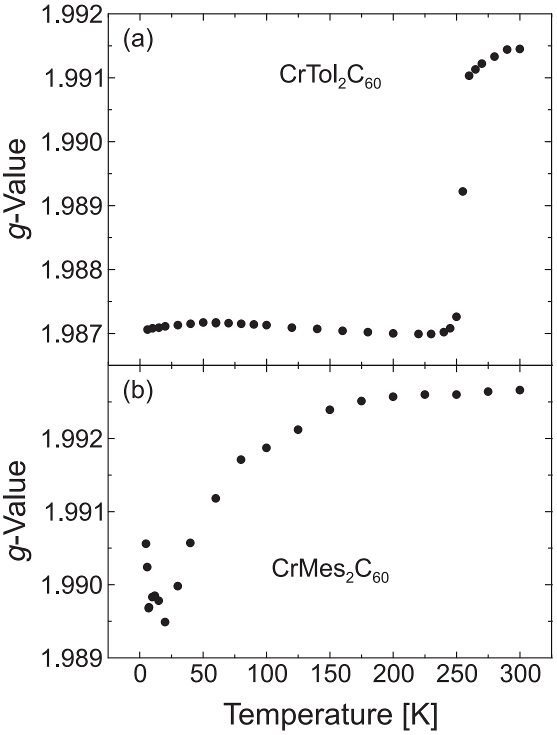

Figure 70: (a) Temperature dependence of the isotropic g-factor of $CrTol_2C_{60}$ at 9 GHz (X-band). (b) Temperature dependence of the isotropic g-factor of $CrMes_2C_{60}$.

The X-band spectrum of the ESR measurements exhibits a single Lorentzian line at all temperatures (Fig. 70(a)). This somewhat unusual result – one would expect the g-factors of the essentially localized unpaired electrons at the chromium complex to be different from the more delocalized ones at the fullerenes – can be understood in terms of an exchange coupling between these spins leading to a single narrowed ESR line. However, at a temperature of 250 K the signal abruptly changes its resonance position. This confirms the spin pairing at the phase transition and provides evidence for the assignment of the electron site.

According to our scenario, at low temperatures the radical C_{60}^{-} anions form diamagnetic dimers, which are ESR silent. Thus the observed signal stems from the electron of the chromium complex. This assignment is supported by the X-band ESR of the reference compound $Cr(C_7H_8)_2I$, which contains the same cation as the investigated fulleride. At temperatures above 250 K, however, the dimers cleave, releasing the electrons from the bonds. The contribution of these electrons to the ESR signal manifests itself in an increase in the susceptibility and in a drastic change of the observed isotropic g-value.

To summarize, at temperatures below 250 K, the rotational diffusion of the complex cations as well as of the anions stops, and C_{60}^{-} dimerizes. A definite proof of this dimerization of the C_{60} molecules can only be provided by crystal structure determination. Since all attempts to grow single crystals of sufficient quality for X-ray single crystal investigations have failed so far, the crystal structure was determined from high-resolution synchrotron X-ray powder diffraction data [Hönnerscheid *et al.*, Acta Crystallographica B **58**, 482 (2002)]. We find that the high-temperature phase of $CrTol_2C_{60}$ crystallizes in a simple CsCl-type structure in which C_{60} represents the chlorine anion and $CrTol_2$ occupies the Cs-site. Both constituents are rotationally disordered as deduced from the NMR results. Upon cooling below 250 K, cubic $CrTol_2C_{60}$ transforms to a triclinic phase, which consists of ordered $Cr(C_7H_8)_2^{+}$ cations and $(C_{60})_2^{2-}$ anions. DTA temperature cycle measurements show that the phase transition is reversible and of first order. The basic primitive cubic (pc) packing of C_{60} molecules is preserved in the low-temperature phase, where the dimer arrangement can be described as rods of C_{60} molecules with short and long distances alternating.

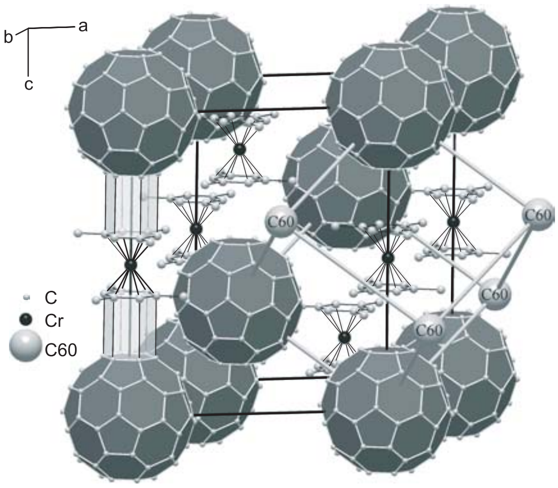

Figure 71: Structure of $CrMes_2C_{60}$. Edges of the hexagonal and primitive rhombohedral unit cell are in black and grey, respectively.

The cell of the related compound $CrMes_2C_{60}$ (Fig. 71) can be derived from the cubic one of $CrTol_2C_{60}$ by a small deformation along one diagonal, corroborating the strong similarity of both structures. The calculated powder pattern of a model of $CrMes_2C_{60}$ (space group R-3) is almost identical to the measured one, thus confirming the validity of the model. The distance between adjacent C_{60}^{-} molecules at room temperature is significantly higher in $CrMes_2C_{60}$ than in $CrTol_2C_{60}$ ($\Delta a = 0.136$ Å), due to the increase in the size of the transition metal complex. Synchrotron powder diffraction measurements at low temperatures reveal no structural changes for $CrMes_2C_{60}$, and no dimerization occurs.

The static paramagnetic susceptibility χ of $CrMes_2C_{60}$ shows that in the range from about 170 K to 360 K the spins in $CrMes_2C_{60}$ exhibit an almost Curie-Weiss like behaviour, with a magnetic moment of $\approx 2.4\,\mu_B$, again consistent with the assumption of a system comprised of two independent unpaired electrons per formula unit, similar to the room-temperature phase of $CrTol_2C_{60}$. At about 170 K a deviation from linearity of the $1/\chi$ versus T curve is observed, which can be attributed to a progressive reduction in the number of spin carriers in

$CrMes_2C_{60}$. This agrees with the ESR measurements, which indicate that in $CrMes_2C_{60}$ the fulleride anions are responsible for the decrease of number of unpaired spins (Fig. 70(b)). In this picture the temperature dependence of χ implies that the number of spin carrying C_{60}^- anions that contribute to the susceptibility decreases continuously in the temperature range between 180 K and 5 K.

The NMR results shed some light on the dynamics and the nature of the phase transition in $CrMes_2C_{60}$. The line width of the static room temperature ^{13}C-NMR spectrum and the absence of any chemical shift anisotropy provide clear evidence for a fast re-orientational motion of the C_{60} cages. The chemical shift of 183 ppm at room temperature again indicates a mono-anionic C_{60} species. Upon cooling, the position of the ^{13}C-MAS NMR signal shifts linearly from 183 ppm at room temperature to 207 ppm at $T = 135$ K. This behavior reflects the typical Curie dependence for the paramagnetic C_{60} mono-anion, suggesting that no $(C_{60})_2^{2-}$ dianions have been formed.

Since the crystal structure remains largely unchanged, only a collective phenomenon can account for the decrease in magnetic susceptibility. Due to the overlapping orbitals of neighboring fullerene anions, their spins are coupled much more strongly than the spins of the smaller $Cr(Mes)_2^+$ cations. Thus one might conceive of a situation where the strongly exchange-coupled fullerene spins build up an antiferromagnetic order, while the coupling to the metal-complexes is too weak to lead to a magnetic order in the investigated temperature range.

Density functional studies of single molecule magnets

J. Kortus; M.R. Pederson (Naval Research Laboratory, Washington, DC, USA)

Single molecule magnets (SMMs) are being extensively studied because of their interesting properties such as quantum tunneling of magnetization and quantum phase interference. One would like to exploit those properties in new data storage systems with significantly higher storage densities and in applications to quantum computing. Below their blocking temperature, these molecules show magnetization hysteresis similar to bulk magnets. Unlike bulk magnetization hysteresis, the hysteresis of molecular magnets shows a step-like structure which arises from the magnetization tunneling. These properties are governed by the magnetic anisotropy barrier of the system whose origin is mainly the spin-orbit coupling as pointed out by van Vleck already in 1937.

A typical example of of a molecular magnet is the octanuclear iron(III) molecular magnet $[Fe_8O_2(OH)_{12}(tacn)_6]^{8+}$, with tacn = 1,4,7-trizacyclononane ($C_6N_3H_{15}$), which is often referred to as the Fe_8 cluster. The structure the Fe_8 molecular crystal, first synthesized by Wieghardt *et al.* in 1984, is shown in Fig. 72. It has an acentric $P1$ crystal structure with $a = 10.52$ Å, $b = 14.05$ Å and $c = 15.00$ Å, $\alpha = 89.90°$, $\beta = 109.65°$ and $\gamma = 109.27°$.

Recently, Pederson and Khanna have developed a method for accounting for second-order anisotropy energies. This method relies on a simple albeit exact method for spin-orbit coupling and a second-order perturbative treatment of the spin Hamiltonian to determine the dependence of the total energy on spin projection.

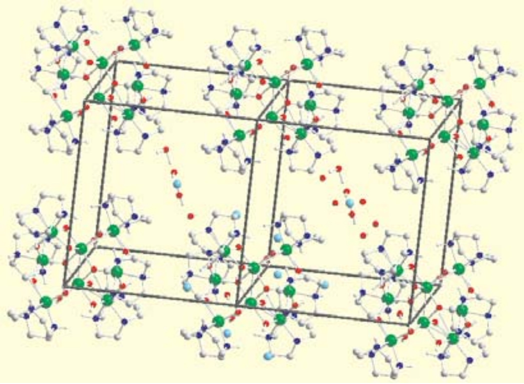

Figure 72: Repeated unit cells of the Fe_8 molecular crystal. Large green balls represent Fe atoms. Typical lattice parameters are $a = 10.52$ Å, $b = 14.05$ Å and $c = 15.00$ Å.

The implementation of the spin-orbit coupling in the NRLMOL code has been tested on calculations of the energy level splittings of several free noble gas atoms because in that case one can compare with non-spin polarized solutions of the Dirac equation. Some results are shown in Tab. 1.

Table 1: Spin-orbit splittings of energy levels (Δ_{SO} in Hartree) for Ar and Kr calculated with NRLMOL compared to results of a full relativistic numerical solution of the Dirac equation.

Δ_{SO}	Ar		Kr	
	NRLMOL	Dirac	NRLMOL	Dirac
2p	0.0796	0.0817	1.8731	1.9635
3p	0.0063	0.0066	0.2775	0.2897
3d	—	—	0.0471	0.0479

Please note that the agreement improves significantly for the outer electronic shells, for which in general relativistic effects become less important. This is very important because a completely filled shell gives no contribution to the magnetic anisotropy energy. Only the states close to the Fermi level are important for the determination of the tunneling barriers.

Now we would like to present results on a molecular magnet which has been synthesized at the University Erlangen-Nürnberg (department of Prof. Saalfrank). In the Ferric star or the Fe_4 cluster $(Fe_4(OCH_2)_6(C_4H_9ON)_6)$ shown in Fig. 73 all iron atoms are Fe^{3+} ions (large red spheres). The inner Fe is coupled antiferromagnetically to the outer Fe atoms, resulting in a ferrimagnetic spin-ordering with total $S = 5$.

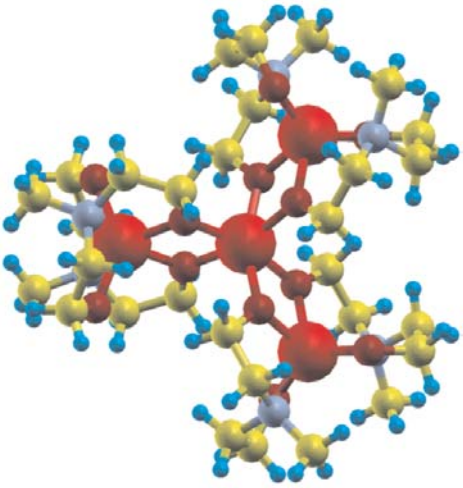

Figure 73: A ball and stick model of the molecular structure of the Fe_4 star. The four Fe atoms are shown by large spheres.

The calculation of the magnetic anisotropy parameters has been carried out in form of a real *blind test*. The group of Prof. Müller also from the University Erlangen-Nürnberg, which performed the magnetic characterization by high-field torque magnetometry and high-field EPR spectroscopy, provided the crystal structure of the ferric star but no information on the magnetic properties. Therefore the calculation can be regarded as a real prediction.

Up to second-order, the spin Hamiltonian which describes the magnetic properties can in general be expressed as

$$H = DS_z^2 + E(S_x^2 - S_y^2), \tag{7}$$

where D and E are known as axial and transverse anisotropy parameters. The predicted magnetic anisotropy parameters ($D = -0.56$ K and $E = 0.064$ K) are in excellent agreement with the experimental ones ($D = -0.57$ K and $E = 0.056$ K).

Table 2: Comparison of the calculated by NRLMOL and experimental magnetic anisotropy parameter *D* for the single molecule magnets.

Molecule	*S*	*D* (K)	
		Theory	Experiment
$Mn_{12}O_{12}(O_2CH)_{16}(H_2O)_4$	10	–0.56	–0.56
$[Fe_8O_2(OH)_{12}(C_6H_{15}N_3)_6Br_6]^{2+}$	10	–0.53	–0.30
$[Mn_{10}O_4(2,2'-\text{biphenoxide})_4Br_{12}]^{4-}$	13	–0.06	–0.05
$Co_4(CH_2C_5H_4N)_4(CH_3OH)_4Acl_4$	6	–0.64	–0.7 ... –0.9
$Fe_4(OCH_2)_6(C_4H_9ON)_6$	5	–0.56	–0.57
$Cr[N(Si(CH_3)_3)_2]_3$	3/2	–2.49	–2.66
$Mn_9O_{34}C_{32}N_3H_{35}$	17/2	–0.33	–0.32
$Ni_4O_{16}C_{16}H_{40}$	4	–0.385	–0.40
$Mn_4O_3Cl_4(O_2CCH_2CH_3)_3(NC_5H_5)_3$	9/2	–0.58	–0.72

The ferric star systems are also very interesting objects for future studies, because a whole family of stars $MeFe_3L_6$ with $Me = Fe, Cr, Al$ are known. Several of these stars exist with different ligands or modifications which also show changed magnetic properties. This could open the possibility to study the complete family in a systematic way and to derive a microscopic understanding of the electronic structure. Eventually this would enable us to correlate the electronic changes to structural or chemical motifs. The ultimate goal would be to derive simple guidelines for chemists how to design magnetic molecular systems with defined magnetic anisotropy properties.

This computational method has been applied to several molecular magnets containing different transition metal ions and ligands.

In Tab. 2 we present the total spin *S* and the calculated *D* parameters for a few single molecule magnets and compare with the available experimental values. We show the actual molecular symbols in the table and refer to these molecules in the text by their transition metal core since it is these atoms which are responsible for their magnetic behavior.

In all the cases presented here the calculated spin ordering is in agreement with experiment. The calculated *D* parameters for Mn_{12}, Mn_{10}, Mn_9, the ferric star Fe_4 and Cr-amide molecular magnets are in excellent agreement with experimental values. The only remarkable discrepancy is found for Fe_8, a system which seems to pose complications for the DFT treatment. Apparently the DFT may be unable to predict the ground-state density accurately enough due to important electronic correlations beyond the mean-field treatment or missing Madelung stabilization (absent in the isolated system).

The SMMs listed in Tab. 2 are in general characterized by a high-spin ground state. However, a high-spin state does not necessarily correlate with a high anisotropy barrier. The prefactor *D* is also very important. In order to increase the barrier one has to understand and control *D*, which will be the main goal of future research in this area. In all cases where the *E* parameter is not zero by symmetry it has been predicted with similar accuracy as *D*.

The results obtained make one confident in the predictive power of the formalism. It has been already mentioned that a microscopic understanding (based on the electronic structure of SMMs) of the magnetic anisotropy parameters is crucial for the rational design of single molecule magnets. From understanding the changes in the magnetic properties from a microscopic point of view we hope to obtain information which will enable us to derive a simplified understanding of how to influence the magnetic anisotropy in chemical terms.

Magnetic properties of the S = 1/2 quantum chain systems CuX_2O_6 (X = Sb, Ta)

M. Ahrens; B.J. Gibson (BOSCH, Stuttgart); R.K. Kremer;
B. Ouladdiaf (ILL Grenoble); A.V. Prokofiev and W. Assmus (Universität Frankfurt);
H. Langbein (Technische Universität Dresden)

In the past years the efforts to understand the physics of high-T_c superconductors have refocused attention on the magnetism of low-dimensional antiferromagnetic (afm) quantum spin $S = 1/2$ systems. A great number of hitherto unknown magnetic systems with unusual low-temperature magnetic behavior and ground-state properties have been synthesized and investigated experimentally and theoretically. New and unexpected phenomena have been observed which stimulated broad theoretical activity. Two recent one-dimensional quantum systems that attracted particular interest are $CuGeO_3$ and α'-NaV_2O_5 about which we have reported in preceding annual reports (see the annual reports of 1995, 1996, 1998 and 1999).

Some years ago we have identified the compounds MX_2O_6 (X = Sb, Ta) with M being magnetic Co^{2+}, Ni^{2+} and Fe^{2+} ions as magnetic systems with characteristic signatures of low-dimensional afm properties, mostly however, with strong Ising anisotropy as e.g., found for $CoTa_2O_6$. MX_2O_6 phases with Cu^{2+} ($S = 1/2$) as magnetic cations may be expected to show Heisenberg-type exchange coupling. The knowledge of the magnetic properties of $CuSb_2O_6$ and $CuTa_2O_6$, however, is only very preliminary, particularly, because of experimental difficulties encountered in the preparation of large single crystals (in the case of $CuSb_2O_6$) and because of the thermal instability of $CuTa_2O_6$ avoiding preparation routes employing typical solid state preparation techniques.

The phases MX_2O_6 (X = Sb, Ta) crystallize in the tri-rutile structure type which is related to the well-known rutile structure via a tripling of the *c*-axis occurring as a consequence of the chemical ordering of the divalent and pentavalent cations. The cations are octahedrally coordinated by oxygen atoms. The cation-oxygen octahedra form edge-sharing chains which are occupied alternately by MO_6 and XO_6 octahedra in a ratio 1:2 with complete chemical ordering (Fig. 74). $CuSb_2O_6$ undergoes a structural phase transition from the tetragonal to a monoclinic structure above room temperature at $\approx 125°C$, however, the deviation of the monoclinic structure from the tri-rutile structure type is only very small.

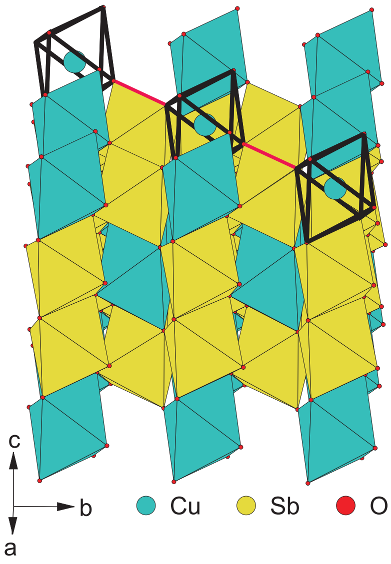

Figure 74: Crystal structure of $CuSb_2O_6$ with distorted oxygen octahedra around Cu and Sb drawn with the respective colors. Red solid lines connecting open-face octahedra around Cu^{2+} indicate the Cu–O–O–Cu bonds which promote strongest afm exchange interaction.

In the tri-rutile structure type two-dimensional character of the magnetic coupling between the divalent cations may be inferred. A closer inspection of the exchange paths, however, reveals the connection of the magnetic ions via the stretched O–O bonds along face diagonals as the most likely paths for the largest exchange coupling. Bonds via O^{2-} ions to cations in neighboring face diagonals include bonding angles close to 90° and increased bond lengths and exchange is expected to be significantly smaller.

Single crystals of $CuSb_2O_6$ were grown by chemical vapor transport at the University of Frankfurt. Magnetic, thermodynamic properties and magnetic structure solutions were determined in Stuttgart. Single-crystal neutron diffraction measurements on $CuSb_2O_6$ were carried out at the Institut Laue-Langevin in Grenoble. $CuTa_2O_6$ is not accessible via the standard preparation routes from CuO and Ta_2O_5, It has successfully been prepared at the TU Dresden via a careful decomposition of precursor oxalates at 300°C.

$CuSb_2O_6$ had been reported to exhibit magnetic strong short-range order signalled by a broad susceptibility maximum centered around 60 K. The susceptibility fitted well to an afm uniform $S = 1/2$ Heisenberg chain ($J \approx -50$ K) model with nearest-neighbor coupling. A sharp decrease in the susceptibility below ≈ 9 K indicated the long-range afm order due to interchain interactions. Preceding powder neutron diffraction experiments performed by Greedan and collaborators resulted in a propagation vector $k = (\frac{1}{2}, 0, \frac{1}{2})$ for the afm ordered phase and the suggestion of various ordering schemes. A conclusive magnetic structure solution was pending.

Figure 75 displays the magnetic susceptibility and the heat capacity of a crystal of $CuSb_2O_6$. Long-range order is evident from the heat capacity anomaly and the kinks in the susceptibility below $T_N = 8.68(5)$ K. The fit of the susceptibility with the model of an $S = 1/2$ Heisenberg chain with uniform afm nearest-neighbor coupling yields close to perfect agreement in a temperature range above long-range ordering ($10\,\text{K} < T < 350\,\text{K}$) with an exchange parameter of $J = -48.0(5)$ K. The low-temperature heat capacity ($T < 10$ K), in addition to a phonon term ($\propto T^3$), contains the typical linear magnetic term ($\propto T$) in very good agreement with the expected value $C_{mag}/R = T/3J$ for a uniform afm $S = 1/2$ Heisenberg chain. Long-range ordering arises from finite interchain coupling. Using standard theoretical results from $T_N \approx 8.7$ K and $J = -48$ K the ratio of interchain to intrachain exchange constant is estimated to 3%.

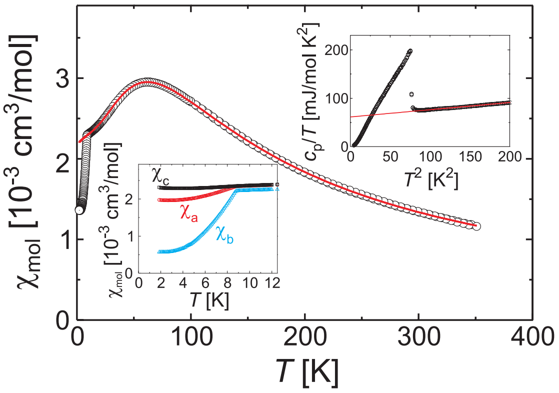

Figure 75: Susceptibility of a single crystal of $CuSb_2O_6$ measured in a field of 0.1 T along the *b*-axis (○). The full line is a fit to the susceptibility of a $S = 1/2$ Heisenberg chain with afm nearest-neighbor interaction with exchange constant $J = -48$ K. Insets: Heat capacity with an anomaly at 8.68(5) K indicating long-range ordering and the linear magnetic contribution above T_N. Susceptibilities along the *c*-, *a*-, and *b*-axis as indicated.

Below T_N the magnetic susceptibility exhibits pronounced anisotropy. With the field aligned along the *a*- or *b*-axis, the susceptibility drops while for the field along the *c*-axis no decrease below T_N can be detected. This observation suggests that the ordered moment lie in the *ab*-plane with their major component along *b*. Single crystal neutron diffraction on $CuSb_2O_6$ at room temperature and at low temperatures revealed additional weak Bragg reflections below T_N which can be indexed on the basis of a propagation vector $k = (\frac{1}{2}, 0, \frac{1}{2})$. A refinement of the nuclear structure at low temperature gave no indication of a structural phase transition. The refinement of the magnetic structure converged equally well to two alternative models with moments either in the *ab*- or the *bc*-plane, respectively. For both models the ordered moment at 2 K amounts to 0.51(2) μ_B. On the basis of the anisotropy of the susceptibility we suggest a magnetic structure as displayed in Fig. 76 with moments tilted 103(6)° (Cu1: (0, 0, 0)) and 70(5)° (Cu2: $(\frac{1}{2}, \frac{1}{2}, \frac{1}{2})$) away from the *a*-axis and oriented antiparallel along (1 1 0).

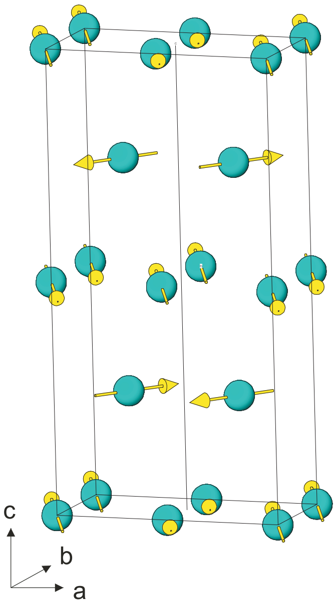

Figure 76: Magnetic structure of $CuSb_2O_6$ at 2 K.

Figure 77 displays first magnetic susceptibility measurements on a polycrystalline sample of $CuTa_2O_6$. A fit to the prediction for a $S = 1/2$ afm Heisenberg chain model with nearest-neighbor coupling indicates that $CuTa_2O_6$, like $CuSb_2O_6$, closely follows theory with an exchange constant $J \approx -25$ K which indicates a reduction by a factor of two as compared to $CuSb_2O_6$. An indication for long-range ordering has not been found yet.

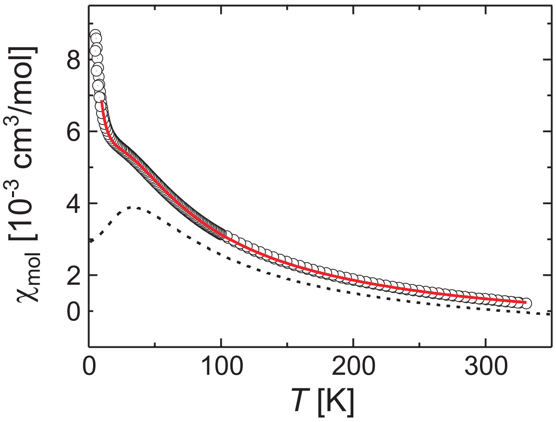

Figure 77: Magnetic susceptibility of $CuTa_2O_6$ (○). The solid line is a fit to the susceptibility of an afm $S = 1/2$ Heisenberg chain with nearest-neighbor interaction with exchange constant $J = -25$ K. A Curie-type contribution has been added to take into account magnetic impurities (≈ 10% $S = 1/2$ impurities) from a partial decomposition of the sample. The dashed line indicates the contribution from the $S = 1/2$ Heisenberg chain.

In summary, $CuSb_2O_6$ and $CuTa_2O_6$ crystallize with structures which promote predominant exchange coupling along a diagonal direction involving exchange via a O–O bond. Magnetic susceptibility experiments clearly prove that the magnetism of Cu^{2+} in $CuSb_2O_6$ and $CuTa_2O_6$ can be understood as that of a $S = 1/2$ Heisenberg linear chain behavior with afm nearest-neighbor coupling of the order of –50 K and –25 K, respectively. Heat capacity experiments and elastic neutron diffraction experiments prove $CuSb_2O_6$ to undergo long-range afm ordering below 8.7 K due to interchain coupling. The resulting spin structure is commensurate with the nuclear structure with the moments $\approx 0.5\,\mu_{Bohr}$ pointing essentially along (0 1 0).

Magnetism, charge order, and giant magnetoresistance in $SrFeO_{3-\delta}$ single crystals

A. Lebon, C. Bernhard, A.V. Boris, A.V. Pimenov, A. Maljuk, C.T. Lin, C. Ulrich, and B. Keimer;
P. Adler (Universität Karlsruhe)

The relationship between spin ordering, charge ordering, and magnetotransport effects has recently received much attention in the context of the ‘colossal magnetoresistance’ (CMR) phenomenon in manganites. Experiments have revealed a key role of phase separation between charge ordered (CO) insulating and charge disordered metallic phases in driving the CMR effect, but many questions about the detailed interplay between spin, charge, orbital, and lattice degrees of freedom remain unresolved. A comparison to other compounds with similar electronic structures can provide insight into the physical properties of the manganites. Iron(IV) perovskites form a Ruddlesden-Popper series of lattice structures akin to the manganites and are particularly suitable for such a comparison, because the high-spin Fe^{4+} ion present in these phases is isoelectronic to the Jahn-Teller ion Mn^{3+}: both ions have three electrons in the t_{2g} level and one electron in the e_g level of the crystal field generated by the surrounding oxygen octahedron. However, while the parent compound of the CMR manganites, $LaMnO_3$, is insulating and shows a cooperative Jahn-Teller effect, its analogue $SrFeO_3$ remains metallic and cubic at all temperatures. Its helical magnetic structure has no counterpart in the manganites, which generally exhibit collinear magnetic order. The different electronic properties of manganites and ferrates have been ascribed to the more pronounced hybridization between transition metal and oxygen orbitals in the ferrates, but a detailed theoretical description is still lacking. Moreover, in contrast to the Mn^{3+}–Mn^{4+} alternation observed in charge-ordered manganites, $SrFeO_3$ frequently adopts charge-disproportionated Fe^{3+}–Fe^{5+} configurations when the valence electron density is modified by substitutions on the Sr-site.

Most remarkably, recent experiments on polycrystalline samples of pseudocubic $SrFeO_{2.95}$ have uncovered anomalies in the magnetic susceptibility and electrical resistivity curves as well as a pronounced negative magnetoresistance (MR) below 50 K. Substantial negative MR was also observed in Co doped iron(IV) perovskites. The origin of these effects is not yet clear, and substantial sample-to-sample variations were observed. In order to advance our understanding of the magnetotransport properties of the ferrates and their relation to magnetic and charge order, we have synthesized a series of $SrFeO_{3-\delta}$ single crystals with controlled oxygen content ($\delta < 0.2$). It is known that the structural phase diagram of $SrFeO_{3-\delta}$ encompasses the stoichiometric cubic perovskite phase (C, $\delta = 0$) as well as the oxygen vacancy ordered tetragonal (T, $\delta = 0.125$, $Sr_8Fe_8O_{23}$) and orthorhombic (O, $\delta = 0.25$, $Sr_4Fe_4O_{11}$) phases separated by miscibility gaps. Our extensive investigations on $SrFeO_{3-\delta}$ single crystals with a variety of techniques including magnetometry, resistivity, Mössbauer spectroscopy and optical spectroscopy reveal a detailed picture of the evolution of the physical properties with oxygen concentration.

Figure 78 shows the resistivity of three representative $SrFeO_{3-\delta}$ single crystals. In agreement with earlier work, the temperature dependence of the resistivity indicates that the C-phase is metallic. The onset of helical magnetic order at 130 K is associated with only a very subtle resistivity anomaly. However, a decrease in resistivity by a factor of 2 is observed at 55 K. This transition exhibits a hysteresis and is related to a previously unobserved magnetic transition.

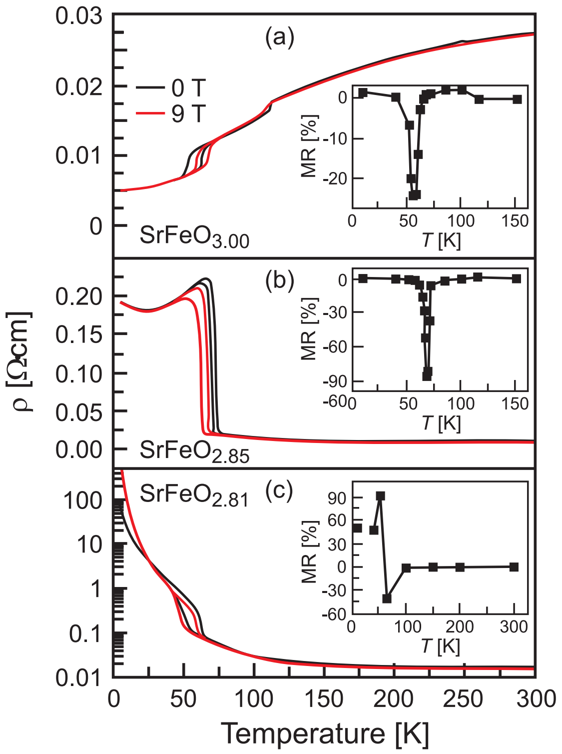

Figure 78: Resistivity in zero field cooling and heating runs (black) compared to field cooling and heating runs with a 9 T field (red) for (a) $SrFeO_{3.00}$, (b) $SrFeO_{2.85}$, and (c) $SrFeO_{2.81}$. As the absolute value of the resistance measurements (lines) was influenced by microcracks, these data were normalized around room temperature to infrared conductivity data extrapolated to zero frequency. Insets: Magnetoresistance (MR) measured at 9 Tesla after isothermal field scans between 0 and 9 T.

The application of a 9 T magnetic field shifts the transition to *higher* temperatures, and accordingly a large negative MR effect occurs in a narrow temperature range around 55 K ($\Delta T_{1/2} \approx 8$ K, max. MR ≈ 25%). The two oxygen deficient samples (which consist mostly of the T-phase) display a weakly activated, semiconducting behavior upon cooling from room temperature to 70 K, where the resistivity increases abruptly by an order of magnitude. The transition is characteristic of the T-phase and shifted to *lower* temperatures by a magnetic field of 9 T, in contrast to the 55 K transition in cubic $SrFeO_3$. Although the two transitions are evidently of different origin, the field-induced shift of the transition again gives rise to a large negative MR effect that peaks sharply in a narrow temperature range. In particular, for $SrFeO_{2.85}$ a giant negative MR of 90% is found. Finally, a pronounced *positive* MR effect is apparent in the low-temperature insulating phase of $SrFeO_{2.81}$.

(a) $SrFeO_{3.00}$

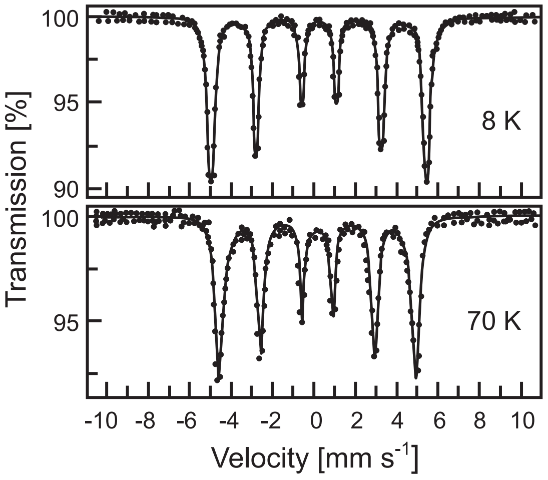

(b) $SrFeO_{2.87}$

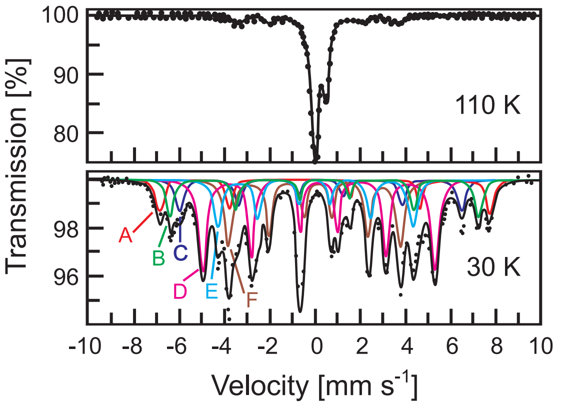

Figure 79: Selected Mössbauer spectra of (a) cubic $SrFeO_{3.00}$ and (b) mostly tetragonal $SrFeO_{2.87}$.

In order to elucidate the nature of the magnetic phase transitions, we have carried out Mössbauer experiments on $\delta = 0$ and $\delta = 0.13$ samples. The spectra of the $\delta = 0$ sample below ≈ 130 K (Fig. 79(a)) consist of a single six-line pattern due to magnetic hyperfine interactions which verifies that only Fe^{4+} is present. The shapes of the spectra are very similar below and above 55 K where the magnetization and resistivity data indicate an additional phase transition.

No anomalies are observed in the temperature dependence of the isomer shift (IS) or the hyperfine field (B_{hf}). This excludes any change in the charge states of the iron ions and suggests that the 55 K transition corresponds to a rearrangement of the Fe^{4+} magnetic moments. This was confirmed by neutron diffraction.

In the spectra of the $SrFeO_{2.87}$ sample (Fig. 79(2b)), on the other hand, there is clear evidence for a combined magnetic CO transition. Above 130 K the whole material is in a paramagnetic state. The spectra (not shown) were analyzed in terms of two components only: one Fe^{4+} single line and one average charge $Fe^{3.5+}$ quadrupole doublet. A first magnetic transition below ≈ 130 K leads to single sextets D that can be assigned to the cubic minority fraction of the sample by comparison to $SrFeO_3$. The second transition, seen at 70 K in the magnetization data, leads to complicated but well-structured low-temperature spectra. From $B_{\mathrm{hf}}(T)$ it is evident that the magnetic order for all components except D vanishes near 70 K.

Thus all sites except D are considered as intrinsic to the T-phase, which is the majority component in this sample. From the IS and B_{hf} values, charge states of 3+, 4+ and 3.5+ are assigned to the sites (A, B), (D, E, F) and C, respectively. A detailed model of the area fractions suggests that the magnetic ordering of the T-phase near 70 K coincides with charge ordering of $Fe^{3.5+}$ into Fe^{3+} and Fe^{4+}. Additional support for a CO transition is obtained from infrared ellipsometry and Raman scattering measurements (not shown) which reveal the appearance of numerous additional optical phonon modes below 70 K.

In summary, we have observed three different magnetoresistance effects in $SrFeO_{3-\delta}$ single crystals ($0 \leq \delta \leq 0.19$). Two of these effects are superficially similar, but arise from entirely different physical mechanisms. First, the large negative MR in cubic $SrFeO_3$ does not involve charge order and is related to a rearrangement of the helical structure of Fe^{4+} moments. Second, a combined Fe^{4+}–Fe^{3+} charge – magnetic ordering, which is different from the Fe^{3+}–Fe^{5+} CO in other iron(IV) containing ferrates, leads to an even larger negative MR in oxygen-deficient samples containing the T-phase as majority component. The giant negative MR near the CO transition of the T-phase is reminiscent of a similar (though smaller) effect near the first-order Verwey transition in Fe_3O_4. Finally, the positive MR in $SrFeO_{2.81}$ is more difficult to understand. Positive MR due to a field-induced decrease of the localization length is commonly observed in the variable range-hopping regime of doped semiconductors, but these effects are typically smaller and are obtained for substantially higher fields. Further experiments are required to ascertain whether an ‘extraordinary magnetoresistance’ effect due to small inclusions of the cubic metallic phase (below the sensitivity limit of the Mössbauer data) can account for this observation.

Transport and dynamics

Transport processes in solids and liquids like transport of particles and charge are rather complex and incompletely understood. The scope covers both basic theoretical consideration as well as more practical research like Li batteries. One guiding light in the investigation of the mechanism promoting ionic conductivity has been the observation that the phase transition in alkaline salts of complex anions to rotational disordered phases is accompanied by an increase of cationic conductivity (paddle wheel mechanism for Li- and Na-triflate. The interaction of gaseous O_2 with oxides is of technical relevance as well as of fundamental interest. In this context the usefulness of a linear free energy relation successfully applied in many organic reactions for the field of inorganic solid state reactions is demonstrated. In RuO_2/Li-cells the effect of nanocristallinity for Li-batteries were studied. The most important feature is a new storage mechanism proposed for Li-batteries. The concept of heterogeneous doping is applied to weak liquid electrolytes. SiO_2 admixtures to a solution of $LiClO_4$ in methanol affects drastically the overall conductivity. Multiscale heterogeneity is typical for charge transfer and valence instable materials showing large anharmonicity. A treatment of these systems in terms of discrete breather formation is proposed.

Ion mobility in alkali metal triflates: another example of the paddle wheel mechanism of ionic conductivity

L. Hildebrandt, N. Sofina, L. van Wüllen, and M. Jansen

Due to the growing need for efficient energy storage systems employing solid electrolytes, the development of new ionic conductors and the investigation of the mechanisms promoting ionic conductivity have continued to be an important area of research. One guiding light in these efforts has been the observation that some alkaline salts consisting of complex anions show phase transitions to rotationally disordered modifications at increased temperatures, which are accompanied by considerable increases in cationic conductivity [Kvist *et al.*, in Solid State Batteries and Devices, pg. 193, Ed. W. v. Gool, North Holland, 1973].

In at least some of these systems, the ionic mobility is greatly aided by the rapid rotation of the complex anions (‘paddle wheel mechanism’), thus lowering the potential energy barriers along the pathways of the cations. E.g., recent studies have produced strong evidence for the existence of such a mechanism in the rotationally disordered high-temperature modification of Na_3PO_4 [Witschas *et al.*, Zeitschrift für Physikalische Chemie **214**, 643 (2000)].

In this context, the alkali salts of the trifluoromethylsulfonate (triflate, $CF_3SO_3^-$) ion are of special interest because the anion has several possible rotational degrees of freedom: the rotation of the CF_3 group (which probably requires the lowest activation energy and is already active at ambient temperatures), the rotation of the SO_3 group around the C–S bond, and finally the isotropic reorientation of the complete triflate anion around its center of gravity.

In order to investigate the influence of the rotational motion on the cationic mobility, we have performed several temperature-dependent solid state NMR and high-frequency conductivity measurements for both lithium and sodium triflate.

In $LiCF_3SO_3$, the triflate anions are arranged in double layers, with the non-polar CF_3 groups facing each other, just as the polar SO_3^- groups [Tremayne *et al.*, Journal of Solid State Chemistry **100**, 191 (1992)]. The lithium ions are embedded in a SO_3 environment, coordinated by four oxygen atoms in distorted tetrahedra. DSC measurements and temperature-dependent powder diffractometry reveal a phase transition ($\beta\text{-}LiCF_3SO_3 \rightarrow \gamma\text{-}LiCF_3SO_3$) at 420 K. The structure of lithium triflate supports the assumption of a correlation between the rotation of the SO_3 group around the S–C bond and the cationic mobility.

Next, we find that the ionic conductivity obeys an Arrhenius relationship, $\sigma T = A\exp(\frac{-E_A}{k_B T})$, where $\sigma(493\,K) = 3.5\cdot10^{-7}\,Scm^{-1}$ and $\sigma(553\,K) = 1.95\cdot10^{-6}\,Scm^{-1}$. From the slope of the conductivity curve, an activation energy of $E_A = 69$ kJ/mol can be derived. The dynamic processes were studied by NMR using active nuclei ^7Li, ^{17}O and ^{19}F. The $^7Li\text{-}T_1$–NMR data indicates the presence of two different motional processes. At lower temperatures ($T < 420$ K), we assume that the $^7Li\text{-}T_1$–relaxation is caused by the fluctuations of the heteronuclear ^{19}F–^7Li dipolar coupling, while above 420 K, the lithium motion begins. Temperature-dependent static ^7Li-NMR spectra were recorded as well. The full width at half maximum (FWHM) measured at different temperatures, show a sharp decrease at 420 K (Fig. 80(a)), which is caused by an averaging of the dipolar coupling to the nearest neighbor atoms with nuclear spin of the lithium nuclei. Probably, this averaging is induced by a higher mobility of the lithium ions ('motional narrowing'). Using the semi-empirical formula of Waugh and Fedin, $E_A \approx 0.156\,T_c$, with T_c (in Kelvin) being the onset temperature for the motional narrowing, the activation energy can be estimated as $E_A = 64$ kJ/mol and nicely agrees with the value resulting from the ac-conductivity measurement ($E_A = 69$ kJ/mol).

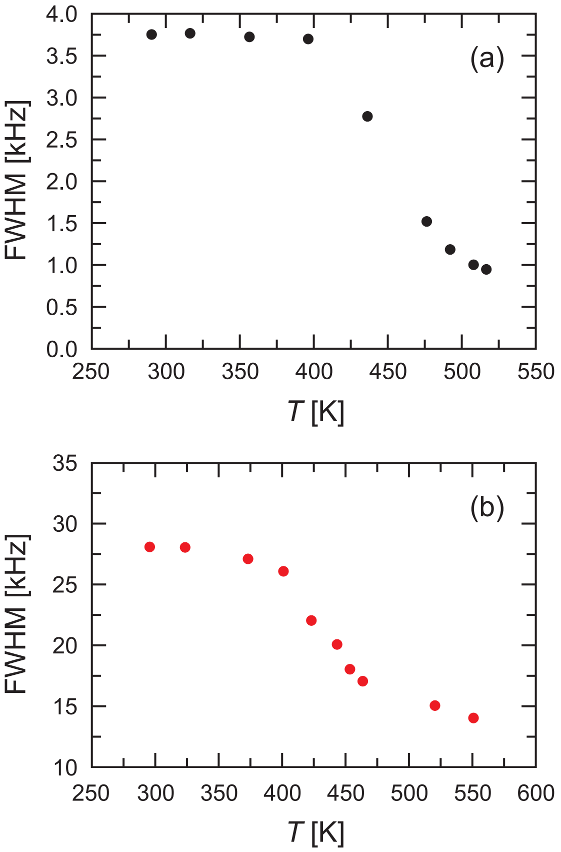

Figure 80: (a) Plot of the line width (FWHM) of the ^7Li-NMR spectra of $LiSO_3CF_3$ as function of temperature. (b) Plot of the line width (FWHM) of the ^{17}O-NMR spectra of $LiSO_3CF_3$ as function of temperature.

Regarding the CF_3 group, $^{19}F\text{-}T_1$-NMR measurements indicate a fast C3 reorientation of this group, with an activation energy of 25.9 kJ/mol and a correlation time of $1.8\cdot10^{-14}$ s, which is in good agreement with earlier publications. To study the reorientation of the SO_3 group, ^{17}O enriched triflate (7% enrichment) was employed. Although the signal to noise ratio of the ^{17}O-NMR spectra is limited, a sharp decrease in the line width at 420 K is obvious (Fig. 80(b)). The activation energy for the SO_3 reorientation ($E_A = 62$ kJ/mol), estimated by the formula of Waugh and Fedin, again agrees well with the activation energy for the lithium motion determined from the impedance spectroscopy and the ^{7}Li-NMR data.

Combining all the experimental results, the following picture of the dynamics can be constructed. At temperatures below 420 K, the only dynamic process is the C3 rotation of the CF_3 group, which does not affect the lithium ion mobility but is reflected by fluctuations in the ^{7}Li-^{19}F dipolar interaction. At the phase transition at 420 K, the lithium ion becomes mobile, while at the same time, the SO_3 group begins to perform a fast hopping motion around the C3-axis along the C–S bond.

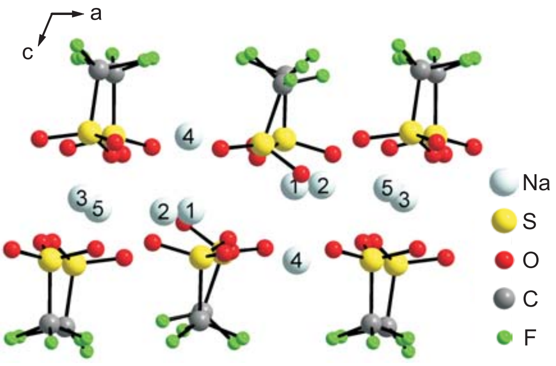

Figure 81: Projection of the crystal structure of $NaSO_3CF_3$, exhibiting the double layers with the different sodium cations. Na(1), Na(2), Na(3) and Na(5) are located in the interstices between two layers terminated by the SO_3-end groups of the triflate anions, Na(4) is located inside the SO_3 layer.

Turning to sodium triflate, we note that its crystal structure (Fig. 81) exhibits double layers similar to $LiCF_3SO_3$ with the CF_3 groups pointing towards each other. But the sodium ions occupy five different crystallographic positions, in contrast to only one for lithium in $LiCF_3SO_3$. Four of these positions – Na(1), Na(2), Na(3) and Na(5) – are located between the SO_3 layers, where Na(5) can be described using a half-occupied split position, and Na(4) (Fig. 81) is located inside the SO_3 layer, respectively. While these positions could not be resolved directly with ^{23}Na-MAS-NMR at ambient temperatures, MQMAS-(multiple quantum magic angle spinning) NMR experiments (Fig. 82) together with calculations of the quadrupole coupling constant, starting with the gradient of the electric field at the positions of the individual sodium ions allowed the identification and analysis of the signals found in the ^{23}Na-MAS NMR spectra. We find that at ambient temperatures, the sodium positions 1, 2, 3 and 4 are static, but Na(5) oscillates between the two split positions. At higher temperatures (390 K), the signals for Na(1), Na(2), Na(3) and Na(5) disappear and a new signal at –9 ppm appears, indicating a fast exchange among these four positions. Na(4), which is more strongly bound to the sulfonate groups due to its position inside the SO_3 layer, remains static until 449 K, above which all sodium ions can equally participate in the exchange.

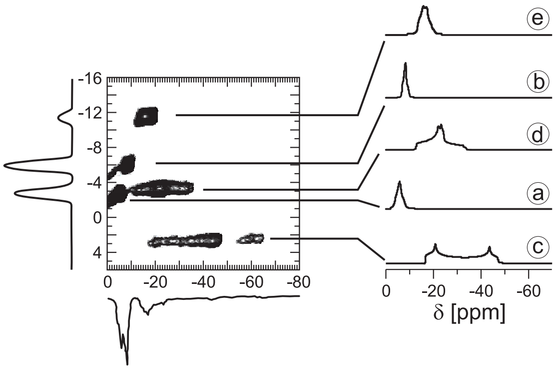

Figure 82: MQMAS (multiple quantum magic angle spinning) ^{23}Na-NMR spectra of $NaSO_3CF_3$.

However, this is not the end of the story, since the ac-conductivity measurements of $NaCF_3SO_3$ are essentially a straight line and do not reflect the dynamic processes suggested by the ^{23}Na-MAS NMR spectra. Preliminary NMR experiments with ^{17}O enriched $NaCF_3SO_3$ indicate that additional important processes are taking place. However, a full understanding of the cation-anion dynamics in sodium triflate will require further investigations that are currently being performed.

A linear free energy relation for gas-solid interactions of electron-rich perovskites

R. Merkle and J. Maier

Reactivity and transport properties can be traced back to materials parameters and control parameters such as partial pressures P of the components, temperature T and dopant content C. While their influence on electronic and ionic charge carrier concentrations is often well-understood, the understanding of kinetic quantities such as activation energies usually requires an atomistic analysis. Phenomenological relations involving kinetic quantities are very rare and, if established, extremely useful. The most prominent examples stem from organic solution chemistry, e.g., the Hammett equation (effect of substrate substitution on organic reactions) or the Brønsted catalysis relation. They correlate variations of the logarithms of rate and mass action constant in a linear way. A few attempts to verify similar linear free energy relations in solid state chemistry have been reported but without deeper insight into the mechanistic details and/or a conclusive correlation between data and model. Here we unambiguously demonstrate the validity of such a linear free energy relation for inorganic solid state reactions.

The interaction of gaseous O_2 with oxides is of technical relevance as well as of fundamental interest, and ^{18}O tracer exchange experiments are an important tool for its investigation. The oxygen incorporation comprises the surface reaction from O_2 to oxide ions in the first bulk layer, and the subsequent oxide ion diffusion within the bulk. The surface reaction is characterized by an effective rate constant ($\bar{k}^*$), the bulk diffusion by the tracer diffusion coefficient (D^*). While the dependence of D^* on materials and control parameters is well-understood, only recently [Maier, Solid State Ionics **112**, 197 (1998)] it was shown how the rate constant $\bar{k}^*$ depends on such parameters for a given mechanistic scheme. Even though thermodynamically independent, a surprising relation [De Souza *et al.*, Solid State Ionics **126**, 153 (1999)] between both quantities could be experimentally established which points towards a more subtle materials feature. To a good approximation both quantities are related via a power law $\log \bar{k}^* = \mathrm{a} + \mathrm{b} \log D^*$ with $\mathrm{a} \approx -1$, $\mathrm{b} \approx 0.5$ (see straight line in Fig. 83).

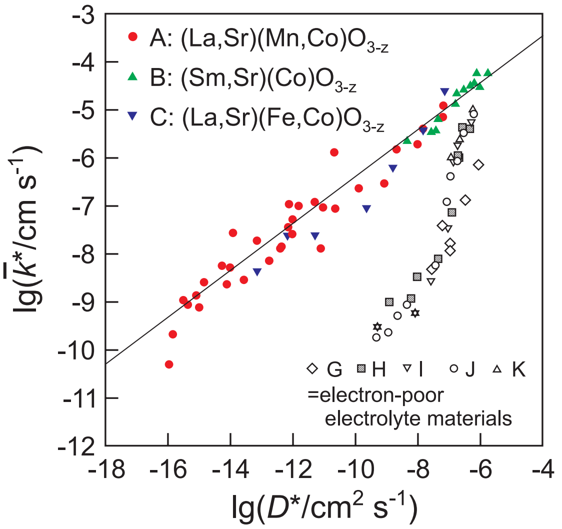

Figure 83: Correlation of effective rate constant $\bar{k}^*$ with tracer diffusion coefficient D^* from [De Souza *et al.*, Solid State Ionics **126**, 153 (1999)]. The linearity (slope $b \cong 0.5$) is explained by the linear energy relation Eq. (8).

This relation even though strongly debated in the literature remained unexplained. In the following we just sketch our analysis which shows that in fact it can be traced back to a Hammett-type relation which we can rationalize and test independently. The data points in Fig. 83 comprise temperature variation as well as compositional variation of the perovskite phase. Figure 83 contains also data for electron-poor electrolyte materials, that deviate strongly from the line to be discussed here, indicating that these correlations hold for families of materials with similar transport properties on a mechanistic level. Since the mobility does not change significantly within the family, the variation of D^*

is determined by the variation of the oxygen vacancy concentration. Hence the $\overline{k}^*$–D^* relation implies a correlation of thermodynamic with kinetic data.

The first step of the explanation, consists in selecting a reasonable mechanism for the surface reaction. As long as the essential conditions are fulfilled (atomic oxygen species and oxygen vacancies are involved in the rate-determining step *rds*), however, the reasoning does not depend on the mechanistic details. Nevertheless, to be specific, we assume the oxygen surface reaction to be rate-determined by the incorporation of a singly negatively charged oxygen atom O' into an oxygen vacancy $\mathrm{V_O^{\cdot\cdot}}$ where it is fully charged by releasing a hole $\mathrm{h}^{\cdot}$ (Kröger-Vink nomenclature):

$$1/2\,\mathrm{O_2} \rightleftharpoons \mathrm{O}' + \mathrm{h}^{\cdot} \qquad \text{pre-equilibrium}$$

$$\mathrm{O}' + \mathrm{V_O^{\cdot\cdot}} \rightleftharpoons \mathrm{O_O^{\times}} + \mathrm{h}^{\cdot} \qquad \text{rate-determining step } (rds)$$

The further analysis then shows that the $\overline{k}^*$–D^* relation is readily explained if the activation enthalpy of the surface reaction $\Delta\overleftarrow{H}^{\neq}$ (in fact $\Delta\overleftarrow{H}^{\neq}$ refers to the back reaction of the *rds*) fulfils the condition

$$\begin{aligned}\Delta\overleftarrow{H}^{\neq} &= b\left(\Delta H_{\mathrm{V}}^{\neq} - \Delta H_{\mathrm{ox}}^{0}\right)\\ &= 0.45\,\mathrm{eV} - 0.5 H_{\mathrm{ox}}^{0} \end{aligned} \qquad (8)$$

($\Delta H_{\mathrm{V}}^{\neq} = 0.9\,\mathrm{eV}$ is the activation enthalpy of the bulk $\mathrm{V_O^{\cdot\cdot}}$ mobility and is composition-independent for the considered materials). This is indeed a linear relation between the activation enthalpy of the rate determining step and the enthalpy $\Delta H_{\mathrm{ox}}^{0}$ of the overall reaction $1/2\,\mathrm{O_2} + \mathrm{V_O^{\cdot\cdot}} \rightleftharpoons \mathrm{O_O^{\times}} + 2\,\mathrm{h}^{\cdot}$. The importance of Eq. (8) lies in the fact that the slope (0.5) and intercept (0.45 eV) do not perceptibly change when the material is varied within the family under concern, i.e., in particular $\delta\Delta\overleftarrow{H}^{\neq} = -0.5\,\delta\Delta H_{\mathrm{ox}}^{0}$. Since the entropies are not expected to change significantly from material to material (and since the mechanical energy term is approximately constant), Eq. (8) also represents a free energy relation. Equation (8) can now also be checked by comparing the activation enthalpies with the independently determined reaction enthalpies (e.g., from thermogravimetry). Figure 84 displays this correlation for experimentally determined $\Delta\overleftarrow{H}^{\neq}$ and $\Delta H_{\mathrm{ox}}^{0}$ values.

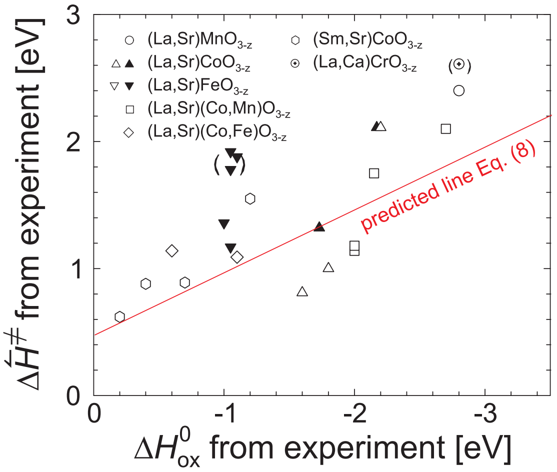

Figure 84: Correlation of surface exchange activation energy $\Delta\overleftarrow{H}^{\neq}$ with reaction enthalpy $\Delta H_{\mathrm{ox}}^{0}$ according to the linear energy relation. Comparison of the predicted relation from Eq. (8) with literature data.

The mechanistic interpretation and reason for Eq. (8) is illustrated in Fig. 85.

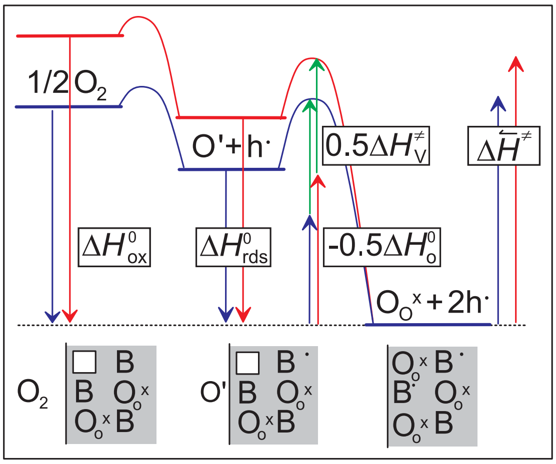

Figure 85: Enthalpy diagram of oxygen incorporation, the red line demonstrates the increase of $\Delta\overleftarrow{H}^{\neq}$ due to increase of $\Delta H_{\mathrm{ox}}^{0}$ (For clarity, we normalized the enthalpy profile such that the final state exhibits the same energetic level for both cases); bottom: mechanistic picture of the reaction.

The *rds* involves a site exchange (transfer of adsorbed O$'$ into a $\mathrm{V}_{\mathrm{O}}^{\cdot\cdot}$) and an electron transfer (oxidation of the transition metal cation B to B$^{\cdot}$). Assuming to a first approximation the site exchange not to be influenced by the compositional variation (because of the observed constancy of $\Delta H_{\mathrm{V}}^{\neq}$), the variation of the activation energy refers to the partial electron uptake in the transition state (the degree of intermediate charging being roughly independent of sample composition). Thus it is related to the compositional variation of the reaction enthalpy $\Delta H_{\mathrm{rds}}^{0}$ of the *rds* by a number between 0 and 1. A value of about 1/2 is expected for a rigid energy profile if $\Delta H_{\mathrm{rds}}^{0} \approx \Delta H_{\mathrm{ox}}^{0}$ and if the activated complex is effectively situated at the middle of the reaction coordinate. The fact that this value does not change from material to material reflects the similarity within the family members as regards mechanism and structure.

This treatment demonstrates the usefulness of the linear free energy relations successfully applied to many organic reactions in the field of inorganic solid state reactions.

Nanocrystallinity effects in lithium batteries

P. Balaya, H. Li, J. Jamnik, L. Kienle, and J. Maier

Lithium batteries belong to the most successful electrochemical devices. In the classical ‘Li-ion battery’, Li^{+} is transferred from a $\mathrm{Li_xCoO_2}$ ($0.5 < x < 1.0$) electrode into a graphite electrode during charge while the reverse process occurs via discharging. The high reversibility of the electrochemical process is caused by the soft insertion/extraction of Li^{+} in these host lattices. A drawback is the limited chemical capacity. If the solubility limit of these oxides is reached, by far not all the chemical driving force is used, rather, upon further incorporation of Li the oxide can be reduced to the metal or even to an alloy of Li with the metal. In such cases, however, an extraction of Li appears difficult owing to the sluggish kinetics. Surprisingly it turned out that these multiphase reactions are partly reversible and may be used for battery purposes [Poizot *et al.*, Nature **407**, 496 (2000)] The reason is that the multiphase mixture is nanocrystalline and/or partly amorphous. Recently, we studied nanocrystallinity effects systematically for lithium batteries. Here we briefly present the following results: (1) $\mathrm{RuO_2}$ as a first example of a fully reversible electrode material, (2) the possibility of using also fluorides such as $\mathrm{TiF_3}$, $\mathrm{VF_3}$, etc., for a reversible complete redox-cycle and (3) proposition of a new storage mechanism that becomes important when dealing with stoichiometric changes in multiphase systems.

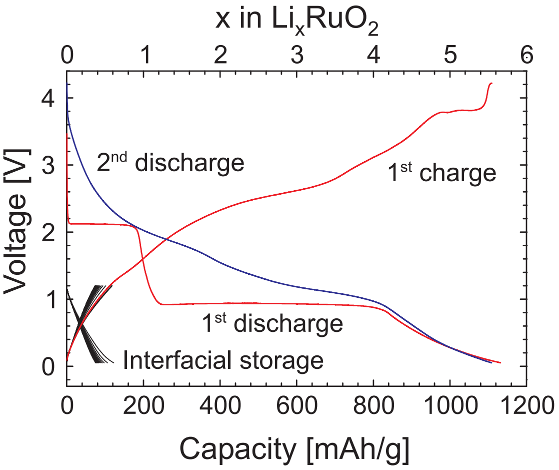

Figure 86: The discharge-charge curves on galvanostatic cycling of $\mathrm{RuO_2}$/Li cell in the voltage range 0.05–4.3 V and 0.05–1.2 V.

A $\mathrm{RuO_2}$ versus Li cell shows (Fig. 86) a highly reversible Li-storage capacity of 1110 mAh/g, with nearly 100% Coulombic efficiency at the first discharge/charge cycle. Based on Raman and HRTEM investigations, it is observed that

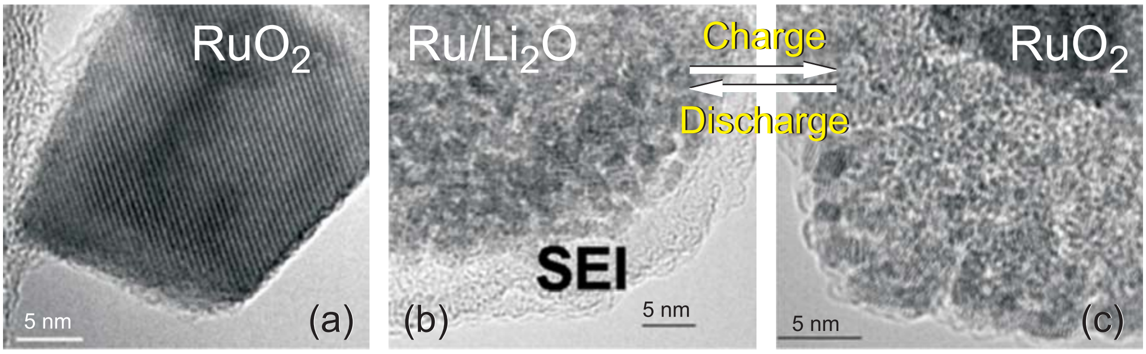

Figure 87: HRTEM images of RuO_2 electrodes: (a) initial, (b) fully discharged to 0.05 V – uptake of 5.6 Li and (c) charged to 4.3 V – extraction of 5.5 Li. SEI: solid/electrolyte interphase.

incorporation of 5.6 Li^+ transforms the initial RuO_2 crystal (Fig. 87(a)) into a nanocrystalline composite of Ru and Li_2O with a grain size of 2–5 nm covered by a 5–10 nm surface solid/electrolyte interphase (SEI) layer (Fig. 87(b)). At full Li extraction (5.5 Li^+), nanocrystalline RuO_2 forms again and the SEI layer disappears completely (Fig. 87). It is worth mentioning that amongst the metal oxides studied so far, only RuO_2 which is known to be a very good electronic conductor as well as a good mixed conductor, allowed for a complete extraction of Li^+ in the first cycle, while in other oxides only 75% or less Li^+ can be extracted.

Transition metal fluorides TiF_3, VF_3, etc., also allow for a similar reaction mechanism. For example TiF_3, which is an insulating material exhibits, when mixed with carbon and graphite, a reversible Li-storage capacity of 615 mAh/g with 66% of Coulombic efficiency. Structural investigation of the decomposed products of TiF_3 after a full Li incorporation reveals an amorphous structure, indicating an atomic-level distribution of LiF and Ti particles.

Apart from the small spacing of interfaces which leads to strongly reduced transport lengths and modified conductivities making thus even materials such as Li_2O or LiF electrochemically active, the appearance of nanocrystallinity leads to further exciting features in the context of Li-batteries: the Gibbs-Kelvin term in the chemical potential leads to modifications of the cell voltage as well as in the shape of the discharge curves; the most important feature is a new storage mechanism that we propose for Li-batteries.

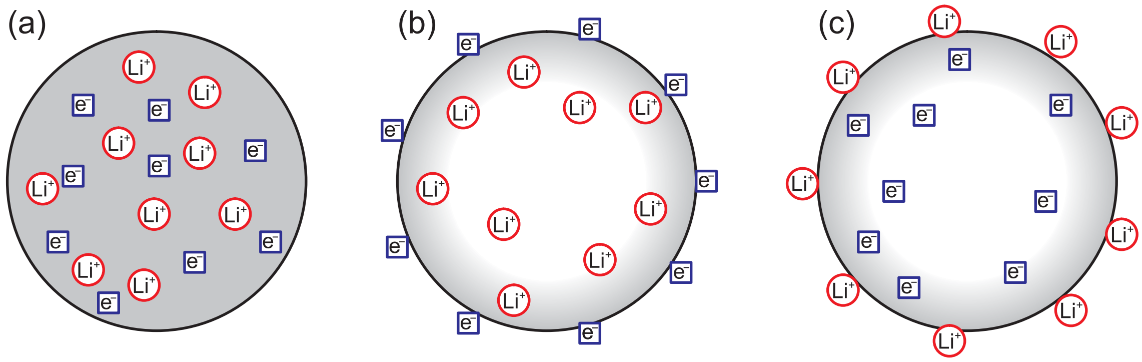

Figure 88: Charge storage in electrode particles by means of (a) insertion reaction; (b) and (c) interfacial reaction associated with charge separation. In case (b) solely ions, and in case (c) solely electrons are injected.

As seen from Fig. 86, at low potential (0.05–1.2 V) a sloping behavior with a quite reversible Li storage capacity of 120 mAh/g is observed in RuO_2. Similar storage effects can be observed in most of the transition metal oxides. Two possible explanations exist in literature, one referring to under-potential deposition of monolayer of Li on metal and the other to a reaction with the liquid electrolyte at the solid/liquid interphase, but fail to explain all the experimental features. Recently, we proposed a new explanation for this Li storage in the low-potential-sloped regime that is thermodynamically based, viz. an interfacial charge storage mechanism. Figure 88 compares the homogeneous storage where Li^+ is inserted into the host lattice (Fig. 88(a)), with this kind of interfacial storage mechanism in which Li^+ can either stay inside or outside the grain depending on whether the particle exhibits only ionic (Fig. 88(b)) or electronic (Fig. 88(c)) conductivity respectively. In Li_2O, e.g., the Li solubility is – owing to its pronounced redox stability – negligible in spite of the availability of interstitial sites for Li^+. At the contact to a metal however, Li^+ can be accommodated at the Li_2O side of the boundary while the electrons are restricted to the metal side. In the light of such mechanisms, the difference between battery and supercapacitor is getting blurred.

'Soggy sand electrolytes': a new class of soft matter electrolytes

A.J. Bhattacharyya and J. Maier

The concept of heterogeneous doping of ion conductors as quantitatively elaborated in our department allows the predictable increase of charge carrier concentrations in the vicinity of a surface active second phase. Al_2O_3 particles included in AgCl, e.g., adsorb cations, hence increasing the concentration of the counter ions (i.e., the cation vacancies) and leading to significantly enhanced conductivities. SiO_2 dispersion in alkaline earth fluorides causes enhanced fluoride vacancy conduction through anion adsorption. Recently we showed that the same concept can be applied even to weak *liquid* electrolytes.

Figure 89 displays schematically the effect of anion adsorption on the charge carrier concentrations along with the energetics. Figure 90 shows how SiO_2 (pH of zero charge in aqueous solution, pzc ≈ 3) admixtures to solution of $LiClO_4$ in methanol ($\varepsilon = 32.6$) affect the overall conductivity. Owing to the comparatively low dielectric constant at least in concentrated solutions, most of the salt is undissociated and present in the form of ion pairs. An appreciable dissociation only occurs at very dilute solutions (inset of Fig. 90). If it were possible to break all the ion pairs in concentrated solutions, the conductivity could be considerably enhanced.

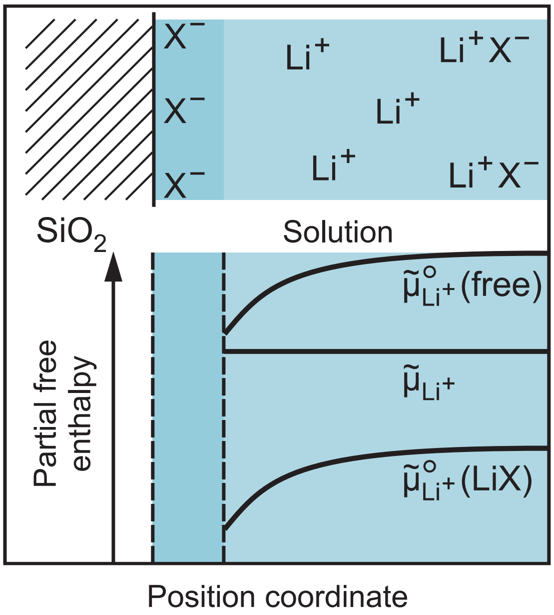

Figure 89: Schematic representation of the influence of anion adsorption at the oxide surface on charge carrier concentration along with the energetics. $\tilde{\mu}^\circ$: standard electrochemical potential; $\tilde{\mu}$: electrochemical potential.

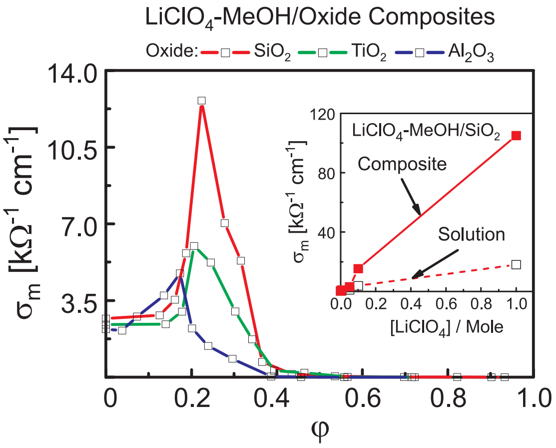

Figure 90: Room temperature variation of composite conductivity (σ_m) versus volume fraction (φ) for various oxides (particle size ≈ 0.3 μm) having different surface acid/base property. Inset: Variation of LiClO$_4$-MeOH solution it's composite with SiO$_2$ (constant φ) as a function of LiClO$_4$ concentration.

According to Fig. 89 and Fig. 90, this is in fact achieved by SiO$_2$ inclusions. Zeta potential measurements indicate that the SiO$_2$ surface is negatively charged and hence has adsorbed ClO$_4^-$. At small volume fractions the charged silica particles repel each other (colloidal regime). But when the particles touch, the conductivity is significantly enhanced (Fig. 91(b)). In principle an ordered SiO$_2$ array could maintain the percolating situation up to quite high volume fractions; the earlier decrease observed in Fig. 90, indicates inhomogeneity effects. The theoretical discussion succeeds with the same relations derived for the heterogeneous doping of solids. (The results also shine light on the relevance of ion pair breaking in oxide containing polymer electrolytes.) Upon variation of the dielectric constant (THF: $\varepsilon = 7.4$; DMSO: $\varepsilon = 46.5$), or of the surface acidity of the oxide (Al$_2$O$_3$: pzc ≈ 8.5; TiO$_2$: pzc ≈ 5) the conductivity response changes in an expected manner. The variation of ionic conductivity of the composite with varying salt concentration (inset of Fig. 90) is in line with the model, too.

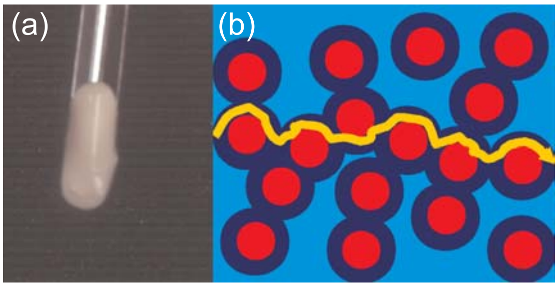

Figure 91: (a) Photograph of LiPF$_6$-EC/DMC:SiO$_2$ 'soggy sand' composite. (b) Schematic depiction of percolation-type behavior of ionic conductivity in the 'soggy sand' regime.

Apart from improved conductivities, the composites also exhibit very interesting mechanical properties. They have the high-effective viscosity of soft matter ('soggy sand'; Fig. 91(a)) and therefore are promising for Li batteries provided we use a durable non-aqueous electrolytes (such as LiPF$_6$ in EC/DMC). Very satisfactory battery performance was obtained with LiPF$_6$ in EC/DMC loaded with nano-sized SiO$_2$ grains. No reaction of Li with the SiO$_2$ inclusion could be observed during such tests.

We showed that in the way described, a new class of electrolytes is generated, which is of high relevance for Li-ion batteries. Obviously even in liquid electrolytes the introduction of interfaces can lead to astonishing effects.

Elastic collapse and discrete breather formation in complex charge transfer and valence unstable materials

A. Bussmann-Holder; A.R. Bishop (Los Alamos National Laboratory)

Charge transfer and valence unstable materials exhibit numerous ground states as functions of doping, pressure and temperature. Multiscale heterogeneity is typical for most of these materials, e.g., relaxor ferroelectrics, manganites, cuprates, tungstates and related compounds. Here, we show that the large anharmonicity in all these systems allows for a distinct form of inherent dynamic inhomogeneity dictated by 'discrete breather' formation, where lattice, charge and elasticity are intimately coupled. The spatial extent of the breather is governed by the amount of anharmonicity it carries and can vary considerably, defining new length scales of inhomogeneity. The coupling of the breather to the host lattice prevents a lattice instability and induces a collapse of the elastic constants and an excess specific heat and entropy as soon as the breather emerges from the continuum of the optic modes. Then a coexistence of local, dynamically distorted patterns with the regular lattice is manifest, defining a two-component system with very different dynamics and a strong analogy to glasses. A self-organization of multiple breathers into ordered patterning takes place as function of temperature and breather density.

Perovskite oxides ABO_3, are prototypical charge transfer or valence unstable systems. By substituting either the transition metal ion B by B' or by doping the mostly alkaline or earth alkaline ion A-site with A', completely new ground states are induced. These *doped* compounds are of increased scientific and technological interest, supporting, e.g., high-temperature superconductivity, giant dielectric constants or colossal magnetoresistance. Here we concentrate on these compounds by considering a *silent* or *cold* yet polarizable host system which is diluted by highly polarizable *hot* or *polar 'defects'*, where these refer to either dopants or valence different ions. The introduction of defects in the silent host matrix leads to enhanced and wavevector-dependent diffuse scattering, evidencing that the global symmetry is locally broken. This observation can be related to strong anharmonicity, which leads to the formation of 'intrinsic localized modes' ('discrete breathers'; ILMs). Many approaches to ILMs have been based on a nonlinear potential in the rigid ion or spin lattice, which considerably constrains their inherent complexity. Here we use a more complete approach in order to correctly include charge transfer effects, of vital importance to the dynamical and electronic properties of the considered systems. The physically most transparent description which can be treated analytically for arbitrary length scales is a diatomic nonlinear shell model representation, with a highly polarizable cluster mass m_1 and a rigid mass m_2. The anharmonicity of the system is *local* and in the relative core shell displacement w_{1n} of ion 1, where the limit $w_{1n} \to \infty$ corresponds to local ionization, while in the case $w_{1n} \to 0$ the electron and its core are tightly bound. The use of this coordinate is the source of the richness of the solutions as compared to previous approaches.

The formation of local modes requires a spatially limited regime of constant frequency which is zero beyond these limits – representing multivibrational quanta bound states. As a first and natural choice for ILMs we have chosen the displacement pattern shown in Fig. 92 which corresponds to discrete breather type solutions. Here the polar impurity at site $n = 0$ with dipole moment 'length' n_c is compensated by its host lattice by creating at site n, counted from the impurity site, a dipole moment in the opposite direction with displacement ξ_n according to: $\xi_n = \xi_0 - \frac{n}{2}$: $n \equiv$ even; $\xi_n = -(\xi_0 - \frac{n}{2})$: $n \equiv$ odd.

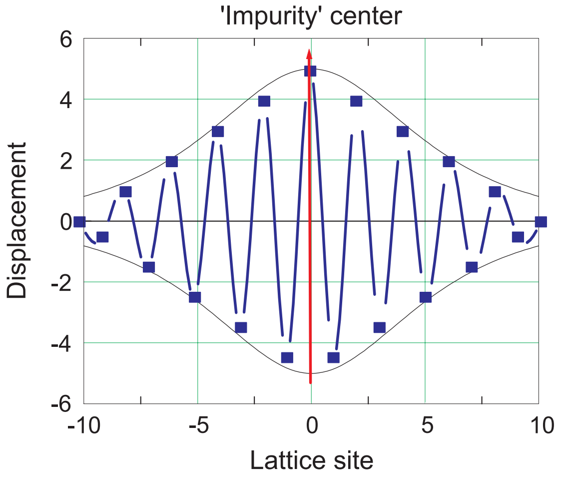

Figure 92: Induced displacement pattern around the *dipole* center. The envelope lines are obtained by superposing the functions $n_c\mathrm{sech}(a/2)$ and $-n_c\mathrm{sech}(a/2)$ on the displacements (a is the lattice constant). Since the shell displacement is coupled to the core a fractional charge accumulation xe is associated with the breather formation.

With the choice that the shell displaces always in the opposite direction by the same amount as the core, the relative polarization displacement becomes $w_n = -2\xi_n$. The time periodic displacements are given by $u_{1n}(t) = \mathrm{A}\xi_{1n}\cos(\omega t)$, $u_{2n}(t) = \mathrm{B}\xi_{2n}\cos(\omega t)$, $w_{1n} = \mathrm{C}\eta_{1n}\cos(\omega t)$, from which two ILM mode frequencies are obtained: Mode 1 has the same frequency as the pseudoharmonic optic zone boundary mode, whereas mode 2 is an in-gap mode with new and interesting properties. Especially its stability requires that its spread is accompanied by a decreasing double-well potential barrier height with increasing distance from the *impurity* center to reach the harmonic limit at the boundary of the discrete breather.

The existence regime of this mode is limited by the energy gap defined by comparing the $q = 0$ propagating linear wave (optic mode) energy of the system with the $q = 2\pi/a$ one (acoustic mode energy), restricting the ILM energies to a regime which has been investigated numerically and is shown in Fig. 93. As evidenced there, only a sufficiently elastically soft lattice strongly supports the breather formation and drives the system in the proximity of a ferroelastic medium. This can be substantiated by coupling the breather solutions to the pseudoharmonic propagating wave solutions. This leads not only to a coupling of the phonon bath to the nonlinear solution, but also stabilizes the lattice, whereas the breather solution becomes temperature dependent due to its coupling to the phonon bath. As long as the coupling to the ILM is active, the lattice is stable at all temperatures even though significant mode softening may occur.

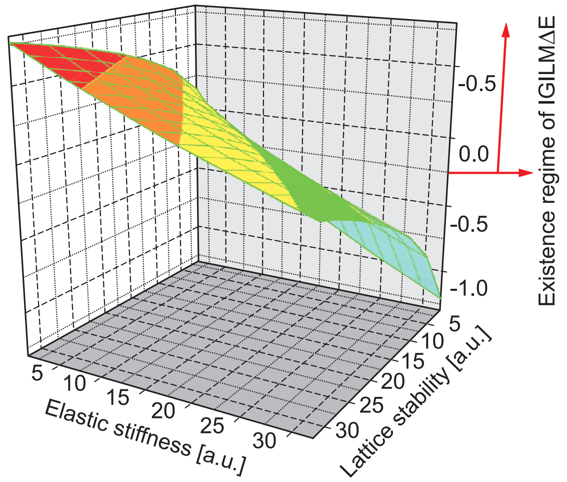

Figure 93: Existence regime of local mode formation as function of lattice stability and elastic softness. The discrete breather formation is restricted to the orange and red colored space where $\Delta E > 0$.

As can be seen in Fig. 94, the breather solution appears at a certain temperature only, when it splits off from the optic mode to appear in the gap. Its energy decreases with decreasing temperature and is in resonance with the zone boundary acoustic mode at a certain critical temperature T_M. Below T_M a rapid decay of the acoustic mode into the breather beyond a critical q-value sets in which is manifested as a *collapse* of the elastic constants. The breather formation has distinct effects on the thermodynamic properties of the system, since an excess in specific heat is associated with it which starts developing at exactly the temperature where the ILM splits off the phonon spectrum. Even if its

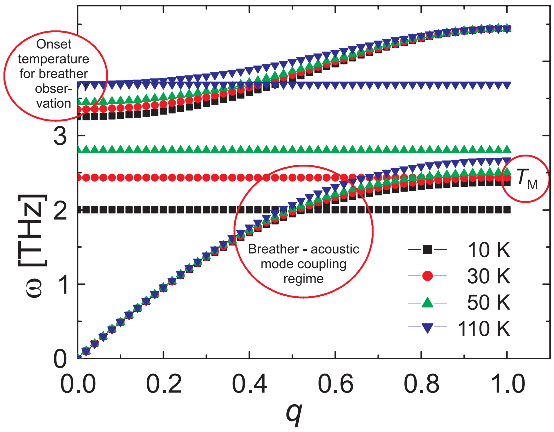

Figure 94: Dispersion relation ω(q) for lowest two modes as a function of temperature. The q-independent breather branch is also shown. At $T = 110\,\mathrm{K}$ the breather mode splits from the optic mode and merges into the acoustic mode at $T_M = 30\,\mathrm{K}$. The mode crossing wavevector of the acoustic and breather mode is temperature dependent and is observed here between $q = 0.4$ and $q = 1$.

contribution to the specific heat has been included also at higher temperatures, there is no effect as compared to a Debye model. The excess specific heat does not manifest itself in a jump at the temperature where the split off is observed, but extends over a broad temperature regime and has a massive contribution at low temperatures due to the combined effect of the collapse of the elastic constants and the very small energies of the ILM. Together with the excess specific heat, an entropy increase is observed which exceeds the ILM formation energy and guarantees their robust stability.

The proposed nonlinear solutions and their coupling to the host lattice are relevant to many complex charge transfer and valence unstable systems. Specifically, the use of the *polarizability* coordinate guarantees that the lattice displacement field accompanying the ILM formation is followed by an electronic field which is charge-rich compared with the surrounding region. Thus charge-rich and -poor areas coexist with locally distorted and undistorted regions. Systematic correlations of anomalous signatures in electronic and ion properties (dielectric constants, elastic constants, spectroscopy, thermodynamics, etc.) will be crucial for the experimental verification of ILMs.

Spectroscopic methods

The development and advancement of spectroscopic techniques has a longstanding tradition and remains a central theme of our research. The reported new developments cover a wide spectrum including microscopy with atomic resolution of phonons in carbon nanotubes, investigation of microwave induced zero-resistance states in two-dimensional electron gases, inelastic X-ray scattering and infrared spectroscopy under high pressure using synchrotron light sources, studies towards a tunable THz pulse source and the investigation of the coupling between optical wave guide modes and plasma resonances in arrays of metallic nanowires.

Phonon spectromicroscopy of carbon nanostructures with atomic resolution

L. Vitali, M. Burghard, M.A. Schneider, and K. Kern;
L. Liu and C.S. Jayanthi (University of Louisville)

The physical properties of carbon nanostructures critically depend on the local molecular structure and bonding, a sensitive fingerprint of which is the local vibrational density of states. A means of characterizing the vibrational spectra with high spatial resolution and sensitivity is therefore highly desirable. Conventional techniques as Raman and Near Field Spectroscopy are limited by the intrinsic resolution limit of visible light probes, which in the second case can be extend to the 20 nm scale. A different approach, which allows achieving local vibrational features of carbon nanotubes on the relevant subnanometer scale is given by inelastic electron tunneling spectroscopy with a low-temperature scanning tunneling microscope (IETS-STM).

As a local probe technique, Scanning Tunneling Microscope (STM), has already been successfully applied to study the electronic structure of single-wall carbon nanotubes (SWCNTs): native and intentionally introduced defects have been characterized topographically and spectroscopically. Besides, through the inelastic component of the tunneling current, also local vibrational density of states have become accessible. A few percent of the electrons tunneling through the STM vacuum junction scatter inelastically, exciting a vibration of the sample under investigation. The onset of this excitation can be detected by measuring the 2nd derivative of the tunneling current versus bias voltage. This quantity shows a peak whenever the energy of the tunneling electrons is in resonance with the energy of the vibrational excitation. This powerful technique has recently been applied in very elegant IETS-STM experiments aiming on the spectroscopy of localized vibrations of single molecules, ranging in size from acetylene to C_{60}, adsorbed on metallic surfaces. The high accuracy phonon measurement of the vibrational modes of the graphite surface has demonstrated the IETS-STM spectrum is directly proportional to the total density of phonon states.

We have now extended these measurement to the local characterization of carbon nanotubes.

In the experiments SWCNTs, deposited on Au/mica substrates, are studied at 6 K in UHV. Individual tubes have been selected and identified according to their chiral index (n,m), which defines the chiral vector of the tubes. For the latter purpose, the separation of the van Hove singularities (vHs) in the electronic LDOS was used to determine the diameter of metallic and semiconducting tubes. In addition, the chiral angle was obtained from atomically resolved STM images. The correlation of the electronic LDOS and atomically resolved images has proven reliable for the tube assignment, as confirmed by the good agreement with theoretical predictions. In the present work, more than 20 tubes have been identified. For each of them, the inelastic tunneling spectrum has been acquired with a lock-in technique.

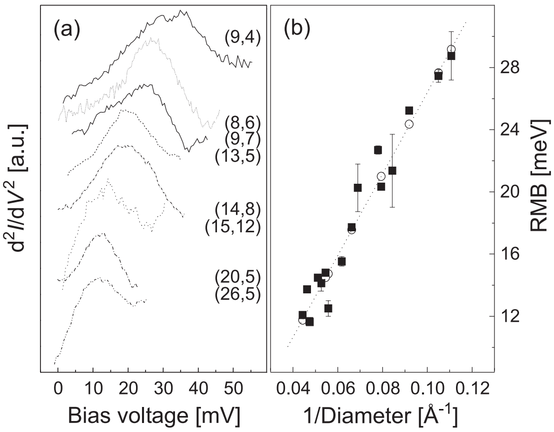

Figure 95: (a) IETS-STM spectra of different isolated SWCNTs. (b) Energy of the radial breathing mode (RBM) mode of isolated SWCNTs plotted against the inverse diameter. The experimentally observed peak energies in the IETS and the theoretically calculated phonon energies, are shown as solid squares and open circles, respectively. It can be seen that the RBM energy scales inversely with the tube diameter, according to the relationship $E_{\mathrm{RBM}} = A/d_{\mathrm{t}}$, where $A = 262\,\mathrm{meV}\cdot\mathrm{Å}$.

Each of the low-energy IETS-STM spectra exhibits one prominent peak, and the voltage position of the peaks is observed to decrease with the increase in tube diameter as shown in Fig. 95(a). In Fig. 95(b), the inverse scaling of phonon energy with tube diameter (d_{t}) and the good agreement of a selected number of tubes with theoretical predictions (circles), based on a sp^3 non-orthogonal tight-binding Hamiltonian, confirm that the peaks originate from excitation of the radial breathing mode (RBM) in the tubes. The linear dependence of the RBM frequency on reciprocal tube diameter is well-documented from Raman spectroscopic studies on isolated SWCNTs and is here proven by a local characterization of individual tubes. The RBM energies obey the relation $E_{\mathrm{RBM}} = A/d_{\mathrm{t}}$, where $A = 262\,\mathrm{meV}\cdot\mathrm{Å}$, in general agreement with values obtained by other theoretical calculations.

Having established that IETS-STM allows for atomic-scale spectroscopy of vibrations in SWCNTs, we extended our studies towards detecting changes in the vibrational structure that arise from the presence of defects. Of special interest in this respect are intramolecular junctions connecting two different tubes, which require at least one pentagon-heptagon pair and the highly curved tube caps containing at least six pentagons.

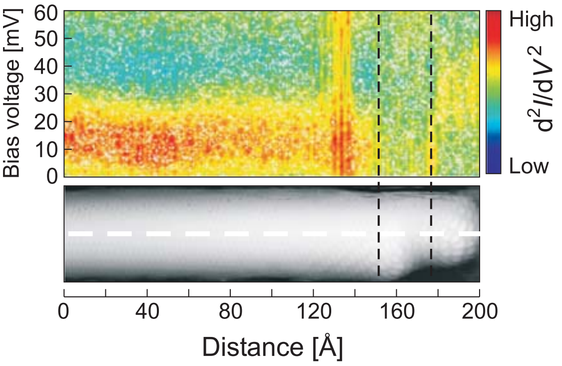

Figure 96: Changes in the local vibrational properties of a SWCNT associated with the presence of local defects. Top: Color scale map of the lock-in signal (d^2I/dV^2) as a function of energy and position along the tube axis. Bottom: Topographic image of a (17,14) tube containing an intramolecular tube junction and a closed ending. The transitions between the corresponding regions are highlighted by black dashed lines. The white dashed line indicates the sampling positions along the tube axis where the IETS spectra were taken.

Figure 96(a) shows the topographic image of an isolated metallic (17,14) tube, which was selected for detailed spectroscopic investigations since it combines both of these features. The presence of an intramolecular junction is visible at a distance of ≈ 5 nm from the tube apex, where the tube diameter abruptly decreases from 21.2 Å to 9.7 Å while the chiral angle is preserved. The short tube segment (denoted as ‘neck region’) that follows has a length of 2 nm and appears closed by an intact cap (‘cap region’).

The IETS-STM spectra measured as a function of position along the (17,14) tube (indicated as white dotted line in Fig. 96(a) are displayed in Fig. 96(b) as a color map. On top of the (17,14) tube, the RBM is found at a constant energy of ≈ 12 meV. One further observes the abrupt disappearance of this RBM at the intramolecular junction. Although one would expect a RBM to occur at 25 meV in the neck region according to its diameter, no such mode is evident. However, when the cap region is reached, a new vibrational feature appears at 29 meV.

A detailed study of the vibrational dynamics of a model system formed by a (5,5) tube capped at both ends by C_{60} hemispheres has been carried out to elucidate the experimental observations. Our calculations for relaxed structures of (5,5) capped tubes of different lengths revealed that the tube is able to sustain a RBM only if its length exceeds 3.5 nm. In the present case, a pronounced influence of the caps is apparent from the fact that the radial displacement abruptly drops to zero in their proximity.

Our calculation also reveals a cap-specific phonon mode at an energy close to that of the RBM of a C_{60} molecule. In Fig. 97, the eigendisplacement of this mode shows that the character of this mode is transformed from a pure radial nature to a tangential-dominant character in the tube (bulk) region. This is the consequence of the resonance between the RBM of the hemispherical C_{60} cap and a bulk mode of the tube.

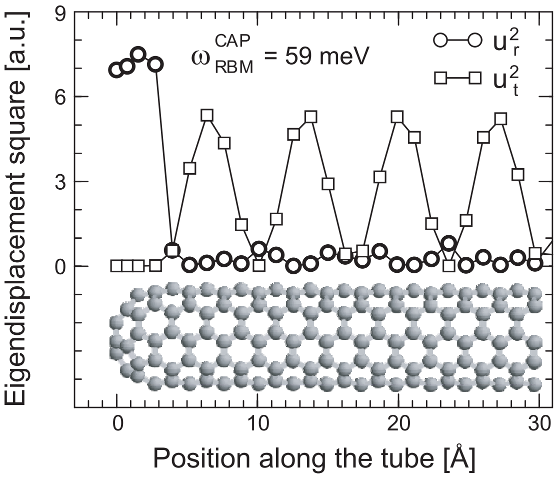

Figure 97: Eigenvector characteristics of a cap-specific eigenmode at ≈ 59 meV in a finite-length (40 nm) carbon nanotube capped by C_{60} hemispheres. This mode has finite radial (u_r) and zero tangential (u_t) displacements in the cap region (0–3.5 Å), akin to the characteristics of the RBM of a C_{60} molecule. The nature of this mode transforms from a radial to a tangential character in the interior of the tube, a consequence of the resonance between the RBM of the C_{60} hemispherical cap and a bulk mode.

This study can now be used to provide a scenario for low-frequency vibrational dynamics of a general capped tube with a ‘neck’. In the tube region of the capped tube, one expects to observe the RBM of the infinite tube if its length is sufficiently long. In the cap region, one expects to observe the resonance of the RBM of the cap structure with the bulk (tube). This scenario is completely reflected by the experimental observations on the capped (17,14) tube shown in Fig. 96: (i) In the tube region, the experimentally observed RBM shows a constant value, consistent with the theoretically calculated frequency of the RBM of an infinite (17,14) tube. (ii) In the neck region, there is no observation of a RBM because of the shortness of the neck (≈ 2 nm). (iii) In the cap region, a mode at 29 meV was experimentally observed, akin to the theoretically predicted resonance mode between the RBM of the cap and a bulk mode.

For future studies, STM-IETS offers the unique possibility to correlate local vibrational changes arising from various types of tube modifications with the local electronic structure. For instance, the study of tube deformations like kinks or twists will deepen the understanding of the effect of stress fields on the electrical transport properties of SWCNTs. Moreover, an elucidation of the local electronic and vibronic structure associated with covalently bonded atoms or groups would provide important clues for electrical device applications that require chemical modification along the tubes, such as diodes or single-electron transistors. On the other hand, the atomic scale structure of chemically functionalized nanotubes could be investigated with chemical specificity if characteristic group vibrations are selected.

Zero-resistance states induced by microwave radiation in a two-dimensional electron system

R. Mani (Harvard); J.H. Smet; V. Umanksy (Weizmann Institute of Science); K. von Klitzing

The observation of vanishing electrical resistance in condensed matter has led to the discovery of new and profound phenomena such as superconductivity and the quantum Hall effects in a two-dimensional electron system exposed to a strong perpendicular magnetic field. In both instances, the appearance of zero resistance coincides with the development of a gap in the energy spectrum. Here, we report on the discovery of zero-resistance states in a surprising setting: an ultrahigh mobility two-dimensional electron system exhibits vanishing diagonal resistance when the specimen is subjected to quasi-monochromatic microwave radiation at low magnetic fields where Landau levels are not yet resolved.

The influence of microwave radiation on the properties of a two-dimensional electron system in a field B was investigated in the experimental setup depicted schematically in Fig. 98. Measurements were performed on devices from an ultrahigh mobility GaAs/AlGaAs heterostructure. This material was characterized by an electron density of $3{\cdot}10^{11}\,\mathrm{cm}^{-2}$ and an electron mobility of $15{\cdot}10^{6}\,\mathrm{cm}^2/\mathrm{Vs}$. Lock-in based four-terminal electrical measurements were carried out with the sample mounted inside a waveguide and immersed in pumped liquid He^3 or He^4. A quasi-monochromatic (10^{-5}) electromagnetic wave in the microwave part of the spectrum, $27 < \omega < 110\,\mathrm{GHz}$, was generated using various tunable sources. The power level in the vicinity of the sample was typically significantly less than 1 mW.

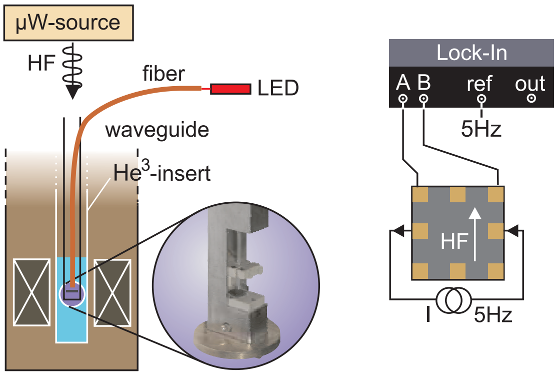

Figure 98: Experimental setup for microwave photoconductivity experiments. The sample is located near the electric field maximum of CW-microwave radiation inside a short circuited and oversized metallic waveguide. To enhance the mobility and carrier density of the 2DES, the sample is initially illuminated with the help of a red LED. A sinusoidal current with a frequency of 5 Hz and an amplitude of 1 μA is driven through the sample. The longitudinal resistance in the direction of the current flow as well as the Hall resistance perpendicular to it is monitored using a lock-in detection scheme.

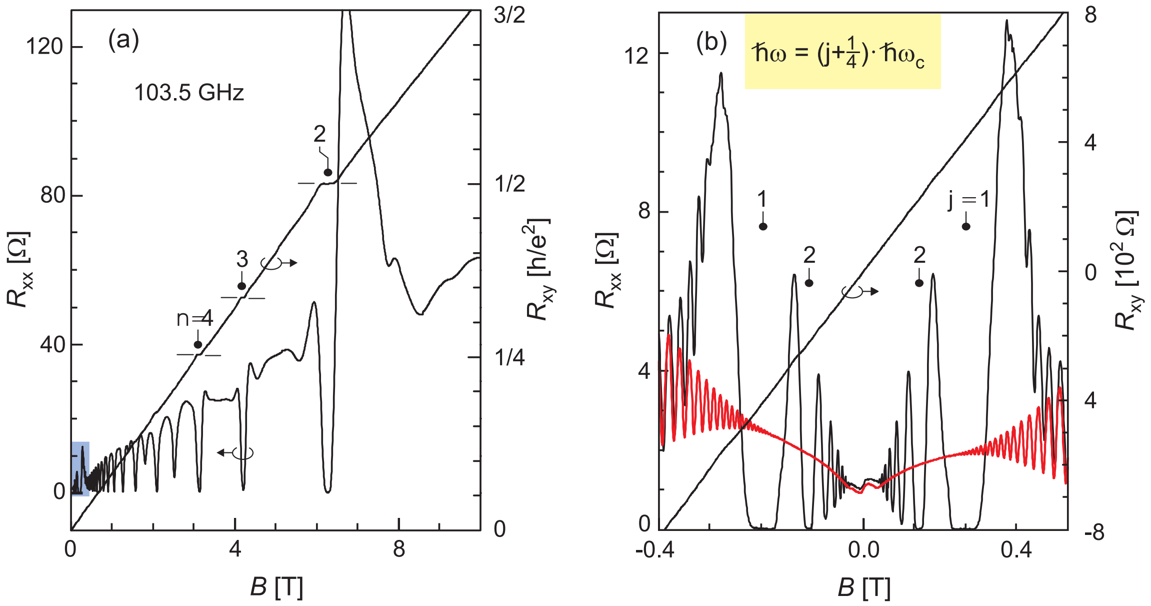

Figure 99: The diagonal (R_{xx}) and Hall (R_{xy}) resistance under 103 GHz excitation at 1.3 K. (a) Large field scan. The quantum Hall effects occur at high B as R_{xx} vanishes. The data above 0.5 T can not be distinguished from traces taken in the absence of microwave radiation. In the blue highlighted region, the diagonal resistance oscillates as a function of ω/ω_c. An expanded high resolution view of this low-field region is shown in (b). The resistance vanishes under radiation in the vicinity of 0.2 and 0.1 T. The red curve represents the low-field R_{xx} data without incident radiation. The Hall resistance is featureless in the presence of radiation on the scale of this figure.

Figure 99(a) shows measurements of the diagonal (R_{xx}) resistance along the direction of the current flow and the Hall (R_{xy}) resistance perpendicular to the current to 10 T, where under microwave excitation at 103 GHz R_{xx} and R_{xy} reveal the usual Shubnikov-de Haas oscillations and quantum Hall behavior for fields above 0.5 T. In contrast, for $B < 0.5$ T where 50 or more Landau levels are filled, a radiation induced signal occurs. An expanded view of the measurement in this low-field regime is displayed in Fig. 99(b). Without EM-excitation, R_{xx} exhibits Shubnikov-de Haas oscillations for $B > 200$ mT. The application of microwaves produces resistance oscillations, which are characterized by the property that the resistance under radiation *falls below* the resistance without radiation. A simple B-field dependent resonant absorption of microwaves can be excluded as a possible explanation as it would heat up the sample and produce an increase of the resistance instead. R_{xx} even vanishes over a broad B-interval about 0.2 and 0.1 T [Mani *et al.*, Nature **420**, 646 (2002)]. Replotting the data on an inverse magnetic field axis unveils that the oscillations are $1/B$-periodic. The frequency-dependent study in Fig. 100(a) demonstrates that the $1/B$-periodicity scales linearly with the applied microwave frequency, so that a given resistance minimum moves to higher fields with increasing microwave frequency. A $1/B$-periodicity is characteristic for resonance phenomena that fulfill the condition $C = (\mathrm{j} + \phi/2\pi)\cdot\hbar\omega_c$. Here, $\hbar\omega_c = \hbar eB/m^*$ is the cyclotron energy with m^* the effective mass of the conduction electrons, j is a natural number $1, 2, \ldots$ and ϕ describes a phase shift of the oscillations. C is the second relevant energy scale in the problem. For the $1/B$-periodic Shubnikov-de Haas oscillations for instance, C equals the Fermi energy and minima occur for zero-phase shift. Another example are magnetophonon oscillations, which are governed by the commensurability of the optical phonon energy $\hbar\omega_{LO}$ and the cyclotron energy. To account for the position of the oscillations in Fig. 99, C has to be substituted by the microwave photon energy and ϕ takes on the value $\pi/2$.

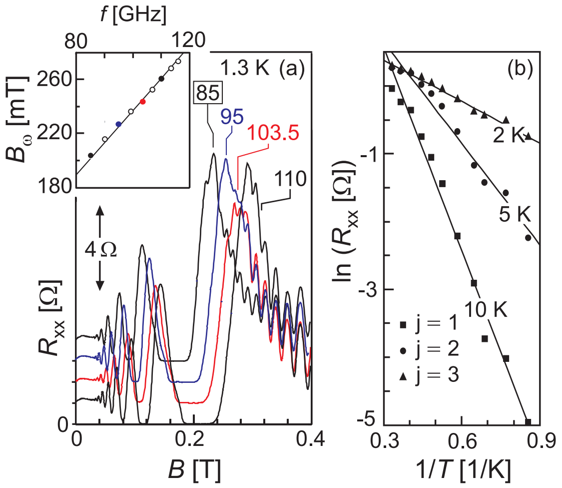

Figure 100: (a) Frequency dependence of the photoresistance. The fundamental field $B_\omega = \frac{1}{\Delta 1/B}$ of the new $\frac{1}{B}$-periodic oscillations drops linearly with decreasing frequency and agrees with the magnetic field position of the cyclotron resonance. (b) Temperature dependence of the magnetoresistance at the principal minima for incident microwave radiation with 85 GHz. The minima display activated behavior and drop exponentially to zero with decreasing temperature. The marked temperatures are extracted activation energies for the first three minima.

As the radiation intensity is enhanced, the amplitude of the oscillations increases. The minimum resistance values saturate as they approach zero and develop a flat bottom as in the quantum Hall regime. A temperature-dependent study, as shown in Fig. 100(b), of the deepest resistance minima suggest activated transport which is normally associated with the existence of a gap at the chemical potential. One might imagine that this exponential temperature dependence and the vanishing of the resistance indicate the formation of a new strongly correlated many-body quantum Hall state. The appearance of a gap would however be difficult to reconcile with the behavior of the Hall resistance. The inevitable disorder-induced localization of charge carriers in the presence of a gap would produce a plateau in the Hall resistance, but in fact the Hall resistivity behaves classically as expected at low magnetic fields and remains largely unaffected by the microwave radiation.

These intriguing experimental discoveries have been confirmed by several other groups and have unleashed a large number of theoretical papers discussing many different possible physical mechanisms. General consensus appears to have been reached that a full theoretical description of this non-equilibrium phenomenon will likely contain two key ingredients. Some mechanism, the precise details of which are still heavily debated, produces a negative contribution to the resistivity and may render the overall resistivity negative for sufficiently large radiation intensities. Such a negative-resistivity state is anticipated to be physically unstable and has led to the inference of a scenario in which current domains form and realize the macroscopic zero resistance observed in experiment.

Despite progress and fair success of the theory in capturing some of the phenomenology of these oscillations and zero-resistance states, many important questions are unresolved. Much the same way as for the quantum Hall effect, this phenomenon suffers apparently a love-hate relationship with disorder that remains largely unexplained. Ultrahigh mobility samples are vital for the observation of the zero-resistances states, but at the same time some of the theory invokes efficient short-range scatterers to outwit Kohn's theorem and circumvent the usual selection rules for transitions between Landau levels with disparate orbital indices. Many of the proposed schemes rely on a Landau ladder of well-resolved levels, at the same time the oscillations occur in a regime where the density of states is at best slightly undulated, since at these fields Shubnikov-de Haas oscillations are not yet resolved. Last but not least, the exponential temperature dependence or activated behavior is entirely unaccounted for.

Plasmon dispersion in sodium at high pressures

I. Loa and K. Syassen; G. Monaco, G. Vanko, and M. Hanfland (ESRF Grenoble)

Probing wavevector-dependent collective electronic excitations (plasmon modes) in condensed matter has been, for many years, the domain of electron energy loss spectroscopy (EELS). With the advent of synchrotron sources, we have witnessed major advances in studying electronic excitations via inelastic X-ray scattering (IXS) spectroscopy. In IXS experiments, photons of typically 10 keV energy are inelastically scattered by electronic excitations in a bulk sample; the energy for collective valence electron excitations of interest here is of the order of 10 eV. Synchrotron-based IXS offers improved energy and wavevector resolution as well as higher photon fluxes compared to experiments using conventional X-ray sources. Compared to EELS, multiple scattering events have a much lower probability.

Historically, the theoretical understanding of the physics behind the collective electronic excitations in metals was mostly based on approximations to the many-body problem in jellium, i.e., the effects of electron-electron correlations. It is only recently [e.g., Ku *et al.*, Physical Review Letters **82**, 2350 (1999); Eguiluz *et al.*, Journal of Physics and Chemistry of Solids **61**, 383 (2000)] that *ab initio* calculations for electrons in metallic systems have addressed the interaction with the lattice, which affects the plasmon dispersion and lifetime to a larger degree than many refinements to the random phase approximation (RPA).

A fundamental parameter in the collective-electron physics of metals is the conduction electron density n; the zero-wavevector plasmon energy ω_P for a free electron gas in 3D is proportional to the square root of n. The application of high pressure is a means to tune n of a given metal, and synchrotron-based IXS opens the possibility for high-pressure spectroscopy of collective excitations because X-rays can penetrate through the beryllium or diamond window of a high-pressure cell. Thus, high-pressure IXS studies are thought to provide valuable input to the emerging new ways of thinking about excitations of interacting electrons in metals.

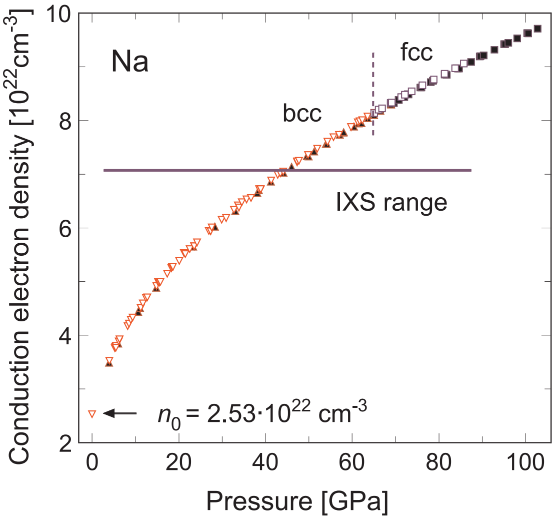

Figure 101: Conduction electron density of sodium as a function of pressure. The horizontal line marked ‘IXS range’ indicates the electron density for the maximum pressure in the experiments described here.

An obvious candidate for exploring the potential of high-pressure IXS experiments is sodium. It is the archetype of a nearly free electron (NFE) metal. Also, sodium is highly compressible, such that the electron density can be varied by a factor of two or more at pressures achievable with diamond anvil cells (Fig. 101). As a consequence, dynamical short-range correlations, expected to be most pronounced at low densities and to vanish in the very-high-density limit, should be affected to some extent, but the electronic bandstructure is also modified significantly.

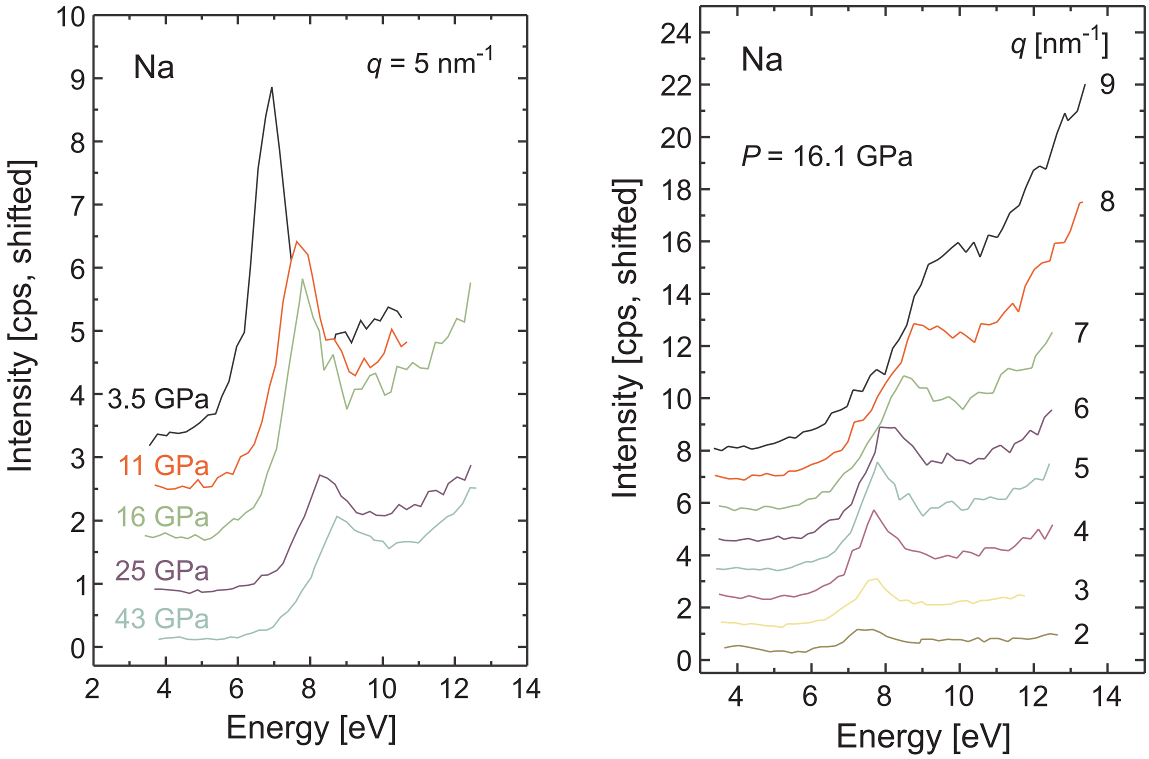

Figure 102: Inelastic X-ray scattering spectra of sodium. The left panel is for constant wavevector transfer at different pressures, the right panel for constant pressure and different wavevectors.

We have measured IXS spectra of sodium at pressures up to 45 GPa, corresponding to nearly three-fold compression and roughly covering the stability range of the bcc-phase. The experiment was performed at the beamline ID16 of the ESRF using 9.7 keV X-rays, a focal spot (on the sample) of about $50 \times 100\,\mu\text{m}^2$, and an experimental resolution of about 0.6 eV.

Representative high-pressure IXS spectra of Na are shown in Fig. 102. They exhibit a well-defined plasmon feature superimposed on a nonlinear background which is mostly due to inelastic scattering by the diamond window. Spectra were not only measured for different pressures, but also for different wavevector transfers at a given pressure in order to determine the plasmon dispersion.

Figure 103 illustrates the effect of pressure on the plasmon energy and width of sodium at a constant wavevector of 5 nm^{-1}. The energy variation expected in a NFE picture, thought to approximately represent the dependence in the RPA, is shown for comparison. The two main observations are that the difference between the free-electron behavior and the observed energies increase dramatically with increasing density and that the linewidth increases too, signalling a reduction in the plasmon lifetime under pressure.

A hint to a possible explanation of the unexpected results for Na follows from similar experiments performed for K and Rb. In contrast to Na, their plasmon energies hardly change with pressure (Fig. 103). Also, the plasmon becomes strongly damped, not being visible any more in spectra taken above 10 GPa. Based on time-dependent density functional theory [Ku and Eguiluz, cited above], it was concluded that the anomalous plasmon damping in K at ambient pressure is governed by single particle excitations involving empty states of *d* symmetry. It is well established that in K and Rb the *d* character of bands near the Fermi level increases

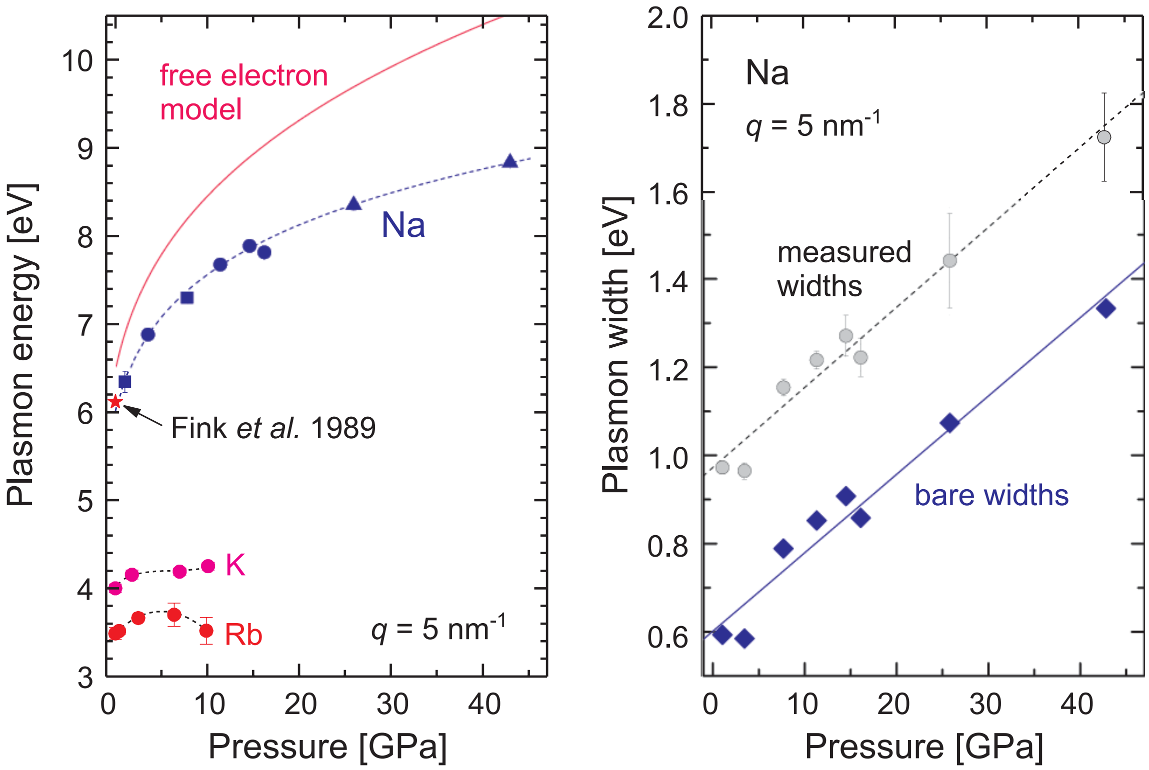

Figure 103: Measured energy and line width of the plasmon line of sodium as a function of pressure at constant wavevector transfer. The free-electron-like behavior for sodium and experimental data for potassium and rubidium are also indicated in the left part. The right frame shows the measured line width and the width corrected for broadening due to limited resolution of the spectrometer.

with pressure. Therefore, our results for K and Rb indicate a strong influence of the bandstructure on the collective excitations, at least for these two heavy alkali metals. Whether this explanation also applies to the anomalous pressure dependence of the plasmon energy and the increased damping under pressure still needs to be explored theoretically.

Based on the high-pressure plasmon IXS studies presented here, we offer three brief conclusions: (i) the study of wavevector-dependent electronic excitations under pressure using IXS is shown to be feasible, (ii) plasmon excitation in solid Na, the archetype NFE metal, exhibit an anomalous dependence on electron density, and (iii) we envision a broader range of applications for IXS in high-pressure research, including the breakdown or transformation of covalent bonds in (carbon-based) solids and the electronic properties of liquid metals.

Synchrotron-based infrared spectroscopy of titanates under pressure

I. Loa, K. Syassen, and X. Wang; Y.-L. Mathis, D. Moss, and B. Gasharova (ANKA, Karlsruhe)

Infrared radiation produced by a synchrotron offers a higher brilliance compared to conventional sources. This makes it possible to study samples of less than 50 μm in size by infrared microspectroscopy at pressures up to the Megabar (100 GPa) region. We report here on the installation of a high-pressure infrared setup at the *Angström-Quelle Karlsruhe* (ANKA) and present selected results of initial experiments on rare earth titanates.

Figure 104: Top: Photograph of a diamond anvil cell for infrared microspectroscopy. Bottom: Photograph of a DAC equipped with a motor drive for pressure change and mounted on the stage of the microscope at the ANKA synchrotron.

In synchrotron infrared spectroscopy, a medium-size diamond anvil cell (DAC) is used for pressure generation (Fig. 104). It fits between two mirror objectives (15×magnification) of an infrared microscope (Bruker IRscope-II). This permits to perform IR experiments both in reflection and in transmission using a Bruker IFS66va Fourier transform spectrometer. With a combination of MCT detector and bolometer, the mid- as well as far-infrared spectral ranges are covered. For *quantitative* reflection and transmission experiments on *single crystals*, the maximum pressure so far amounts to ≈ 30 GPa, due to the combined constraints of the sample size and diffraction effects. Higher pressures can be used in transmission measurements on powder samples.

Transition metal compounds have hardly been studied by high-pressure IR spectroscopy, although they are otherwise subject of extensive research. Our efforts at ANKA aim at filling this gap. Application of high pressure provides a tool to tune the structural and physical properties of a solid. This is particularly promising for transition metal oxides because they often show an intimate interplay of structural, spin, charge, and orbital degrees of freedom. Infrared spectroscopy can then be used to investigate electronic excitations as well as the lattice dynamics.

$LaTiO_3$ and $YTiO_3$ are two Mott-Hubbard-type insulators that have attracted much attention over the last decade. Initially they were studied in the context of high-T_c cuprate superconductors. More recently, the observation of unexpected magnetic properties led to the concept of a so-called *orbital liquid state* in $LaTiO_3$ [Keimer *et al.*, Physical Review Letters **85**, 3946 (2000); Khaliullin *et al.*, Physical Review Letters **85**, 3950 (2000)]. A distorted perovskite-type structure is adopted by both $LaTiO_3$ and $YTiO_3$. Electronically, they are characterized by a single 3*d* electron occupying t_{2g} orbitals. Electron correlation leads to a bandsplitting and an insulating state. In this situation, the energy gap near the Fermi level is an important parameter to describe the electronic properties.

The optical gap of $YTiO_3$ is less than 1 eV. We could directly determine the shift of the absorption edge with pressure by *mid-IR absorption* measurements on high-quality (stoichiometric) single crystals [Lorenz *et al.*, Universität Köln] as shown in Fig. 105. We observe a red-shift of the optical absorption edge, which clearly reflects the trend towards metallization (gap closure) under pressure.

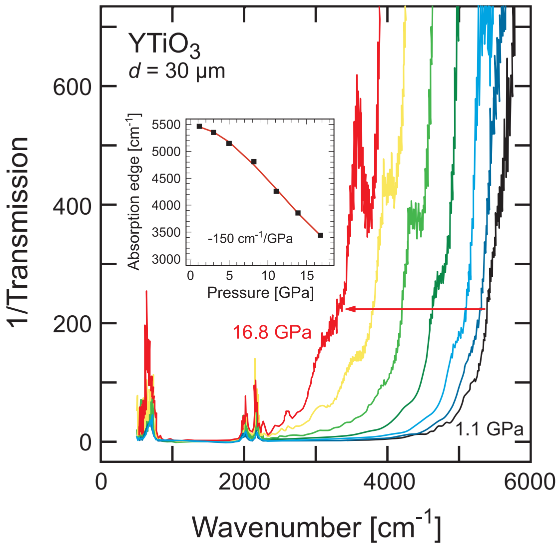

Figure 105: Infrared absorption spectra of YTiO$_3$ under pressure. The shift of the absorption edge towards lower frequencies indicates a pressure-induced closure of the gap. The inset shows the pressure dependence of the absorption edge.

LaTiO$_3$ has a less distorted structure compared to YTiO$_3$ and, as a consequence, a smaller bandgap on the order of 0.1 eV at ambient conditions. Therefore, one should be able to drive the system into a metallic state within the currently available pressure range. The mid-IR *reflection spectra* recorded on a single crystal [Lorenz *et al.*, Universität Köln] under pressure indeed demonstrate a massive redistribution of spectral weight into the IR optical range (Fig. 106). It is an indication for a pressure-driven carrier delocalization in LaTiO$_3$ at quite moderate pressures. This interpretation is supported by modelling the mid-IR reflectance spectra in terms of the spectral dependence of the optical conductivity. A direct determination of the excitation gap in LaTiO$_3$ will be subject of further experiments.

The inset of Fig. 106 shows reflection spectra in the phonon region recorded with a bolometer detector. In the 2.3 GPa spectrum numerous phonon modes can be resolved that separate into three groups. These data are in good overall agreement with recent ambient-pressure results [Lunkenheimer *et al.*, Physical Review B **68**, 245108 (2003)]. The most prominent phonon modes can be followed as a function of pressure up to 15 GPa, although with a decreasing signal-to-noise ratio. The increasing reflectance due to the electronic changes leads to a diminishing amplitude of the phonon-related features. Altogether, these results demonstrate the possibility to also study the lattice dynamics by IR spectroscopy at high pressures.

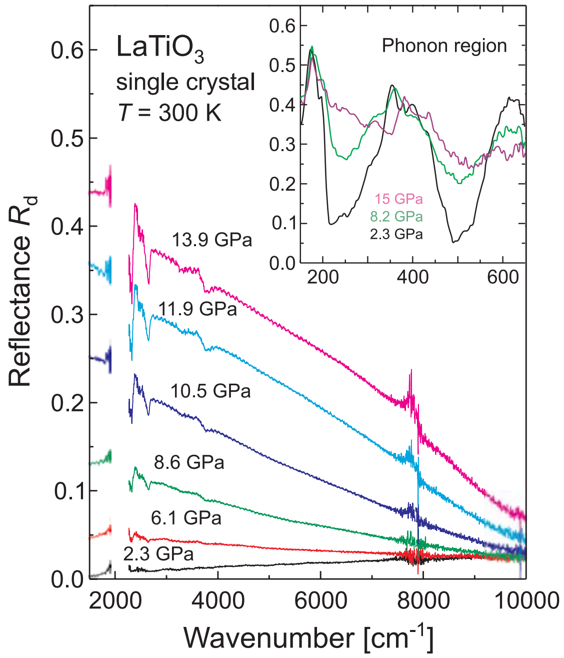

Figure 106: Pressure-driven insulator-to-metal transition in LaTiO$_3$ probed by IR reflectance spectroscopy. R_d refers to the reflectance at the interface between sample and diamond anvil which are in direct contact. The inset shows the reflectance in the phonon region.

In summary, the recently installed high-pressure option at ANKA makes it possible to investigate electronic and phononic excitations of solids in the mid- and far-infrared region. Using this setup, we investigated the pressure-induced gap closure and trends towards metallization in YTiO$_3$ and LaTiO$_3$. In combination with our detailed X-ray diffraction studies of YTiO$_3$ and LaTiO$_3$ under pressure, the experiments provide input for testing recent developments in the electronic structure theory of correlated electron systems, such as the *Dynamical Mean Field Theory* approaches pursued in the departments of Andersen and Metzner.

Effective tunable THz pulse generation by optical rectification of ultrashort laser pulses with tilted pulse fronts

J. Hebling, A.G. Stepanov, and J. Kuhl

During the last decade, time-domain THz spectroscopy and imaging have become widely used techniques in various fields of physics, chemistry and biology. The access to the interesting THz spectral region, which has remained almost unexplored for a long time, has been enabled by rapid progress in two fields: (1) the development of powerful THz sources such as photoconductive switches irradiated by ultrashort laser pulses or optical rectification of femtosecond laser pulses in nonlinear crystals and (2) the development of sensitive THz detection schemes utilizing, e.g., electrooptic sampling of THz fields with femtosecond optical pulses or photoconductive autocorrelation techniques.

Probably one of the most important present challenges of THz technology is up-scaling of the THz pulse energy to a level suitable for nonlinear spectroscopy. As usual for nonlinear processes, generation of high-energy pulses requires phase matching between the optical and the THz pulses. Above the TO phonon frequency of the nonlinear crystal, this can be accomplished by angle tuning in birefringent crystals. This technique does not work, however, below the TO-frequency due to the strong contribution of the lattice vibration to the dielectric function.

Here we describe a novel phase matching technique, which applies laser pump pulses with a tilted intensity front [Hebling *et al.*, Optics Express **10**, 1161 (2002); Stepanov *et al.*, Applied Physics Letters **83**, 3000 (2003)] thus reducing the effective velocity of the visible pulses to the velocity of the THz wave and creating THz pulses with energies of several 100 pJ. The experimental setup consists of a MIRA/REGA Ti:sapphire oscillator-amplifier system supplying 170-fs-long pump pulses at 800 nm with up to 2.3 μJ energy at 200 kHz repetition rate. A 2000 lines/mm grating is applied to tilt the intensity front of the pump pulses and a $f = 60$ mm lens is used to image the spot of the pump beam on the grating with a demagnification of 2 into a stoichiometric LiNbO$_3$ (LN) crystal with only 0.6 mol% Mg doping which is still sufficient to prevent photorefractive damage but has significantly lower absorption in the THz range than LN crystals with higher Mg doping [Hebling *et al.*, Applied Physics B **78**, 593 (2004)].

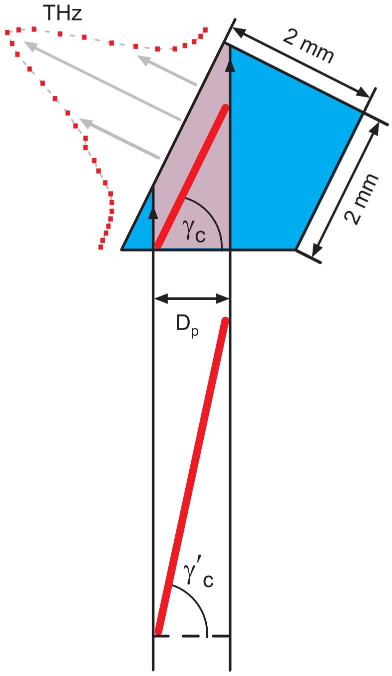

Figure 107: The scheme shows the LiNbO$_3$ crystal piece in blue, in red color the tilted intensity front of the pump pulse before and after entering the crystal, and the spatial distribution of the THz radiation leaving the crystal.

Figure 107 illustrates the tilted front of the pump pulse before and after entering the crystal, the crystal size and shape and the measured spatial distribution of the emitted THz pulse. The tangent of the tilt angle is reduced by the group refractive index of the LN when the pump pulse enters the crystal. This effect was taken into account in the calculation of the tilt angle for a given geometry characterized by angles of incidence and diffraction on the grating and demagnification of the lens. The excitation of an extended plane THz wave leads to a rather low THz beam divergence.

A calibrated liquid He cooled Si bolometer was used to measure the average power of the THz pulses. The spectra of the THz pulses are obtained by Fourier transformation of the amplitude autocorrelation curves that were recorded by double-pulse excitation inserting a Michelson interferometer into the pump beam path, which provides a variable delay between the two pulses. The temporal shape of the THz pulse was determined by electrooptic sampling using a 0.6-mm-thick ZnTe crystal.

Using 2.3 μJ pump pulses, we have generated THz pulses with energies of 100 pJ and 400 pJ at 300 K and 77 K, respectively. The energy conversion efficiency of $1.7 \cdot 10^{-4}$ at 77 K is equivalent to a quantum efficiency (QE) of 3.4%, which is more than 50 times higher than the value achieved for rectification in birefringently phase-matched GaSe in spite of the 250 times smaller pump pulse energy. One explanation for this high efficiency is the higher nonlinearity of LN compared to that of GaSe [Hebling *et al.*, Applied Physics B **78**, 593 (2004)]. The second reason is the 1 mm effective length of our LN, which exceeds the length of the GaSe crystal by a factor of 5. Interestingly, this QE also exceeds the value obtained by quasi-phase matching in periodically poled $LiNbO_3$ (PPLN) by more than one order of magnitude. It is worth to mention that a simple theoretical model even predicts a still 100 times higher QE. Thus there exists hope that the QE can be further increased if the imaging of the tilted pulse intensity front into the nonlinear crystal can be improved.

400 pJ pulse energy and 200 kHz repetition rate correspond to an average power of 80 μW. Since the THz pulse duration is shorter than 1 ps, the peak power amounts to more than 400 W. The THz pulses are emitted from an area of less than 1 mm^2. Without any focusing the intensity at the crystal is larger than 40 kW/cm^2, and the peak electric field amplitude is close to 6 kV/cm. Therefore, we can conclude that the THz pulses delivered by our source are appropriate for nonlinear optical measurements in the FIR spectral range.

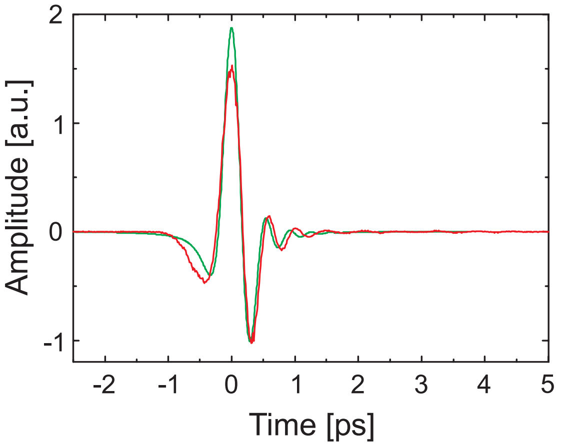

Figure 108: Calculated (green) and measured (red) electrooptic signal of the generated THz pulses.

The electrooptically sampled signal of the THz pulses generated in the LN crystal at room temperature (red line in Fig. 108) consists of about one and a half oscillations with a duration shorter than 1 ps followed by a few oscillations with significantly smaller amplitudes. The figure also shows the convolution of the temporal shape of the THz pulse calculated by our simple model with the NIR probe pulse (obtained from the pump pulse) that was applied for electrooptic sampling. Considering that we did not take into account the absorption and dispersion of the ZnTe crystal used for sampling, the measured signal shape agrees fairly well with the calculated signal (green line in Fig. 108).

Figure 109(a) depicts spectra of the THz pulses generated at 10 K using a few different tilt angles γ between 59° and 64°. These experimental data show good agreement with calculated spectra presented in Fig. 109(b). The variation

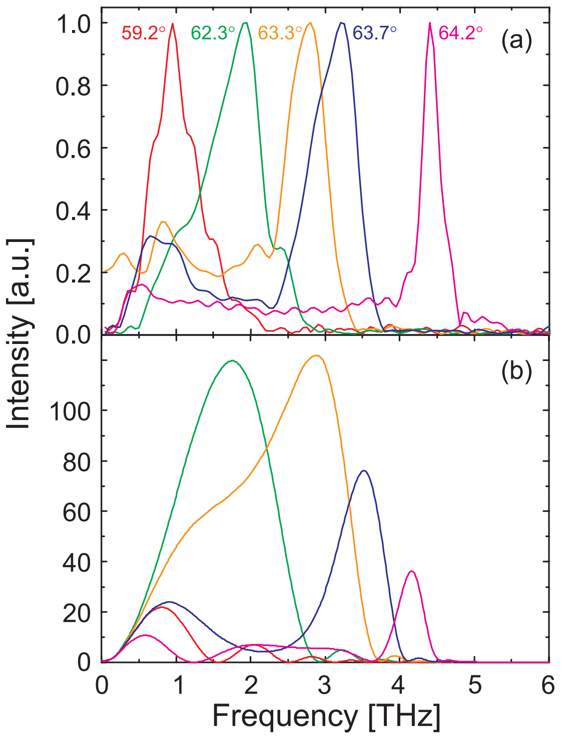

Figure 109: (a) Spectra of the THz pulses measured for different tilt angle γ. The maxima of the spectra are normalized. (b) Calculated spectra of THz pulses generated in 1.5-mm-long $LiNbO_3$ at $T = 10$ K by optical rectification of 170-fs-long NIR pulses. For the green, orange, blue, and magenta curve, velocity matching for 1, 100, 120, and 140 cm^{-1}, respectively, has been assumed. The red curve is calculated for a group velocity of the pump pulses being 2% faster than the phase velocity of the 1 cm^{-1} THz radiation.

of the center frequency and pulse energy as a function of the pulse front tilt angle are plotted in Fig. 110. It should be noticed that the pulse energies represent the measured values without any correction taking into account the frequency dependence of the detector sensitivity. The drop of the THz pulse energy below 2 THz probably is partly due to the decreasing sensitivity of the bolometer. Figure 110 demonstrates tuning of the THz output across the range of 1.0–4.4 THz. Whereas the high-frequency limit results from the increasing absorption in $LiNbO_3$ and the finite bandwidth of the NIR 170 fs pump pulses (corresponding to a bandwidth of approximately 2.5 THz), the energy drops at low frequency because the efficiency is proportional to the square of the frequency.

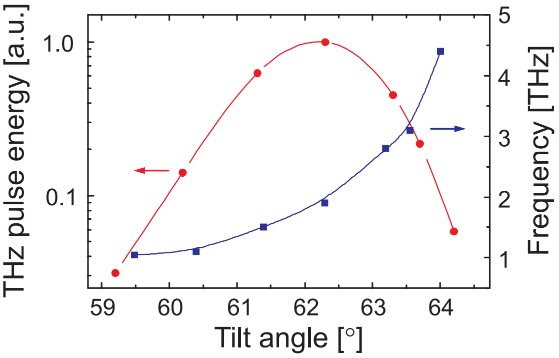

Figure 110: Dependence of the energy and frequency of the THz pulses on the tilt angle γ. The lines are guides to the eye.

In summary, we have described generation of THz pulses via optical rectification in $LINbO_3$ with low MgO doping level using pump pulse front tilting for phase matching. Employing 2.6 μJ pump pulses in the NIR, we have demonstrated a record quantum conversion efficiency of 3.4% and tunability of the THz peak frequency between 1.0 and 4.4 THz. Model calculations predict narrower THz spectra and a broader tuning range for our technique if shorter NIR pulses are used and $LiNbO_3$ is replaced by GaSe.

Observation of strong coupling in metallic photonic crystal slab structures

A. Christ, T. Zentgraf, and J. Kuhl;
S.G. Tikhodeev and N.A. Gippius (General Physics Institute Moscow);
H. Giessen (Universität Bonn)

Metal nanostructures have attracted considerable attention in recent years due to their surprising optical properties. Especially the important class of so-called *polaritonic* photonic crystal structures has gained widespread interest because of their ability to control electronic and photonic resonances simultaneously [Christ *et al.*, in Photonic Crystals, Ed. Föll, Wiley, 2004]. Prominent examples are periodically modulated metal surfaces, including surface corrrugation and hole arrays. The particular optical properties of these metallic nanostructures can be attributed to the excitation of particle or surface plasmons which are a consequence of collective oscillations of the conduction band electrons. Thus, their impressive possibilities of tailoring the light-matter interaction already have inspired the development of various nanooptical devices for future technical applications.

Here, we present results on another important new realization of such metallic photonic crystal structures. We used one-dimensional (1D) periodic gold nanowire arrays deposited on top of a dielectric waveguide as an ideally suited model system. Such a photonic crystal slab (PCS) structure provides simultaneous particle plasmon resonances and optical waveguide modes in the same energy range, which can be controlled separately by changing the geometrical parameters of the structure [Linden *et al.*, Physical Review Letters **86**, 4688 (2001)]. It is obvious that different interaction phenomena have to be taken into account for a detailed analysis of such a PCS. Although near-field coupling effects play an important role for periods with $d \sim a$ (where d is the distance between the nanostructures and a is their characteristic size), we will concentrate on optical far-field interaction effects for structures with periodic modulation on a length scale comparable to optical wavelengths with $d \gg a$. In the following we demonstrate clear evidence of strong coupling between electronic and optical modes [Christ *et al.*, Physical Review Letters **91**, 183901 (2003)]. In principle, all phenomena reported in this work also occur for two-dimensional gold nanocluster arrays deposited on top of dielectric substrates. However, the nanowire structure is advantageous for highlighting the coupling effects since the particle plasmon resonance can be turned off for measurements with light polarization parallel to the gold nanowires.

Figure 111(a) displays a schematic view of our sample structure and the experimental measurement geometry. Gold grating structures were prepared by electron beam lithography on top of 140-nm-thick indium tin oxide (ITO) waveguide layers on top of a quartz substrate. Samples with grating periods d_x between 300 nm and 600 nm have been produced. The nanowire height of 20 nm and the wire width of 100 nm were kept fixed for all samples. The grating extension was restricted to $100 \times 100\,\mu\text{m}^2$ due to limitations of the electron beam writing system. In order to demonstrate the effect of the waveguide modes, an additional second set of identical grating structures was prepared on top of a non-waveguiding 15-nm-thick ITO layer. A conventional white light transmission setup with a small aperture angle of 0.2° was used for recording period and angle-dependent extinction spectra. Also distinct light polarizations (linear) could be selected by either turning the electric (TE) or the magnetic (TM) fields parallel to the wires. Theoretical spectra have been calculated by a scattering matrix based formalism.

An excellent theoretical description of the experimental results has been obtained without additional fitting parameters, using the known dielectric constants and the measured geometrical properties of the structure as input parameters.

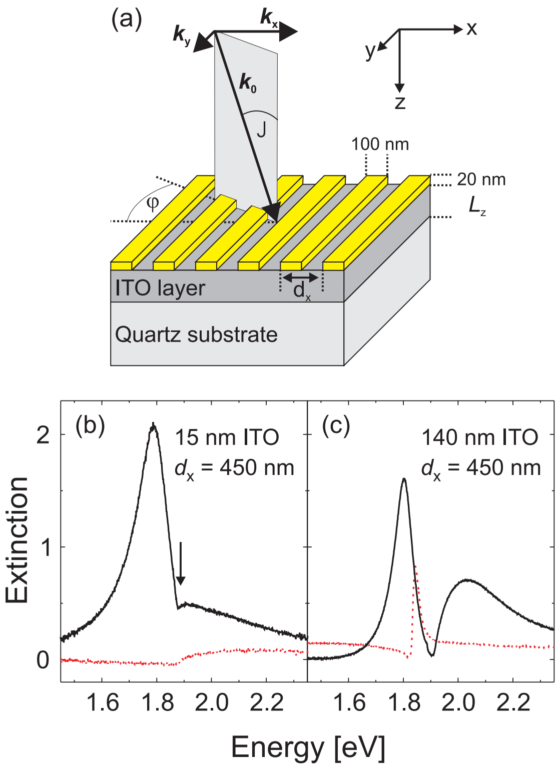

Figure 111: (a) Schematic view of the gold nanowire array on top of an indium tin oxide (ITO) layer. Period-, angle-, and polarization-dependent transmission measurements are possible. Spectra of samples with (b) 15-nm-thick and (c) 140-nm-thick ITO layers are shown for comparison in TE (dotted red lines) and TM (solid lines) polarization for a period of $d_x = 450$ nm at normal incidence. The arrow in (b) marks the position of the Rayleigh anomaly.

The waveguide induced modifications of the nanowire extinction spectra can be observed by comparing Fig. 111(b) and (c) for TE and TM polarization, respectively. Exemplary, measured spectra of gold nanowire arrays with identical periods of $d_x = 450$ nm are shown in this figure for sample structures with 15-nm-thick (b) and 140-nm-thick ITO layers in this figure. As common for metal nanowires, particle-plasmon-like resonances can only be observed for TM polarization and therefore oscillation of the conduction band electrons perpendicular to the metal wires. While the nanowire plasmon resonances of structures with non-waveguiding substrates are only influenced by Rayleigh type anomalies (cusp-like anomalies, marked by an arrow in panel (b)), associated with the opening of new diffraction orders into the quartz substrate, the thicker ITO waveguide induces a more complex spectral shape in panel (c). Now the spectra for TE and TM polarization are characterized by an additional extinction maximum due to the excitation of the lowest TE or TM waveguide modes.

For a more detailed analysis of the waveguide induced modifications, we have to consider the period-dependent measurements of Fig. 112. In this figure, (a) measured and (b) calculated extinction spectra of gold nanowire arrays deposited on top of 140-nm-thick ITO layers are shown for normal light incidence and grating periods d_x ranging from 375 nm to 575 nm in TE and TM polarization. Additionally, the extracted dispersion of the extinction maxima is shown for the more relevant case of TM polarization in panel Fig. 112(c) in dependence on d_x.

As already shown in Fig. 111(c), all depicted TE spectra are characterized by a single and spectrally asymmetrically shaped resonance. In our measurement geometry, these features arise due to the grating induced Bragg resonance of the lowest TE waveguide modes (quasi-guided or leaky modes). Therefore a change of the Bragg condition caused by increasing the grating period results in a shift of this Fano-type resonance to lower energies. Generally, such modes are characterized by relatively long lifetimes and large quality factors and can lead to resonantly enhanced fields inside the PCS structures.

In contrast to the case of TE polarization, all depicted spectra show two extinction maxima for TM polarization. A broader nanowire plasmon resonance appears around 1.9 eV (e.g., d_x =375 nm), in addition to a narrow peak

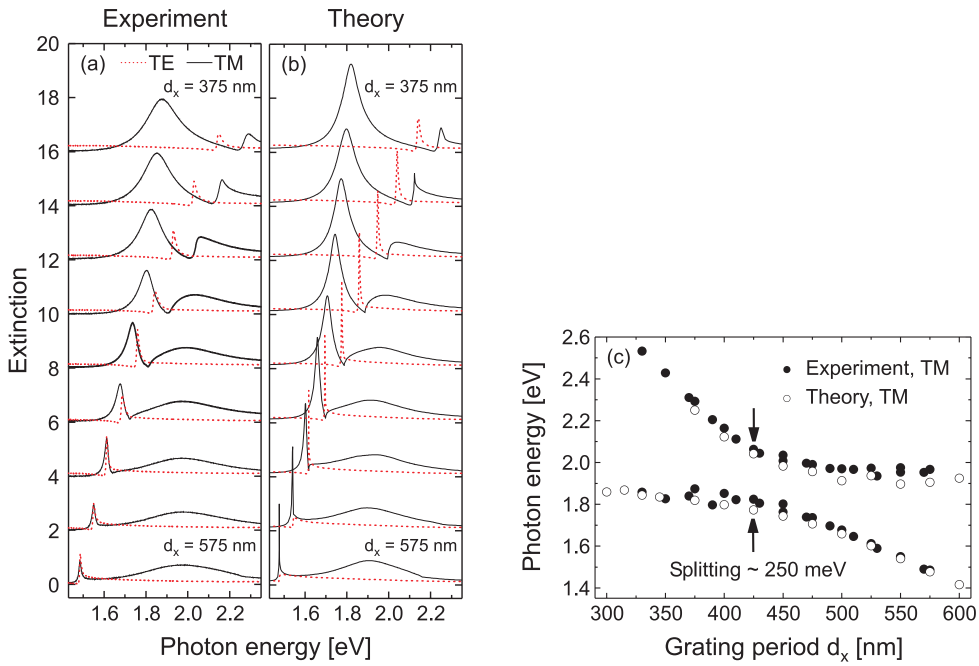

Figure 112: (a) Measured and (b) calculated extinction spectra of gold nanowire arrays deposited on top of 140-nm-thick ITO layers for normal light incidence and nanowire periods d_x ranging from 375 nm to 575 nm in steps of 25 nm. The individual spectra are shifted upwards for clarity in each panel. The extracted extinction maxima are shown in panel (c) in dependence on d_x for TM polarization.

due to the excitation of the lowest TM quasi-guided modes. Due to the fixed nanowire dimensions for the whole sample series, only the quasi-guided waveguide mode can be spectrally shifted by increasing the grating period. If waveguide resonance and the nanowire plasmon are then tuned to the same energy range, a clear anticrossing behavior or Rabi splitting of both resonances can be observed. This anticrossing can be easily interpreted in terms of the formation of a new quasiparticle: a *waveguide-plasmon polariton* emerges from the bare modes of the metallic PCS structure, comparable to the normal mode coupling in semiconductor microcavities. Especially the excellent correspondence between the experimental and calculated values and the large Rabi splitting of 250 meV between the lower and upper polariton branches in Fig. 112(c) are very conspicuous.

Additional important features of the strongly coupled waveguide-plasmon system can be extracted from angular-dependent transmission measurements. (a) Measured and (b) calculated extinction spectra for a fixed nanowire period of $d_x = 450$ nm are shown in Fig. 113 for TM polarization. The angle θ is varied between 0° and 20° while $\varphi = 0°$ remains unchanged.

In contrast to the spectra at normal incidence, a third extinction peak appears at inclined incidence. The appearance of this additional resonance can be easily understood, when the waveguide resonance is investigated in more detail. In principle, we have to consider that the periodic surface corrugation will remove the degeneracy of the quasi-guided waveguide modes of the structure, even for measurements at normal incidence. Due to the mirror symmetry of the structure and differences in the field distribution of modes with different symmetry, only the upper symmetric mode can be excited in measurements at normal incidence. As is common for such structures, the lower antisymmetric mode only gets optically active under inclined incidence and shows up as an

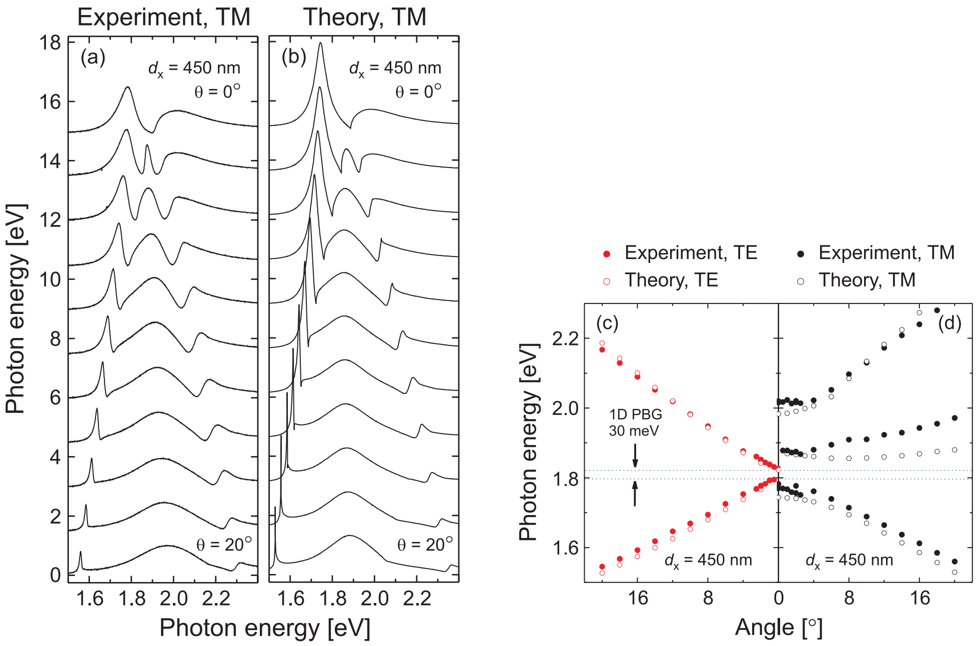

Figure 113: (a) Measured and (b) calculated extinction spectra (TM polarization) for a fixed nanowire period of $d_x = 450$ nm. From top to bottom, the angle θ is increased from 0° to 20° in steps of 2° while $\varphi = 0°$ remains unchanged. Measured (solid circles) and calculated (open circles) positions of the extinction spectra maxima in (c) TE and (d) TM polarization for a nanowire period of $d_x = 450$ nm. The arrows show the full 1D photonic band gap.

additional resonance in TE and TM polarization. Therefore the spectra of Fig. 113(a) and (b) have to be explained by the interaction of three resonances. Both waveguide modes shift in opposite directions for increased angles θ (additional in-plane momentum), therefore reducing the spectral overlap and coupling efficiencies.

In Fig. 113, the angle-dependent dispersion of the different polariton branches is shown for a nanowire period of $d_x = 450$ nm in TE (c) and TM (d) polarization separately. It is clearly visible that at the center of the first Brillouin zone a small stop band independent on polarization appears for light propagating in the *z*-direction. Near the plasmon resonance, such a behavior is directly connected with the opening of a full 1D photonic bandgap of 30 meV for light propagating in the waveguide along the *x*-direction. This feature is a promising property of metallic PCS structures which may be of importance for creating defect waveguides and microresonators based on such PCS.

We would like to remark that similarly strong coupling phenomena of gold nanowires and optical resonances must be observable for single gold nanoparticles in the center of dielectric photonic crystal microcavities with high Q-factors. A large Rabi splitting is predicted for this case too.

In conclusion, we have presented experimental and theoretical results, which reveal new coupling phenomena in metal based photonic crystal slab structures. Especially, a large Rabi splitting of 240 meV was found due to strong coupling of optical waveguide modes and nanowire particle resonances. Considerable advantages for the design of novel nanooptical devices may arise by using these new physical phenomena.